THE APEX SOUTHERN SKY SURVEY OF HIGH MASS STAR FORMING REGIONS

Dissertation

zur

Erlangung des Doktorgrades (Dr. rer. nat.)

der

Mathematisch-Naturwissenschaftlichen Fakultät

der

Rheinischen Friedrich-Wilhelms-Universität Bonn

vorgelegt von

Carolin Dedes

aus

Bochum

Bonn, Dezember 2008

Angefertigt mit Genehmigung der Mathematisch-Naturwissenschaftlichen Fakultät
der Rheinischen Friedrich-Wilhelms-Universität Bonn

1. Gutachter: Prof. Dr. K. M. Menten
2. Gutachter: Prof. Dr. P. Kroupa

Tag der Promotion: 27.02.2009

Diese Dissertation ist auf dem Hochschulschriftenserver der ULB Bonn unter
http://hss.ulb.uni-bonn.de/diss_online elektronisch publiziert.
Erscheinungsjahr: 2009

Für Leonidas
und meine Familie

για τον Λεωνιδα
και την οικογενεια μου

Contents

1 Introduction **1**
1.1 Massive star formation . . . 1
1.1.1 Theory . . . 2
1.1.2 Observations . . . 3
1.2 Motivation . . . 4
1.3 The source sample . . . 6
1.4 Outline . . . 7

2 The Atacama Pathfinder EXperiment **9**
2.1 General description . . . 9
2.2 DSB receivers . . . 10
2.3 Frontends and backends . . . 11
2.3.1 Frontends . . . 11
2.3.2 Backends . . . 12
2.4 Observing strategy . . . 12
2.5 Commonly encountered observing problems . . . 13
2.6 Data reduction . . . 14

3 Pilot Study **17**
3.1 Introduction . . . 17
3.1.1 Source details . . . 18
3.2 Observations and data reduction . . . 19
3.2.1 Atacama Pathfinder EXperiment . . . 19
3.2.2 ATCA . . . 21
3.3 Observational Results . . . 21
3.3.1 Line data . . . 21
3.3.2 Continuum data . . . 22
3.4 Derivation of physical parameters . . . 29
3.4.1 LTE modeling . . . 29
3.4.2 Spectral energy distributions . . . 40
3.4.3 Spectral types . . . 43
3.4.4 Mass estimates . . . 43
3.5 Molecular outflows . . . 46
3.6 Discussion . . . 49
3.6.1 Molecular line data . . . 49

3.6.2 Continuum data . . . 51
3.7 Conclusions . . . 54

4 Dust Continuum studies **55**
4.1 Introduction . . . 55
4.1.1 Connection with other samples . . . 55
4.1.2 Observations . . . 56
4.2 Results . . . 56
4.2.1 Distances . . . 56
4.2.2 Source identifications . . . 57
4.2.3 Morphology and multiplicity . . . 58
4.2.4 Masses, densities and linear diameters . . . 58
4.2.5 Radial fits . . . 60
4.2.6 Sample B - outer Galaxy . . . 61
4.3 Discussion . . . 68
4.3.1 Dust properties . . . 68
4.3.2 The infrared environment . . . 77
4.4 Conclusions . . . 81

5 Molecular line surveys **83**
5.1 Introduction . . . 83
5.1.1 Observations . . . 83
5.2 Infall study . . . 84
5.2.1 CO, HCO^+ . . . 84
5.3 Line surveys . . . 85
5.3.1 Hot cores . . . 88
5.3.2 Virial masses . . . 89
5.3.3 Outer Galaxy line survey . . . 89
5.4 Discussion . . . 92
5.4.1 Line profiles . . . 92
5.4.2 Line survey . . . 93
5.4.3 Hot cores . . . 98
5.4.4 Virial masses . . . 99
5.4.5 Turbulent core model . . . 101
5.4.6 Outer Galaxy sample . . . 102
5.4.7 Conclusions . . . 105

6 Summary & Outlook **107**
6.1 Summary . . . 107
6.1.1 Three luminous southern hemisphere hot cores . . . 108
6.1.2 Dust continuum survey . . . 108
6.1.3 Molecular line surveys . . . 109
6.2 Outlook . . . 110
6.2.1 Turbulent support or gravitational collapse? . . . 110
6.2.2 Distance estimates . . . 110

6.2.3 Chemical properties 111
6.2.4 Stellar environment 111

Acknowledgments **113**

A **115**
A.1 Tables 115
A.2 Figures 175
A.3 Report 213

Bibliography **221**

Chapter 1

Introduction

1.1 Massive star formation

Massive stars ($M > 8$–$10\ M_{\odot}$) are important building blocks of galaxies. Despite being rare, they provide most of the luminosity and heavily influence their surroundings through energetic interactions throughout their short lifetime. Supernovae and massive winds feed chemically enriched material back into the interstellar medium, mixing it up and creating turbulent motions. On the small scales, their presence influences the creation of stars and planets (Bally et al., 2005) as well as the chemical and kinematical structures of whole galaxies on the large scales (Kennicutt, 2005). A further understanding of the role of massive stars involves understanding their formation processes.

In the case of low mass star formation, a sequential formation mechanism has been proposed (i.e. André et al., 2000), where a so-called class 0 source accretes material from the surrounding envelope, dispersing it in the process and eventually turns into a pre-main-sequence star surrounded by a proto-planetary disk (Guilloteau & Dutrey, 2008).

For massive stars however, studying the stages of star formation is severely hindered by the facts that they are very rare, have a short lifetime, (hence their earliest stages are even more difficult to detect), are on average far away and form exclusively in clusters. The latter two points imply that when observing massive star forming regions, one is likely observing the whole cluster in a single dish beam.

In the last decade, much progress has been made in trying to answer if massive star formation can be explained with a scaled up version of the low mass accretion model for star formation, or if new mechanisms have to be found. While the fact that collimated outflows have been observed towards massive stars of luminosities equivalent to B-type stars (Beuther & Shepherd, 2005) seems to indicate that massive star formation does occur as a scaled up version of low mass star formation up to stars of about $30\ M_{\odot}$, one has to consider that there are nonetheless very different physical processes involved in massive star formation. Zinnecker & Yorke (2007) discuss in detail why massive star formation cannot just be a scaled up version of low mass star formation, naming photoevaporization of the massive accretion disks, feedback on the surrounding material through non-ionizing UV flux and radiation driven bipolar winds as processes which are unique to high mass star forming regions.

In the following two sub-sections, I will give a short, by no means exhaustive overview of the current theoretical and observational status of massive star formation.

In this work, the terms “massive star formation” and “high mass star formation” are used concurrently. When talking about massive star formation, particularly when comparing observations to theory, there can be a misconception about the words “clumps” and “cores”. In this work, a clump denotes the whole region of massive star formation resolvable with a single dish telescope, i.e. $10''$–$20''$ or 0.2–0.4 pc at a distance of 4 kpc. A clump can harbor several cores, in which the star formation takes place.

1.1.1 Theory

For a long time, the main obstacle for the formation of massive stars was seen in the radiation pressure on the infalling dust grains halting the accretion process (Wolfire & Cassinelli, 1987; Yorke & Sonnhalter, 2002). Several models were developed to explain how this obstacle could be overcome. There are three main pathways to be discussed.

- In the first model, the formation is thought to proceed through monolithic collapse and disk accretion (Yorke & Sonnhalter, 2002; Krumholz et al., 2005), which assumes that the natal material has already been assembled in a massive turbulent pre-stellar core (McKee & Tan, 2003).

- In the second model, a star forming in a globally collapsing cluster sweeps up cluster material in competition with its companions and grows through Bondi-Hoyle accretion (e.g. Bonnell & Bate, 2006). Zinnecker & Yorke (2007) describe this process of competitive accretion as *location, location, location* and *the rich get richer*, since a forming star with a prime location in the center of a cluster can accrete more material and the more massive a forming star starts out, the more material it can sweep up.

- The third model, which is thought nowadays only to occur in the most extreme environments is that of stellar mergers and coalescence (Bally & Zinnecker, 2005), in which low and intermediate mass stars are formed and merge to higher mass stars in the densely packed centers of stellar clusters.

A sequence of massive star formation proposed by Zinnecker & Yorke (2007) starts with gravitationally bound turbulent cold and dense cores that develop into hot, dense massive cores once the central object started to heat up its surrounding gas. In this stage also collimated outflows and masers appear. The object then reaches the zero age main sequence (ZAMS) and starts to burn hydrogen (Palla & Stahler, 1992, 1993) while accreting its mass through disk accretion. The fact that a massive star will continue accreting while having reached the ZAMS already constitutes one of the major differences with the low mass star formation process. Technically speaking there are no massive proto-stars, since a protostar is thought to be at the stage where it gets most of its luminosity from accretion. When the word protostar is used in this work, one has to keep in mind that it refers to a high mass object that is still accreting.

1.1.2 Observations

The definition of an evolutionary sequence of massive star formation from an observer's point of view is highly debated, and I will just give one example which has the most relevance to this work. Beuther et al. (2007) classify the sequence of massive star formation as follows:

- High mass starless cores, which are dense, cold and IR quiet
- High mass cores which harbor accreting low- and intermediate mass objects
- High mass proto-stellar objects – proto-stars $> 8M_{\odot}$which might or might not have formed hot molecular cores and hyper-compact HII regions yet
- Final stars

With a rough approximation, one can show that the number of accreting early O-type massive stars in our Milky Way is about three per 1 kpc^2 (Zinnecker & Yorke, 2007), making it an extremely tedious search to detect them. In addition, their earliest stages are heavily obscured in the optical and infrared regimes through their natal dust cocoons.
From an observational point of view, the study of high mass star formation is taking a huge step forward with the availability of new sub-mm instruments such as the Atacama Pathfinder EXperiment (APEX) and the Submillimeter Array (SMA).
The mm and sub-mm regimes are very well suited to study the formation of massive stars, since the earlier stages of this process are deeply embedded in their natal dust clouds, which obscures all optical light. In the mm regime, one can observe rotational transitions of many molecules which are evaporated off the dusty grain mantles in the hot core stage or formed subsequently from evaporated ones. The sub-mm regime however is especially useful to study massive star formation, since at these frequencies, many light species have their transitions and many molecules exhibit higher excited transitions and let us probe the hot dense gas deep inside the star forming cores.
The optimum solution to study high mass star forming regions in depth would be to observe a large number of sources in a wide frequency range, which is not yet feasible. In the past, there have been many studies of limited frequency setups on individual sources (see Beuther et al. (2006b), Olmi et al. (2003), MacDonald et al. (1996), Cesaroni et al. (1994) to name a few). While this kind of line surveys allow a good classification of the studied sources, as has been done in such prominent cases such as Orion-KL (Blake et al., 1996; Schilke et al., 2001; Comito et al., 2005; Beuther et al., 2006a) and Sgr B2 (Sutton et al., 1991; Turner, 1991; Nummelin et al., 2000; Friedel et al., 2004), one needs to study the conditions in a statistically significant sample of sources to be able to describe global properties of high mass star formation.
Such surveys have mostly been performed on the northern hemisphere with only a very limited frequency range (Sridharan et al., 2002; Mueller et al., 2002; Molinari et al., 2002; Shirley et al., 2003; Churchwell et al., 1992). On the southern hemisphere, Purcell et al. (2006) and Urquhart et al. (2007b) have performed line surveys in the mm regime. The earliest stages of cold dark clouds have been studied e.g. by Carey et al. (2000) and Pillai et al. (2006). In addition, many samples of high mass star formation regions have been observed in the dust continuum, such as Beuther et al. (2002a); Faúndez et al. (2004); Hill et al. (2005)

and Beltrán et al. (2006).

High spatial resolution observations of massive star forming regions like G9.62+0.19 (Liu, 2005) display the traces of a wide range of objects at different evolutionary stages, such as hot molecular cores and UCHII regions. In addition, the occurance of molecular outflows and photon dominated regions (PDRs) adds complexity to the high mass star forming regions. Interferometers are needed to resolve the regions spatially and disentangle the different contributions from the numerous objects most likely picked up by the single dish beam.
Commissioning for the Atacama Large Millimeter Array (ALMA) is scheduled to begin in 2009 on the Chajnantor Plateau in Chile. With ALMA, it will be possible to resolve high mass star forming regions at distances of 10 kpc with resolutions of a few hundred AU (Cesaroni, 2008)!
While ALMA will be able to reveal unprecedented detail about the small scales in the massive star forming regions, the study of high mass star forming regions with single dish telescopes gives us valuable insight into the properties of the large scale structures of the regions, such as global infall, mass reservoirs in the clumps and the evolution of the clumps themselves. To properly understand the details which ALMA will deliver in the future, it is necessary to place them in the context of the evolutionary stages derived from the large scale studies.
Using single dish telescopes does not limit us to study only the large scale structures. With high excitation lines observed in a source, the small scales of the cores are probed even with them.

1.2 Motivation

When ALMA will be fully operational to study the southern sky, it will be necessary to have a catalog of high mass proto-stellar objects to observe at high resolution. Most of the studies of the well-studied hot cores and the samples of high mass star forming candidates defined by Molinari et al. (2002) and Sridharan et al. (2002) have targeted the northern hemisphere.
While a single dish instrument cannot resolve details of the high mass star forming regions at large distances, it is an important tool to study the global parameters of the regions and effectively "zoom" into the small scales of the hot cores with high excitation lines. To be able to pick out interesting candidates for further high resolution studies, the single dish data help us to study dust morphologies and radial profiles, the associations with IR sources, the molecular content and to discover line rich sources (hot molecular cores). The corresponding single dish surveys in the north have triggered many high resolution follow-ups that led to important new insights into the formation process of high mass star formation by detecting highly collimated outflows (Beuther & Shepherd, 2005) and evidence for accretion disks (Cesaroni et al., 2007).
In this work, I defined and studied a sample of high mass star forming candidates in the southern hemisphere. The sample was chosen similar to the sample of Sridharan et al. (2002) (see section on the source sample for a discussion of the selection criteria). The 47 sources were

not only observed in the 870 μm dust continuum but a partial line survey between 336.9 and 338.9 GHz has been done for a subsample of 31 sources. The sample was selected to include both radio-quiet and radio-loud sources, which might be regarded as an early and late stage of the high mass proto-stellar phase.
Unlike many previous works, which were limited to the study of one type of object, our combined sample includes high mass proto stellar objects (HMPOs), hot cores and UCHII regions, allowing for a comparative analysis of objects at a potentially broad range of evolutionary stages, with the aim of classifying properties of high mass star forming regions on a statistically significant basis. By including the sources at Galactocentric radii $R_{\rm G}$ between 9 kpc and 18 kpc, effects of varying $R_{\rm G}$ in the process of star formation can be examined.
This dissertation work is the first sub-mm line survey on a larger sample of high mass star forming sources. Apart from characterizing the sample, I wanted to address the question whether the combination of dust continuum data with the high frequency line survey and a few chosen line tracers of kinematic motion allows us to find evolutionary stages in the sample.
While individual sources are difficult to compare with predictions of the star formation theory, it might be possible to find indications to support one of the above-mentioned formation scenarios when observing a large sample of sources.
Another goal was to study new hot molecular cores that might be found in the sample and compare them to known northern hemisphere sources and get an estimate of the time spent in that stage.

Hot molecular cores
Following the classical definition found in the literature, a hot molecular core (or hot core) is a small ($<$ 0.1 pc), dense ($> 10^7 \mathrm{cm}^{-3}$) and hot ($>$ 100 K) region with a centrally peaked density structure inside a massive star forming cloud often found associated with or in the vicinity of UCHII regions (Walmsley et al., 1992; Kurtz et al., 2000). While the objects are defined by a narrow range of densities and temperatures, they exhibit a large range of luminosities and masses. They are often found through searches for FIR- and radio continuum emission (Kurtz et al., 2000), even though one has to keep in mind that single dish studies do not have the resolution to distinguish whether or not these tracers are associated with the embedded hot core source or if they are found in their vicinity. While the dense core region is quiescent and cold, molecules freeze out on dust grain mantles and grow in complexity by adding hydrogen (hydrogenation) also frozen out. Once the newly formed protostar ignites, the ices in the inner region are evaporated by heating, which leads to a rich gas phase chemistry. The heating is often provided by an internal heating source (the protostar), but cases of external heating have also been found (e.g. Watt & Mundy, 1999). In the line spectra of hot cores, one finds high abundances of fully hydrogenated species and complex organic molecules (Schöier et al., 2002). Among most of the studied hot cores, it seems to be the case that their chemical properties neither correlate with the properties of the accompanying UCHII regions (Hatchell et al., 1998) nor do their abundance patterns vary significantly among each other (Kurtz et al., 2000). The phenomenon of hot molecular cores can be observed during just a short moment in the formation of a massive star. Comparing the resolved hot cores in the massive star forming region W49N with the number of resolved UCHII regions, Wilner et al. (2001) estimate the lifetimes to be shorter than 10^5 yrs.

Our sample gives us the possibility to study the eight hot cores that were found with the line observations and have been observed in the same setups both in line and dust continuum emission. With this albeit still small sample of hot molecular cores I want to adress the question if all hot cores are basically the same, due to their extremely short lifetimes or if it is possible to observe hot cores at different stages during the hot core phase. It has to be noted however that this is the work of a "passive astrochemist" (van der Tak, 2008), i.e. someone who uses the spectral lines to extract physical information only, but does not construct chemical models, which would have gone beyond the scope of this thesis.

Most observations were performed with the Atacama Pathfinder EXperiment (APEX), a 12m telescope operated by the Max-Planck-Institut für Radioastronomie, ESO and the Onsala Space Observatory on Llano de Chajnantor in Chile. When this thesis was started, APEX was still undergoing science verification and the progress of this work has been strongly linked with APEX getting operational and developing to be a superb sub-mm instrument. Therefore in the following chapter, I give a short description of this new telescope and the instruments used in this work.

1.3 The source sample

Based on the sources observed by Faúndez et al. (2004) and Walsh et al. (1997), we compiled a new sample of southern high mass star forming regions, where 35 sources follow the selection criteria of Sridharan et al. (2002). They have to

- satisfy the Wood & Churchwell far-infrared color-criteria ($F_{60\ \mu\mathrm{m}}/F_{12\ \mu\mathrm{m}} \geq 1.3$ and $F_{25\ \mu\mathrm{m}}/F_{12\ \mu\mathrm{m}} \geq 0.57$)
- be detected in the Bronfman et al. (1996) CS(2-1) survey, ensuring the presence of dense molecular gas and delivering velocities
- be bright at FIR wavelengths ($F_{60\ \mu\mathrm{m}}$ >90 Jy,$F_{100\ \mu\mathrm{m}}$ >500 Jy)
- be free of 5 GHz emission detected in the Parkes-MIT-NRAO survey to within $5'$ from the peak position

In addition, twelve sources which satisfy the first three criteria, but have 5 GHz radio continuum emission (Parkes-MIT-NRAO survey) were chosen. These 47 sources are in the following referred to as sample A or the inner Galaxy sample. To create a more heterogenous sample, another 23 sources at Galactocentric radii between 9 kpc and 18 kpc were taken from the samples of Wouterloot & Brand (1989) (hereafter WB89) and from the sub-mm continuum survey of Klein et al. (2005). While the five sources from outer Galaxy sample of WB89 (sample B) are part of the dust continuum study presented in this paper, the 18 sources taken from Klein et al. (2005) were observed in the partial 338 GHz line surveys only and the continuum measurements obtained by Klein et al. (2005) will be discussed for comparison in this work. The Galactic distribution of all sources can be seen in Fig. 1.1. Since the distance ambiguities could not be resolved for all sources (see Sec. 4.2.1 for more details), they were shown in the plot both assuming a location at their near and at their far

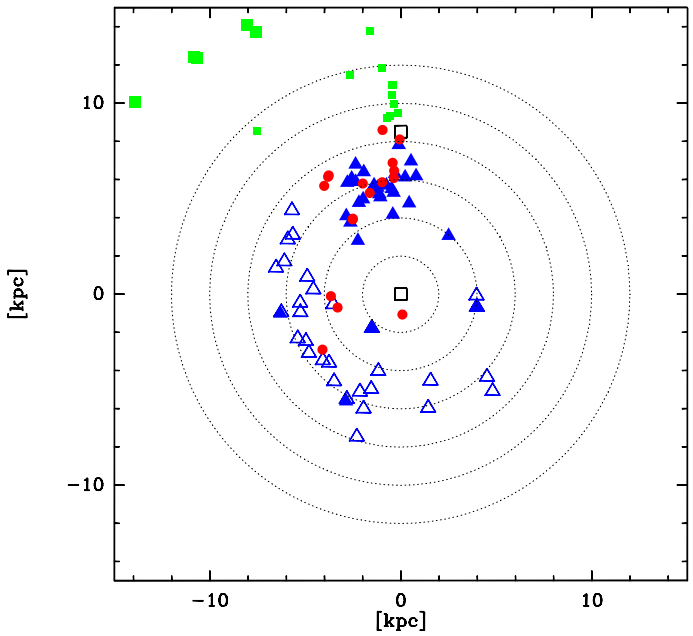

Figure 1.1: Galactic distribution of the sources in the sample. Shown are the sources from the inner Galaxy sample (filled triangles assuming near distance, open triangles assuming far distance and filled circles when the distance ambiguity could be resolved) and the outer Galaxy sample (WB sources large filled squares, sources from Klein et al. small filled squares). The location of the Galactic center and the sun are marked with open squares.

distance.

1.4 Outline

The motivation of this work and its connection to the scientific background, as well as an overview over the current status in massive star formation research are discussed in the introduction.

Chapter two describes the properties of the Atacama Pathfinder EXperiment (APEX), the telescope with which the majority of this work was conducted. The observing strategies used and the data reduction process are presented.

I discuss the pilot study, conducted with three sources at the beginning of the project, in chapter three. This was done with the goal of studying the feasibility of the observational setups proposed for the project. Detailed follow-up observations of the studied sources are also discussed.

The results of the 870 μm dust continuum survey are presented in chapter four. This survey was used to characterize the sample and compare its properties with other existing samples. From the dust continuum and the correlation with the IR emission, one can get first

impressions which sources might be suitable candidates for high mass star forming sites.

In chapter five, I discuss the molecular line surveys at 338 GHz, which together with the observations of several optically thick lines reveal further information about the sources of the sample. We can deduce their chemical composition and try to classify them further in conjunction with the data obtained in chapter four. The line survey also allows to detect hot molecular cores and their evolutionary stage can be studied both with respect to the rest of the sample and within their own subsample.

I finish in Chapter six with a summary of the work conducted for this thesis and an outlook.

Most of the tables and plots, as well as a report written about the performance of the APEX2a receiver can be found in the appendix.

Chapter 2

The Atacama Pathfinder EXperiment

2.1 General description

The majority of the data for this dissertation was taken with the Atacama Pathfinder EXperiment (hereafter APEX). APEX was build by the Max-Planck-Institut für in conjunction with the European Southern Observatory (ESO) and the Onsala Space Observatory (OSO) – see Güsten et al. (2006) for details.
In this chapter, I shall give an introduction to the APEX telescope and its first light receivers. Then I shall discuss the observing strategy used for the survey as well as some of the commonly encountered problems during this kind of observations. Last, an overview of the data reduction process, to be discussed in more detail in the respective chapters, is given.

APEX was build on the Llano de Chajnantor (Latitude: 23°00′20.8" south, Longitude: 67°45′33.0" west) at 5105 m altitude in the Chilean Atacama desert, next to the ALMA site. This site was chosen after many years of site testing, since it has better atmospheric conditions than Hawaii and a better infrastructure than Antarctica, the only site on Earth which is even dryer than the Atacama dessert. In the southern winter, about 25% of the nights have an atmospheric opacity smaller than 0.5 mm precipitable water vapor, needed for observations at the highest frequencies, while about 50% have around 1.0 mm precipitable water vapor. In Fig. 2.1, the atmospheric transmission is plotted over the range of 200 – 1600 GHz for 0.5, 1.0 and 2.0 mm precipitable water vapor at the APEX site.
As its name implies, APEX serves as a pathfinder for several upcoming sub-mm missions and is most directly connected with ALMA. It was constructed by VERTEX Antennentechnik with the technical specifications listed in Table 2.1, which could indeed be attained.

Diameter	12 m
Mass	125000 kg
Mounting	Alt–Az
Surface Accuracy (rms)	17 μm
Pointing Accuracy (rms)	2″ rms over the sky

Table 2.1: Technical specifications for the APEX telescope

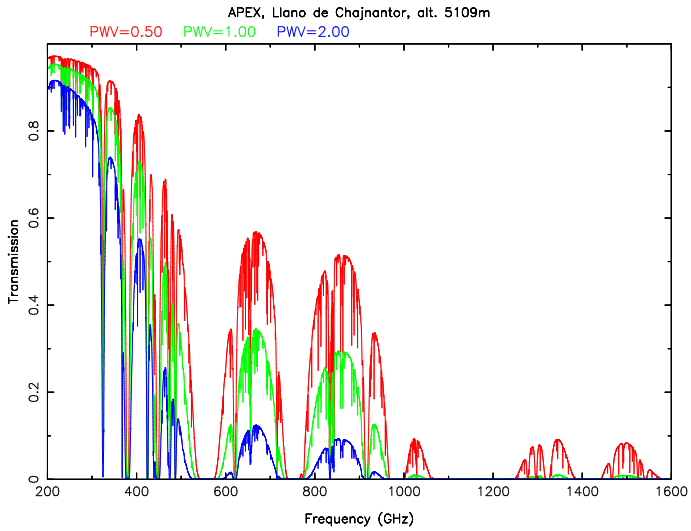

Figure 2.1: Zenith atmospheric transmission at the APEX site for 0.5 (red), 1.0 (green) and 2.0 mm (blue) precipitable water vapor. The atmospheric transmission was modeled with the atmospheric model of Juan Pardo.

Since APEX houses a different set of receivers and additional detector arrays than those that are planned for ALMA, it is equipped with the usual Cassegrain cabin and two additional Nasmyth cabins.

2.2 DSB receivers

Before describing the receivers at the APEX telescope, I will give a short general overview of the heterodyne receiver principle and, in particular, double side band receivers. At the time the data for this dissertation were taken, they were the only ones available at the telescope. When observing in the millimeter or sub-millimeter regime, the arriving radiation has to be mixed down to a lower frequency, the so called intermediate frequency ($\nu_{\rm IF}$), because there are no amplifiers working at the high frequencies. In a heterodyne receiver, this happens in the mixer, a non-linear element, where the incoming radiation is mixed with the local oscillator frequency ($\nu_{\rm LO}$). Currently, superconducting-insulating-superconducting (SIS) elements are mostly used as mixers. The basis of the heterodyne principle is to superpose the frequency one is interested in, ν, with a local oscillator frequency, $\nu_{\rm LO}$ to create, principally, two intermediate frequency (IF) bands. Both have width $\nu_{\rm IF} = |\nu - \nu_{\rm LO}|$, are centered at $\nu^{\rm LSB} = \nu_{\rm LO} - \nu_{\rm IF}$ and $\nu^{\rm USB} = \nu_{\rm LO} + \nu_{\rm IF}$ and are called lower and upper sidebands, respectively (LSB and USB). The reason for this "mixing" is the down conversion of the technologically difficult to handle sub-millimeter frequencies to radio wavelength frequencies, where low noise amplifiers are available and, in the case of APEX, to feed the signal directly into the Fast Fourier Transform Spectrometer backend (see Sec. 2.3.2). The APEX 2a receiver has a 4 GHz wide IF band, centered at 6 GHz. This means that the LSB and USB frequencies are separated by 12 GHz. The FLASH460 and FLASH810 receivers have 2–4

and 4–8 GHz wide IF band, respectively; see Sec. 2.3.1.
It has to be noted that the same intermediate frequency can be produced by two incoming frequencies (upper and lower sideband). These represent two mixing products $\nu - \nu_{\rm LO}$ and $\nu + \nu_{\rm LO}$, which are located symmetrically above and below the local oscillator frequency $\nu_{\rm LO}$. Therefore, the desired signal will be in one of the sidebands, which we call the signal sideband.
When only observing a single line, which can be located in one of the two sidebands, towards sources which are not line rich, the only disadvantage of DSB operation is the additional noise that is added to the spectrum through the second sideband. When doing line surveys of sources with a rich spectrum of emission lines however, as it is done in this work, DSB mode turns out to add additional difficulties to the analysis, since there will be a multitude of lines in both sidebands. This can lead to a contamination of the signal sideband with lines from the image sideband and blending between the lines from the different sidebands. It is then necessary to devise strategies for line identification and proper sideband calibration, since it is not clear which sideband a line is coming from. See Sec. 2.4 for a discussion on how this difficulty is overcome by shifting the LO frequency.
Newer sub-mm receivers such as CHAMP$^+$ and the Swedish Heterodyne Facility Instrument (SHFI - see [1] for details) are single sideband instruments, which either use side band separating mixers (SHFI) or reject the image sideband with a filter (CHAMP$^+$).

2.3 Frontends and backends

This section describes the instruments at APEX used for this work. For an overview of the current receiver status at APEX, see [2].

2.3.1 Frontends

The heterodyne receivers
The heterodyne data used in this dissertation has mainly been observed with the APEX2a heterodyne receiver (Risacher et al., 2006). Having been an interim solution until the SHFI receivers arrived, APEX2a was decommissioned in February 2008. The high frequency data presented in this work were taken with the dual frequency 460/810 GHz First Light APEX Submillimeter Heterodyne (FLASH) receiver (Heyminck et al., 2006). The specifications of APEX2a and FLASH460/810 can be seen in table 2.2. Both APEX2a and FLASH460/810 are double sideband (DSB) receivers.
LABOCA
On APEX, there are two facility bolometer arrays, the Large APEX BOlometer CAmera (LABOCA) and the Submillimeter APEX Bolometer Camera (SABOCA). This work made use of data taken with LABOCA, a 295 pixel bolometer operating at 870 μm (Siringo et al., 2007). LABOCA has a field of view of 11.4′ and a beam-size of 18″.

[1] http://www.apex-telescope.org/heterodyne/shfi/
[2] http://www.apex-telescope.org/instruments

Receiver	Frequency Coverage	Beam-width	Beam Efficiency	Facility Receiver
APEX 2a	279 - 381 GHz	18″	0.73	yes
FLASH460	430 - 492 GHz	14″	0.6	PI
FLASH810	780 - 887 GHz	7″	0.43	PI

Table 2.2: Heterodyne receivers at APEX at the time of observations for the thesis.

2.3.2 Backends

The spectral line observations with APEX2a and FLASH460/810 made use of the APEX digital Fast Fourier Transform Spectrometer (FFTS) (Klein et al., 2006) as backend. It is a novel 2×1 GHz bandwidth digital spectrometer built on a commercially available digitizer board. With 16384 frequency channels, it allows for a frequency resolution of 98 kHz, corresponding to $0.098\mathrm{km\,s^{-1}}$. To better match the (typically few $\mathrm{km\,s^{-1}}$) wide lines of interest here, the obtained spectra were routinely "smoothed" by averaging channels in order to increase the signal-to-noise ratio.

2.4 Observing strategy

Different approaches were used to observe the sources in the inner and outer Galaxy both with the heterodyne instruments and with LABOCA on APEX.
Since LABOCA was not available at the beginning of the survey, $\mathrm{HCO^+}$(4–3) was mapped around each 1.2 mm peak position from Faúndez et al. (2004) to double check the accuracy of the pointing of the SEST telescope, with which Faúndez et al. (2004) obtained their data. Since $\mathrm{HCO^+}$ is a good tracer of dense gas, the peak of its emission determines what is referred to as the hot core position. All subsequent frequency setups were observed at this new position. The mean offset from the initial 1.2 mm peak position was 1 ″in x and 0.3 ″in y with a standard deviation of 6 ″ in x and y (x and y are offsets in east and north respectively). The outer Galaxy sources from the sample of Klein et al. (2005) were observed with the $\mathrm{CH_3OH}$(6–5) setup with APEX2a, using the published sub-mm continuum peak positions for pointing. The same method was initially used in the case of the WB89 sources with the peaks of the CO maps used as pointing centers. Since this did not yield any results, those sources were re-observed at the end of 2007 with LABOCA to obtain the sub-mm peak positions. Due to time constraints, these sources were not re-observed in line emission at the new positions.
In summer 2007, also the inner Galaxy sample could be successfully imaged with LABOCA. It would have been a better starting point of the survey to first determine the dust peak position with LABOCA, but the bolometer data was not available before summer 2007.

In the case of the three template sources 12326–6245, 16060–5146 and 16065–5158 we obtained exact positions from interferometric observations with the Australia Telescope Compact Array (ATCA) in October 2006, which were then used for further line observations with APEX, even though the line data could not be used in this work (see section 2.5 for details).

In order to counter the problem of line confusion and blending due to the DSB mode (see previous section), we observed some of the line-rich setups with frequency shifts of a few MHz, since lines from the image sideband are shifted in the opposite direction from lines in the signal sideband and can therefore be more easily assigned to one of the two bands for further identification.
Tables A.1 and A.2 in the appendix list the frequency setups observed per source for the sources in the inner and outer Galaxy.

2.5 Commonly encountered observing problems

The work on this survey started in autumn 2005, just after the inauguration of the APEX telescope. Such an early use of a new telescope comes inevitably with a number of bugs and problems which are discovered in the first few months of extensive use. Many of these problems can only be noticed after extensive use and when performing non-standard operations.
To give an example, two problems of this type, which required a re-calibration and therefore re-reduction of the data, were noticed during the course of summer 2006, while working on this dissertation. One was a problem with the image frequency, which was written into the data header without application of all necessary LSR corrections, which is required by the CLASS software when performing operations in the image sideband of the data. This could be corrected a posteriori.
The other problem concerned the calibration of the data, which was done in the rest frequency frame instead of the sky frequency frame. For frequencies close to the tuning frequency, this may not cause a problem, but when, as was the case in this work, IF setups which are more than 500 MHz away from the tuning frequency are chosen, this effect has to be corrected for.
An additional problem, which is common for sub-mm observations is the dependence of the data quality on weather. One has to keep in mind that we are trying to perform observations from the ground which are severely hindered by the atmosphere and therefore rely on superb weather conditions, which even at an excellent high altitude site such as Chajnantor are not always given. While the observations at 345 GHz could be done in most nights, observations with the high frequency receivers FLASH460/810 were very sensitive to the given weather conditions.
The atmosphere at sub-mm wavelength hinders the observations in several ways. One problem is the existence of the telluric lines, absorption lines of H_2O, O_2 and O_3 in the atmosphere. These absorption lines are frequent at the high frequencies and the pressure broadened H_2O lines determine the width of the observable frequency windows. To minimize their effects on the observations, it helps to go as high in altitude as possible, to avoid a large part of the troposphere, but additional care when selecting frequency setups has to be taken, since the broad wings of these lines have to be avoided in both sidebands. The major influence from the absorption of water vapor in the troposphere can be expressed by measuring the precipitable water vapor (pwv). In order to correct for this effect, which can, depending on the weather and the stability of the atmosphere, fluctuate on small timescales, the pwv has to be measured often. For a very unstable atmosphere, the effects of pwv fluctuations cannot always be calibrated out. Since the receivers used in this work were DSB receivers,

one could have different sideband ratios based on different calibration in each sideband. The atmosphere itself also emits and adds noise to the spectra, which results in a high system temperature $T_{\rm sys}$ and worse noise in the spectra.

The main receiver used in this work, APEX2a was supposed to be an interim receiver until the main Swedish facility receivers were delivered, but these receivers got delayed until the beginning of 2008, therefore APEX2a was used throughout this work. This receiver was prone to instrumental instabilities, which often resulted in bad spectral baselines, so that the data either had to be re-observed or in some cases discarded from the analysis if it was not possible to fit and substract the baselines with the reduction software. Additionally, several frequency setups had to be re-designed since the receiver introduced instrumental artifacts at certain frequencies into the spectra depending on the placement of the backends.
In 2007, several frequency setups from the pilot study were re-observed, since a new pointing position was tested. Having observed these setups already in 2006 at the same positions, it turned out that the observations were not reproducable. A variation of sideband gain ratios over the whole band was found in the 2007 spectra. While it is possible, as mentioned earlier, to have different sideband ratios due to calibration problems between different observations, one would still expect them to be constant within one observation. After a few weeks of checking for possible error sources such as pointing and calibration, it was concluded that this non-reproducible error was most likely a result of a change of the mixer in the APEX2a receiver, which had happened at the end of 2006. The report I wrote regarding this problem is attached in the appendix. Due to the fact that the source of the error could not be understood or reproduced, the APEX2a data from 2007 was discarded from this work. In the meantime, the receiver has been de-commissioned and substituted by the facility receiver APEX2.

2.6 Data reduction

The APEX heterodyne data were reduced using the GILDAS software package [3]. When the data were observed under good atmospheric conditions, it was sufficient to remove a first order polynomial baseline which had to be determined in a line free window, correct for the appropriate beam efficiency and sum up the individual scans. The challenge in this step, particularly in the line rich sources, lies in finding a window free of line emission to determine a proper baseline. If the data were observed under bad conditions, each spectrum had to be inspected by eye and several measures had to be taken.
In many cases, the order of the polynomial for the baseline subtraction had to be raised. While this is a procedure that has to be used with extrem care to not taper with the data, it could still be applied to the kind of data we took, since the width of the lines is so small that there is no danger of accidentally removing real structure with this procedure. In a few cases, atmospheric lines were not properly removed in the calibration process and left artefacts in the data, in which case the spectrum was discarded if they overlapped with regions where the lines were. Some setups where showing high frequency ripples which had to be removed from the spectra. These data often had to be discarded, since the frequencies of the ripples were of the order of the line widths and could not be reliably removed.

[3] http://www.iram.fr/IRAMFR/GILDAS

The LABOCA data were reduced using the BOA software package (Schuller et al., in prep.). Using the scripts provided with BOA, we determined the opacity correction from the skydips, the calibration and clipped off noise and bad channels. A more detailed discussion of the reduction process is given in chapter 4.

For the ATCA data, we used the MIRIAD software package [4] for the data reduction. The data were inspected to flag for bad data points, then the bandpass was determined from the bandpass calibrator 1253−055 and applied to the phase calibrator. From the phase calibrator (J1147−6753 for 12326−6245 and 1613−586 for 16060−5146 and 16065−5158), the gains were determined. Mars was used as absolute flux calibrator. After the gain and flux solutions were applied to the visibility data for each source, it was inverted and cleaned using the CLEAN algorithm.

[4] http://www.atnf.csiro.au/computing/software/miriad

Chapter 3

Pilot Study

3.1 Introduction

As was discussed in the introduction, large surveys of massive star forming regions are needed to draw statistically significant conclusions on high mass star formation scenarios and the evolutionary stages involved. To adress the lack of statistically significant sub-mm surveys of southern hemisphere sources in both lines and continuum, we have started to conduct a survey of 47 high mass star forming regions in the southern hemisphere in 870 μm dust continuum and molecular line emission in several frequency ranges, based on color selected IRAS point source criteria, which we are observing between 290 GHz and 806 GHz. Our selection criteria follow the criteria described in Sridharan et al. (2002), i.e. IRAS color selected and absence of radio continuum, with the addition of several methanol maser sources. The class II CH_3OH masers (Menten, 1991) are regarded as exclusive signposts for massive star formation, since they are only found associated with massive star forming regions: Despite extensive searches, not a single class II CH_3OH maser was ever found toward a low mass star forming region or an evolved stellar object (Minier et al., 2003). This is in stark contrast to H_2O masers and makes class II CH_3OH masers *unique* signposts for ongoing high mass star formation. Based on the bias that some of the most prominent class II masers were detected toward archetypical UCHII regions/strong OH maser sources such as W3(OH) and NGC 6334 F it was originally thought that these masers are, like OH masers, associated with such more developed phases of massive star formation. Later, it was found that actually *most* class II CH_3OH masers are *not* associated with UCHII regions and rather that most of them are associated with the earlier, youngest hot core phases. For example, only 3 out 18 massive star-forming regions contained them (Beuther et al., 2002c); see also Minier et al. (2005). In particular CH_3OH maser emission may *a priori* be expected from all the sources of our hetereogeneous sample.
This large sample contains sources at very different stages of evolution and will allow a consistent and comparative analysis of these regions.
Out of this survey, we will present three high luminosity southern hemisphere hot cores in this chapter, which served as targets for a template study for our large survey (Chap. 4 and 5). Based on the results obtained in these three sources, the most promising (and feasible) frequency setups for the remaining 44 sources were decided upon. In addition, this pilot study also served as a demonstration study for the capacities of the newly commissioned

Source	R.A. (J2000)	Dec. (J2000)	l,b	d (near/far) (kpc)
IRAS 12326−6245	12:35:35.90	-63:02:29.00	G301.14-0.22	4.4
IRAS 16065−5158	16:10:20.01	-52:06:13.26	G330.88-0.38	4.0 / 10.8
IRAS 16060−5146	16:09:51.40	-51:55:06.98	G330.95-0.17	5.5 / 9.4

Table 3.1: Peak coordinates of the 1.2 mm dust continuum data and distances of the three hot core sources.

APEX telescope and its first generation receivers.
IRAS 12326−6245, IRAS 16060−5146 and IRAS 16065−5158 (Table 3.1, from now on we omit the IRAS in the name for brevity, when talking about our sample) were chosen to be studied in the sub-mm and mm regime, as they were the most luminous and line rich sources observed at the beginning of our study, based on their HCO^+, SO_2 and $H^{13}CN$ spectra and therefore the most suitable targets to test the feasibility of the project.
A fourth very strong hot molecular core of the sample, IRAS 17233-3606, has been analyzed and published separately (Leurini et al., 2008).

3.1.1 Source details

The three sources had already been observed in the course of several maser studies (Caswell, 1998; Walsh et al., 1998, 1997; MacLeod et al., 1998; Caswell, 2001), as well as in the mm continuum survey of Faúndez et al. (2004), the CS survey of Bronfman et al. (1996) and the HNCO survey of Zinchenko et al. (2000). In the following, the characteristics of the sources are summarised.

We derived the kinematic distances to the sources from the center velocities of the $C^{17}O$(3–2) line.

12326−6245 features class II CH_3OH masers at 6.7 GHz, OH masers at 1.6 GHz (Caswell, 1998) and H_2O masers (MacLeod et al., 1998).
It was included in the 1.2 mm dust continuum survey of Hill et al. (2005). Miettinen et al. (2006) studied 12326−6245 in 1.2 mm dust emission, CH_3CCH and SiO line emission. 12326−6245 has been observed by Araya et al. (2005) in CH_3CN(5-4),CH_3CN(6-5), CH_3CN(8-7) and CH_3CN(12-11) Wu et al. (2004) detect a bipolar CO outflow in 12326−6245. This source has also been thoroughly studied by Henning et al. (2000) in 1.3 mm dust continuum, H,J,K',H_2, N, Q bands and several molecular tracers at 145 GHz and 230 GHz.
The kinematic distance estimated for 12326−6245 from its systemic velocity of $-39.3\,\mathrm{km\,s^{-1}}$ is 4.4 kpc, by using the Galactic velocity field of Kalberla et al. (2007).

16060−5146 as well has class II CH_3OH masers at 6.7 GHz and OH masers at 1665 MHz, 1667 MHz (Caswell, 1998). Caswell (2001) also reports a 6035 MHz OH maser at the site of 16060−5146.
16060−5146 has been studied by Hill et al. (2005) and Miettinen et al. (2006) in 1.2 mm dust emission and in CH_3CCH and SiO by the latter authors. We derived 5.5 kpc and

9.4 kpc for the near and far distance respectively from the systemic velocity of 16060−5146 ($-90.95\ \mathrm{km\,s^{-1}}$) . The kinematic distance estimates for this source found in the literature differ somewhat between 5.3 – 6.1 kpc for the near distance and 9.6 kpc for the far distance.

In 16065−5158, OH maser emission at 1665 MHz, 1667 MHz and 1612 MHz and a CH_3OH 6.7 GHz maser has been observed (Caswell, 1998), but it was only included in the mm continuum surveys of Faúndez et al. (2004).
We derive a kinematic distance of 4 kpc and 10.8 kpc for the near and far value, using a systemic velocity of $-62.17\ \mathrm{km\,s^{-1}}$.

3.2 Observations and data reduction

3.2.1 Atacama Pathfinder EXperiment

Line data

The sub-mm data were taken between November 2005 and November 2006 with the Atacama Pathfinder Experiment (APEX) telescope. We used both the APEX2a heterodyne receiver (Risacher et al., 2006) and the dual frequency 460/810 GHz Flash heterodyne receiver (Heyminck et al., 2006) for our observations (see Table 3.2 for details on the receiver setups). As backend, the MPIfR-build Fast Fourier Transform Spectrometer (FFTS) (Klein et al., 2006) was used, which consists of two units with 1 GHz bandwidth each. The pointing accuracy was checked on G327.3−0.6 (Wyrowski et al., 2006b), and was accurate within 2″. Most of the data were observed as single pointings. When mapping was done, raster maps with a map size of $40'' \times 40''$ and beam spacing were observed. All observations were obtained in double sideband mode. Calibration errors were estimated to be of the order of 30 %. These errors are influenced by pointing and atmospheric fluctuations, but the largest part of the uncertainty stems from uncertain knowledge of the sideband gain ratios. As was mentioned in Sec. 2.5, irreproducible problems with the sideband gain ratios were obvious with the APEX2a receiver. Since not all observed frequency setups could be double-checked for inconsistencies over the course of the two years of observations, an uncertainty remains, which is reflected in the 30 % calibration error. The data were reduced using the CLASS software package [1].

Table 3.2 lists the frequencies of the bands of the molecular lines observed with APEX that are subject of the pilot study. These lines were the targets of the frequency setups, but since up to 1.8 GHz bandwidth could be used, lines from many other molecules were observed. To analyze the chemical composition and physical properties of the three sources, five major setups were observed, CH_3OH(7–6) at 338 GHz, CH_3CN(16–15) at 294 GHz, H_2CO(4–3) at 291 GHz and H_2CO(6–5) at 436 GHz. CH_3CN is a good tracer of temperature and column density, since it is a symmetric rotor (Araya et al., 2005). Its K components for a given J transition are very close together and can be observed simultaneously in one setup together with some optically thin $CH_3^{13}CN$ transitions, thereby eliminating calibration un-

[1] http://www.iram.fr/IRAMFR/GILDAS

Transition	Center frequency (GHz)	Receiver	Θ_{HPBW} ($''$)	$F_{\rm eff}$	$B_{\rm eff}$	Tracer	$T_{\rm sys}$ (K)
CH_3OH(6–5)	290.8	APEX2a	20	0.95	0.73	d, t	170 - 190
CH_3OH(7–6)	337.8	APEX2a	17.5	0.95	0.73	d, t	180 - 210
CH_3CN(16–15)	294.5	APEX2a	20	0.95	0.73	d,t	140 - 200
H_2CO(4–3)	290.0	APEX2a	20	0.95	0.73	d, t	214 - 291
H_2CO(6–5)	436.9	FLASH460	14	0.95	0.6	d, t	730 - 839
CO(3–2)	345.8	APEX2a	17	0.95	0.73	o	550
CO(4–3)	461.0	FLASH460	13	0.95	0.6	o	1000 -1100
CO(7–6)	806.7	FLASH810	7	0.95	0.43	o	5100 - 5700
$C^{17}O$(3–2)	337.8	APEX2a	17.5	0.95	0.73	cd	180 - 210
HCO^+(4–3)	357.0	APEX2a	17	0.95	0.73	d, o	240 - 324

Table 3.2: Frequency setup for the molecular line observations. In the column marked 'Tracer', d stands for density, t for temperature, o for outflow and cd for molecular column density.

certainties. The same applies for CH_3OH, which has many closely spaced frequency bands throughout the sub-mm regime that cover a large range of excitation conditions (Leurini et al., 2007, 2004). The setup at 338 GHz is particularly useful, since it contains not only the CH_3OH(7–6) band, but also $C^{17}O$(3–2) and a number of hot core molecules. Together with H_2CO, those molecules can be found in a wide range of star forming conditions. In order to determine the total column density and search for outflow signatures, also CO(3–2), CO(4–3), CO(7–6) and $C^{17}O$(3–2) were observed.
The positions of the hot cores were first defined as the peak positions of HCO^+(4–3) maps at 357 GHz and later refined by 3 mm continuum ATCA maps.
On source integration times for APEX2a were around 5–8 min per single pointing setup, and 12–20 min per pointing for FLASH, depending on the weather conditions.

Continuum data

In summer 2007, we obtained continuum data for our sources from the Large Apex Bolometer Camera (LABOCA) (see Sec. 2.3.1).
LABOCA is a 295 channel bolometer with a field of view of 11.4 $'$ and a beam of 18.6 $''$. The pixel separation is 36 $''$. To produce a fully sampled map, the data were observed in the raster-spiral mode, with 35 sec integration time on source, a spacing of 27 $''$ and 4 subscans. This sets the scanning velocity to about 4$'$/s and the total integration time on source was on average 2.3 min. 12326−6245 was observed in two scans.
The atmospheric opacity was determined every hour through skydips. The zenith opacity was 0.3 for 12326−6245 and 0.09 for 16060−5146 and 16065−5158. The rms for 12326−6245 is 100 mJy/beam, while the rms for 16060−5146 and 16065−5158 is 50 mJy/beam.
IRAS16293−2422, IRAS13134−6242 and η Carinae were used as flux calibrators and the pointing was checked on η Carinae for 12326−6245 and on IRAS16293−2422 for 16060−5146 and 16065−5158. The pointing was good within 3$''$.

The data were reduced using the BOA software package (Schuller et al., in prep.).

3.2.2 ATCA

High spatial resolution data at 3 mm were taken in October 2006 with the Australia Compact Array (ATCA) interferometer at Narrabri, Australia. The array was in the H75 configuration with a synthesized beam of $6'' \times 4''$ for 16060−5146, $5'' \times 5''$ for 16065−5158 and $6'' \times 6''$ for 12326−6245 and in the FULL_16_256−128 correlator configuration.
The $H^{13}CN$(1–0) line at 86.34 GHz was observed with a bandwidth of 16 MHz and a frequency resolution of 0.076 MHz, whereas the continuum was observed at 87.89 GHz with a bandwidth of 128 MHz and a resolution of 8.8 MHz. This setup also includes some HNCO(4–3) lines at 87.9 GHz.
The sources were observed during 2 nights, PKS 1253−055 was used as bandpass calibrator, Mars was observed on the second night as flux calibrator, the gain calibration for 12326−6245 was done on PKS 1147−6753, and on PKS 1613−586 for 16060−5146 and 16065−5158. The theoretical continuum RMS noise level was 3 mJy/beam for the continuum and 130 mJy/beam for the line observations, respectively. The data were reduced using MIRIAD [2] and the dirty images were de-convolved using the CLEAN algorithm (Högbom, 1974).

3.3 Observational Results

3.3.1 Line data

To verify the peak position observed in the 1.2 mm continuum maps of Faúndez et al. (2004), the three sources were mapped in HCO^+(4–3) at 357 GHz. First, the regions were mapped with beam spacing to locate the peaks, then we continued with fully sampled maps around the thus found peak positions (see Fig. 3.1). The peak positions in 12326−6245 and 16060−5146 are significantly offset from the 1.2 mm peak positions as determined by Faúndez et al. (2004). This is mostly likely due to a pointing problem in the 1.2 mm data, since the peak positions derived by Faúndez et al. (2004) are offset by 6 and 15 ″from the LABOCA and ATCA peak positions for 12326−6245 and 16060−5146 respectively. The pointing positions for the line observations were corrected several times during the course of the survey. The final pointing positions agree with the LABOCA and ATCA peak positions for 16065−5158 and agree within 6 ″for 12326−6245 and 16060−5146. Several line setups were re-observed at a later stage to have consistency in the positions. Therefore, not all lines could be found in the spectra of each source which were finally included in the analysis.
In order to determine the total column density and the properties of the envelopes, the sources were also mapped in CO(3–2) (Fig. 3.2) and observed in CO(4–3), CO(7–6) and $C^{17}O$(3–2) on the peak positions (see Fig. 3.3). The off-positions were checked to be free of CO emission.
Both the CO lines and the HCO^+(4–3) line show clear signs of outflow activity in the wings of all sources and self-absorption in the case of 16060−5146 and 16065−5158. The three

[2] http://www.atnf.csiro.au/computing/software/miriad

sources were observed in CH_3OH(6–5), CH_3OH(7–6), CH_3CN(16–15), H_2CO(4–3) and H_2CO(6–5) to determine temperatures and densities (see Figs. 3.6 and Figs. A.1 – A.6 of the Appendix). Parameters of the lines (determined from Gaussian fits) can be found in Tables A.20 to A.28 in the Appendix.
The line widths of the optically thin CH_3OH lines in the three sources are 3.5 $\mathrm{km\,s^{-1}}$, 3 $\mathrm{km\,s^{-1}}$ and 6 $\mathrm{km\,s^{-1}}$ for 12326−6245, 16060−5146 and 16065−5158 respectively in the hot component and 4 $\mathrm{km\,s^{-1}}$, 7 $\mathrm{km\,s^{-1}}$ and 6 $\mathrm{km\,s^{-1}}$ in the cold component. 16060−5146 has a slightly broader profile than the other two sources. In CH_3CN(16–15), one can see a double-peaked profile (Fig. 3.6), which might suggest that the larger line widths seen in this source in the other species are due to the superposition of two velocity components.
As will be further discussed in the next section, all three sources exhibit a rich spectrum of molecular lines, in 12326−6245 and 16065−5158, 18 different species were found, while in 16060−5146, 16 species were found. As is typical for hot core sources, highly excited lines up to energies of 346 K above the ground state and lines from vibrationally excited states were observed. Especially the setup around 338 GHz is very line rich, with detections of about 20 lines per GHz.

The above mentioned setups were also used to study the chemical complexity in the hot cores. The lines were identified by using the programme XCLASS (Comito et al., 2005; Schilke et al., 1999) and the rest frequencies provided by the Cologne database for Molecular Spectroscopy (CDMS) [3] (Müller et al., 2005, 2001) and JPL molecular spectroscopy database [4] (Pickett et al., 1998). Since the line identification went hand in hand with the LTE modeling of the lines, it is described in more detail in Sec. 3.4.1.

3.3.2 Continuum data

LABOCA

To obtain source positions, sizes and peak fluxes, the LABOCA data (see Fig. 3.5) were analyzed with the *sfind* routine in the MIRIAD software package. The integrated fluxes were obtained over the area inside the 10% contour of the peak flux. The size of the sources was determined assuming the area which includes the 10% flux as circularly symmetric. The source positions, fluxes, sizes and the H_2 column density can be found in Tables 3.3 and 3.4. The positions agree within the pointing uncertainties with the 3 mm peak positions derived from ATCA. The column density was obtained from Equ. 3.1, following Miettinen et al. (2006)

$$N(\mathrm{H_2}) = 1.67 \times 10^{-22} \frac{I_\nu^{\mathrm{dust}}}{B_\nu(T_\mathrm{d})\mu m_\mathrm{H} \kappa_\mathrm{d} R_\mathrm{d}} \ [\mathrm{cm^{-2}}] \tag{3.1}$$

where I_ν is the peak flux in Jy/beam, θ_{FWHM} the FWHM of the beam in radian, $B_\nu(\mathrm{T_d})$ the Planck function of a black body at dust temperature T_d, μ is the mean molecular weight assuming 10% contribution of helium , m_H=1.673534$\times 10^{-27}$ kg is the weight of the hydrogen atom, κ_d the dust absorption coefficient of 0.176 $\mathrm{m^2/kg}$ linearly approximated at 870 μm

[3] www.cdms.de
[4] http://spec.jpl.nasa.gov/

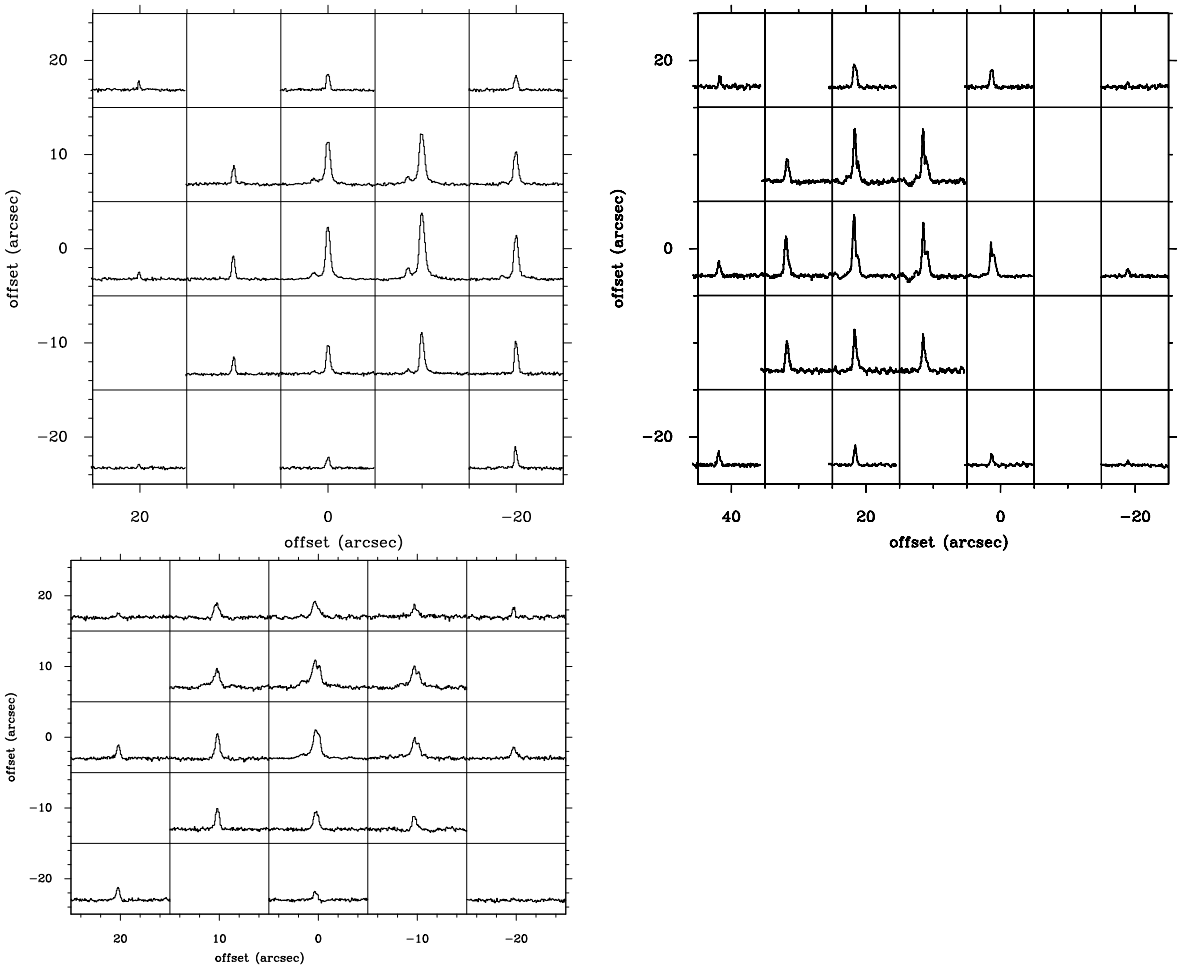

Figure 3.1: Map of HCO^+(4–3) for 12326−6245 (top left), 16060−5146 (top right) and 16065−5158 (bottom left). The (0,0) positions correspond to the 1.2 mm peak positions of Faúndez (2004) listed in Tab. 3.1. The velocity and $T_{\rm mb}$ temperature scales go from -100 – 20 $\rm km\,s^{-1}$ and -5 – 25 K, -150 – 0 $\rm km\,s^{-1}$and -5 – 20 K and -120 – 0 $\rm km\,s^{-1}$and -5 – 20 K respectively for 12326−6245, 16060−5146 and 16065−5158.

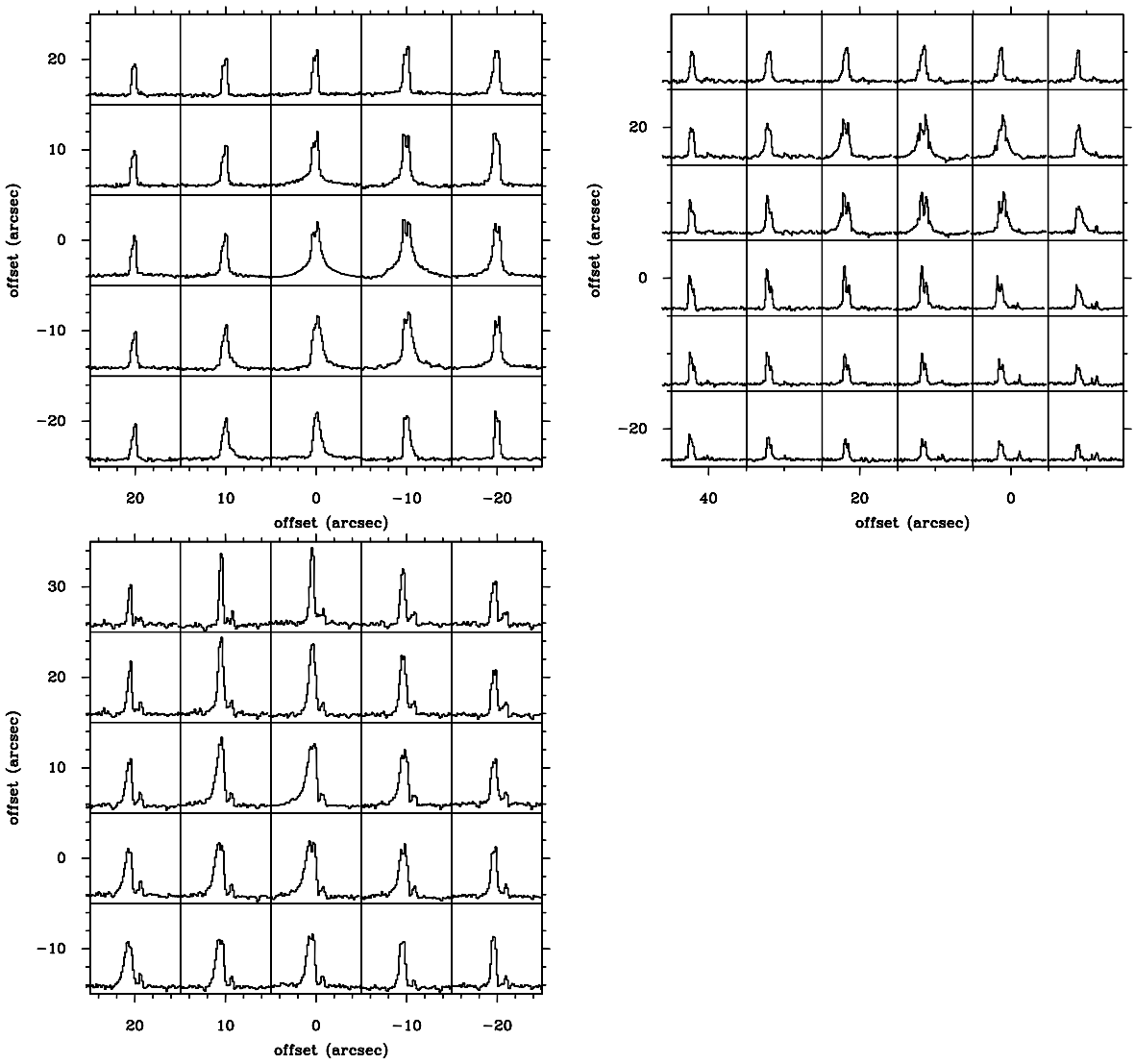

Figure 3.2: Map of CO(3–2) for 12326−6245 (top left), 16060−5146 (top right) and 16065−5158 (bottom left). The (0,0) positions correspond to the 1.2 mm peak positions of Faúndez (2004) listed in Tab. 3.1. The velocity and $T_{\rm mb}$ temperature scales go from -100 – 20 $\rm km\,s^{-1}$ and -5 – 60 K, -150 – 0 $\rm km\,s^{-1}$and -5 – 50 K and -120 – 0 $\rm km\,s^{-1}$and -5 – 60 K respectively for 12326−6245, 16060−5146 and 16065−5158.

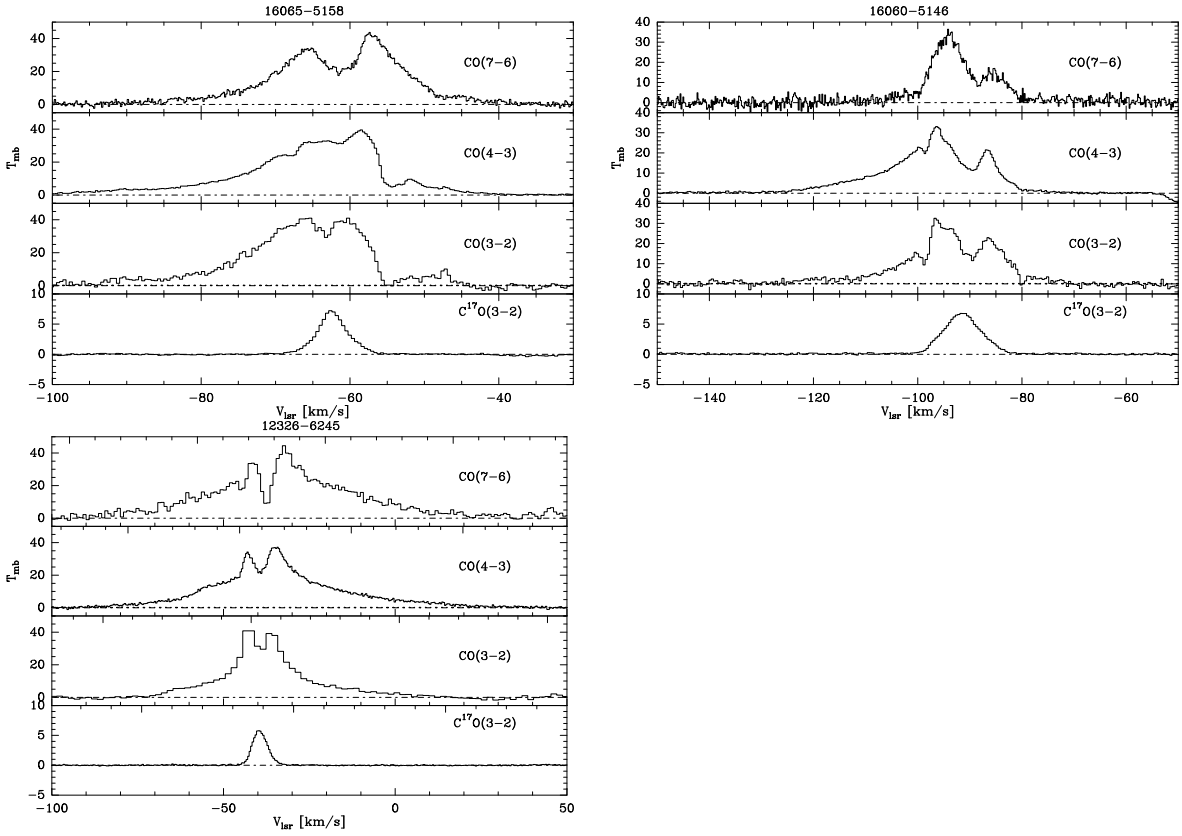

Figure 3.3: $C^{17}O$(3–2), CO(3–2), CO(4–3) and CO(7–6) transitions. While $C^{17}O$(3–2) is observed on the peak positions in 16065−5158 (top left), 16060−5146 (top right) and 12326−6245 (bottom left), the specta of the remaining transistions were produced by averaging all the spectra taken at the map positions. The dashed line marks the zero level.

from model V (thin ice mantles, $n = 10^6$ cm^{-3}, $\beta = 1.8$) of Ossenkopf & Henning (1994) and a dust-to-gas mass ratio $R_{\rm d} = \frac{1}{100}$. Model V is suited for sources in which considerable depletion on ice occurs. Unlike the models with thick ice mantles, which apply for dark clouds, the conditions in model V include the influence of a heating source which is starting to evaporate the ices. Ossenkopf & Henning (1994) give the uncertainties for the dust absorption coefficient to be a factor of 2 for ice covered dust and state that it can be up to a factor of 5 higher in disk regions, where the ice mantles are already evaporated off the grains. As provided by model V, we use $\beta = 1.8$ ($\kappa \sim (\nu/\nu_0)^\beta$) in this work, which is consistent with values of $\beta = 1.5 - 2.0$ found in massive star forming regions (Molinari et al., 2000). Using the dust opacities derived by Hildebrand (1983), as has been done by Beuther et al. (2002a), leads to masses and column densities which are about a factor of 4 lower.
We also list the source multiplicity, in this case all the sources above 3 σ found within the 11.4$'$ field of view.

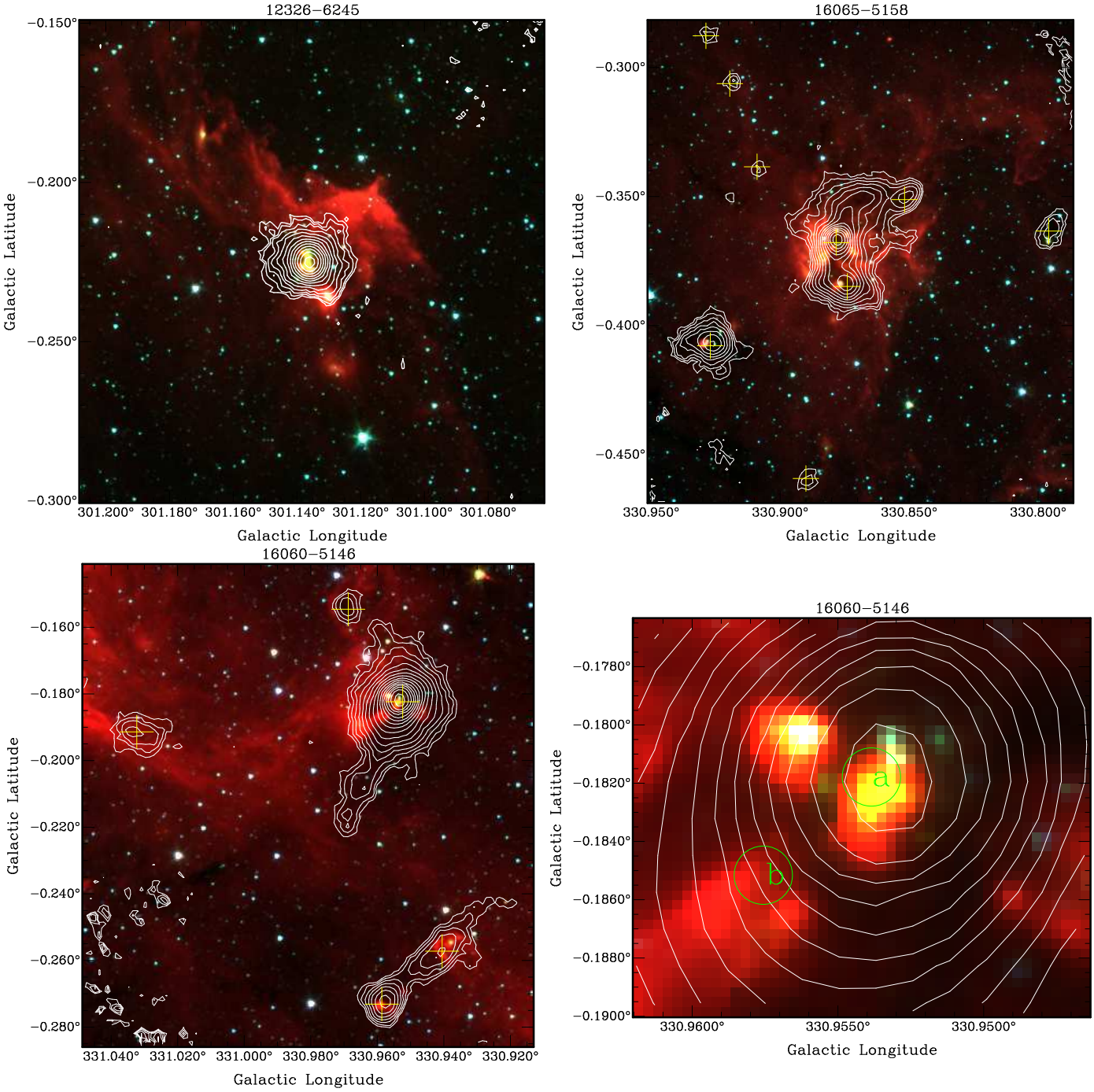

Figure 3.4: Spitzer GLIMPSE composite image of 3.6, 4.5 and 8 μm emission. LABOCA 870 μm emission is shown as contours, starting from 5 σ and continuing in multiples of 1.4 σ (see Table 3.3). The yellow crosses mark the sub-cores in 16060−5146 and 16065−5158. In the lower right plot, the 870 μm emission peak is shown with the 3 mm sources ATCA-a and ATCA-b marked as circles.

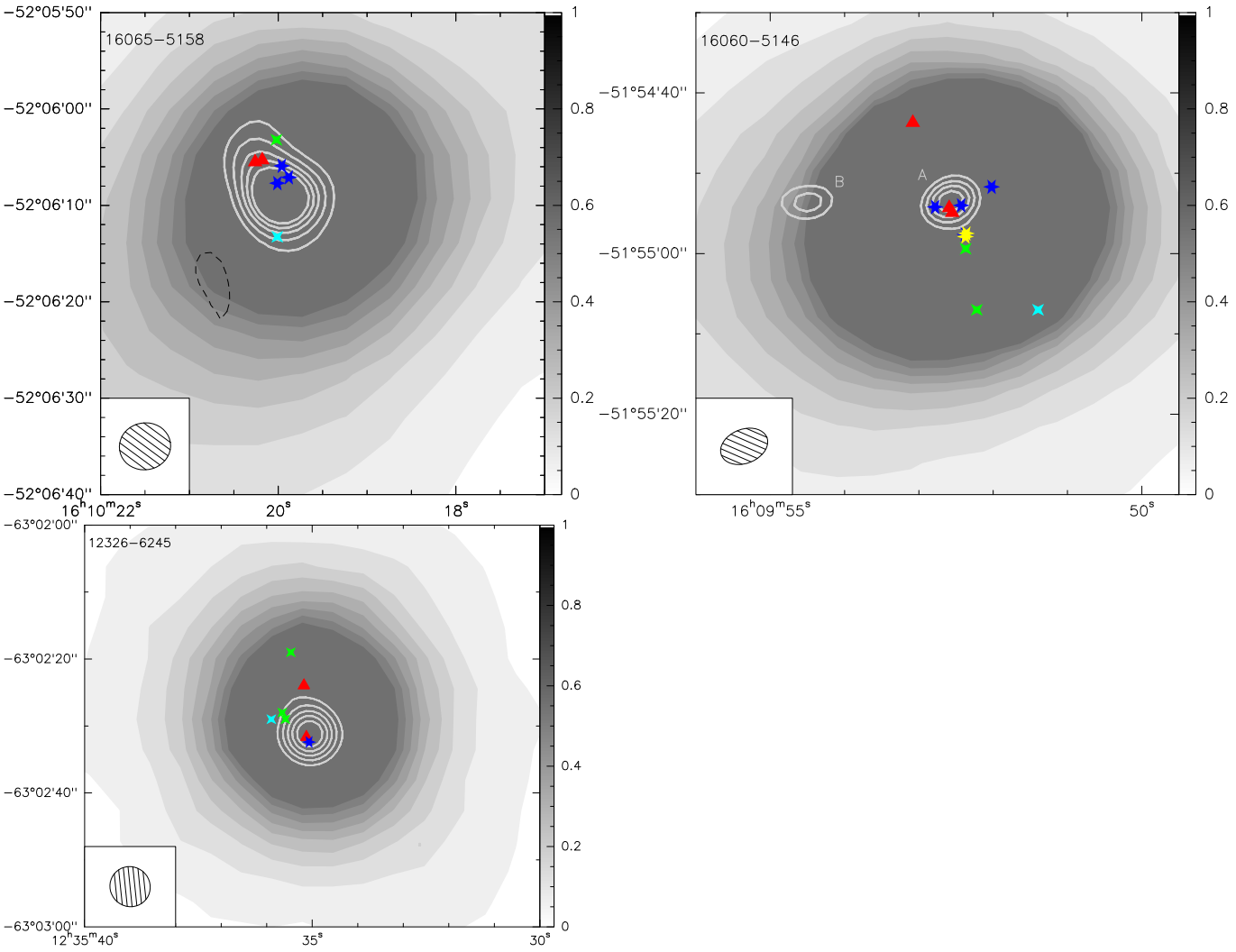

Figure 3.5: ATCA 3 mm continuum data (solid lines) top left 16065−5158 (contour steps -3,3,5,7...σ, with σ=8 mJy/beam), top right 16060−5146 (contour steps -3,3,5,7...σ, with σ=0.1 Jy/beam) and bottom left 12326−6245 (contour steps -3,3,5,7...σ, with σ=0.14 Jy/beam). The synthesized ATCA beam is shown in the lower left corner. LABOCA 870 μm continuum is shown in gray-scales. The LABOCA beam is shown in the bottom right corner. The red triangles mark the radio continuum regions observed by Urquhart et al. 2007, the blue stars OH maser positions, the green stars the offsets of the APEX line observations, the turquoise stars the IRAS position and the yellow star in 16060−5146 a CH_3OH maser (Caswell et al. 1998).

Source	R.A. (J2000)	Dec. J(2000)	l,b	Rms (mJy/beam)
12326−6245	12:35:35.0	-63:02:28.9	301.14,-0.22	100
16065−5158	16:10:19.8	-52:06:09.7	330.88,-0.37	50
16065−5158 LABOCA-A	16:10:23.4	-52:07:06.1	330.87,-0.38	
16065−5158 LABOCA-B	16:10:07.8	-52:06:31.4	330.85,-0.35	
16065−5158 LABOCA-C	16:09:55.1	-52:09:20.8	330.80,-0.36	
16065−5158 LABOCA-D	16:10:44.7	-52:05:56.2	330.93,-0.41	
16065−5158 LABOCA-E	16:10:47.9	-52:09:43.0	330.89,-0.46	
16065−5158 LABOCA-F	16:10:21.2	-52:03:35.9	330.91,-0.34	
16065−5158 LABOCA-G	16:10:15.6	-52:01:47.4	330.92,-0.31	
16065−5158 LABOCA-H	16:10:13.2	-52:00:35.5	330.93,-0.29	
16060−5146	16:09:52.5	-51:54:55.3	330.95,-0.18	50
16060−5146 LABOCA-A	16:09:49.6	-51:53:03.7	330.97,-0.15	
16060−5146 LABOCA-B	16:10:08.7	-51:58:43.0	330.94,-0.26	
16060−5146 LABOCA-C	16:10:18.1	-51:58:43.1	330.96,-0.27	
16060−5146 LABOCA-D	16:10:17.3	-51:52:06.2	331.03,-0.19	

Table 3.3: Positions of the LABOCA 870 μm continuum emission peaks. The sub-cores 16065-5158 A-H and 16060-5146 A-D are marked in Fig. 3.4.

Source	$S_{\rm peak}$ (Jy/beam)	$S_{\rm int}$ (Jy)	$N(\mathrm{H_2})$ x10^{23}(cm^{-2})
12326−6245	19.9	42.6	4.2
16065−5158	17.9	41.8	3.8
16060−5146	46.2	81.0	8.2

Table 3.4: Properties of the 870 μm continuum as derived from the LABOCA observations.

ATCA

Figure 3.5 shows the 3 mm ATCA data of the three sources. These data provided a precise position of the core, which is confirmed by the molecular emission peaks determined by line observations done simultaneously, and they give a good estimate of the source size (see Table 3.5). The beam de-convolved source sizes, positions and fluxes for the sources were determined using the *imfit* task in the MIRIAD software package. Overlaid on the data are the interferometric positions of associated OH (Caswell et al. 1999, 2001, 2004) and $\mathrm{CH_3OH}$ masers (J. Caswell, priv communication), as well as the 3 cm and 6 cm peaks of radio continuum emission (Urquhart et al., 2007a). It is remarkable that in 16060−5146, only core A (position 16060−5146 ATCA-a) has associated masers and radio continuum, suggesting that core 16060−5146 ATCA-b might be in a very early evolutionary stage. This core is neither evident in the LABOCA continuum data nor in the Spitzer GLIMPSE MIR data.

Source	Position (J2000)	source size ($''$)	S_ν (Jy/beam)	$S_{\rm int}$ (Jy)
12326-6245	12:35:35.06 -63:02:31.00	3.3×2.0	1.96	2.36
16060-5146 ATCA-a	16:09:52.57 -51:54:53.69	4.6×2.2	1.24	1.95
16060-5146 ATCA-b	16:09:54.52 -51:54:53.56	6.5×1.7	0.78	1.33
16065-5158	16:10:20.00 -52:06:08.79	6.4×3.1	0.15	0.28

Table 3.5: ATCA 3mm continuum parameters

3.4 Derivation of physical parameters

3.4.1 LTE modeling

We observed our sources in lines from CH_3CN, CH_3OH and H_2CO, which are useful tracers of temperature. While classically rotational diagrams have been used to determine T and N (see Olmi et al. (1993); Mangum & Wootten (1993)), we make use of an LTE approach developed by Schilke et al. (1999) and further improved by Comito et al. (2005). Implemented into the program XCLASS, it allows to model synthetic spectra which take line blends and optical depth effects into account and furthermore allows to simulate a double sideband (DSB) spectrum. Input parameters for the simulation are source size, temperature, column density, line widths and offset from systemic velocity. It is possible to simultaneously model transitions in several frequency bands and include more than one component, i.e. a core and an envelope component or several velocity components. Figs. 3.6, 3.7 and 3.8 give an example of a synthetic spectrum for a single molecule overplotted on the measured sub-spectra, while Figs. A.1 – A.6 in the Appendix show the synthetic spectra of all included species. The degeneracy between column density and source size can be solved for species where both optically thin and thick lines are present, as was the case for CH_3CN and to some degree CH_3OH. With interferometric observations, such as the ATCA images, it is possible to determine a source size which can serve as a starting point for further iterations of the LTE modeling for species which are expected to form in the compact core. In case of species where only one or two lines were available to model, only the beam-averaged column density was derived. The systemic velocities with respect to which the velocity offsets of the lines were determined are -39.3 $\mathrm{km\,s^{-1}}$ for 12326−6245, -62.2 $\mathrm{km\,s^{-1}}$ for 16065−5158 and -91 $\mathrm{km\,s^{-1}}$ for 16060−5146.

The lines were identified using the catalogues of the CDMS and JPL (Müller et al., 2005, 2001; Pickett et al., 1998) as a reference for the rest frequencies. In case of ambiguous detections, a comparison of the synthetic model spectrum and the data could show if all predicted transitions for a certain molecule were also observed. Where available, comparison with the literature was done to confirm line identifications. The double sideband mode of the observations proved to be an additional challenge to the identification, since it was often not clear from which sideband a line is coming from. In some cases, spectra shifted in frequency were observed, which helped in disentangling the line contribution from the two sidebands. The spectra for this pilot study, apart from the 337 GHz setup are also affected by the problem of the mirrored lines: It turned out that at the edges of the spectra, lines from

outside the observed frequency band could be folded into the spectrum due to processing in the spectrometer (aliasing). Since these lines were not calibrated properly, they could not be included in the models and are marked "mirror" in the figures.
The tables with the detected lines for the three sources can be found in the appendix (Tables A.9 to A.4) – here we will present the results of the modeling.

As mentioned above, for species where only one or two lines are included in the setups, beam-averaged column densities were derived, since the degeneracy between source size and column density cannot be resolved. Of these, for species which we assume to reside in the hot core, a rotation temperature $T_{\rm rot}$ =150 K (Schilke et al., 2006) was assumed and for species from the more extended envelope 50 K was chosen, unless we had both optically thick and thin lines to derive a temperature from the model. Those fixed temperatures are marked ^{a} in the tables. In the case of the size, this foot-note indicates that the size was either fixed to the hot core size derived from the CH_3CN data or the beam averaged column density was derived, since we could not determine a source size.
For sources labeled ^{b}, the lines are weak and/or blended with many other lines, so that the fit is less accurate than a fit marked ^{c}. XCLASS produces a synthetic spectrum (model) of all species and transitions included in the modeling which is then overlaid with the data. For CH_3CN, a χ^2 analysis was performed on the synthetic model spectrum to determine the best fit model, while for the remaining setups a comparison by eye was done to decide on the best fit. This was necessary to account for the high complexity when modeling several, often blended, transitions in the double sideband spectra.
For those cases where both temperature and source size were fixed, the column density could be determined to an accuracy of 10%. The uncertainties introduced when modeling both source size and temperature are discussed in the following two sections. When performing this kind of modeling, one has to bear in mind however that we are using the assumption of LTE, which, while being a reasonable choice given the high densities, is not necessarily valid for every molecule and source. Nonetheless, this method gives us a good, fast overview on the chemical composition of the sources and can be applied to a large sample of sources with considerably less effort than individual non-LTE modeling would require. Tests with CH_3OH and H_2CO showed that the use of the large velocity gradient (LVG) method, which assumes the source to have a spherical geometry and requires the knowledge of collisional rate coefficients does not greatly improve the modeling results for our sources. To effectively use a complex radiative transfer model requires detailed knowledge of the spacial structure of the sources, which is not available yet. For some species, marked as ^{f}, we modeled isotopologues, using $^{12}C/^{13}C$=60, $^{32}S/^{34}S$=23, $^{14}N/^{15}N$=300 and $^{16}O/^{17}O$=1500.
The results of the modeling can be found in Tables 3.6 to 3.11. Tables 3.9 to 3.11 show the model results for those species that were modeled in several frequency setups, namely CH_3OH, CH_3CN, H_2CO and SO_2. The data are described in more detail in the following sections.

CH_3CN data

The symmetric top molecule CH_3CN, is the best temperature tracer. The results of the CH_3CN modeling are listed in Tables 3.9-3.11 and the data with the synthetic spectra are

Species	Size (")	$T_{\rm ex}$ (K)	$N_{\rm b}$(mol) ($\rm cm^{-2}$)	$N_{\rm s}$(mol) ($\rm cm^{-2}$)	Δv ($\rm km\,s^{-1}$)	Offset ($\rm km\,s^{-1}$)	$N_{\rm b}/N_{\rm H_2}$	
C_2H_5CN	-[a]	150[a]	5.0(13)	-	3.0	2.0	1.7(-10)	[b]
CCH	-[a]	50[a]	3.2(14)	-	6.0	-1.0	1.1(-09)	[c]
CH_3CCH	-[a]	50[a]	3.0(15)	-	7.0	0.0	1.0(-08)	[c]
CH_3OCH_3	-[a]	200	1.3(15)	-	2.5	3.0	4.5(-09)	[b]
CH_3OCHO-a	-[a]	150[a]	4.0(14)	-	3.0	0.0	1.4(-09)	[b]
CO	-[a]	50[a]	4.0(19)	-	5.5	-0.5	1.4(-04)	[c], *f*
CS	4.0	90	3.3(15)	7.0(16)	5.0	0.0	1.1(-08)	[c], *f*
H_2CS	-[a]	50[a]	3.0(14)	-	6.0	0.0	1.0(-09)	[c]
HC_3N	0.8	240	7.9(13)	4.0(16)	7.0	1.0	2.7(-10)	[c]
	10.0	40	4.7(14)	2.0(15)	7.0	1.0	1.6(-09)	
HCN	4.0	150[a]	1.4(15)	3.0(16)	6.0	0.0	4.9(-09)	[c], *f*
HNCO	-[a]	150[a]	1.0(14)	-	6.0	1.0	3.5(-10)	[c]
SO	8.0	30	8.2(15)	5.0(16)	7.0	1.0	2.9(-08)	[e], *f*

[a]Fixed Parameter; [b]based on weak or partially blended lines only; [c]based on one or a few lines only; [d]includes vibrationally excited lines; [e]non-LTE, see text; [f]based on isotopologues, see text. The column labeled offset shows the offset in velocity relative to the systemic velocity of the source. N_{ms} are the source averaged column densities, N_{mb} are the beam averaged column densities and N_{mb}/N_{mH_2} gives beam averaged abundances.

Table 3.6: Results of the line modeling for 16065−5158

Species	Size (")	$T_{\rm ex}$ (K)	$N_{\rm b}$(mol) ($\rm cm^{-2}$)	$N_{\rm s}$(mol) ($\rm cm^{-2}$)	Δv ($\rm km\,s^{-1}$)	Offset ($\rm km\,s^{-1}$)	$N_{\rm b}/N_{\rm H_2}$	
C_2H_5CN	10.0	150[a]	2.4(13)	1.0(14)	3.0	0.0	4.2(-11)	[b]
CCH	-[a]	50[a]	5.0(14)	-	10.0	-4.0	8.8(-10)	[c]
CH_3CCH	-[a]	100	2.5(15)	-	7.5	-1.50	4.4(-09)	[c]
CH_3OCH_3	-[a]	150[a]	1.0(14)	-	2.0	2.0	1.8(-10)	[b]
CH_3OCHO-a	-[a]	150[a]	1.0(14)	-	2.0	0.0	1.8(-10)	[b]
CO	-[a]	50[a]	6.3(19)	-	9.0	-0.5	1.1(-04)	[c], *f*
CS	10.0	55	1.4(15)	6.0(15)	7.0	-0.5	2.5(-09)	[c], *f*
H_2CS	-[a]	50[a]	2.6(14)	-	10.0	-0.5	4.6(-10)	[c]
HC_3N	-[a]	150[a]	1.0(13)	-	6.0	0.0	1.8(-11)	[c]
HNCO	1.0[a]	80	1.5(14)	5.0(16)	6.0	-2.0	2.6(-10)	[c]
SO	4.0	40	1.9(16)	4.0(17)	6.0	-0.5	3.3(-08)	[e], *f*

indices as Tab. 3.6

Table 3.7: Results of the line modeling for 16060−5146

Species	Size (")	$T_{\rm ex}$ (K)	$N_{\rm b}$(mol) ($\rm cm^{-2}$)	$N_{\rm s}$(mol) ($\rm cm^{-2}$)	Δv ($\rm km\,s^{-1}$)	Offset ($\rm km\,s^{-1}$)	$N_{\rm b}/N_{\rm H_2}$	
C_2H_5CN	-[a]	150[a]	6.0(13)	-	3.0	0.0	3.1(-10)	[b]
CCH	-[a]	50[a]	2.8(14)	-	4.0	0.0	1.4(-09)	[c]
CH_3CCH	-[a]	50[a]	1.5(15)	-	5.5	0.0	7.7(-09)	[c]
CH_3OCH_3	-[a]	70	1.3(15)	-	4.5	.0	6.6(-09)	[b]
CH_3OCHO-a	-[a]	150[a]	5.0(14)	-	3.0	0.0	2.6(-09)	[b]
CO	-[a]	50[a]	2.8(19)	-	4.5	-0.5	1.4(-04)	[c], *f*
CS	-[a]	50[a]	2.6(15)	-	6.0	0.0	1.3(-08)	[c], *f*
DCN	-[a]	150[a]	3.0(13)	-	6.0	0.0	1.5(-10)	
H_2CS	-[a]	50[a]	2.5(14)	-	5.0	0.0	1.3(-09)	[c]
HC_3N	1.6	100	1.6(14)	2.0(16)	6.0	-5.0	8.2(-10)	[c]
HNCO	1.6	75	2.4(14)	3.0(16)	6.0	0.0	1.2(-09)	[c]
SO	10.0	50[a]	7.1(15)	3.0(16)	6.0	0.0	3.6(-08)	[e], *f*

indices as Tab. 3.6

Table 3.8: Results of the line modeling for 12326−6245

displayed in Fig. 3.6. It has to be noted that $\rm CH_3CN$, which has been observed at the beginning of the project, was observed at a position offset from the position later used as pointing position for the molecular survey. Since the $\rm CH_3CN$ included in the 338 GHz setup is heavily blended, it cannot be used for a characterization of the hot and dense gas, which is why the setup at the offset position was included in the analysis. One should keep in mind however that the values derived here stem from a position which is 1″ (12326−6245), 5″ (16065−5158) and 8″ (16060−5146) away from the hot core position used for the remaining analysis. While the line ratios for lines originating in the compact cores are not affected by this, the lines are weaker, which makes unambiguous modeling of the weaker transitions more difficult. Due to the presence of the $\rm CH_3CN$ lines up to the K=7 transition in 16065−5158, we used a compact hot component to model the higher excitation lines and additionally a more extended, cooler component to model the K=0 – K=2 transitions. Since this setup also includes some $\rm CH_3^{13}CN$ lines, we had both optically thick and thin transitions to help us solve the N/θ degeneracy. While 16065−5158 and 12326−6245 can both be modeled with a two component fit displaying one hot, compact component and one extended, cooler one, it is also possible to obtain reasonable results for 12326−6245 using only a hot compact component. The two-component structure is attributed to a hot dense core inside a colder, extended envelope. 16060−5146 had to be modeled with two hot, compact components having a velocity difference of 9 $\rm km\,s^{-1}$. This effect, which is not obvious in every species studied in this paper (see next section), suggests a complicated velocity structure for parts of the molecular gas in this source. There is also evidence for a multi-component velocity structure in 3 mm Mopra line data obtained by the us, which is subject of a forthcoming paper.

This $\rm CH_3CN$ setup includes several optically thick and thin lines, as well as the K=0 component of the optically thin $\rm CH_3^{13}CN$ isotopologue, which makes it possible to solve the N, θ degeneracy and obtain sizes for the the three sources. Their physical sizes were obtained

to be 0.03 pc for the hot component in 16065−5158 and 12326−6245 and 0.02 pc each for the two components in 16060−5146. The extended components in 16065−5158 and 12326−6245 are 0.1 pc each. To estimate the errors of the modeled parameters, a χ^2 analysis was performed for 12326−6245 with fixed source size and varying temperature T and column densities N. This indicated uncertainties of up to 40% in T and up to 23% in N within the 3σ confidence limit, which we consider as typical.
Tables 3.9 to 3.11 show the results for the CH_3CN modeling. It was not in all cases possible, to model the CH_3CN emission consistently over several frequency ranges. In 16065−5158, the size of the compact hot core differs by a factor of 1.9, the temperature by a factor of 1.1 and the column density by a factor of 2.1. In the cold component, the column densities differ by a factor of 10.8. There are several possible explanations for this discrepancy. It could be intrinsic to the source and indicate that the higher frequency observations at 349 GHz trace a hotter, denser component than the transitions at 291 GHz. When modeling more than one component, an additional degeneracy could be introduced, in this case between the hot and cold component. The 349 GHz transitions are however coming from the image sideband and blended with strong CH_3OH and CCH transitions at 338 GHz. This makes a reliable determination of the model parameters difficult for the CH_3CN(19–18) lines, which could also explain parts of the difference in the column density for the cold component. Another factor are calibration uncertainties, which, as mentioned before, can amount to about 30%. Those should however affect both components equally. Particularly for the cold, extended component, the assumption of LTE might not be correct. All this is however not enough to explain the large difference between the cold component in the two transitions. Since we know now that the receiver with which the data have been taken happened to produce irreproducible line intensities in a few documented cases where spectra where re-observed after a few months, it cannot be excluded to be at least partially responsible for this discrepancy as well. The fact that the CH_3CN could be modeled consistently in 12326-6145 and with only a factor of 1.5 difference in the column density of 16060−5146 seems to exclude however that the discrepancy comes from the receiver.

CH_3OH data

For all three sources, the CH_3OH(J=7–6) data was obtained in a setup at 338 GHz, including also the torsionally excited v_t=1 CH_3OH lines at 337.6 GHz. The CH_3OH(J=6–5) data at 290 GHz was observed in all three sources, while in the case of 12326−6245, also the torsionally excited lines at 289 GHz were observed in a different frequency setup. Both J=6–5 and J=7–6 were modeled under the assumption of LTE. Using XCLASS, it was possible to include line blends with other molecules, mainly CCH(4–3) and CH_3CN(19–18) from the image sideband, and optical depth effects in the model.
To obtain the temperature for the hot compact component in the J=7–6 band, the optically thin torsionally excited lines were used. In combination with optically thick lines in the band, the N/θ degeneracy could be resolved and also source size and column density could be obtained. From the optically thin torsionally excited lines together with the higher excitation lines in the v_t=0 bands, it is possible to obtain the temperature of the hot compact component. The torsionally excited lines at 289 and 337 GHz also contain a line with higher optical depth, which makes it possible to obtain an estimate of the source size for this component. In the

Species	Transition	Source Size ($''$)	T_{ex} (K)	N_s (cm^{-2})	N_b (cm^{-2})	Δv ($km\,s^{-1}$)	Offset ($km\,s^{-1}$)	N_b/N_{H_2}
CH_3CN	19–18	1.6	100	8(15)	6.3(13)	5.4	0.0	3.2(-10)
CH_3CN	19–18	7.0	20	1(15)	1.3(14)	5.4	0.0	6.7(-10)
CH_3CN	16–15	1.6	100	8(15)	6.3(13)	5.4	0.0	3.2(-10)
CH_3CN	16–15	7.0	20	1(15)	1.3(14)	5.4	0.0	6.7(-10)
CH_3OH	6–5	1.0	240	4(18)	1.2(16)	4	0.5	6.3(-08)
CH_3OH	6–5	12.0	50	1.5(16)	4.6(15)	4	0.0	2.4(-08)
CH_3OH	7–6	1.3	200	1(18)	5.2(15)	3	-1.0	2.7(-08)
CH_3OH	7–6	12.0	50	1(16)	3.1(15)	4	0.0	1.6(-08)
H_2CO	4–3	-	75	-	4(14)	5	0.0	2.0(-09)
SO_2	290 GHz	-	35	-	2.5(16)	6	-0.5	1.3(-07)
SO_2	338 GHz	-	35	-	1.8(16)	6	0.5	9.2(-08)

Table 3.9: Properties of the source 12326−6245 as derived from LTE modeling of CH_3CN, CH_3OH, H_2CO and SO_2. Given in the table are exitation temperature T_{ex}, source averaged column density N_s, beam averaged column density N_b, velocity width Δv, velocity offset from systemic velocity, and abundances. If two entries per transition are given, they refer to the cold extended envelope and the hot compact core.

Species	Transition	Source Size ($''$)	T_{ex} (K)	N_s (cm^{-2})	N_b (cm^{-2})	Δv ($km\,s^{-1}$)	Offset ($km\,s^{-1}$)	N_b/N_{H_2}
CH_3CN	19–18	0.7	250	3.0(15)	4.5(12)	4.5	-1.0	1.6(-11)
CH_3CN	19–18	5.0	30	1.0(17)	7.2(15)	4.5	-1.0	2.5(-08)
CH_3CN	16–15	1.3	220	1.4(15)	7.3(12)	4.5	1.0	2.5(-11)
CH_3CN	16–15	5.0	30	9.4(15)	6.7(14)	4.5	1.0	2.3(-09)
CH_3OH	6–5	1.8	140	2.0(18)	2.0(16)	6.0	0.0	6.9(-08)
CH_3OH	6–5	13.0	30	5.0(15)	1.7(15)	6.0	0.0	6.0(-09)
CH_3OH	7–6	1.8	140	7.0(17)	6.9(15)	6.0	1.5	2.4(-08)
CH_3OH	7–6	13.0	30	5.0(15)	1.7(15)	6.0	1.0	6.0(-09)
H_2CO	4–3	2.1	160	1.0(16)	1.3(14)	6.0	-0.5	4.7(-10)
H_2CO	4–3	-	50	-	4.0(14)	6.0	-0.5	1.4(-09)
H_2CO	6–5	2.1	160	4.8(16)	6.4(14)	6.0	-0.5	2.2(-09)
H_2CO	6–5	-	50	-	5.0(13)	6.0	-0.5	1.7(-10)
SO_2	338 GHz	-	30	-	3.0(16)	8.0	0.0	1.0(-07)
SO_2	338 GHz	-	250	-	1.0(15)	8.0	0.0	3.5(-09)
SO_2	430 GHz	-	30	-	3.0(16)	8.0	0.0	1.0(-07)
SO_2	430 GHz	-	250	-	1.0(15)	8.0	0.0	3.5(-09)

Table 3.10: Properties of the source 16065−5158 as derived from LTE modeling of CH_3CN, CH_3OH, H_2CO and SO_2. Given in the table are exitation temperature T_{ex}, source averaged column density N_s, beam averaged column density N_b, velocity width Δv, velocity offset from systemic velocity, and abundances. If two entries per transition are given, they refer to the cold extended envelope and the hot compact core.

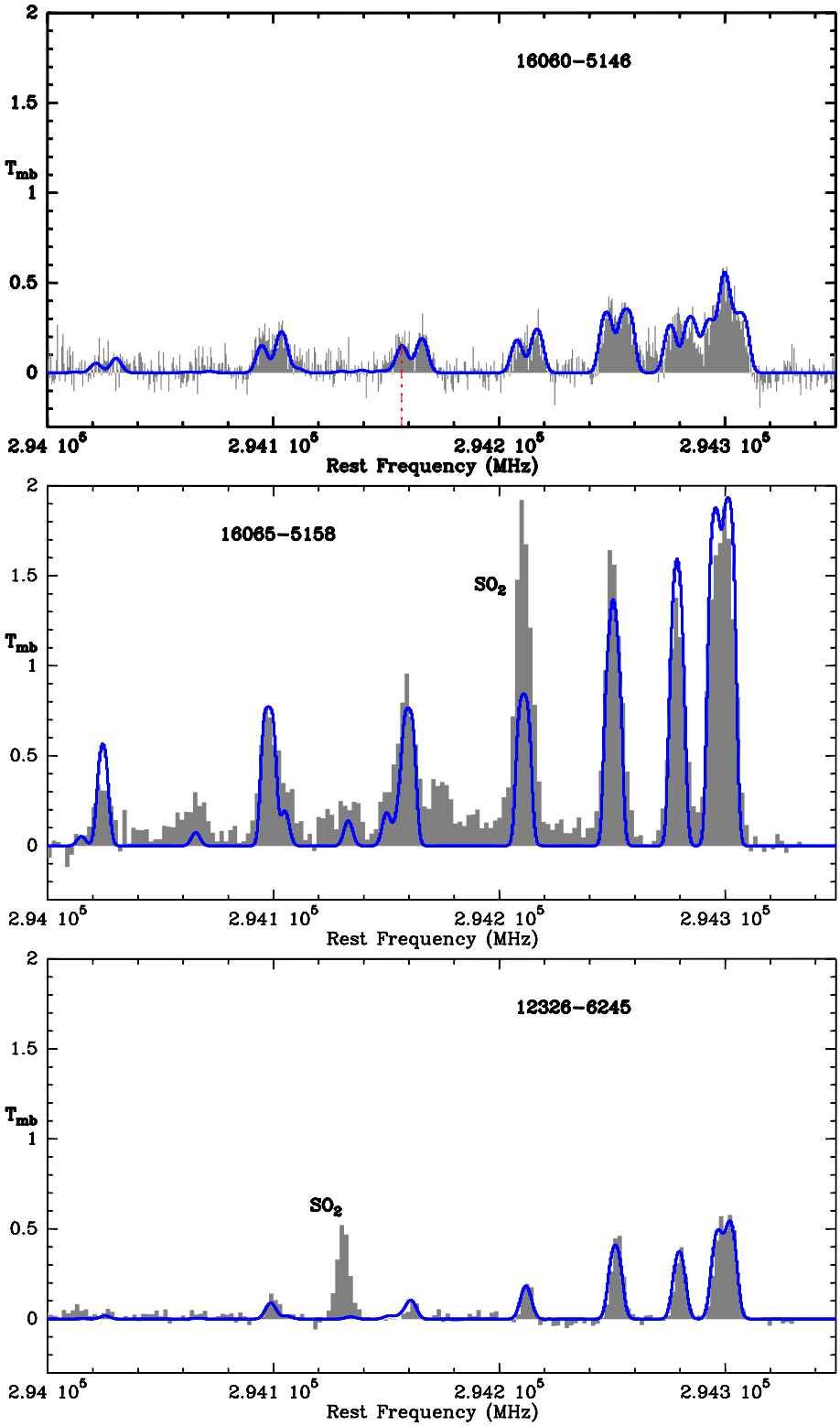

Figure 3.6: CH_3CN data at 294 GHz. In blue, the synthetic model spectrum is shown. Note that the spectra for the three sources have been observed with different frequency setups, therefore the SO_2 line from the image sidebands appears at different frequencies. The rest frequency of the $CH_3^{13}CN$ lines is marked in red.

Species	Transition	Source Size ($''$)	$T_{\rm ex}$ (K)	$N_{\rm s}$ ($\rm cm^{-2}$)	$N_{\rm b}$ ($\rm cm^{-2}$)	Δv ($\rm km\,s^{-1}$)	Offset ($\rm km\,s^{-1}$)	$N_{\rm b}/N_{\rm H_2}$
CH_3CN	19–18	1.1	170	1.0(16)	3.7(13)	5.5	2.0	6.5(-11)
CH_3CN	19–18	1.0	180	2.0(16)	6.2(13)	5.5	-6.0	1.1(-10)
CH_3CN	16–15	1.1	170	1.5(16)	5.6(13)	5.5	4.0	9.8(-11)
CH_3CN	16–15	1.0	180	3.0(16)	9.2(13)	5.5	-5.0	1.6(-10)
CH_3OH	7–6	1.0	170	5.0(17)	1.5(15)	3.0	5.0	2.7(-09)
CH_3OH	7–6	1.0	170	5.0(17)	1.5(15)	3.0	-5.0	2.7(-09)
CH_3OH	7–6	-	30	-	4.0(15)	7.0	-2.0	7.0(-09)
CH_3OH	6–5	1.0	170	1.0(17)	3.1(14)	3.0	5.0	5.4(-10)
CH_3OH	6–5	1.0	170	1.0(17)	3.1(14)	3.0	-5.0	5.4(-10)
CH_3OH	6–5	-	30	-	2(15)	7.0	-2.0	3.5(-09)
H_2CO	4–3	1.3	170	5.0(16)	2.6(14)	7.0	0.0	4.6(-10)
H_2CO	4–3	-	70	-	3.0(14)	10.0	0.0	5.3(-10)
H_2CO	6–5	1.3	170	5.0(16)	2.6(14)	7.0	0.0	4.6(-10)
H_2CO	6–5	-	70	-	6.0(13)	10.0	0.0	1.1(-10)
SO_2	338 GHz	-	30	-	5.0(16)	10.0	0.0	8.8(-08)
SO_2	430 GHz	-	100	-	1.0(15)	8.0	0.0	1.8(-09)

Table 3.11: Properties of the source 16060−5146 as derived from LTE modeling of CH_3CN, CH_3OH, H_2CO and SO_2. Given in the table are exitation temperature $T_{\rm ex}$, source averaged column density $N_{\rm s}$, beam averaged column density $N_{\rm b}$, velocity width Δv, velocity offset from systemic velocity, and abundances. Due to its line profiles, 16060−5146 had to be modeled with two hot compact components in some molecules instead of the core/envelope model used for the other two sources.

case of 12326−6245, where two bands including torsionally excited lines were available, the accuracy of the source size determination is of the order of $0.3''$, while the column density estimate is accurate to about a factor of 2, due to the degeneracy between N and θ. The estimates of N and θ for the extended component are more uncertain, since the optically thin transitions of the cold component contain a contribution of the hot component as well as blends with other molecules such as CCH(4–3) and CH_3CN(19–18). For details of the model in 12326−6245, see Figs. 3.7 and 3.8, while plots of the remaining two sources can be found in the appendix.

For 16065−5158 and 16060−5146, the CH_3OH J=6–5 transitions were only observed as part of the H_2CO(4–3) setup and included only the main band at 290 GHz, not the torsionally excited lines. The accuracies for the source size and column density estimations are also of the order $0.3''$ and a factor of 2 for the hot component. In 16060−5146, the line profiles are much broader due to a blend of two hot compact components and one extended component and the spectra suffer from a worse baseline than the other two sources. It was possible to obtain a good fit for two hot components, but due to the complexity of the data, only a beam-averaged column density was obtained for the cold component. The results of the CH_3OH modeling can be found in Tables 3.9-3.11. In 16060−5146 and 16065−5158 it was possible to model the CH_3OH(6–5) and CH_3OH(7–6) transitions with consistent temperatures. The

column densities for the hot component differ by a factor of 2.9 in 16065−5158 and a factor of 5 in 16060−5146. The column densities for the cold component in 16060−5146 differ by a factor of 2. Under the conditions described above, those factors are considered consistent with effects of calibration between the different frequency setups, data quality and the effects of line blending between the two sidebands. While the line blending between Gaussian components in one sideband is accounted for in XCLASS, line blending between the two sidebands adds additional confusion when trying to judge the quality of a model.

H_2CO data

Being a slightly asymmetric rotor, H_2CO is a good tracer of kinetic temperatures and also sensitive to spatial densities $\geq 10^5 \mathrm{cm}^{-3}$ (Mangum & Wootten, 1993) and it is quite ubiquitous in regions of star formation (Mangum et al., 1990; Mangum & Wootten, 1993).
In this survey, we observed H_2CO in all three sources in the H_2CO(4–5) transition at 291 GHz, H_2CO(5–4) at 363 GHz and in 16065−5158 and 16060−5146 also in H_2CO(6–5) at 437 GHz. During the analysis, inconsistencies in the H_2CO(5–4) spectra were discovered, which led to the setup being excluded from the analysis. It is possible to obtain a reasonable fit to the remaining two transitions using a hot compact core and a cold extended envelope component. The results of the H_2CO modeling can be found in Tables 3.9–3.11, while the spectra and synthetic models can be found in Figs. A.1, A.3 and A.5 in the Appendix. For 12326−6245, only one H_2CO transition was observed. In 16060−5146, it was not possible to model the H_2CO emission with two hot velocity components, as was the case for CH_3OH and CH_3CN. The model results of the hot component nonetheless agree well for the two transitions, while the column densities of the cold component differ by a factor of 5. In 16065−5158, the column densities of the hot components differ by a factor of 4.8, while the cold components differ by a factor of 8. The fact that less cold gas is detected at the higher frequencies, indicates that the H_2CO(6–5) transitions are less sensitive to the cold extended component than H_2CO(4–3). It is noteworthy that 16065−5158 shows again a large discrepancy between the column densities of the cold component, which could be a result of non-LTE effects.

S-bearing species

The S-bearing species, CS, H_2CS, SO and SO_2 were observed in our frequency setups. In the case of H_2CS(10–9), only the beam averaged column density for a fixed temperature of 50 K could be determined, while the other species were observed in several lines.
CS was observed in its isotopologues $C^{33}S$(9–8), $C^{33}S$(6–5) and $C^{34}S$(7–6), while $C^{32}S$ was not included in the setups. Assuming isotopic ratios of $^{32}S/^{34}S$=23 and $^{32}S/^{33}S$=127, it was possible to model CS and SO consistently over the frequency bands. The same was not possible for SO_2.
Apart from the SO_2(5–4) line at 351.3 GHz, which has a lower level energy of 19 K above ground state, the other SO_2 lines cover higher excitation conditions, being between 76 K and 770 K above ground state energy. When trying to model the lines with a single temperature component, the two observed $^{34}SO_2$ lines at 338.32 GHz and 436.8G Hz are underestimated in 16065−5158. These discrepancies in the modeling can reflect calibration uncertainties between the different frequency setups as well as indicate that the transitions trace a different

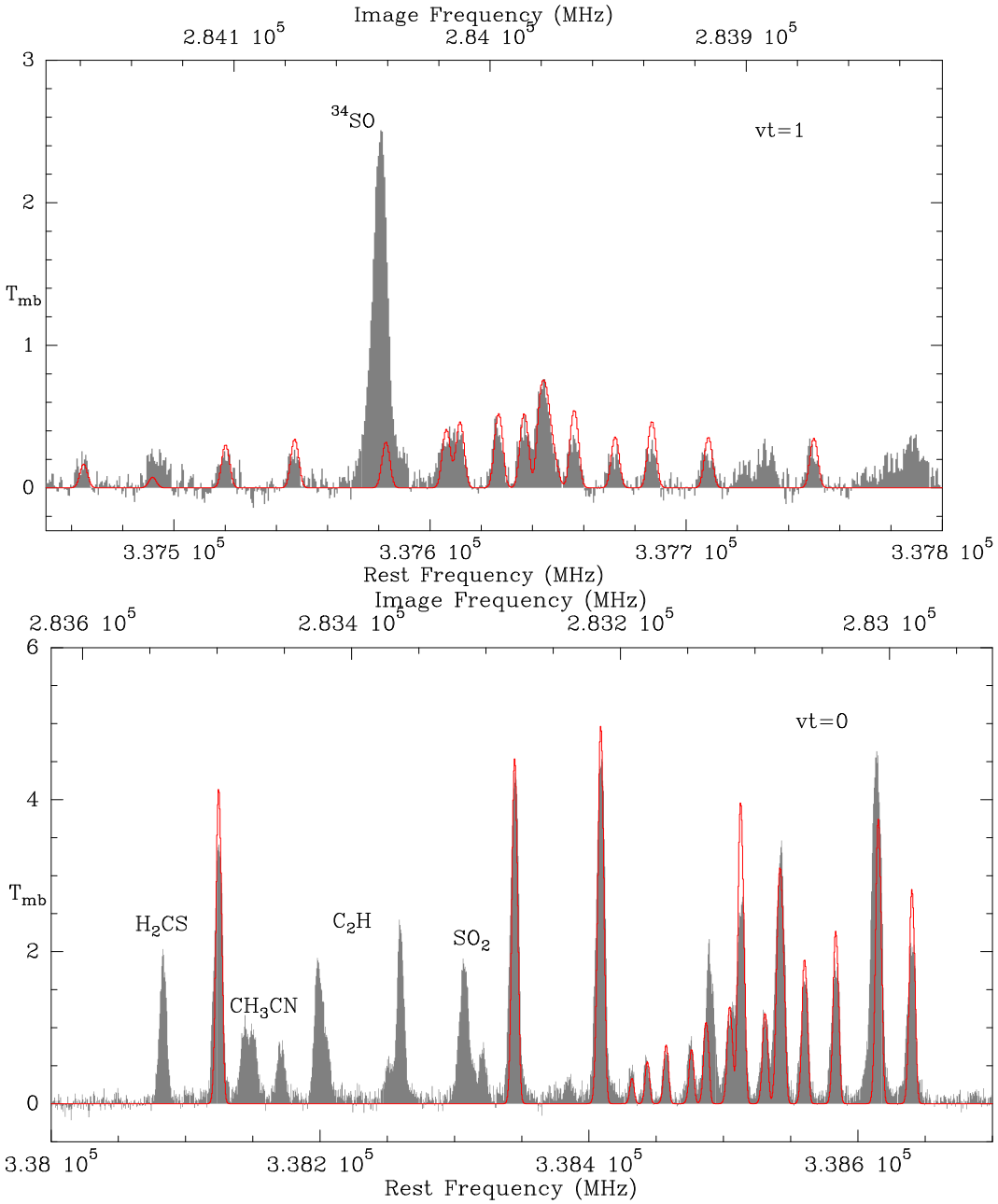

Figure 3.7: Spectrum of 12326−6145. The synthetic model spectrum of CH_3OH(7–6) is shown in red. In the upper plot ($v_t = 1$), the synthetic spectrum of the torsionally excited CH_3OH transitions (red) is shown.

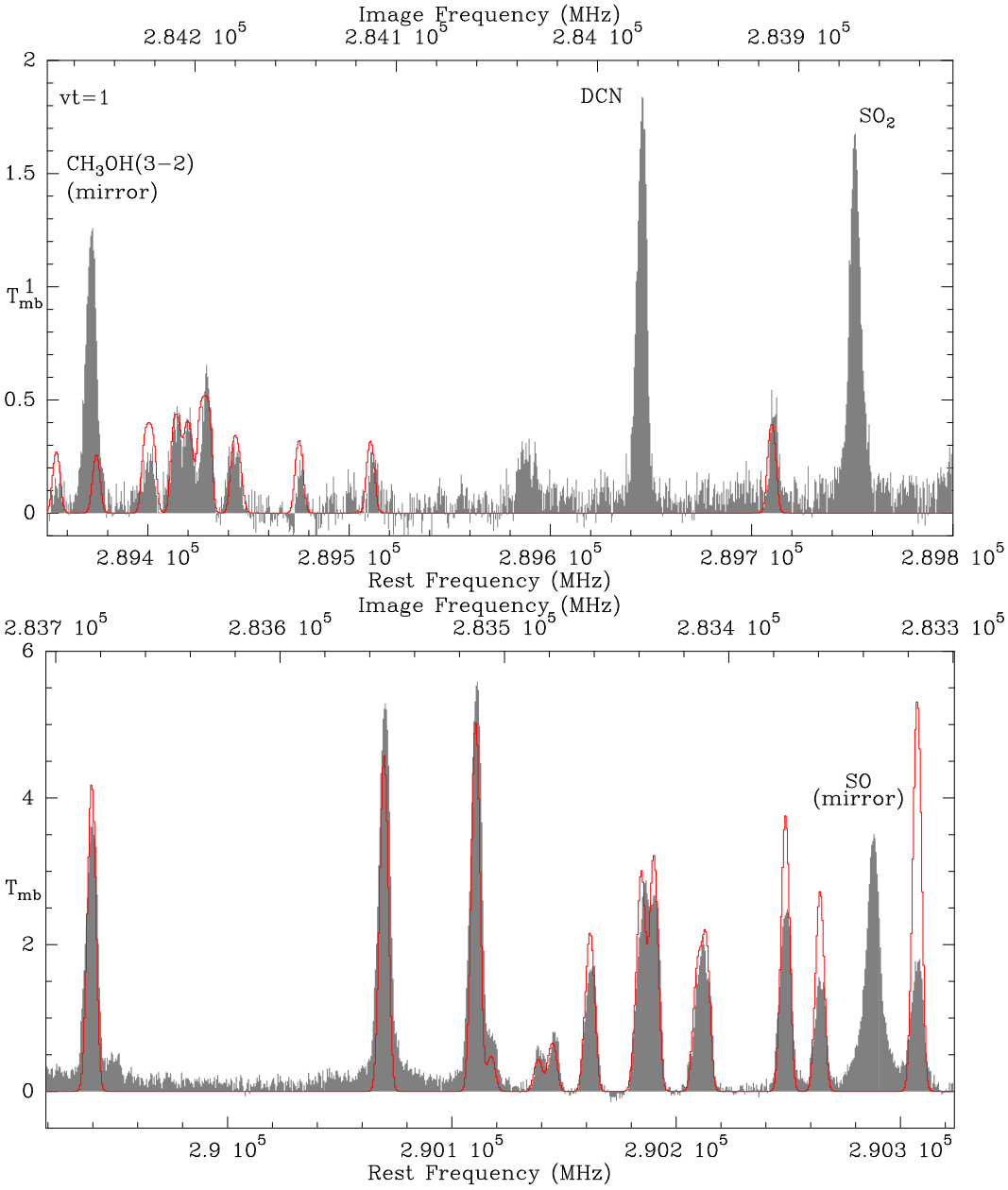

Figure 3.8: Spectrum of 12326−6245. The synthetic model spectrum of CH_3OH(6–5) is shown in red. In the upper plot ($v_t = 1$), the synthetic spectrum of the torsionally excited CH_3OH transitions (red) is shown. The two lines marked (mirror) in both plots show lines that lie outside the shown frequency range but were folded into the spectrum due to a problem with the receiver.

type of gas.
The results of the SO_2 modeling can be found in Tables 3.9–3.11, while the results of the remaining species can be found in Tables 3.6–3.8.
The SO_2 emission in the cold component differs by a factor of 1.4 in 12326−6245, while in 16060−5146 only the cold component could be modeled at 338 GHz while only the hot component could be modeled at 430 GHz.

3.4.2 Spectral energy distributions

To obtain the dust temperatures and luminosities for the three sources, the spectral energy distribution (i.e., flux density vs. frequency) was analyzed for each source. In addition to the 870 μm continuum observed with LABOCA and 3 mm continuum observed with ATCA (this work), the associated IRAC point source fluxes from the Spitzer GLIMPSE mission (Benjamin et al., 2003) at 3.6, 4.5, 5.6 and 8 μm and from the MSX mission at 8.3, 12.1, 14.7 and 21.3 μm (Egan et al., 2003) were obtained. Photometry on the MIPSGAL 24 and 70 μm images (Carey et al., 2006) could not be performed, since the sources are saturated in all cases. All the three regions show extended 8 μm emission, which is commonly associated with emission of photon-dominated regions (PDRs) due to the features of polycyclic aromatic hydrocarbons (PAHs).
In order to find the infrared point sources associated with the 870 μm dust peaks, we searched the catalogs within a radius of 18″, the LABOCA beam, around the dust peak. When studying environments of high mass star formation one frequently encounters a situation where many infrared sources cluster in one single dish beam – in this case the LABOCA beam – because massive stars form exclusively in clusters (see Fig. 3.4). Since many of the young high mass proto-stellar candidates are very red and bright, they are saturated in the 8 μm band and therefore appear with null values in the GLIMPSE point source catalog (Kumar & Grave, 2007), so when a null value at 8μm was found, we did a manual check on the image to distinguish between sources with no detectable emission at 8μm and those that are saturated. In the case where there was no Glimpse data at 8μm, the MSX value was used.
For 16060−5146 and 12326−6245, both MSX and GLIMPSE emission is associated with the hot core traced by the 3 mm continuum observed with ATCA. In 16065−5158 however, there is neither an MSX nor GLIMPSE source at the position of the hot core, yet both types of sources can be found a few seconds of arc offset from the hot core, which might indicate an external heating source or a deeply embedded UCHII region.
For cm wavelengths, archival 3 cm and 6 cm ATCA data was obtained from Urquhart et al. (2007a) at the positions of the hot cores in 12326−6245 and 16060−5146. In 16065−5158, there is an offset of 4.3″ between the mm position obtained from ATCA and the ATCA cm position (see Fig. 3.4). The cm emission in this source has a negative spectral index of -0.9, hinting at synchrotron emission. No extragalactic object could be found at this position in the NED database. This could be similar to the situation in W3(H_2O), where a synchrotron source (Reid et al., 1995) can be found in the hot core.
It has to be noted however that Urquhart et al. (2007a) state that the spectral indices of individual sources might not be reliable for all sources, since the ATCA is not a scaled array at the observed frequencies (meaning comparable resolution at the different wavelengths) and the measurements sample different spacial scales.

Fig. 3.9 shows a zoom-in on the region of the 870 μm peak. In 12326−6245, the IR flux is coming from a bright cluster of objects. One can see green emission at 4.5μm surrounding the cluster, which is a sign of shocked gas (Cyganowski et al., 2008) and can point to outflow emission. In 16060−5146, the peak of the 870 μm emission can be associated to a single object. There is weak 4.5 μm emission at the edge of the IR source. 16065−5158 has no associated IR source at the position of the 870 μm peak. There is however a strong elongated 4.5 μm emission. This situation is suggestive of an deeply embedded young object with a strong outflow.

Temperature estimates

Estimates of the dust temperatures were obtained by fitting grey-body plus free-free spectra to the SEDs (see Fig. 3.10). For all three sources a power-law dependency of the dust opacity with $\beta = 1.8$ was used (see Sec. 3.3.2), based on the dust properties used to derive the masses and column densities of the three sources (Ossenkopf & Henning, 1994). We also estimated total luminosities by integrating the fluxes under the SED.
The sources were modeled using three different components (only one in the case of 16065-5159). The data at 3.6 – 12 μm trace the hot, compact radiation source which is already well developed in the infrared, while the data points between 24 μm and 3 mm represent contribution from the colder, more extended dust envelope. The IRAS points at 60 and 100 μm are upper limits to the true flux, due to the large flux of the IRAS beam. The cm continuum data, which represents the contribution of free-free emission from an associated UCHII region is modeled as third component. In 16065−5158, only the cold, extended envelope was modeled, since the radio continuum and infrared data are offset from the dust peak.

For 12326−6245, a dust temperature of 77 K was modeled with the gray-body fit for the extended component. For the hot component traced by the SPITZER IRAC points, the black-body fit resulted in a temperature of 390 K. The luminosity of the 77 K extended dust component is 1.0×10^5 $L_\odot$ and the one derived from the 390 K compact component 74 $L_\odot$.
16060−5146 has a dust temperature of 63 K, a temperature of the compact component of 500 K and luminosities of 2.4×10^5 $L_\odot$ and 490 $L_\odot$ for the extended and compact components respectively.
In the case of 16065−5158, the dust temperature was modeled to be 50 K, but in this source, it is hard to constrain the parameters, since only the ATCA 3 mm emission and the LABOCA 870 μm emission are associated with it, as IRAS and MSX values give but upper limits. The luminosity of the extended component is 0.6×10^5 $L_\odot$.
The spectral energy distributions show that the 3 mm sources in 12326−6245 and 16060−5146 are dominated by free-free emission and by dust radiation for 16065−5158.

As an alternative, we made use of the online model fitter of Robitaille et al. (2007), who have created a grid of 200000 YSO model SEDs. These models represent pre-main sequence stars in combination with disks, infalling envelopes and outflow cavities (Robitaille et al., 2006). The grid of models can be fitted to a given SED to determine the range of different models which are consistent with the data provided. For the current analysis we focused on stellar temperature, stellar mass, envelope accretion rate, disk mass and total luminosity.

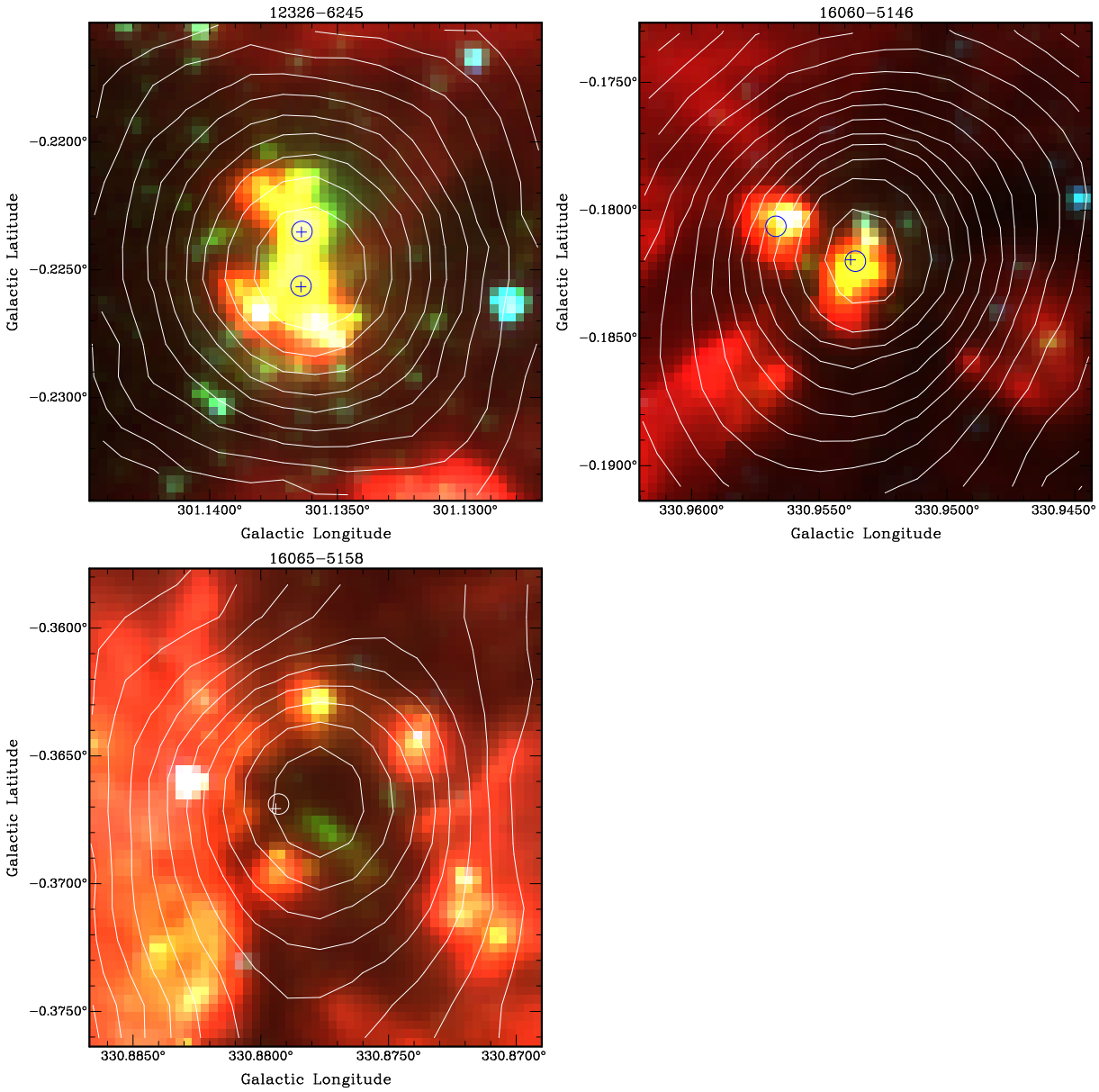

Figure 3.9: Zoom-in of the Spitzer GLIMPSE composite image of 3.6, 4.5 and 8 μm emission. LABOCA 870 μm emission is shown as contours, starting from 5σ (see Table 3.3). The small blue circles mark the position of the 6 cm continuum and the blue crosses the position of the 3.6 cm continuum (Urquhart et al. 2007). In the plot of 16065−5158, the cross and circle marking the radio continuum emission are shown in white.

Source Name	Mass(*)	Temperature(*)	Total Luminosity	Envelope Accretion Rate	Disk Mass
	$M_\odot$	10^3 K	$10^5 L_\odot$	10^{-3} $M_\odot$/yr	$M_\odot$
16060−5146 (d)	14.7 - 29.7	12.2 - 35.7	0.57 - 1.4	0.74 - 3.3	0.04 - 1.0
16060−5146 (nd)	30.1 - 47.5	5.7 - 22.4	2.1 - 4.5	9.8 - 6.3	-
12326−6245 (nd)	35.2 - 49.2	6.4 - 45.5	2.4 - 4.3	7.1 - 1.6	-

Table 3.12: Parameters for the best fit models of the online model fitter (Robitaille et al. 2007). A range of the ten best fits is given. (d) indicates that the best fit models assumed a disk, while (nd) are models without a disk.

For the results in table 3.12, the ranges provided by the ten best fits were considered. For 16060−5146, both the models with and without disk are given, while in 12326−6245, there was no disk model among the ten best fits.

3.4.3 Spectral types

To obtain the spectral type of the mm-sources, the Lyman continuum flux was estimated from the cm observations of Urquhart et al. (2007a) which trace the free free emission of the UCHII region.
Since both regions are optically thick, we obtained their parameters by fitting the spectral energy distribution with the theoretical spectrum of a homogeneous constant density plasma (Garay et al., 2006). For 12326−6245, an emission measure of 2.6×10^9 pc cm^{-6} and a Lyman continuum flux of 8.2×10^{48} s^{-1} were obtained, leading to a spectral type between O6.5 and a stellar luminosity of $L = 1.5 \times 10^5$ $L_\odot$, according to Panagia (1973).
For 16060−5146, the emission measure is 4.0×10^8 pc cm^{-6}, the Lyman continuum flux 1.5×10^{49}s^{-1} and the spectral type was found to be between O6 and O5.5 with $L = 2.5 - -4.0 \times 10^5$ $L_\odot$.
In this kind of analysis, it is assumed that the Lyman continuum luminosity of the source is dominated by the emission of one object.

3.4.4 Mass estimates

Table 3.13 lists the dust masses derived from the 870 μm LABOCA observations as well as the virial masses derived from the line velocity dispersion of the $C^{17}O$(3–2) line. The derivation of the virial masses is described in more details in chapter 5. We estimated the dust masses in two ways. $M_{\rm warm}$ gives a measure of the masses of the warmer component associated with the IRAS source, as traced by the grey-body fit of the SED, while $M_{\rm ext}$ traces the masses of the extended cooler envelopes. The dust masses were derived using Equ. 3.2, following Miettinen et al. (2006), with a dust absorption coefficient, $\kappa_{\rm d}$, of 0.176 m^2/kg (Ossenkopf & Henning, 1994) (model V) and a dust-to-gas ratio $R_{\rm d} = \frac{1}{100}$. $B_\nu(T_{\rm d})$ is the Planck function of a black body at dust temperature $T_{\rm d}$, S_ν the integrated flux in Jy and d the kinematic distance in kpc.

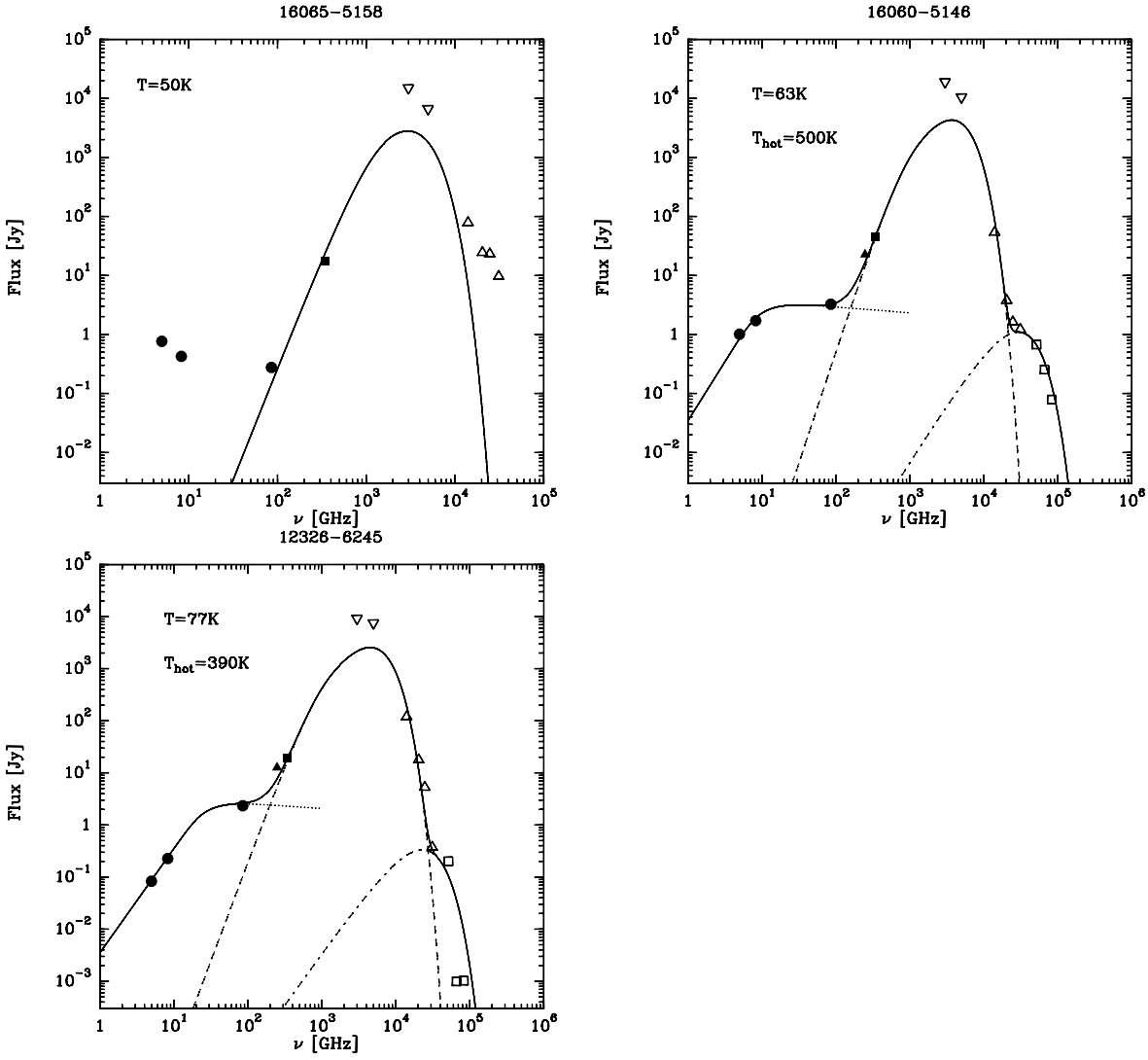

Figure 3.10: Spectral energy distributions for the three sources. The IRAS fluxes (downwards pointing triangles) are taken as upper limits due to the large beam size. The empty squares and triangles show the MSX and Spitzer GLIMPSE fluxes respectively, the filled circles the ATCA fluxes and the filled triangle and square the bolometer fluxes from SIMBA and LABOCA.

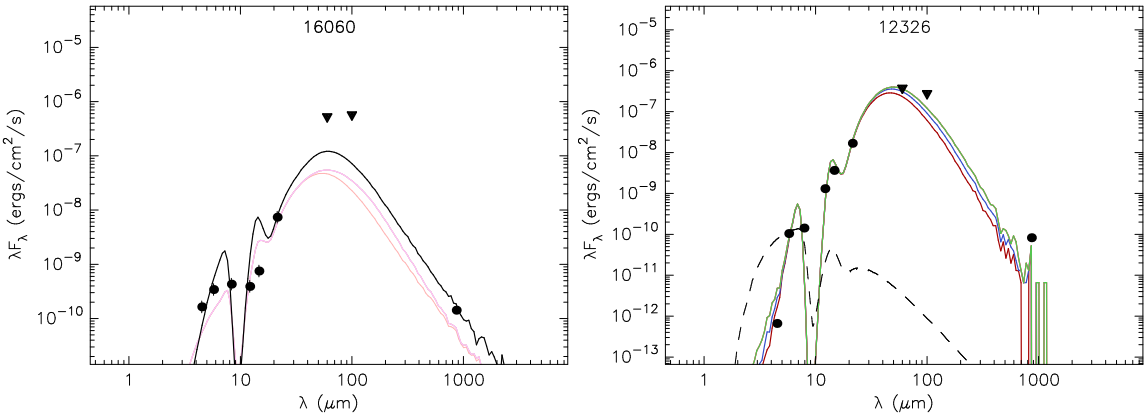

Figure 3.11: Best fit models of the SEDs for 16060−5146 and 12326−6245 (colored lines) created with the online model fitter of Robitaille et al. (2007). The dashed line represents the model of a stellar photosphere.

In the case of the warm component, $T_{\rm d}$ as derived from the SED and the peak fluxes were used, while the mass of the extended dust emission was derived using the integrated intensity within the 10% contour and assuming a dust temperature of 20 K for 12326−6245 and 30 K for 16065−5158 and 16060−5146, respectively. They were assumed to be equal to the gas kinetic temperatures derived in the CH_3CN modeling, following Miettinen et al. (2006). In the case of 16060−5146, where the CH_3CN was modeled without a cold component, the temperature derived from CH_3OH was taken instead.

$$M_{\rm gas} = \frac{S_\nu d^2}{B_\nu(T_{\rm d})\kappa_{\rm d} R_{\rm d}} \ [{\rm M}_\odot] \tag{3.2}$$

source	$M_{\rm warm}$ $10^3{\rm M}_\odot$	$M_{\rm ext}$ $10^3{\rm M}_\odot$	$M_{\rm vir}$ $10^3{\rm M}_\odot$	$R_{\rm warm}$ pc	$R_{\rm ext}$ pc	$n_{\rm warm}(H_2)$ $10^8{\rm cm}^{-3}$	$n_{\rm ext}(H_2)$ $10^4{\rm cm}^{-3}$
12326-6245	0.42	1.6	1.2	0.03	0.6	6.7	3.6
16060-5146	1.9/5.5	4.1/12	5.3/9.2	0.04/0.07	0.6/1.1	12/6.9	6.5/3.7
16065-5158	0.51/3.7	2.0/14	2.5/6.6	0.03/0.08	0.6/2.1	8.2/3.1	1.7/0.63

Table 3.13: Dust masses derived from LABOCA 870 μm emission; the first entry gives the mass of the hot component traced by the SED, the second of the whole dust envelope traced at 870 μm and the third column lists the virial masses derived from $C^{17}O$(3–2) emission. In the last three columns, the radii for the hot compact component (taken from the XCLASS line modeling) and the extended dust emission as well as the H_2 number densities for both components are listed. If two values are listed, they indicate near/far distances used for the calculations.

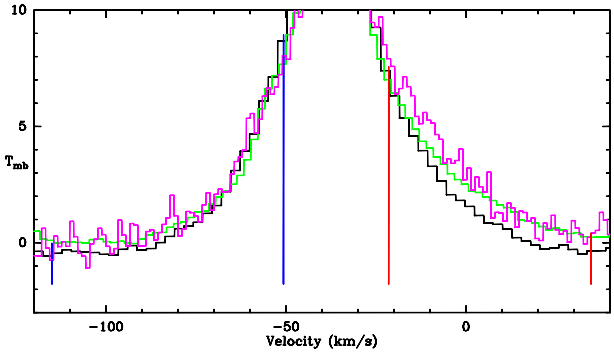

Figure 3.12: CO spectra of the central position of the outflow in 12326−6245. CO(3–2) is shown in black, CO(4–3) in green and CO(7–6) in magenta. All spectra have been smoothed to the spacial resolution of the CO(3–2) data.

3.5 Molecular outflows

While all three sources were initially mapped in the CO(3–2) line, the data quality of these maps only allowed to map the outflows in 12326−6245 and 16060−5146. For 12326−6245, the outflow was also mapped in the CO(4–3) and CO(7–6) transitions. The data of the CO(4–3) and CO(7–6) transitions were smoothed to the spacial resolution of the CO(3–2) data and all data were re-sampled to a velocity resolution of 3 $\mathrm{km\,s^{-1}}$ to reduce the noise in the wings. Fig 3.12 shows the spectra at the central position, with the blue lines marking the blue wing in the velocity range $-115\ \mathrm{km\,s^{-1}}$ to $-51\ \mathrm{km\,s^{-1}}$and the red lines marking the red wing from $-22\ \mathrm{km\,s^{-1}}$ to $35\ \mathrm{km\,s^{-1}}$.
In Fig. 3.13, the outflow maps of 12326-6145 are shown, with the red and blue triangles showing the location of the peak of emission of the red and blue wing, as determined from the CO(7–6) data. The black triangle shows the center of the 3 mm continuum emission. The 3 mm emission looks to be offset from the origin of the outflow, which suggests that a younger, more embedded source is powering the molecular outflow.

To get an overview of the outflow parameters, we follow the method outlined in Cabrit & Bertout (1990) and Beuther et al. (2002b) and assume a temperature of 50 K for the outflow. The results can be found in tables 3.14 and 3.15. A more thourough study of the outflow properties would require maps of the whole extent of the outflow wings and to observe the outflow in an optically thin tracer to get an idea of the optical depth in the wings.
To obtain the column density in the wings, we integrated in the outflow emission between $-114\ \mathrm{km\,s^{-1}}$ and $-50\ \mathrm{km\,s^{-1}}$ and $-21\ \mathrm{km\,s^{-1}}$ and $-35\ \mathrm{km\,s^{-1}}$/. Having avoided the core emission, one has to take into account that the derived mass is a lower limit. The momentum, p, energy, E and characteristic time scale, t, are derived assuming a constant velocity flow with its true velocity equal to its maximum velocity observed. In addition to the work outlined in Beuther et al. (2002b), we also corrected for the inclination angle θ between outflow and line of sight (Leurini et al., 2006). For comparisons to other works, we adopt an inclination angle of 57.3 degrees, the average over a uniform distribution of random orientations (Henning et al., 2000).

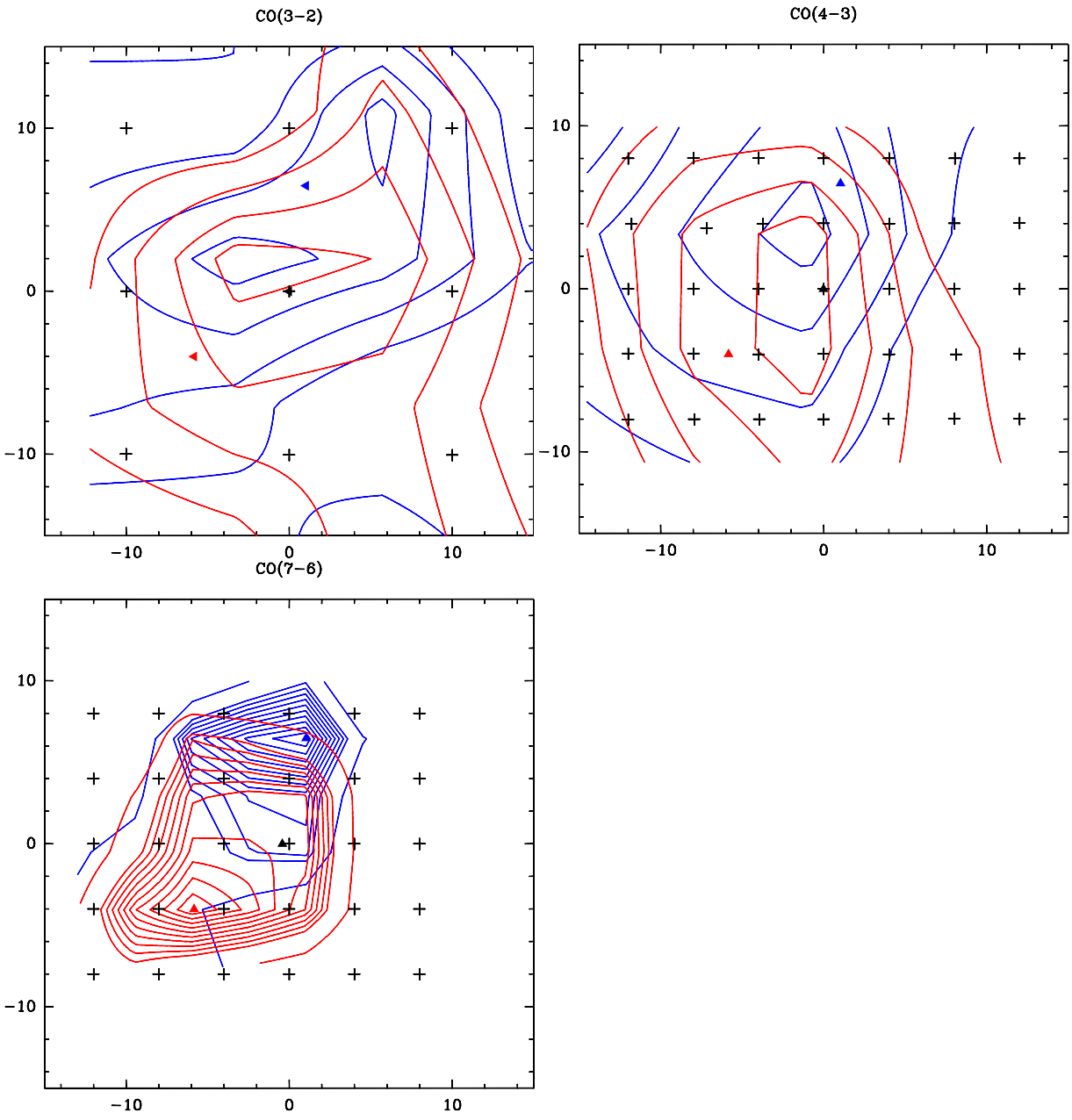

Figure 3.13: Outflow maps of 12326−6245 in CO(3–2) (top left), CO(4–3) (top right) and CO(7–6) (bottom left). The 3 mm continuum (black triangle) as well as the peaks of the two outflow lobes (red and blue triangles) are marked. The crosses indicate the location corresponding to the spectra shown in Fig. 3.12.

$N_{\rm blue}$ [cm^{-2}]		2.89e+20	
$N_{\rm red}$ [cm^{-2}]		2.33e+20	
	θ=0	θ=57.3	θ=70
$M_{\rm blue}$ [M$_\odot$]	0.67	0.92	1.06
$M_{\rm red}$ [M$_\odot$]	0.58	0.80	0.92
$M_{\rm tot}$ [M$_\odot$]	1.25	1.72	1.98
t [10^3 yr]	2.84	3.04	2.33
p [M$_\odot$ km s^{-1}]	96.89	181.43	241.56
E [10^{47} erg]	0.94	2.40	3.69
F [M$_\odot$ km s^{-1} yr^{-1}]	0.03	0.06	0.10
L [L$_\odot$]	271.94	650.88	1308.17
$\dot{M}$ [10^{-3}M$_\odot$ yr^{-1}]	0.44	0.56	0.85

Table 3.14: Physical Parameters of the CO(4-3) outflow in 12326-6245.

$N_{\rm blue}$ [cm^{-2}]		2.17e+20	
$N_{\rm red}$ [cm^{-2}]		2.77e+20	
	θ=0	θ=57.3	θ =70
$M_{\rm blue}$ [M$_\odot$]	0.22	0.31	0.35
$M_{\rm red}$ [M$_\odot$]	0.26	0.36	0.41
$M_{\rm tot}$ [M$_\odot$]	0.48	0.66	0.76
t [10^3 yr]	2.62	2.81	2.14
p [M$_\odot$ km s^{-1}]	34.52	64.64	86.06
E [10^{47} erg]	0.32	0.82	1.26
F [M$_\odot$ km s^{-1} yr^{-1}]	0.01	0.02	0.04
L [L$_\odot$]	100.57	240.70	483.77
$\dot{M}$ [10^{-3}M$_\odot$ yr^{-1}]	0.18	0.24	0.36

Table 3.15: Physical Parameters of the CO(7–6) outflow in 12326-6245

3.6 Discussion

3.6.1 Molecular line data

The three sources were mapped in HCO^+(4–3) and CO(3–2). As can be seen in Figs. 3.1 and 3.2, the line profiles, particularly around the peak of the emission, show non-Gaussian line shapes in the wings. This can be a sign of outflow activity, which is consistent with the detection of 4.5μm emission in the GLIMPSE data. 16060−5146 and 16065−5158 show an asymmetric line profile with a stronger blue shoulder at the peak position of the HCO^+(4–3) emission. As will be discussed in Chap. 5, this is a sign of motion in the core. At the resolution of the current study, it is not possible to distinguish between infall and rotation as possible origin of the large scale motions.

The sources were observed in a partial line survey based around the CH_3OH(6–5), H_2CO(4–3) and CH_3OH(7–6) bands to study their chemical composition. For the ease of comparison, the molecular emission was divided into two classes, the hot and the cold molecules, having rotational temperatures above 100 K and below 100 K respectively, which corresponds to the ice evaporation temperature for complex organic molecules (Bisschop et al., 2007).

The molecular content of the three sources is similar, the most striking difference being the presence of a double peaked profile in several molecules found in 16060−5146. This was first noticed in the CH_3CN(16–15) transitions and later also in CH_3OH(6–5) and CH_3OH(7–6). Lines from most of the other molecules are significantly broader than in the other two sources, the velocity resolution is not high enough however to distinguish a large line width from an unresolved double peak profile. Being present in the warm and dense gas traced by CH_3CN, this double line profile hints at the presence of a complicated velocity structure down to the compact hot core level.
Several molecules, CH_3OH, CH_3CN, H_2CO and SO_2 were observed in more than one frequency setup. In these cases it was not always possible to model the species with one consistent set of temperatures and column densities. The reason for this might be either calibration uncertainties between the bands or deviations from local thermal equilibrium.
For the analysis, abundance ratios with respect to CH_3OH were formed. When comparing the abundance ratios [mol/CH_3OH], for a given molecule (mol), the abundance ratios are relatively constant with respect to CH_3OH among the three sources. For the cold molecules, the abundance ratios seem to be constant around 0.1, with the exception of the [SO/CH_3OH], [SO_2/CH_3OH] and [CS/CH_3OH] abundance ratios, which are around 1.0, while the ratio of [HNC/CH_3OH] is significantly lower. In the hot molecules, one can see a trend toward lower abundance ratios for the N-bearing species, [HNCO/CH_3OH], [HC_3N/CH_3OH], [CH_3CN/CH_3OH] and [C_2H_5CN/CH_3OH] when compared with the [$HCOOCH_3$/CH_3OH] ratio.
A chemical differentiation between N- and O-bearing species has been observed in several high resolution studies of hot molecular cores, among them W3(OH) (Wyrowski et al., 1999) and Orion-KL (Sutton et al., 1995). In the latter, the “hot core” is abundant in complex, saturated N-bearing species, while the “compact ridge” shows a high abundances of complex

O-bearing molecules. With interferometric observations, Liu (2005) resolve a similar differentiation in the sources E and F in G9.62+0.19, a high mass star forming region with similar distance and luminosity to the three sources presented here. Since the chemical differentiation is only resolved with high spatial resolution observations, one would expect not to find the difference in a single dish beam. This leaves the question why one sees a higher abundance of O-bearing species in the three sources of our sample. One possibility is that the complex O-bearing molecules stem from a more extended region and are therefore less beam-diluted.

Rodgers & Charnley (2001) discuss that a higher abundance of O-bearing species might suggest an earlier evolutionary stage where the hot core has developed into a rich O-bearing chemistry in the first 10^4 yr before evolving into a nitrogen rich state, but placing our sources at such a young state is inconsistent with the nonetheless high abundance of CH_3CN found in the three sources.

On the other hand, it is possible to imagine that the complex N-bearing species, which according to the above-mentioned interferometric studies, are expected to be found closest to the hot core have already been destroyed by the radiation of the young star, placing the sources at a slightly later stage of the hot core phase.

For 16060−5146 and 12326−6245, this would be consistent with the discovery of cm continuum emission at the position of the 870 μm peak.

Another source of the high abundance of O-bearing species could be a different composition of the initial grain mantles as discussed by Charnley et al. (1992) and modeled by Caselli et al. (1993) with thermal effects.

The line-widths of the organic species more complex than CH_3OH, C_2H_5CN, CH_3OCH_3 and CH_3OCHO are surprisingly small in the three sources, compared to the rest of the species. One would normally expect the line-widths of the hot component, in which the three species are detected, to be broader then the line-widths of the cold component.

In Fig. 3.14, the abundances are compared with those derived for G327.3-0.6 (blue), NGC6343I (green, Schilke et al., 2006) and 17233-3606 (turquoise, Leurini et al., 2008)), which were also obtained with APEX and analyzed in the same fashion as our data. To compare with a typical northern hemisphere hot core, the abundances of G34.3+0.15 (MacDonald et al., 1996) were also included. Overall, one can see good agreement between our data and the other four hot cores for the cold envelope molecules, apart from the slight overabundance of SO and SO_2 in our sources.

According to Viti et al. (2004), the sulfur species show a time-dependent signature. In their models, Viti et al. (2004) predict the SO/H_2CS ratio to be around one at earlier times and then decline, which is not observed in any of our sources. Comparing the hot species, it is obvious that while line rich, our sources are weaker in their line emission than the other sources. The lack of nitrogen bearing species in the hot component is pronounced when comparing with the other sources. Beuther et al. (2008b) do not detect any N-bearing species towards two young sources in their study of high resolution SMA hot core observations. They explain the lack of N-bearing species by saying that the N-bearing species need more time to evolve or warmer gas. Since we are detecting lines from gas with $T > 200$ K, it is not likely that the gas is not warm enough for the nitrogen chemistry. The association of 16060−5146 and 12326−6245 with UCHII regions also rules out the thesis that they are still at an early evolutionary stage.

A prominent feature of the three sources is the high abundance of sulfur species. Van der Tak et al. (2003) model the sulfur chemistry in the envelopes of young massive stars. The abundances they derive for CS and H_2CS agree with those found in our work. SO_2 and SO, however, are observed by us to have much higher abundances. This effect is particularly strong in SO_2, where the abundances we derive compare to those van der Tak et al. (2003) find for a model where SO_2 "jumps" to higher abundances in the inner envelopes. Beuther et al. (2008b) discuss the use of CS, SO and SO_2 as chemical clocks, with CS being a suitable tracer for the earlier stages while SO and SO_2 better trace the more evolved stages. This picture is consistent with our data and supports our hypothesis that the tree sources, particulary 16060−5146, are at a more evolved stage.
Comparing our modeling to the hot core model of Garrod et al. (2008), it is very difficult to make a direct comparison, since the model was adapted to observations of the Sgr B2 region. As a trend, one can say that the temperatures we derive often agree well with their model predictions, while the abundances vary, mostly in the late species. To obtain a better database for the comparison, it would be necessary to get the calibration uncertainties and the line confusion due to double sideband mode better under control, since these factors are large error sources in the abundances. Additionally, a larger selection of lines should be observed to include optically thin lines and interferometric observations at the sub-mm wavelengths are needed to obtain better estimates of the source sizes to solve the degeneracies while modeling.
For a better understanding of the chemistry in these regions, it would also be very helpful to image the spatial distribution of the different chemical species at high angular resolution, to see where they are located with respect to each other.

3.6.2 Continuum data

The three hot cores were imaged with LABOCA at APEX at 870 μm and at high resolution with ATCA at 3 mm.
While 12326−6245 (see Fig. 3.4 for the three sources) shows a spherical, centrally peaked morphology at 870 μm, 16060−5146 and 16065−5158 show an extended morphology. Both sources are also surrounded by secondary peaks, unlike 12326−6245, which is isolated within the LABOCA field of view. In the LABOCA field of view, the bright MIR cluster on which 12326−6245 is centered is the only sign of activity in the region, while the region just around the dust emission traced by LABOCA is dominated by 8 μm emission, a sign of PDR emission. In 16060−5146, the dominant feature in the LABOCA field of view is a large bubble visible in the MIR emission. The 870 μm emission of 16060−5146 corresponds to an active star forming site located, at least in projection, at the edge of the bubble. The other cores traced by 870 μm can be found tracing the rim of the bubble and in another region to the south of 16060−5146. 16065−5158, which is only 12′ away from 16060−5146, can be found in a region of very active star formation. One finds a very extended region of 8 μm emission, interspersed with infrared dark clouds and an association of bright young stars at the center. 16065−5158 is located right at the center of the association, in a deeply embedded region free of MIR emission. An elongated green structure at 4.5 μm seems to be coming from this deeply embedded region. Since 4.5 μm is associated with hot

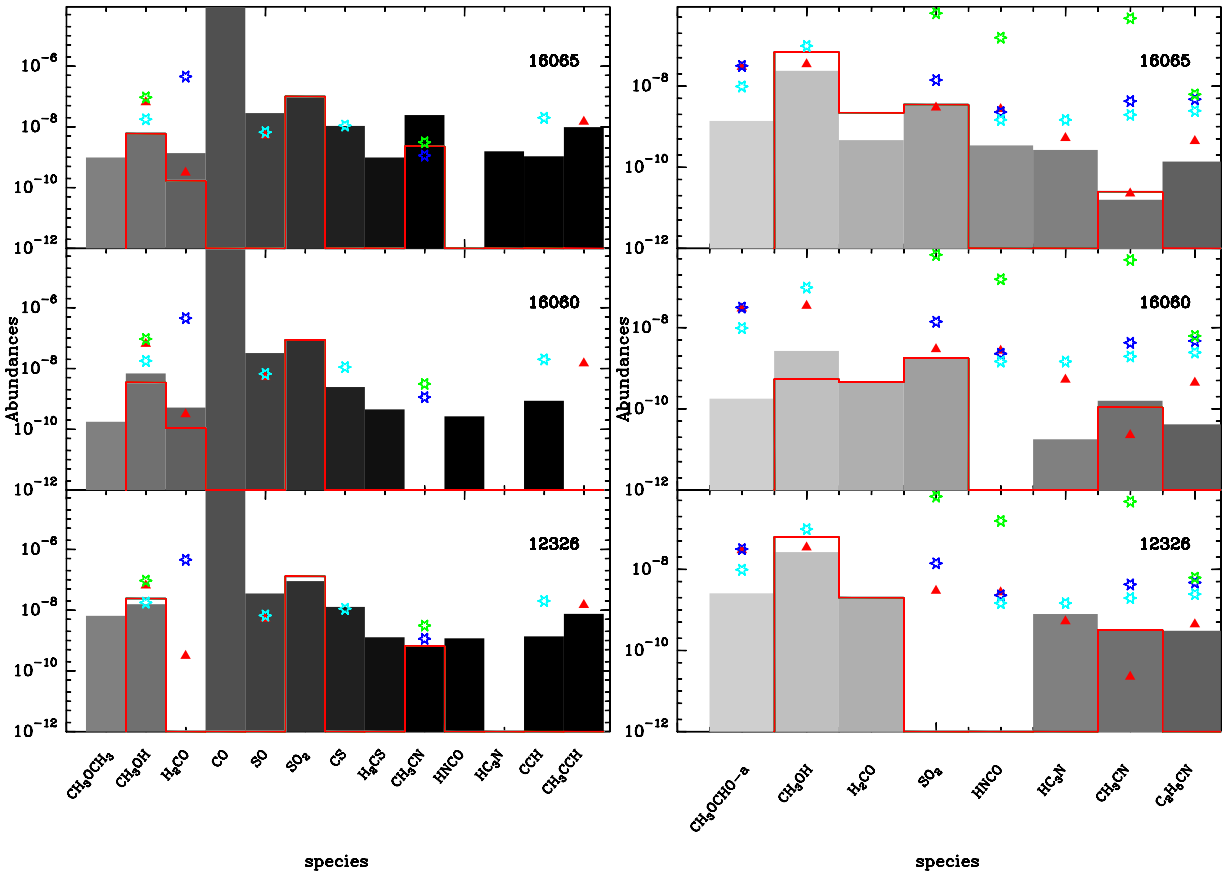

Figure 3.14: Abundances in the three sources for T $<$ 100 K (cold component) and T $>$ 100 K (hot component). Red triangles show abundances for G34.3+0.15 (Macdonald et al. 1996), green stars for NGC6334I, blue stars for G327.3-0.6 (both Schilke et al. 2006) and turquoise stars for 17233-3606 (Leurini et al. 2007). The shades of grey and black are chosen to distinguish between the columns for the different species. The black and red line in the plot of the hot and cold abundances respectively indicates those molecules where the modeling of different transitions resulted in different column densities (see Tables 3.9 to 3.11).

shocked gas (Cyganowski et al., 2008), this situation is very suggestive of a massive outflow stemming from 16065−5158. The very extended 870 μm emission found in the LABOCA field of view for 16065−5158 traces nearly the whole extent of the active star forming region visible in the GLIMPSE data.
Fig. 3.5 shows the mm continuum emission imaged with ATCA. One can see that its distribution agrees well with the peak of the LABOCA 870 μm emission. Given the modeled hot core sizes of the order of 1″, the ATCA continuum emission is not resolved yet. In 16060−5146, two cores can be found in the 3 mm emission, while only one of them is associated with the LABOCA peak, the other is too far away to be picked up with the APEX beam of about 19″ and can therefore not be responsible for the double peaked structure in 16060−5146. Fig. 3.5 also shows the location of the offset positions determined for the molecular line observations. While the rather crude determination of the position via the HCO^+ peaks meant we missed the position of the hot cores by a few seconds of arc, we were still close enough to pick up the hot core emission in the beams.

Modeling of the spectral energy distributions of the three sources revealed that the 3 mm continuum in 16060−5146 and 12326−6245 is dominated by free-free emission, pointing towards a more evolved stage of the sources. This is consistent with the infrared data and the radio continuum data observed by Urquhart et al. (2007a), which also point towards 16065−5158 being the most embedded and least developed object of the three.
The luminosities derived from the ionized regions in 12326−6245 and 16060−5146 differ by about a factor of 2 from the FIR luminosities derived from the IRAS fluxes. As Garay et al. (2006) discuss, this differences might result from the fact that part of the stellar luminosity is absorbed by the dust or there might be stars in the region contributioning to the FIR luminosity but which are not hot enough to ionize the gas. The derived luminosity also indicates that the three sources are most likely placed at their near distance, since they would otherwise have to harbor an unrealistically massive star <O4. The online model fitter of Robitaille et al. (2007) was used as an alternative way to model the SEDs for 12326−6245 and 16060−5146. The range of masses and luminosities derived agree for the models without disks with those obtained for the ionizing sources from the cm continuum.
Comparing the dust mass estimates for the three sources, the virial and continuum masses agree well for the near distance, indicating that the sources are likely bound. To get an estimate of the upper limit of the mass that might be concentrated at the innermost hot component, we determined the mass using the temperature derived from the SED model and the peak flux of the 870 μm continuum. These masses are a factor of about four lower than the envelope masses for 12326−6245 and 16065−5158, while they are about a factor of 2 lower for 16060−5146, indicating that this source is very centrally peaked.
All three sources have been observed by Faúndez et al. (2004), while 12326−6245 and 16060−5146 have also been observed by Miettinen et al. (2006) and Hill et al. (2005). Taking into account the different ways the integrated fluxes used, our masses agree well within factors of about 2 with the estimates by these authors.
They are, however, more massive than the average sources in the samples of Williams et al. (2004), Beltrán et al. (2006) and Mueller et al. (2002), whose samples contain generally less massive and luminous sources.

3.7 Conclusions

We observed the three sources 12326−6245, 16060−5146 and 16065−5158 in several molecular lines and in the mm and sub-mm continuum as a pilot study for the two surveys of the sample of 47 high mass star forming regions described in Chaps. 4 and 5. The goal of the pilot study was, first, to define and test frequency setups to be used with the new APEX telescope for the two surveys and, second, to study the three sources in more details, since they all show a hot core type molecular spectrum, which is found in high mass star forming regions.

The approach that was finally chosen, as a result of the pilot study, for the two surveys was to map the 47 regions in a setup containing HCO^+(4–3) and CO(3–2) to pinpoint the location of the peak of the dense gas and to derive information of the kinematics of the regions from the line shapes of the two tracers. The sources were then observed in a setup targeted at CH_3OH(7–6) to obtain abundances for the envelope component and a potential hot core component.

Once LABOCA was operable, the sources were imaged at 870 μm to study their dust content.

The sources were observed in five frequency setups targeted at CH_3OH(6–5), CH_3OH(7–6), H_2CO(4–3), H_2CO(6–5) and CH_3CN(16–15). The line surveys resulted in the detection of lines from 19 different species. Following Hatchell et al. (1998), the sources are all three classified as line rich sources due to the detection of highly excited CH_3OH transitions. Since also complex organic species were detected, the sources were classified as hot cores. For the three sources, both lines from an extended, cooler envelope component, as well as from a hot compact component were modeled.

All three sources show an overabundance of oxygen-bearing species compared to nitrogen-bearing species. Together with the a high abundance of sulfur species, the chemistry in the three sources points them towards a slightly more evolved stage.

16060−5146 and 16065−5158 both show secondary clumps in their surroundings. While they are all three located in regions of active ongoing star formation, the 870 μm peak of 16065−5158 is not associated with any FIR source. Spectral energy distributions including the ATCA 3 mm data were modeled for all three sources to derive their dust properties.

The three sources imaged in 870 μm and 3 mm continuum data are massive, luminous hot cores. While 16065−5158 seems to be a very young deeply embedded object sitting at the center of a young association, 12326−6245 and 16060−5146 seem more evolved and have already developed UCHII regions. The star forming activity in the region of 16060−5146 might have been triggered by the large bubble at which edge it is located.

The three sources of the pilot study are also discussed in Chap. 5 as part of the hot core sample.

Chapter 4

Dust Continuum studies

4.1 Introduction

In this chapter, I discuss a sample of massive star forming regions in the southern hemisphere observed in sub-mm dust continuum. This comprises a valuable template sample to be observed at high angular resolution with ALMA. Aim of this chapter was to characterize the physical properties, the column densities, masses, sizes and radial density distribution of the sample and compare the properties of two subsamples with and without associated 5 GHz radio continuum emission. We observed a number of sources in the inner Galaxy (Sample A) and in the outer Galaxy (sample B) to study how the physical properties vary with Galactocentric radius.
In Section 4.1, I present the sample and the observations, in section 4.2 the results of the observations are presented and, finally, I discuss these results in section 4.3.

4.1.1 Connection with other samples

Since many surveys are, just like ours, based on the IRAS Point Source Catalog (PSC), there is often an overlap of sources between the different samples. Listed below are the number of sources from Sample A that have also been included in previous works.
Our source list was compiled from the samples of Faúndez et al. (2004) (with 42 sources in common) and Walsh et al. (1997) (with 29 sources in common). Ten and four sources, respectively, were also included in the SIMBA and SCUBA surveys of cold cores done by Hill et al. (2005, 2006). Out of the fields that were observed in cm radio continuum with the ATCA as part of the RMS survey (Urquhart et al., 2007a), 26 include at least one of the sources of this work, while 23 fields targeted in the ^{13}CO survey of Urquhart et al. (2007b) contain at least one source of our sample. The study of Busfield et al. (2006) contains five sources from our sample, while two sources have also been included in the sample of Beltrán et al. (2006). The Osterloh et al. (1997) study of cold southern IRAS sources includes five of our sources.

4.1.2 Observations

Both, the inner and the outer, Galaxy samples were observed with the Large Bolometer Camera (LABOCA) at the Atacama Pathfinder EXperiment (APEX) on Chajnantor in Chile. The data were observed in two observing runs in August 2007 and December 2007. In August, the sources in the inner Galaxy were observed, while the sources in the outer Galaxy were observed on 2 nights in August and on 3 nights in December 2007. To reiterate, LABOCA is a 295 channel bolometer with a field of view of 11.4′ and a beam of 18.6″. The channel separation is 36″. To produce a fully sampled map, the data were observed in the raster-spiral mode, with 35 seconds integration time on source, a spacing of 27″ and 4 subscans. This sets the scanning velocity to about 4′/s and the total integration time on source was on average 2.3 min.
The atmospheric opacity was determined every hour through skydips. In August 2007, the zenith opacity on the first three days was on average 0.3, while on the fourth it was 0.09. The sources from sample A observed during the first three days have an average rms of 140 mJy/beam, while the sources observed on the last day have an average rms of 45 mJy/beam. Sample B was observed both in August and December with an average opacity of 0.18 in August and 0.23 in December. The noise level is on average 16mJy/beam and the average integration time on source is 30 minutes.
Calibration was done once an hour by observing Neptune, IRAS16293−2422, G10.62−0.38 and IRAS13134−6242 for the inner Galaxy and V883-Ori, J0609−157, PMNJ0633−2223, PKS0733−17, IRAS13134−6242, PKS0537−441 and VY−CMa for the outer Galaxy. Pointing was checked every 30 minutes for sample A on G5.89−0.39, G10.62−0.38, NGC6334I, IRAS16293−2422, G34.3+0.15, G45.1+0.1 and η Carinae, and every 30–60 minutes for sample B on η Carina, Mars, VY-CMa and PKS0537−441. The pointing was good within 3″.
The data were reduced using the BOA (BOlometer Array Analysis Software) software package (Schuller et al., in prep.).

4.2 Results

4.2.1 Distances

The derivation of the kinematic distances was done using the Bonn Mass Milky Way model (Kalberla, 2003; Kalberla et al., 2007) with the velocities obtained from the $C^{17}O$(3–2) line velocity. Where no $C^{17}O$ line was observed, the velocity of the H_2CO(5–4) or HCO^+(4–3) lines was taken (see Table A.29 in the Appendix for details on which molecular tracer was used for which source.) To get a better understanding of the accuracy of the distance estimate, we looked at the distances calculated within a velocity range of ± 5 $\mathrm{km\,s^{-1}}$ around the center velocity of the observed line. While it is possible to obtain the center velocity of the lines through Gaussian fits with an accuracy of about 1 $\mathrm{km\,s^{-1}}$, a higher value was chosen for this estimate to reflect larger scale motions in the region. The high mass star forming regions are located in areas which are thought to be dominated by turbulence and are under the influence of large streaming motions. This random motion introduces a random change in the local velocities. Independent of the near/far ambiguity distance one should

remember that the kinematic distances provide only an order of magnitude estimate for the distances. For want of a better method of distance estimation for the high mass star forming regions and to be consistent with the literature, we will treat the results of the kinematic distance analysis as the true distances of the sources. The uncertainty introduced through the spread in velocity is around 10%, depending on the distance of the source. The error will be larger for sources closer to us, but for close distances, the kinematical velocity determination will anyway break down and one has to realize that the estimate of kinematic distance does not provide reliable results for sources with distances less than 1 kpc away from us.
To solve the near/far distance ambiguity, we apply the results of Busfield et al. (2006), who solved distance ambiguities by comparison with HI self absorption. This applies to eight sources from our sample. For five sources which can be found in Walsh et al. (1997), we follow their solution of the ambiguity, which was achieved considering the derived luminosities in both cases. The solution for another two sources can be found in Urquhart et al. (2007b). Five sources could be placed at their near distance, since otherwise their z height would have been too far above the plane (Beltrán et al., 2006). In total, we could solve the near/far distance ambiguity for 20 out of 47 sources. For the remaining 27 sources, both distances are given. To solve the distance ambiguity for all the sources in the inner Galaxy, one would have to use HI absorption measurements, which is beyond the scope of this work. When determining the distances toward the sources in the outer Galaxy, the CO(1-0) line velocity observed by Wouterloot & Brand (1989) was used (see Table A.1 in the appendix for the details of the outer Galaxy sources.)

4.2.2 Source identifications

The sources were identified using the *sfind* routine in the MIRIAD software package. This routine utilizes the FDR (False Discovery Rate) algorithm (Hopkins et al., 2002), with a FDR threshold of 2.0% and an rms-box size of 20 pixels. It derives the source parameters by fitting a 2D elliptical Gaussian. The sources are shown in Figs. A.7 – A.14 in the Appendix. In Table A.29, column 1 gives the source name, columns 2 and 3 give the peak position of the 870 μm emission in right ascension and declination, columns 4 and 5 the peak position of the 870 μm emission in Galactic coordinates, columns 6 and 7 the kinematic distance estimates (near and far), column 8 the Galactocentric radii and columns 9 and 10 the multiplicity of the regions. Column 11 lists the IR morphology and column 12 the rms. In Table A.30, column 1 gives the source name, column 2 the peak flux, column 3 the integrated flux within the 10% contours, column 4 the beam deconvolved angular diameter, column 5 the dust temperature taken from Faúndez et al. (2004) and column 6 the dust column density (see Sec. 4.2.4). Columns 7 and 8 list the luminosities based on IRAS fluxes taken from Faúndez et al. (2004), Walsh et al. (1997) and Purcell et al. (2006) and scaled to match our near and far distance estimates. The LSR velocities are listed in column 9. Column 10 lists the molecular tracers with which the velocities were determined.
The multiplicity was determined, first, as the number of sources within a 2 pc radius around the central source and, secondly, as the number of sources in the observed field. The distributions of these values are shown in histograms in Fig. 4.2.6.
The results for the sources in the outer Galaxy are listed in Table A.1. Column 1 lists the name of the associated IRAS source, columns 2 and 3 the peak positions of the 870 μm

emission in R.A.(J2000) and Dec.(J2000), column 4 and 5 the peak and integrated flux of the dust emission in Jy, column 6 and 7 the kinematic distance and Galactocentric radius in kpc, and column 8 the beam de-convolved angular diameter.

4.2.3 Morphology and multiplicity

To classify the sources, the multiplicity in the fields was determined. Having sources with kinematic distances between 0.4 and 14 kpc in the sample, comparing only the sources in the whole observed LABOCA field of view can be misleading, since the 11.4′ of the LABOCA field correspond to linear diameters between 1.3 and 46 pc, depending on the distance. To avoid comparing multiplicities in the vicinity of the sources with those in the large scale environment, we also determined the number of companion sources within a fixed, distance independent linear radius of 2 pc. Over the whole field, the average number of sources per field of view is 3.1, while there are on average 1.5 sources within 2 pc. Following Williams et al. (2004), we determine the companion clump fraction (CCF) considering both the detections in the whole field and within 2pc. The CCF is calculated using the expression

$$CCF = \frac{B + 2T + 3Q + 4P}{S + B + T + Q + P} \tag{4.1}$$

with S,B,T,Q,P the number of single, binary, triple, quadruple and quintuple clumps in the sample. Over the whole field of view, the CCF is 2.1, while within 2 pc around the central source, the CCF is 0.4. We count several peaks within one extended source as individual clumps (see Fig. 4.2.3). If one would count the extendend sources containing multiple clumps as one single contribution, the CCF over the whole field is 1.8, while the CCF within 2 pc becomes 0.2.
It also has to be noted that we assume that all the sources found within the field are at the same distance and associated to the main core, which does not have to be the case.
When studying the relation of multiplicity in the field with distance (see Fig. 4.2.6), one cannot see a clear trend, while the plot of multiplicity within 2 pc versus distance (same figure) shows that most sources are singular and only a few sources at close distance can be resolved into multiple cores. Since the largest distance to which a source could be resolved into smaller cores within 2 pc was 4.6 kpc, we looked at the multiplicity within the subsample of 33 sources within 4.6 kpc. Out of these sources, 64% were singular sources, 21% were binary sources and the remaining 15% were resolved into 3–5 cores.

4.2.4 Masses, densities and linear diameters

Sample A - inner Galaxy

Tables A.32 and A.33 in the Appendix give the parameters determined from the 870 μm emission for sample A. In Table A.32, column 1 gives the source name, columns 2 – 5 the mass within the 10 % contour and within 0.6 pc radius at the near and far distance, respectively and columns 6 and 7 give the luminosity-to-mass ratios. In Table A.33, column 1 gives the source name, columns 2 –5 the densities derived within the 10 % contour and within 0.6 pc radius at the near and far distance, respectively and columns 6 and 7 the beam

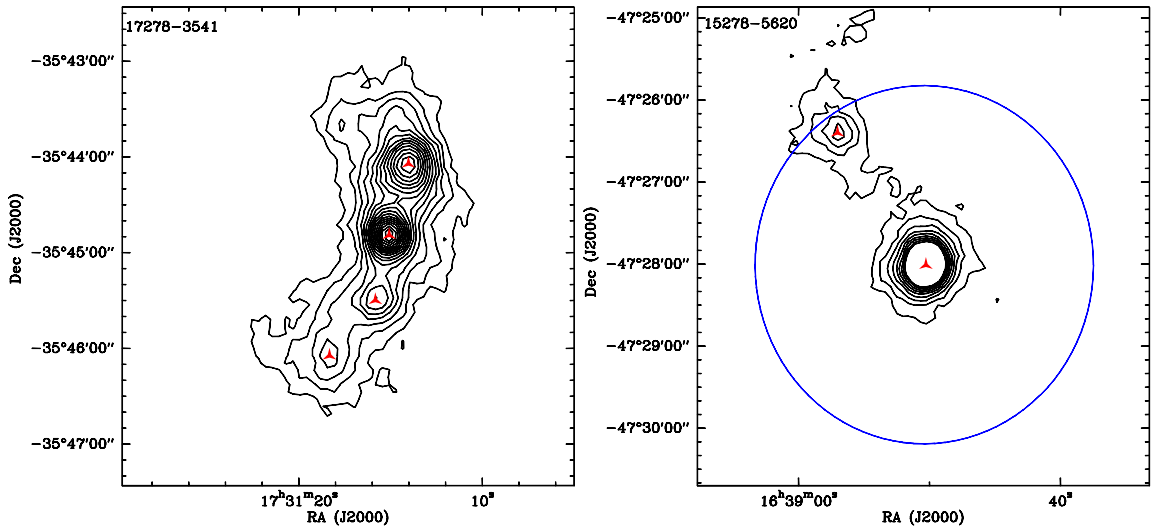

Figure 4.1: Left panel: contour plot of 17278-3541. Here one can see how individual peaks in an extended source were treated in the definition of the multiplicity. Contours start at 3 σ, with steps of 3 σ ($\sigma = 0.35$ Jy). The red triangles mark the positions of individually counted clumps within the source. Right panel: contour plot of 15278-5620. The blue circle marks the 2 pc radius around the source. In a case like this one, when a clump is at the edge of the 2 pc radius, it is considered for the calculation. Contours start at 3 σ, with steps of 3 σ ($\sigma = 0.49$ Jy). Both 17278-3541 and 15278-5620 are located at their near distance.

deconvolved linear diameters. In Fig. 4.2.6, histograms showing the distribution of these values are given.

The masses and column densities were derived using

$$M_{\rm gas} = \frac{S_\nu d^2}{B_\nu(T_{\rm d})\kappa_{\rm d} R_{\rm d}} \ [{\rm M}_\odot] \tag{4.2}$$

and

$$N({\rm H}_2) = 1.67 \times 10^{-22} \frac{I_\nu^{\rm dust}}{B_\nu(T_{\rm d})\mu m_{\rm H}\kappa_{\rm d} R_{\rm d}} \ [{\rm cm}^{-2}] \tag{4.3}$$

as outlined in Miettinen et al. (2006) under the assumption of optically thin gas, with a dust absorption coefficient, κ_d, of 0.176 m^2/kg linearly approximated at 870 μm from model 5 of Ossenkopf & Henning (1994) and $\rm R_d = \frac{1}{100}$ (thin ice mantles, $n = 10^6 {\rm cm}^{-3}$). The dust temperatures were taken from Faúndez et al. (2004), where available and assumed to be 30 K for the remaining sources, which agrees well with the average value obtained by these authors, as well as Beltrán et al. (2006) and Molinari et al. (2000). To determine the distance dependence of the integrated flux, we derived both the masses within the 10% contour and within a fixed source size of 0.6 pc, which is close to the average size of the sources. Fig. 4.2.6 shows the mass and luminosity-to-mass ratio (L/M) derived from fluxes determined within the 10% contour as well as the distance independent masses and L/M within 0.6 pc. In the histograms, the values are shown as solid lines for the sample of 20 sources where the

distance ambiguity could be resolved, in grey for the resolved sources plus the remaining sources projected to their near distances and in dashed lines for the resolved sources plus the remaining sources projected to their far distances. The mean and median values for the masses, L/M, densities, column densities and source sizes can be found in Table 4.2 for each of the three samples.
For sources of the sample located at their far distance, their masses are most likely overestimated when determining the masses within the 10% contour, while for sources with distances larger than 5.9 kpc, the 0.6 pc source size corresponds to angular sizes smaller than the beam. Those sources are marked with an asterix in Table A.32. The mean column density for the sample is 2.7×10^{23}cm^{-2}.
The luminosities for sample A are based on IRAS fluxes taken from Faúndez et al. (2004), Walsh et al. (1997) and Purcell et al. (2006) and have been scaled to match our distance estimates.
One can see from Fig. 4.2.6 that the scatter of the mass derived within the 10% contours shows a clear dependence on distance, which is not so pronounced for the mass within 0.6 pc source size, where the influence of the distance should have canceled out. One has to note, however, that due to our selection criteria of strong IR sources we will have included a bias towards very massive sources in our sample and are most probably observing exceptionally massive sources at the large distances.
To obtain the source sizes, the area within the 10% flux contours was defined as the equivalent size of the source. To obtain linear diameters, it was beam deconvolved and converted into parsec. The average linear diameter is 0.6 pc.
In the plot of the mass within 10% contours versus the source diameter (see Fig. 4.2.6), a line at constant density is included. 1.0×10^5 cm^{-3} is the average density derived within 0.6 pc source size and 3.0×10^4 cm^{-3} is the average density derived within the 10% contours and the corresponding source size.
In the plot of the mass within 0.6 pc, the filled dots represent the sources which are still resolved by the beam, while the empty stars represent the sources further than 5.3 kpc, for which 0.6 pc corresponds to an angular size smaller than the 18.6 $''$ of the LABOCA beam.

4.2.5 Radial fits

To study the morphology of the regions, radial fits were obtained for the inner part of the cloud fitting the flux distribution derived with the *elint* routine in the MIRIAD software package. The innermost two points were not considered for the fits to correct for the beam and the points outwards of 80$''$ were also left out due to the increased noise.
The slope $m_{\rm i}$ of the radial flux distribution of the remaining points was determined from power law fits to the data. A rough estimate of the density profiles $n \sim r^{-p}$ was made, following the procedure outlined in Beuther et al. (2002a). Assuming optically thin dust emission, spherical cores, and the Rayleigh-Jeans approximation, the density index p depends to first order on

$$m = -1 + p + Q \times q + \epsilon_{\rm f} \tag{4.4}$$

if the density and temperature can be described by power laws.
As described in Adams (1991), Q is a temperature and frequency dependent correction factor,

which was assumed to be ≈1.3 at 870 μm and 30 K. $\epsilon_{\rm f}$ is a correction factor of the order of 0.1 for finite source size. Beuther et al. (2002a) argue that the temperature index q ($T \sim r^{-q}$) can be taken as $q = 0.4$. The errors on m_i and p are estimated to be $\Delta m \approx 0.3$ and $\Delta p \approx 0.5$ (Beuther et al., 2002a).
The results of the fit can be found in Table A.35 in the appendix, where m_i is the slope of the inner region and p the density index.
The average inner slope of the radial flux distribution is -2.0$\pm$0.3, while the average density index $p \approx 1.6 \pm 0.4$. Fig. 4.2.5 shows the radial fits for four sources, illustrating some of the caveats encountered when automatically fitting a large number of sources. In the case of 12326−6245 and 16060−5146, both sources have steep slopes and one can see that the cut-off towards the outer edge, where the signal-to-noise ratio gets too large, is appropriately chosen. The innermost points form a plateau and correspond to the peak flux of the source. For 16065−5158, one can see that at about 40″, a second source component becomes visible which means that the fit of the inner slope for this sources has been underestimated. In the case of the weak source 16458−4512, the signal-to-noise ratio already gets low at radii larger than 20″. In this case, the steepness of the inner slope has been overestimated.

4.2.6 Sample B - outer Galaxy

The parameters derived for the outer Galaxy sample B can be found in Table A.1 in the appendix. Column 1 lists the source name, columns 2 and 3 mass and density and columns 4 and 5 the luminosity taken from Wouterloot & Brand (1989) and the luminosity to light ratio.
Given their weak fluxes, which are a result of the large distances of these sources, the integrated flux within the FWHM was taken to determine the masses. To compare with the inner Galaxy sample, Equ. 4.2, a dust-to-gas ratio of $R_{\rm d} = \frac{1}{100}$ and $T_{\rm d}$=30 K was used. The average mass of the sample is 237 $M_\odot$and the average L/M=35 $L_\odot/M_\odot$.
The average density is 2.5×10cm^{-3}and the average column density for the sources is $N(\mathrm{H_2}) = 5.0 \times 10^{21}\mathrm{cm}^{-2}$. When using a dust temperature of 20 K and a dust-to-gas ratio of 1/150 as has been suggested by Klein et al. (2005) for the outer Galaxy, the masses become a factor 2.76 larger.

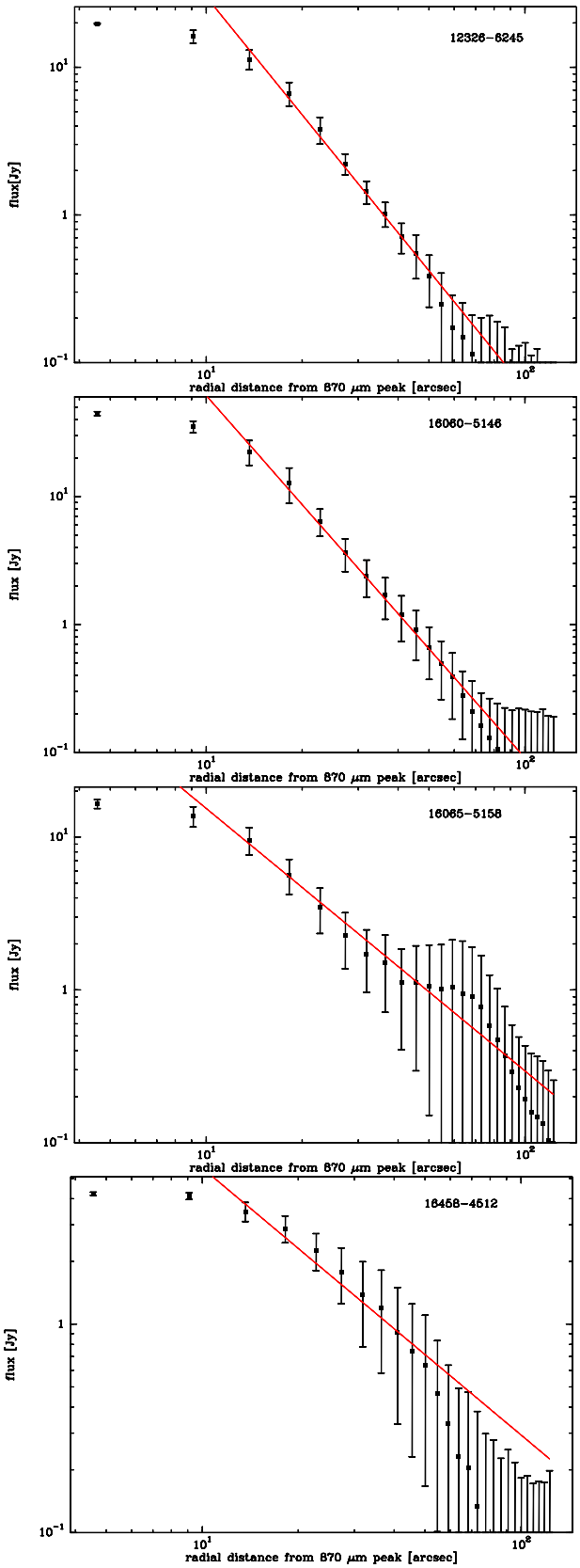

Figure 4.2: Plots showing the radial fits of the inner slope. Flux is plotted versus distance (″) from the peak of the emission. The innermost two points as well as the points outwards of 80 ″ radius have been excluded from the fit.

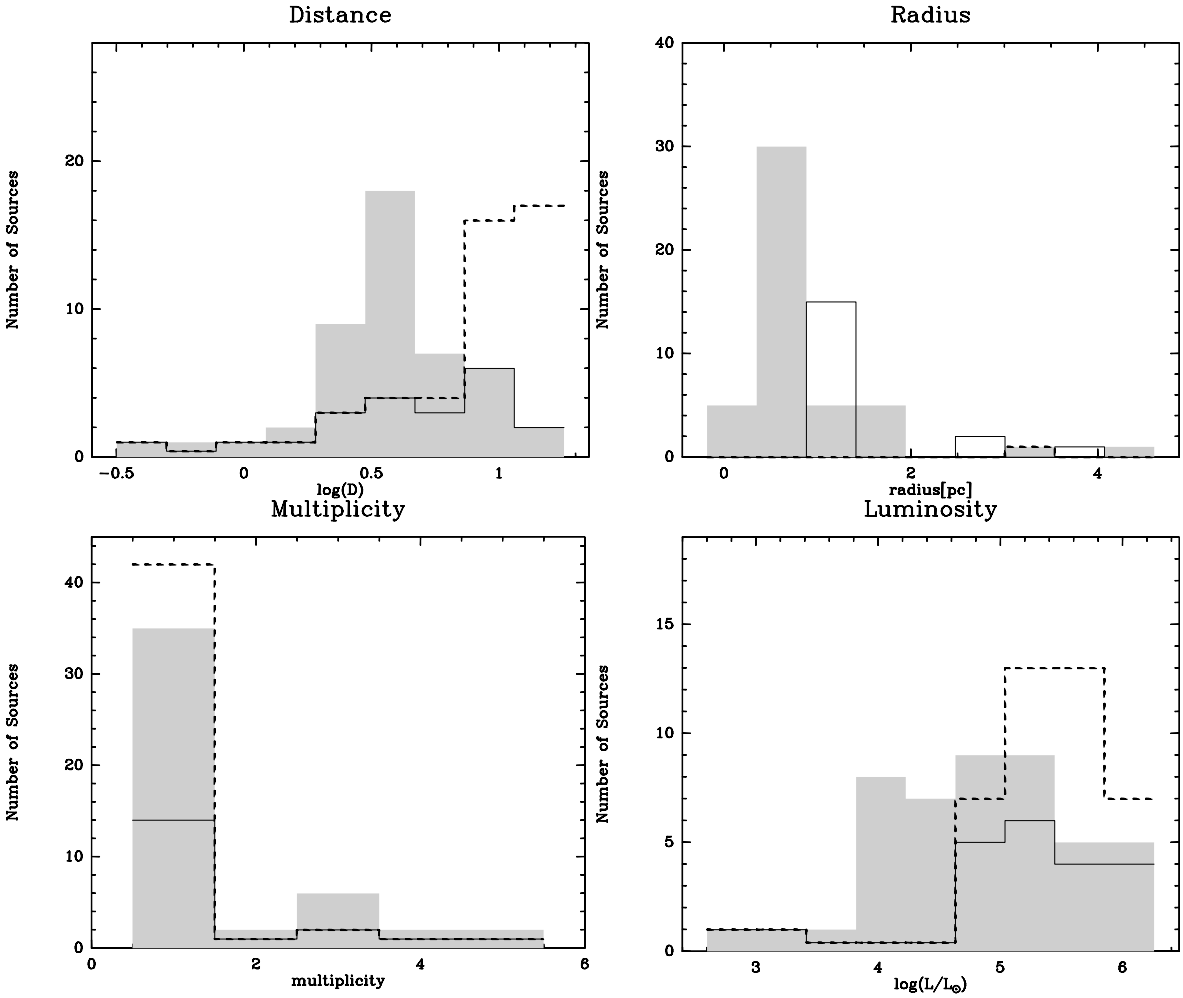

Figure 4.3: Histograms for kinematic distance, source radius in pc, number of sources within 2 pc radius, and luminosities of the inner Galaxy sample. The grey area represents the distribution of sources projected to their near distance plus the sources where the distance could be resolved, the dashed line the distribution of sources projected to the far distance plus the sources where the distance could be resolved, and the solid black line the distribution of sources where the distance could be resolved.

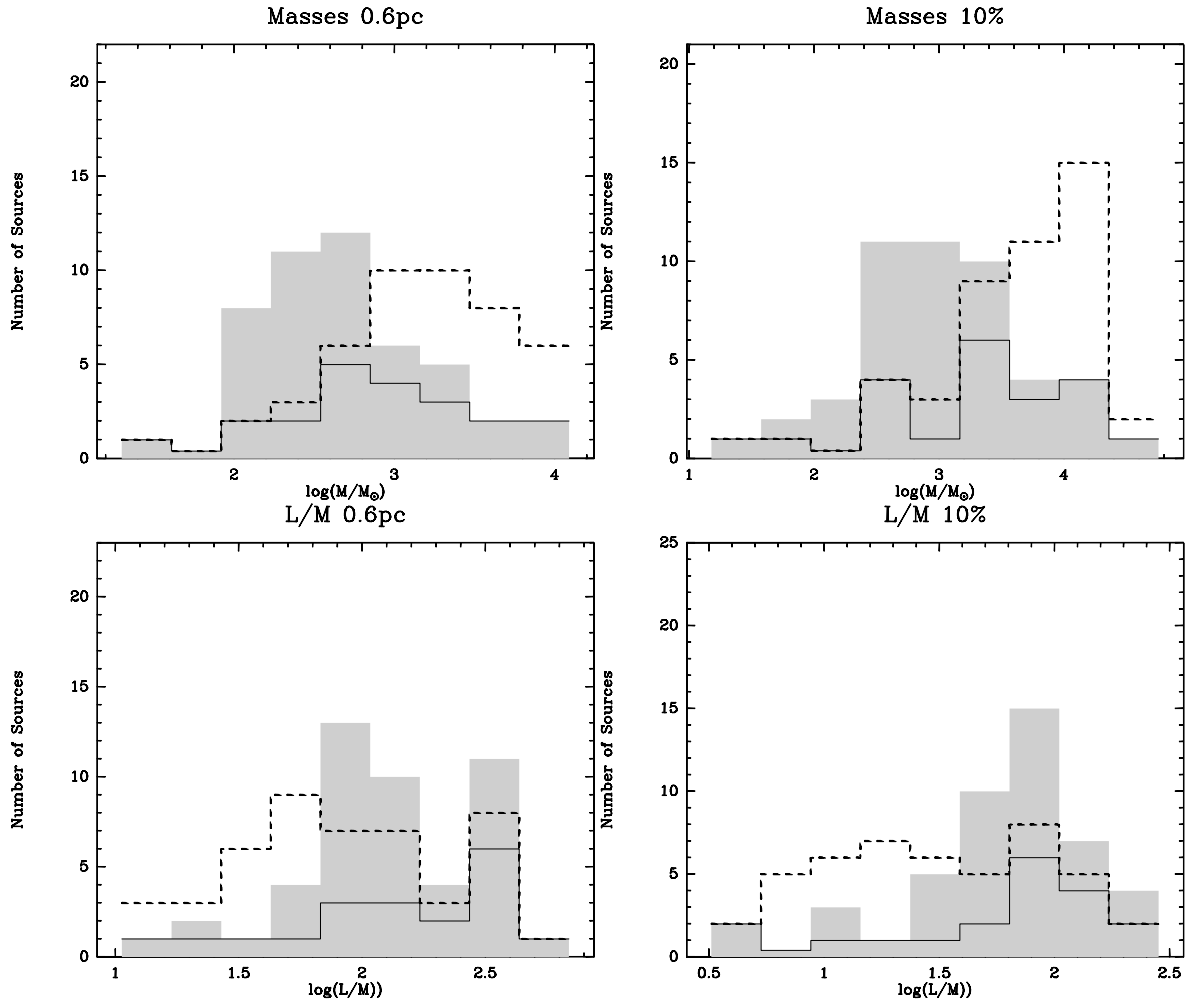

Figure 4.4: Histograms of mass distribution within 0.6 pc radius, L/M ratio within 0.6 pc and mass and L/M within 10% flux contour. The grey area represents the sources at their near distance, the dashed line the sources projected to the far distance and the solid black line the sources where the distance could be resolved.

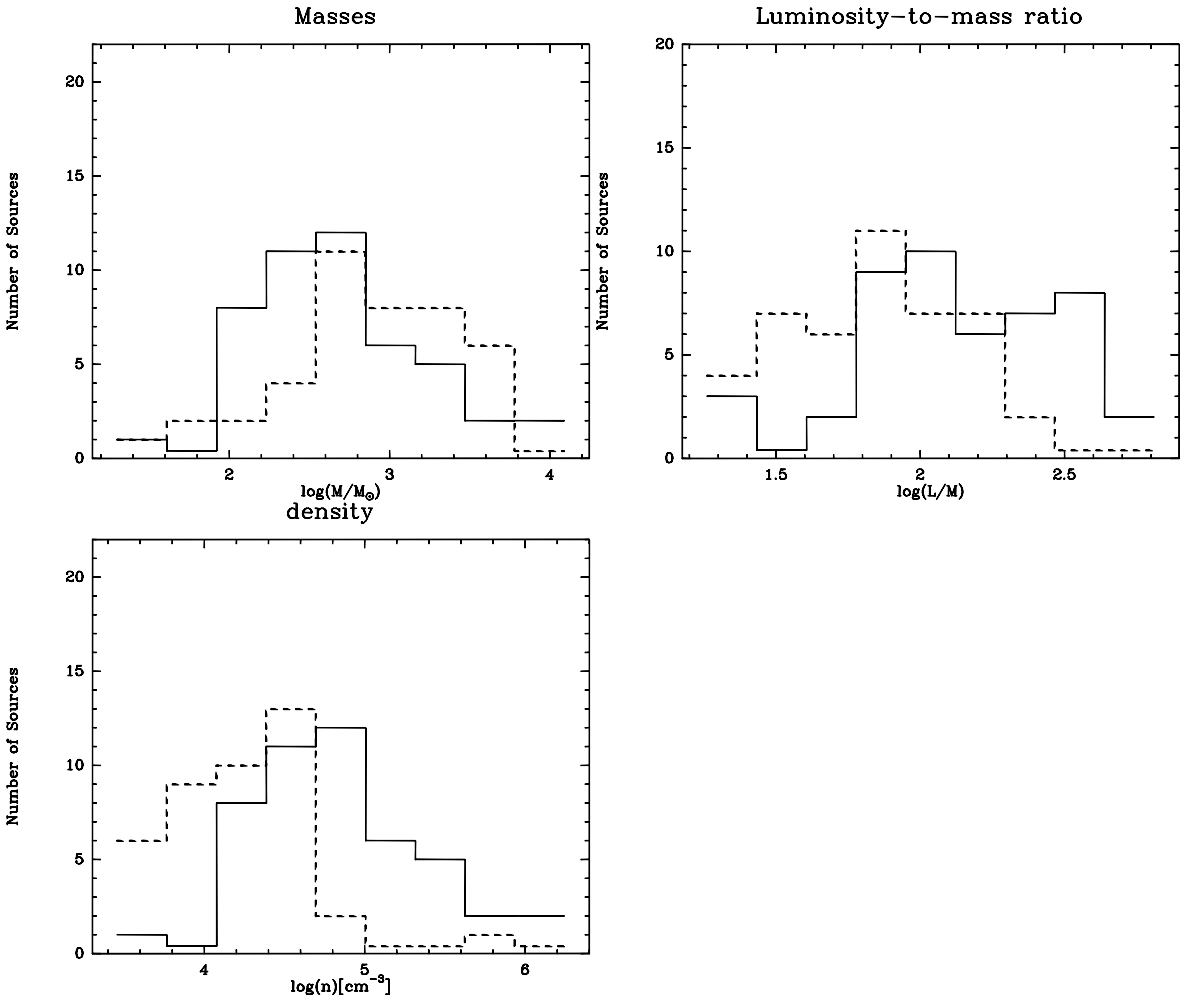

Figure 4.5: Histograms of mass, L/M and mean density distribution. Compared are the values derived with the flux obtained within the 10% contours (dashed line) and those derived within 0.6 pc radius (solid line). For sources where the distance ambiguity was not resolved, near distance was assumed.

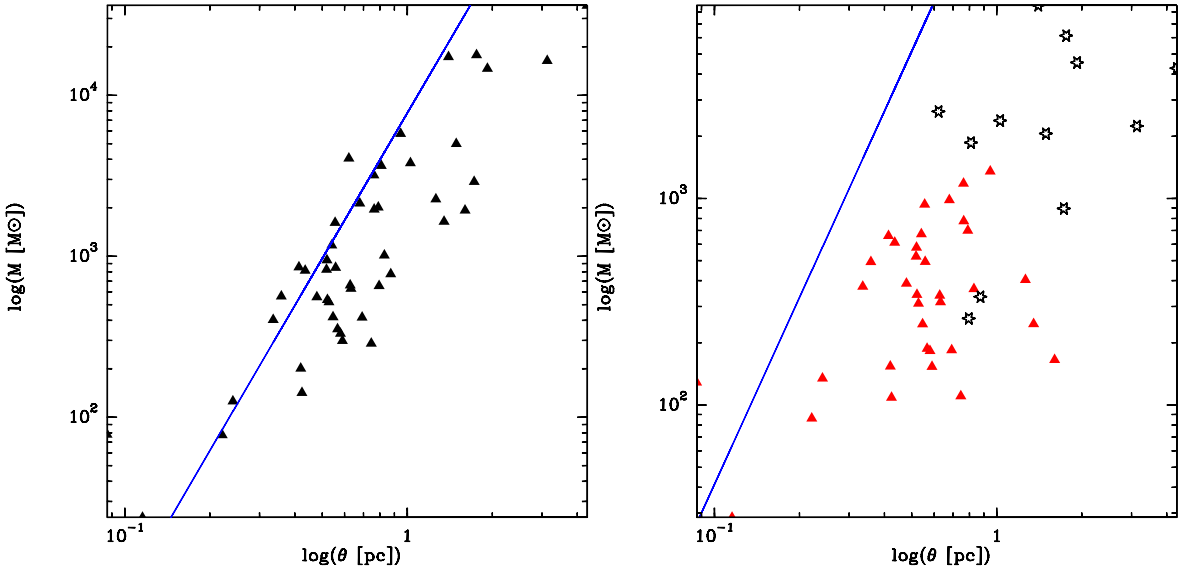

Figure 4.6: Left panel: Mass derived from flux within 10% contours vs source size in pc. The blue line shows the masses derived from the given source sizes assuming a constant density of $2.8\times10^4\mathrm{cm}^{-3}$. Right panel: mass derived from flux within 0.6 pc vs source size in pc. The stars mark sources at distances larger than 5.9 kpc. For those sources, the mass had to be derived from the peak flux, since 0.6 pc could not be resolved any more. The blue line shows the masses derived from the given source sizes assuming a constant density of $1.6\times10^5\mathrm{cm}^{-3}$. For sources where the distance ambiguity was not resolved, near distance was assumed.

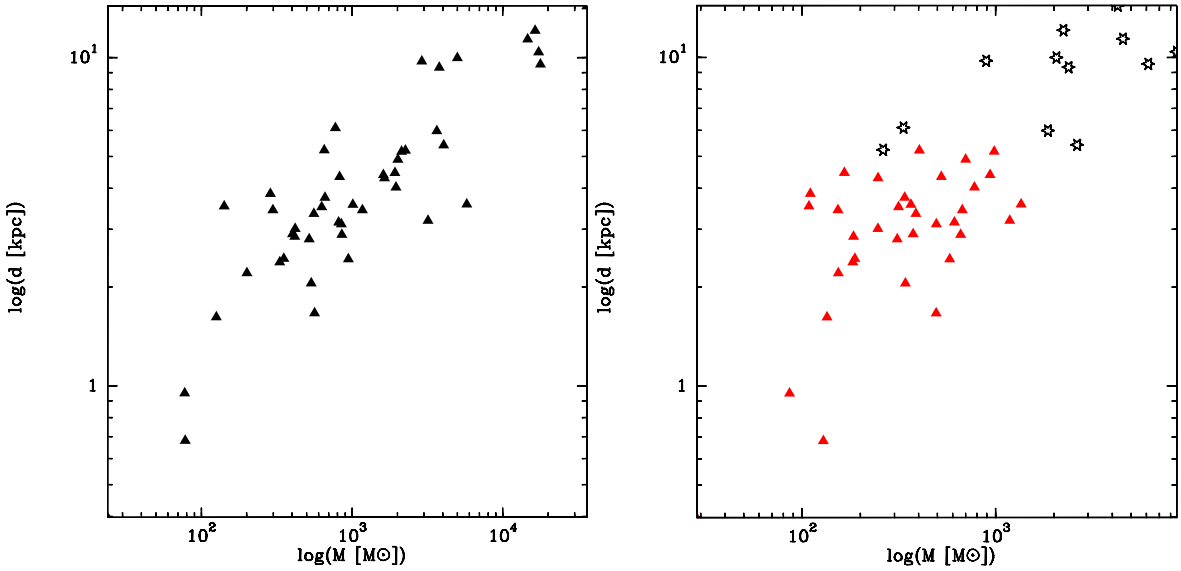

Figure 4.7: Left panel: Distance in kpc vs mass determined from flux within 10% contours. Right panel: Distance in kpc vs mass determined from flux within 0.6 pc. The empty stars mark the sources for which 0.6 pc cannot be resolved by the beam anymore and the peak flux was taken.

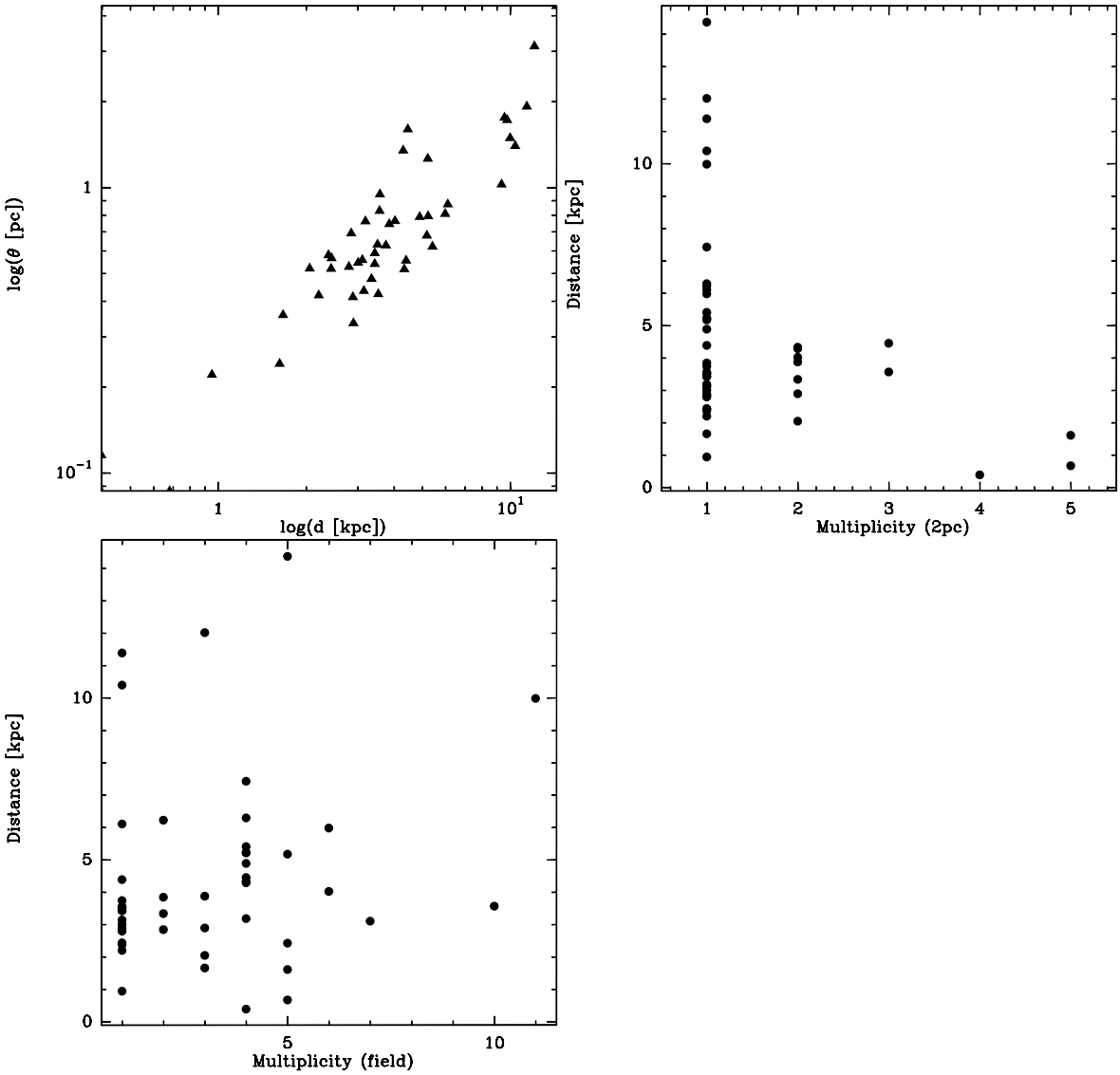

Figure 4.8: Top left panel: Source size in pc vs distance in kpc; top right panel: Distance in kpc vs multiplicity within 2 pc; bottom left panel: Distance in kpc vs multiplicity (field).

4.3 Discussion

4.3.1 Dust properties

The multiplicity of the sources was determined through the CCF, the companion clump fraction (Williams et al., 2004). Over the whole LABOCA field of view of 11.4 $'$ the CCF is 2.1, while within a 2.0 pc radius, the CCF is 0.4 We included this distinction to take into account that the LABOCA field of view corresponds to linear distances between 1.3 and 46 pc. Since the CCF is around unity in a region within 2.0 pc radius of the cores, it indicates that the objects we study have on average one companion.
Williams et al. (2004) find a CCF of 0.65 for their sample of northern hemisphere sources. Their data were obtained with SCUBA, which had a field of view of 2.5 $'$, corresponding to 3.3 pc at a distance of 4.5 kpc. Counting the companion sources within 3.3 pc, the CCF of our sample becomes 0.64, agreeing well with the result of Williams et al. (2004) that about 65% of the regions have a companion.

The masses were first derived inside the contours of 10% of the peak flux. Since this method is heavily dependent on distance, the masses of the sources scale with distance squared (see Fig. 4.2.6). To minimize the influence of distance on the mass, we determined the mass inside a fixed 0.6 pc diameter as well. This value corresponds to the average size of a clump. The masses determined this way show less dependence on distance, yet on can see that there is a weak distance dependence, since we are only sensitive to the most massive objects at higher distances and therefore neglected to include less massive objects at the large distances when selecting the sample.
Table 4.2 lists the mean and median masses, densities, L/M ratios and H_2 column densities for both methods using three approaches. First, only sources which could be placed at either near or far distance were considered, then all sources with distance ambiguities were projected to the near distance and lastly to the far distance.
Assuming near distances, our median values for the dust masses derived from the flux within the 10% contours are on average a factor of six higher than those derived by Beltrán et al. (2006), Williams et al. (2004) and Mueller et al. (2002) and about a factor of 1.5 higher than those of Hill et al. (2005). Faúndez et al. (2004) derive values which are about a factor of 1.5 higher than the values derived in our work. The differences in the values indicates that our sample, which was mainly composed of sources from Faúndez et al. (2004) and also has 10 sources in common with the sample of Hill et al. (2005), contains more massive sources than the three samples of Beltrán et al. (2006), Williams et al. (2004) and Mueller et al. (2002). This is supported by the fact that the average luminosities of the sources in our sample are much higher than e.g., those of the Beltrán et al. (2006) sources. Using different dust properties also adds additional uncertainty. We derived the column densities using the dust opacity model V of Ossenkopf & Henning (1994) and then re-did the analysis using the same dust properties as Beuther et al. (2005), which resulted in column densities a factor 1.5 higher than with the former model. Column densities of the different samples agree within factors of a few.
We obtained the densities by using the mass derived within a fixed 0.6 pc size, and also by using the radius of the sources within which the 10% mass was determined.

Method	Mean $\times 10^5$ cm^{-3}	Median $\times 10^5$ cm^{-3}
$M(0.6\,pc)/V(\theta(0.6\,\mathrm{pc}))$	1.6	0.58
$M(10\%)/V(\theta(10\%))$	0.28	0.14
$M(10\%)/V(\theta(\mathrm{FWHM}))$	9.7	3.5
$N/\theta(\mathrm{FWHM})$	2.8	1.5

Table 4.1: Comparison of the densities in our sample (near distance) obtained in several different ways. V(θ(...)) shows with which source size the volume was calculated.

Table 4.1 lists the different ways of density determination. In rows 1 and 2, the densities as determined in our work are listed, while rows 3 and 4 show the results of determining the density in two other ways as found in the literature, for comparison. The densities we derive for the flux within the 10% contour are one order of magnitude lower than values commonly found in the literature. While these values are distance biased, they do however represent the density over the whole source, which for our type of objects is mostly the dusty envelope. The higher values derived via the column density, and in our study the density within 0.6 pc source size, represent a density that might be called the peak density, since it only refers to the innermost, centrally peaked regions. When densities are derived using the mass obtained over the source and the FWHM source size, the high density values of the order of 10^6cm^{-3} overestimate the density in the source by about an order of magnitude.

From the source finding routine *sfind* used on our sample, we find an average beam deconvolved source size of 0.6 pc with a median of 0.5 pc, which agrees well with the 0.6 pc found by Williams et al. (2004) for the Sridharan sample and with 0.6 pc as found by Beltrán et al. (2006). As the latter authors already mention, both Hill et al. (2005) and Faúndez et al. (2004) derive larger diameters, but it is not clear whether or not these values have been deconvolved.
The average diameter of the regions over which the 10% flux was integrated is 1.8 pc with a median of 1.0 pc. This diameter has to be taken as an equivalent diameter, since it was derived by assuming that the area above a threshold of 10% of the peak flux was circularly symmetric, which is not a good assumption for the regions with more complex morphologies.
Regarding the error introduced by fitting a circularly symmetric Gaussian to a non-circular symmetric source and taking this size as the relevant radius within which to determine the density, we believe that the method of taking the 10% equivalent radii still gives better values.
All in all, our sample seems to contain more massive and embedded sources than the samples of Beuther et al. (2002a), Beltrán et al. (2006), Williams et al. (2004) and Mueller et al. (2002) This is most likely due to the selection, which encompasses sources with radio continuum as well as those without.

The sources in the outer Galaxy are about an order of magnitude less massive than the sources we observe in the inner Galaxy, yet their masses are consistent with the lower range of masses observed by us and in the surveys discussed above. Given their larger sizes and

	0.6pc		10% flux contours	
	Mean	Median	Mean	Median
M[M$_\odot$]	1807	895	6.3×10^3	2.1×10^3
L/M	233	231	93	85
n [cm^{-3}]	2.6×10^5	1.3×10^5	1.9×10^4	1.5×10^4
N(H$_2$) [cm^{-2}]	2.9×10^{23}	2×10^{23}		
θ [$''$]	-	-	42	39

	0.6pc		10% flux contours	
	Mean	Median	Mean	Median
M[M$_\odot$]	1.1×10^3	400	3.4×10^3	850
L/M	180	120	82	70
n [cm^{-3}]	1.6×10^5	5.8×10^4	2.8×10^4	1.4×10^4
N(H$_2$) [cm^{-2}]	2.7×10^{23}	1.9×10^{23}		
θ[$''$]	-	-	39	37

	0.6pc		10% flux contours	
	Mean	Median	Mean	Median
M[M$_\odot$]	3.0×10^3	2.0×10^3	9.3×10^3	5.8×10^3
L/M	220	205	82	70
n [cm^{-3}]	4.4×10^5	2.9×10^5	1.2×10^4	0.65×10^4
N(H$_2$) [cm^{-2}]	2.7×10^{23}	1.9×10^{23}		
θ [$''$]	-	-	39	37

Table 4.2: Statistical properties of the sample of 47 high mass star forming regions in the inner Galaxy. The top table lists the properties of the sources for which the distance ambiguity could be resolved, the middle table of the resolved sources plus the remaining sources projected to their near distance, and the bottom table the resolved sources plus the remaining sources projected to their far distance. The row θ shows the equivalent source size as defined by the region of 10% flux.

lower densities, it is likely that we are observing whole cloud complexes at these distances. Klein et al. (2005) find similar values for their sample of proto-clusters. The sensitivity of the observations was not good enough to do radial fits on those sources.

Radio-loud & radio-quiet subsamples

To find out if there is any difference between sources in their earlier stages and those that have already developed UCHII regions, the sample was divided into two subsamples, one of 30 sources having associated cm radio continuum observed with interferometers and the other of 16 sources being free of radio continuum emission. For one source, 14206−6151,

08448-4343[1]	*16524-4300*[1]
12326-6245[1]	*16562-3959*[1]
12383-6128[1]	17016-4142[3]
13134-6242[3]	*17136-3617*[3]
16060-5146[1]	*17204-3636*[7]
16065-5158[1]	*17220-3609*[3]
16172-5028[1]	*17233-3606*[3]
16175-5002[3]	*17244-3536*[7]
16071-5142[3]	*17258-3637*[3]
16318-4724[1]	17271-3439[3]
16351-4722[1]	17470-2853[3]
16385-4619[1]	*17545-2357*[7]
16445-4459[3]	*17589-2312*[8]
16458-4512[1]	18232-1154[3]
16484-4603[3]	18319-0834[3]

Table 4.3: Subsample of radio loud sources. These sources have been detected in high resolution studies of cm radio continuum. Sources in italics have been classified as free of radio continuum following the single dish definition of Sridharan(2002). [1]:Urquhart(2007), [3]:Walsh(1998) , [7]:Becker(1994)

no high resolution interferometric observations are available. This division shows that the initial selection criterion that the sources be free of cm continuum emission in the 5 GHz single dish surveys (Sridharan et al., 2002) does not well describe the true evolutionary stage of the sources. It has to be noted that this is not a shortcoming of the selection criterion itself but results from the single dish surveys being sensitivity limited. When applying this (single dish) criterion, there are 35 sources to which the Sridharan et al. (2002) selection criteria apply and 12 sources which have been detected in the 5 GHz radio continuum surveys.
We analyzed the two subsamples to see how much the sensitivity limitation in the single dish vs. interferometric observations makes a difference in the analysis. Tables 4.3 and 4.4 show the distribution of the sources into the subsamples according to both definitions and Table 4.5 shows the median values of mass, density, L/M, $N(\mathrm{H_2})$, source size and distance in comparison for the sources in both kinds of subsamples.
For the comparison of the two subsamples, the median for each parameter was chosen, since the sources at their far distance introduce values far larger than those of the bulk of the sample. It can be seen from Table 4.5 that the sources which have already developed an UCHII region have a higher mass and luminosity-to-mass ratio than the sources without radio continuum. Given that the average size of the sources is the same in both subsamples, the sources with UCHII regions seem to concentrate more mass per given radius. These trends are the same, regardless of how the subsamples are defined. It cannot be said however that they are more centrally peaked, since the slope of the inner radius agrees within the errors for both sub-samples. .

When comparing the average masses in our radio quiet sample following the selection criteria of Sridharan et al. (2002), we derive a median mass of 663 $\mathrm{M_\odot}$ from the fluxes derived

13079-6218[2]	16076-5134[4]
14164-6028[2]	16272-4837[5]
14453-5912[2]	16489-4431[2]
14498-5856[2]	17158-3901[2]
15278-5620[2]	17269-3312[6]
15394-5358[2]	17278-3541[4]
15437-5343[2]	*18236-1205*[4]
15557-5215[4]	*18335-0711*[4]

Table 4.4: Subsample of radio quiet sources. These sources have been observed, but were not detected, in high resolution studies of cm radio continuum. Sources in italics have been marked as having radio continuum in the single dish definition of Sridharan (2002). [2]:Urquhart(2007), [4]:Walsh(1998) , [5]:Garay(2006),[6]:Forster(2002)

	Interferometric Criterion		Single Dish Criterion	
	Radio Quiet	Radio Loud	Radio Quiet	Radio Loud
$M_{0.6\mathrm{pc}}$ [$\mathrm{M}_\odot$]	388	581	264	914
$L/M_{0.6\mathrm{pc}}$	96	149	132	471
$n_{0.6\mathrm{pc}}$ [1×10^4 cm^{-3}]	5.6	8.3	6.5	23
M_{10} [$\mathrm{M}_\odot$]	830	949	663	3200
L/M_{10}	61	78	61	130
n_{10} [1×10^4 cm^{-3}]	0.8	1.9	1	2.6
N[1×10^{23}cm^{-2}]	1.9	2.5	1.4	4.4
m_i	-2.0	-2.0	-2.0	-2.1
Σ [g cm^{-2}]	0.12	0.22	0.11	0.35
θ [$''$]	35	37	37	31

Table 4.5: Comparison of the median values for the radio quiet (no cm continuum emission) and radio loud (detected in cm continuum emission) sub-sample. Values marked $_{0.6pc}$ have been derived from the flux within a 0.6 pc radius and values marked $_{10}$ from the flux within the 10% contour of the peak flux. m_i is the mean of the inner slope as determined in the radial fits.

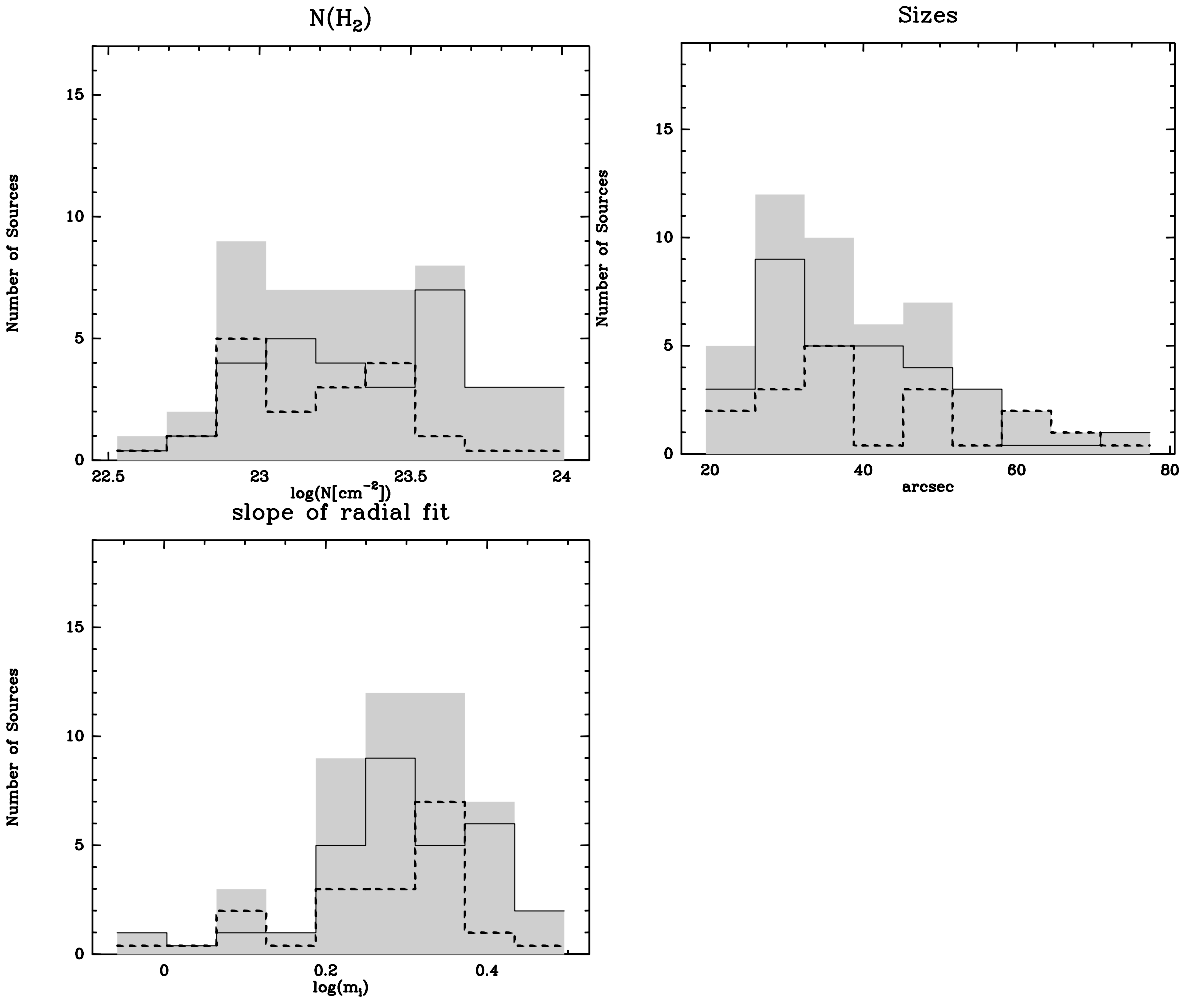

Figure 4.9: Histograms for the radio loud and radio quiet subsamples. In all histograms, the gray shaded area shows the distribution of the whole sample, the solid line shows the distribution of the radio loud subsample and the dashed line the distribution of the radio quiet subsample. Top left panel: Column densities, top right panel: source sizes, bottom left panel: inner slope of the radial fit. For all three distributions the sources with distance ambiguities were projected to their near distance.

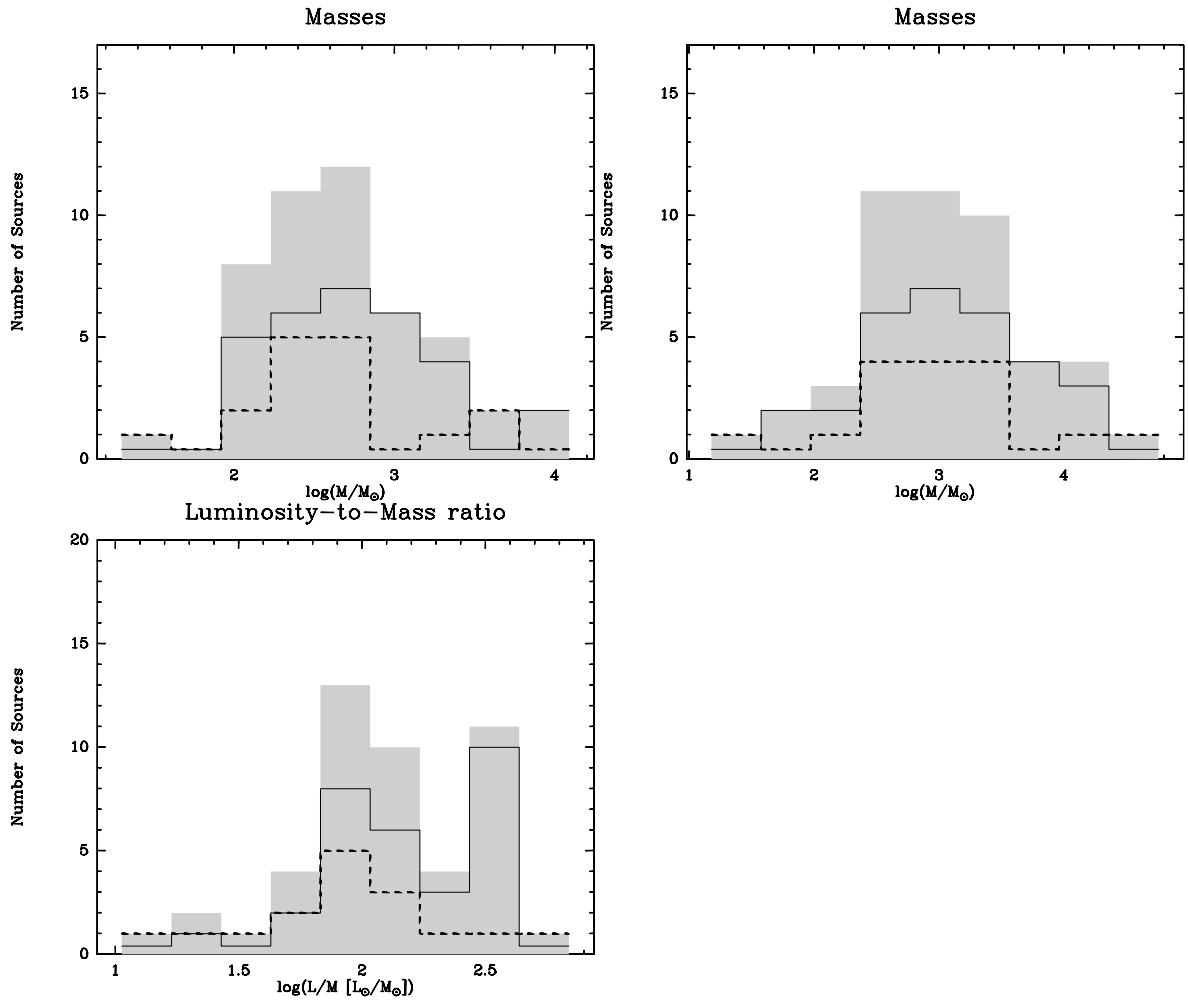

Figure 4.10: Histograms for the radio loud and radio quiet subsamples. In all histograms, the gray shaded area shows the distribution of the whole sample, the solid line shows the distribution of the radio loud subsample and the dashed line the distribution of the radio quiet subsample. Top left panel: Masses determined from flux derived within 0.6 pc, top right panel: masses determined from fluxes derived within 10 $\%$ contours, bottom left panel: L/M ratio for masses derived within 0.6 pc. For all three distributions the sources with distance ambiguities were projected to their near distance.

within 10% contours and 388 $M_{\odot}$for fluxes derived within 0.6 pc for the projection to the near distance, which is again a factor of 6 higher than the values of Williams et al. (2004) and supports the hypothesis that our sample contains more massive regions than theirs.
One has to be careful, however, when comparing masses determined in different samples of high mass star forming sources. Not only does it play a role which sources are selected, but the distance dependence of the individual sources can strongly alter the averages. In our study, we compared the median values for the radio loud and radio quiet subsamples determined with different sensitivity limits (see Table 4.5). As can be seen from Tables 4.3 and 4.4, using the higher sensitivity interferometric surveys to define the absence of radio continuum emission leads to a very different composition of the two subsamples. Even within our source sample, the median values for the two approaches differ by a factor of 1.3 for the radio quiet subsamples. For the radio loud samples, which contain more evolved and more massive sources, the two approaches differ by as much as a factor of 3.
Distance independent values such as the masses derived within a source size of 0.6 pc or the column densities should be used for comparison between different samples.

Radial fits

The radial fits to the dust continuum give a mean and median inner slope of 2.0±0.3 and a mean and median density index of 1.6±0.5.
This is more consistent with the theoretical prediction of a proto-stellar density power law distribution proposed by Shu et al. (1987) than with a logatropic equation of state (McLaughlin & Pudritz, 1996). Our values are consistent within the errors with the density distribution derived by Beuther et al. (2002a) ($< p >= 1.6\pm0.5$) and agree with the average values derived by Hatchell & van der Tak (2003) ($< p >$=1.5), which have been re-analysed by Beuther et al. (2002a) ($< p >$=1.9) using the same method they use for the radial fit. The values obtained by van der Tak et al. (2000b) for the whole sample of massive star forming regions are lower ($< p >\sim$ 1.0–1.5), while they find a radial density distribution $< p >\sim$ 1.5–2.0 for the hot core sources in their sample.
Beuther et al. (2002a) proposed an evolutionary sequence based on the steepness of the inner slopes m_i. While our inner radial intensity indices are generally larger than the ones observed by Beuther et al. (2002a), one can see the same trend that they propose. The sources at an early stage (without cm continuum emission) have a flatter intensity distribution with $< m_{\rm i} >$=2.0, the line rich hot core stage is very peaked with $< m_{\rm i} >$=2.7 and the sources with cm emission (in this case excluding the hot cores sources) flatten out again with $< m_{\rm i} >$=2.2.

Luminosity-to-mass relation

The meaningfulness of the luminosity-to-mass relation, L/M, depends strongly on how the masses and luminosities are estimated. For this work, the luminosity estimates were taken from Walsh et al. (1997) and scaled to match our distance estimates. The masses were, as discussed in a previous section, determined both within 10% of the peak flux and within a fixed source size of 0.6 pc. While the mass within 10% of the peak flux is most likely tracing

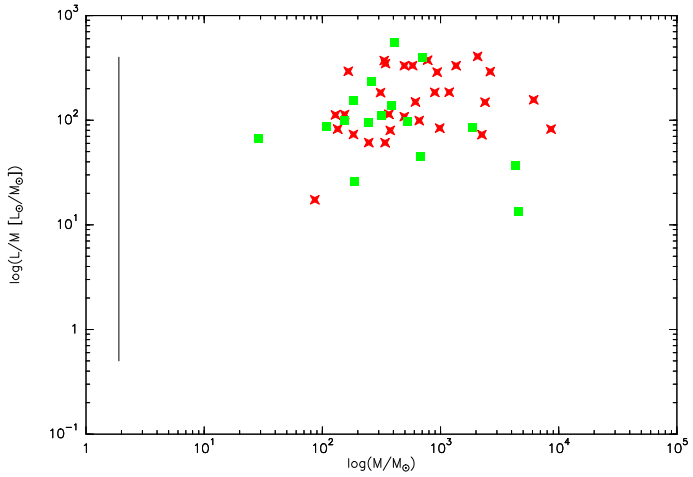

Figure 4.11: Luminosity-to-mass ratio versus mass. The green squares are the sources without radio-continuum, while the red crosses belong to the subsample with radio-continuum. The range on the y-axis represents the spread in L/M found in studies of molecular clouds (Evans 1991, Mueller 2002).

much of the extended cluster environment, the mass within 0.6 pc better represents the star forming site and is therefore used for the following discussion. We derive an average ratio of $< L/M >$=167 $L_\odot/M_\odot$ for a projection to the near distance, $< L/M >$=137 $L_\odot/M_\odot$ for the far distance and $< L/M >$=217 $L_\odot/M_\odot$ when averaging only over the distance ambiguity resolved sources.
In the two subsample with and without radio continuum, the averages are $< L/M >=$ 184 $L_\odot/M_\odot$ with a median of 149 $L_\odot/M_\odot$ for the radio-loud sample and $< L/M >$=140 $L_\odot/M_\odot$ with a median of 96 $L_\odot/M_\odot$ for the radio-quiet sample.

Comparing the median values, the sample which has already developed UCHII regions has also the higher L/M ratio, consistent with theory (Sridharan et al., 2002). The values we derive for L/M are consistent with those found by Mueller et al. (2002) for a sample of high mass star forming regions and those by Hunter et al. (2000) for a sample of UCHII regions. The values derived by Sridharan et al. (2002) for a comparable sample in the northern hemisphere are on average lower than the ones we derive, but when comparing the masses within 10% of the peak flux and scaling their values to the dust properties used in this work, the two samples agree well.

Fig. 4.11 shows the L/M ratio versus the mass. In this plot, the data in the radio-loud and radio-quiet subsample are compared. While both subsamples have a large scatter, they show no correlation with mass nor any systematic differences. Shirley et al. (2008) discuss a similar behaviour seen in other surveys of high mass star formation. Assuming the bolometric luminosity to be proportional to the star forming efficiency, we find a constant star forming rate per unit mass in both subsamples (c.f. Fig.1 in Shirley et al. (2008)).

In Fig. 4.12, adapted from Tan (2006), the surface density Σ is plotted versus mass. We derive $< \Sigma >= 0.35\ \mathrm{g\ cm^{-2}}$ (plotted in red), which is lower than the $< \Sigma >$ derived by

Mueller et al. (2002) (grey squares) and even lower than the value suggested by Tan & McKee (2002) who derive $< \Sigma >= 1.0\ \mathrm{g\ cm^{-2}}$ for massive star forming regions. The values in our sample agree well with the values found in the Orion Nebula Cluster (ONC) (green line). It has to be noted, however, that the value of Σ depends crucially on the mass and radius estimates. While Tan & McKee (2002) use the virial mass and radius, Mueller et al. (2002) use the isothermal mass within 120″ and a radius based on their density modeling. We, on the other hand, use the mass derived within the region where the flux has 10% of the peak flux and the radius of the equivalent area.

To answer the question whether or not the difference between the two subsamples of radio-loud and radio-quiet sources could be an evolutionary effect, we compare our bolometric luminosities and masses with the evolutionary models derived by Molinari et al. (2008). These authors model source evolution based on the turbulent core model (McKee & Tan, 2003). Their observational sample is based on Molinari et al. (2000), who define a sample of color selected sources based on Richards et al. (1987). Sources which are similar in their color selection criteria to the sources selected by the colour criteria of Wood & Churchwell (1989) are called "High" sources, while the remaining sources are called "Low" sources. Fig. 4.13 shows the evolutionary models of Molinari et al. (2008), the red and blue lines represent the modeled accretion and envelope-clearing stages respectively, while the green lines represent the pre-main-sequence phase. For details of the model, see Molinari et al. (2008). When comparing our sources with this model, it can be seen that the sources from both subsamples can be found in the same region of the plot representing the model results (our Fig. 4.13), i.e. in the envelope-clearing phase after the accretion has presumably finished. This scenario would speak against them being at different evolutionary stages, but rather just a sample of sources some of which have not developed detectable radio continuum emission.

4.3.2 The infrared environment

When trying to classify the evolutionary stage of a massive star forming core, it is important to also study its environment at infrared wavelenghts, to distinguish between the earliest stages when most of the luminosity is emitted in the mm and sub-mm ranges and the more evolved stages when the protostar has started to emit in the IR.
For sample A, we have obtained positions of MSX and Spitzer GLIMPSE I and GLIMPSE II point sources within 18″ of the 870 μm peak from the point source catalogs (Egan et al., 2003; Benjamin et al., 2003). For 24 of the sources in our sample we could detect one or more 8 μm sources within 18″ of the peak, while 38 sources have associated MSX 20 μm sources (see Figs. A.15 – A.22). The histograms in Fig. 4.14 show that the average offset between the sub-mm peak and the 8 μm emission is 0.1 pc, while the MSX sources have an average offset of 0.12 pc. This values are similar to the separation Sridharan et al. (2002) observe between mm and cm emission peaks. For both distributions, only the closest source to the peak was taken into account in the cases where there were more than one source within 18″. Of the 24 sources with 8 μm emission within 18″, only seven are not associated with cm continuum emission. Both the sources with and without associated cm continuum have an average separation of 0.1 pc between sub-mm peak and the 8 μm emission.
Since many of the 870 μm sources are located in regions of active star formation with in-

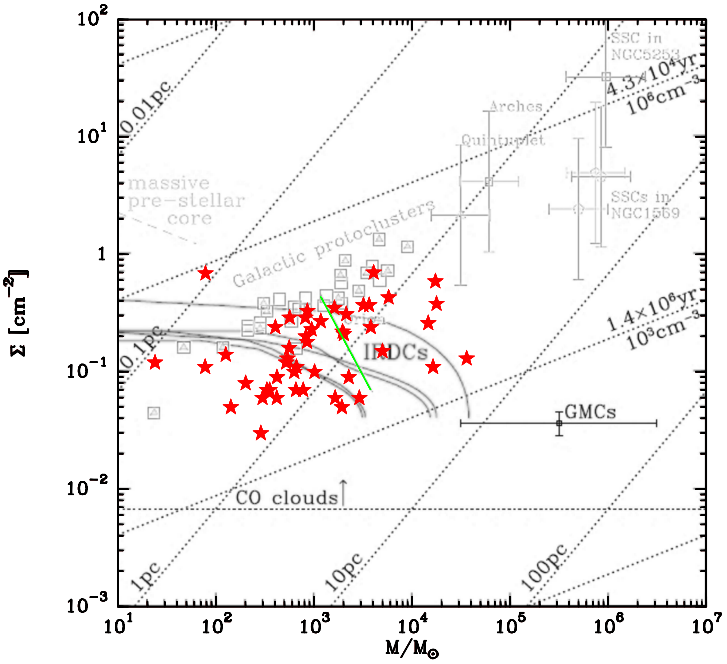

Figure 4.12: Surface density versus mass for the massive star forming regions in our sample (red). The plot is adapted from Tan et al. 2006. The sources from our sample are marked with red stars, the sources from Mueller et al. (2002) with grey squares. The crosses mark surface densities of several Galactic and extragalactic superclusters. The dotted lines give contours of constant radius, R, hydrogen number density, $n_{\rm H}$ and free-fall timescale, $t_{\rm ff}$. The horizontal lines trace typical values of $< \Sigma >$ in CO clouds, Giant Molecular Clouds (GMCs) and Infrared Dark Clouds (IRDCs). The green line traces conditions found from the inner to the outer part of the ONC.

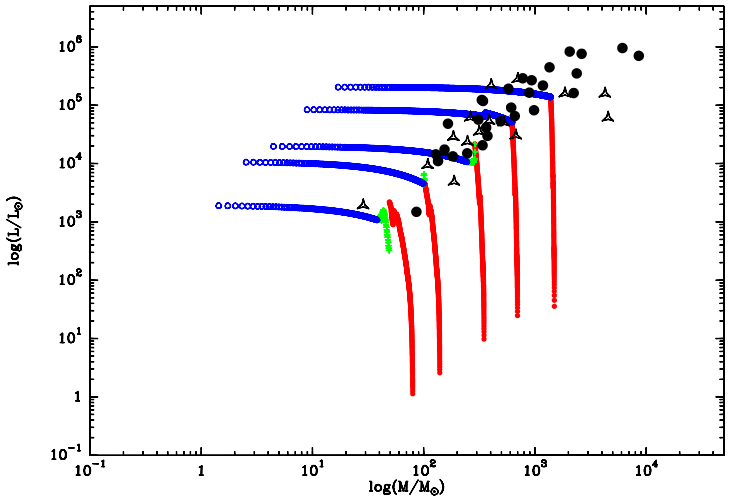

Figure 4.13: Luminosity versus mass plot adapted from Molinari (2008). The full circles show sources from the radio-loud subsample, the empty triangles from the radio-quiet subsample. The thick lines are evolutionary tracks of the massive stars. The red track shows the accretion phase, the green track the pre-main sequence phase and the blue track the envelope-clearing phase.

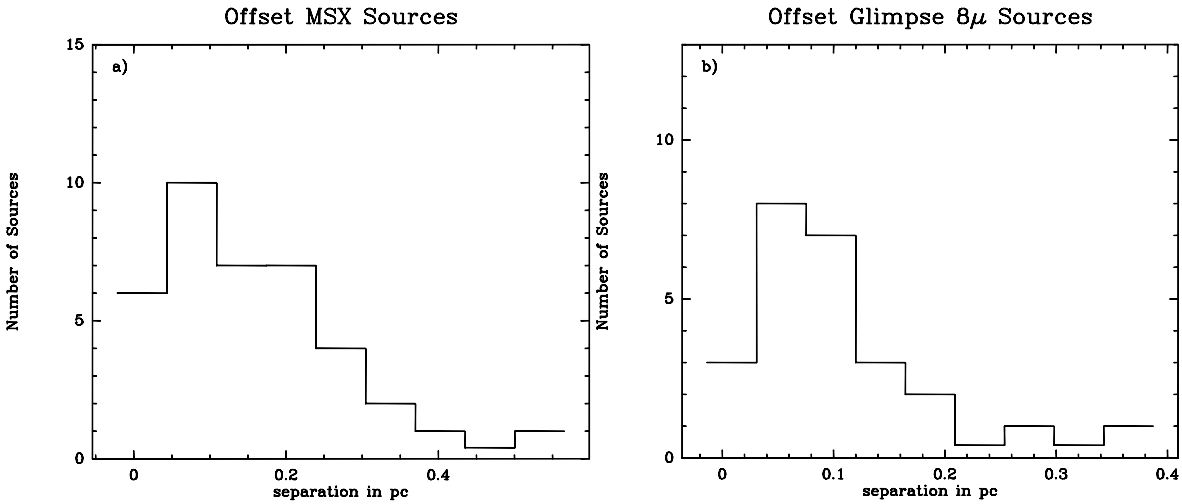

Figure 4.14: Histograms showing the offset in pc between the 870μm peak and the IR point sources. a) Offsets between dust peak and 20μm MSX sources; b) Offsets between dust peak and GLIMPSE 8μm sources.

tense 8 μm emission, we wanted to understand how isolated sources with no 8 μm emission at the 870 μm peak really are. Therefore, we divided sources with associated 8 μm emission into associations within 0.25 pc and 0.5 pc of the 870 μm peak and searched for MIPSGAL 24 μm emission at the peak. There are 14 sources which have no associated 8 μm emission within 0.25 pc. Out of those 14 sources, 12 were covered by the MIPSGAL survey and show 24 μm emission. For two of those sources, 16065-5158 and 16489-4431, the MIPSGAL 24 μm emission is offset by around 8″. These two sources might be the closest to the mm primary sources reported by Molinari et al. (2008). Twelve of the 14 sources which do not have 8 μm emission within 0.25 pc are associated with 8 μm emission within 0.5 pc. Fig. 4.15 shows scatter plots of the mass determined within 0.6 pc source size, 10% flux equivalent source size and distance versus the 8 μm flux integrated over 18″. The sources which have no 8 μm counterpart within 0.25 pc are shown in green, those that do have one, either within 0.25 pc or 0.5 pc, are shown in red.

Table A.29, column 11 gives an overview over the 8 μm environment the dust sources are located in. The comparison with the infrared data was possible for all but three sources (08448−4343, 16484−4603, 17278−3541), for which there is no GLIMPSEI or GLIMPSEII data available. We divided the different characteristics of the IR emission into the following 6 categories (see Table 4.6 for a summary):
f for field emission, consisting of distinct point sources, d for diffuse emission, e for extended emission (stronger and more compact than the diffuse emission), c for cavities, which corresponds to the situation where only the location of the dust peak is devoid of 8 μm emission, bs for structures resembling bow shocks and b for bubbles. As can be seen from Table A.29 and Figs. A.15 – A.22, one often finds the combination of 8 μm point sources surrounded by diffuse emission, yet there seems to be no interaction with the dust and the IR emission. In the case of 14453−5912, the IR emission seems to form a ridge. Out of the four sources that exhibit a cavity-like morphology, three (13079−6218, 16065−5158 and 17158−3901) do not have a MSX source associated within 18″, while in the fourth, 17220−3609, the MSX

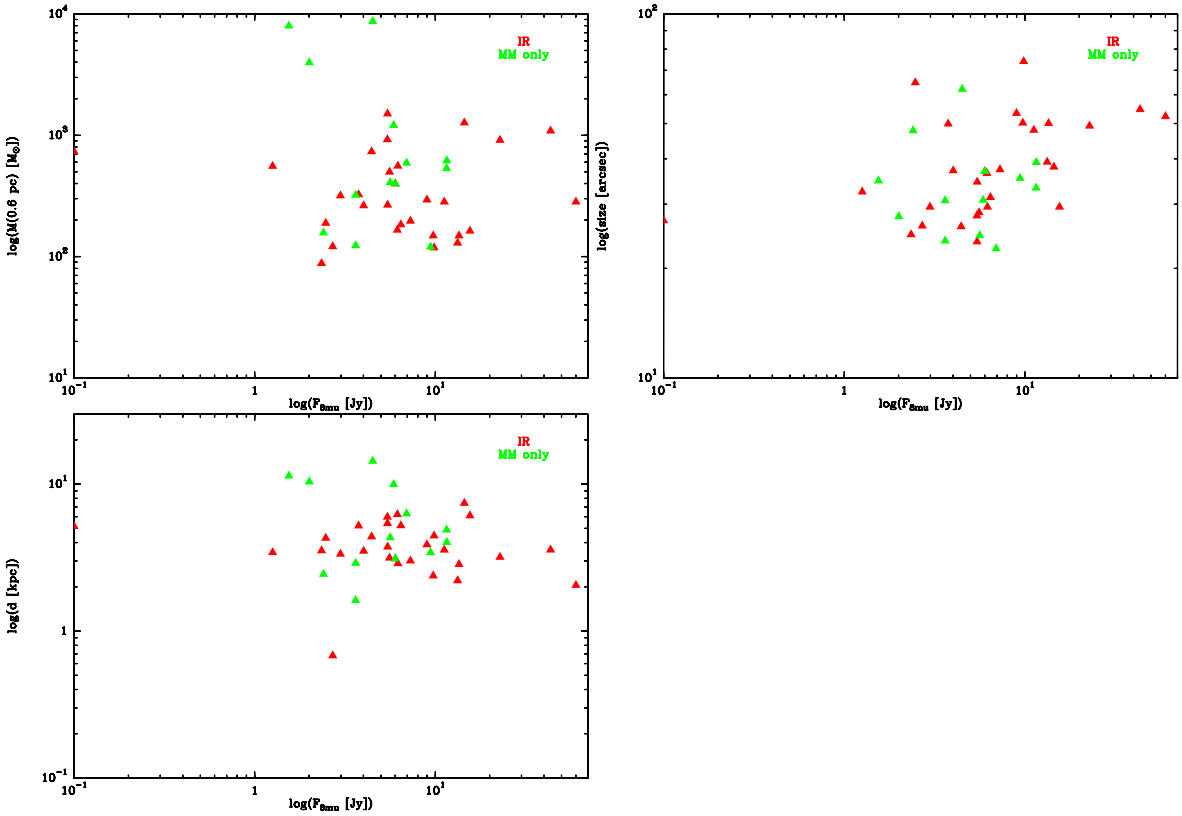

Figure 4.15: Scatter plots showing the relation between mass and 8 μm peak flux (top left), source size and 8 μm peak flux (top right) and distance and 8 μm peak flux (bottom left). In red, sources with a counterpart at 8 μm are plotted, while sources in green have no 8 μm counterpart within 0.25 pc.

8 μm Environment	Number Of Sources
field emission	28
diffuse emission	13
extended emission	4
cavities	4
bow shocks	3
bubbles	4

Table 4.6: The number of sources in the different 8 μm environments as described in the text, is listed. The field emission consists of distinct point sources. Several sources were counted towards more than one category.

source is offset by 0.6 pc, making these four sources good candidates for star forming regions at a very early stages prior to the onset of star formation.
Another four sources, 15278−5620,15557−5125, 16445−4459 and 17269−3312, seem to be located at the edge of larger bubbles or shells. Keeping in mind that one would first have to exclude projection effects, these suggest triggered star formation.

4.4 Conclusions

In this chapter, I studied the properties of the 870 μm dust continuum of the sample.
While the kinematic distance ambiguities between near and far distance could only be resolved for about 50% of the sample, comparison of the distributions of resolved and unresolved sources projected to their near and far distances, respectively, has shown that the majority of the sources will most likely be found at their near distance. It is, however, a necessary step in further analysis of the sample to resolve the remaining ambigutities. The morphologies of the dust continuum sources are varied and studying a distance limited subsample of the sources showed that 64 % of them do not have a companion within 2 pc of the core.
The sources are more massive than those in comparable surveys, which was expected since they were chosen to be luminous.The sources observed in the outer Galaxy at large Galactocentric radii are less massive and dense, but their masses agree with the lower range of masses found in massive star forming surveys. At these large distances, we are observing scales of cluster formation.
Radial fits to the flux distributions were performed for the sample. With p =1.6, the average radidal density index is well consistent with the theory of singular isothermal spheres, as described for low mass star formation, and values found in comparable samples. The sources in the inner Galaxy have been studied in two subsamples, of radio-loud and radio-quiet sources. The radio-loud sources which already have associated UCHII regions are more massive, have higher luminosity-to-mass ratios and seem to concentrate more mass in a given radius. The average density index between the two subsamples does not show variations.
It was analyzed how the composition of the samples can influence statistical results on the sample averages. To derive meaningful averages and be able to compare different samples, care has to be taken to resolve the kinematic distance ambiguities and use masses derived within a given linear size to mimimize distance effects instead of using masses derived within angular scales, as is mostly the case.
The surface density, Σ, is consistent with values found for the Orion Nebula Cluster and average IRDC values.
Assuming the bolometric luminosity to be proportional to the star forming efficiency, we find a constant star forming rate per unit mass in both subsamples. Comparing the luminosity-to-mass ratio of the two subsamples with evolutionary models, both subsamples are found in the envelope-clearing phase, after accretion has halted. This does not support the hypothesis that the radio-loud and radio-quiet subsamples are at different evolutionary stages.
Studying the infrared environment of the sample, we found that the 870 μm peaks are on average 0.1 pc offset from the peaks of the 8 μm emission. More detailed analysis revealed that all but two cores, 16065$-$5158 and 16489$-$4431, are associated with either 8 or 24 μm emission. No trend can be found when comparing properties of sources associated with 8 μm emission within 0.25 and within 0.5 pc of the 870 μm peak. Most sources are located in regions of active on-going star formation and one can find the sources located in various infrared backgrounds, like in cavities, bow-shocks and at the edges of large bubbles.

Chapter 5

Molecular line surveys

5.1 Introduction

In this chapter, I discuss the partial line survey that was conducted in the 0.85 mm window for 31 out of the 47 sources in the inner and 24 regions in the outer Galaxy.
Aim of this study was to analyze the chemical properties of the sample, particularly identify and study hot molecular cores, study the global kinematic motions through the line profiles and combine the chemical properties of the sources with the physical properties derived in the previous chapter.
In Section 5.1, I present the sample and the observations, in section 5.2 the results of the observations are presented and, finally, I discuss the results in section 5.4.

5.1.1 Observations

The list of sources observed in the 0.85 mm window can be found in Table A.1. After determining the HCO^+(4–3) peak positions from $60'' \times 60''$ maps, as described in Chap. 3, the 31 sources were observed at those positions in the CH_3OH(7–6) setup at 338 GHz which included $C^{17}O$(3–2), $C^{34}S$(7–6), CCH(4–3) as the most prominent lines apart from the CH_3OH band. The observations in both setups were conducted in August 2006, using the APEX2a receiver and the FFTS (see chapter 3) as backend. It was initially planned to observe the whole sample of 47 sources in the molecular line survey, but this turned out not to be feasible due to time constraints.
The CH_3OH(7–6) setup was tuned to 337.8 GHz and covered 1.9 GHz from 336.8 to 338.7 GHz with a velocity resolution of 0.87 $\mathrm{km\,s^{-1}}$. On source integration time was on average 8 minutes per source with an average system temperatures of $\sim$ 250 K. The pointing accuracy was checked on G327.3−0.6 (Wyrowski et al., 2006b), and was accurate within 2″. Most of the data were observed as single pointings. In the case where maps were made, raster maps with a map size of $40'' \times 40''$ and beam spacing were observed. All observations were obtained in double sideband mode. Calibration errors are estimated to be of the order of 30%. These errors are influenced by pointing and atmospheric fluctuations.

5.2 Infall study

5.2.1 CO, HCO^+

The CO(3–2) and HCO^+(4–3) maps were used to study the line profile for signs of infall and outflow activity. Fourteen sources show asymmetric line profiles in CO(3–2) with self-absorption in the line center and the emission in the blue part of the center velocity stronger than in the red part, which is often taken as an indication for infall (Mardones et al., 1997). When using a tracer such as CO(3–2) for studying the line profile shape, one has to take into account the fact that a reference position is not necessarily completely free of CO emission as well that CO velocity components along the line of sight can also alter the line profiles. Therefore, using the CO(3–2) line shapes only as first indication, the line profiles of HCO^+(4–3) spectra which were mapped in the same setup as the CO(3–2) line, were studied further. A few representative spectra of the sources can be found in Fig. 5.1, where the spectra in a map have been summed up to increase the signal-to-noise ratio in the wings of the line profiles. Table A.36 lists the observed sources and their HCO^+(4–3) line properties. Column one gives the source name, column two the area under the Gaussian fitted to the line profile, column three the LSR velocity as derived from the Gaussian fit and column four the FWHM line widths in $\mathrm{km\,s^{-1}}$. In column five, comments indicate the shape of the line profile in case it deviates from Gaussian. We denote outflow wings (a), a self-absorption profile indicating infall (b), a self-absorption profile indicating expansion (c) and a self-absorption profile with neither sign of infall nor expansion (d). Sources marked with '-' show no sign of asymmetric line profiles or outflow wings.

In case the optically thick HCO^+(4–3) lines show a double peaked line profile, the ratio of [T_{blue}]/[T_{red}] (Wu & Evans, 2003) was calculated for the two line peaks. If that ratio for a source was exceeding unity by more than 1σ of the distribution, it was counted as a blue-peaked source and if it was smaller than unity, the ratio was counted as a red-peaked source. Among the nine sources detected with a double peak profile, two show a blue-peaked profile and one a red-peaked profile. In case of lower column densities, a skewed profile with a shoulder can be found instead of the double peak profile. Following the procedure outlined in Mardones et al. (1997), we used

$$\delta V = (V_{\mathrm{thick}} - V_{\mathrm{thin}})/\Delta V_{\mathrm{thin}} \tag{5.1}$$

to quantify this asymmetry of the line profiles, using the HCO^+(4–3) line as the optically thick tracer and the $C^{17}O$(3–2) line (see Tab. A.37 in the appendix) from the 338 GHz setup as the optically thin line. The line positions V_{thick} and V_{thin} of the optically thick and thin lines respectively and the line widths, ΔV_{thin}, are obtained by fitting a Gaussian to the line profiles. In case of a double peaked profile, the position of the stronger peak is determined. For a number of sources, no HCO^+(4–3) data was available, so the peaks and line-widths of HCO^+(1–0) and $H^{13}CO^+$(1–0) (Purcell et al., 2006) were used instead (those sources are marked [a)] in Tab. A.38). When determining the excess parameter as the difference between the number of sources with significant blue shift (δV <-0.1), N_-, and those with significant red shift (δV >0.1), N_+, E = (N_+ - N_-)/N_{tot} (Mardones et al., 1997), it turned out that there is a blue-excess of E=0.3 in the sample. The threshold of δV =0.1 for a significant shift

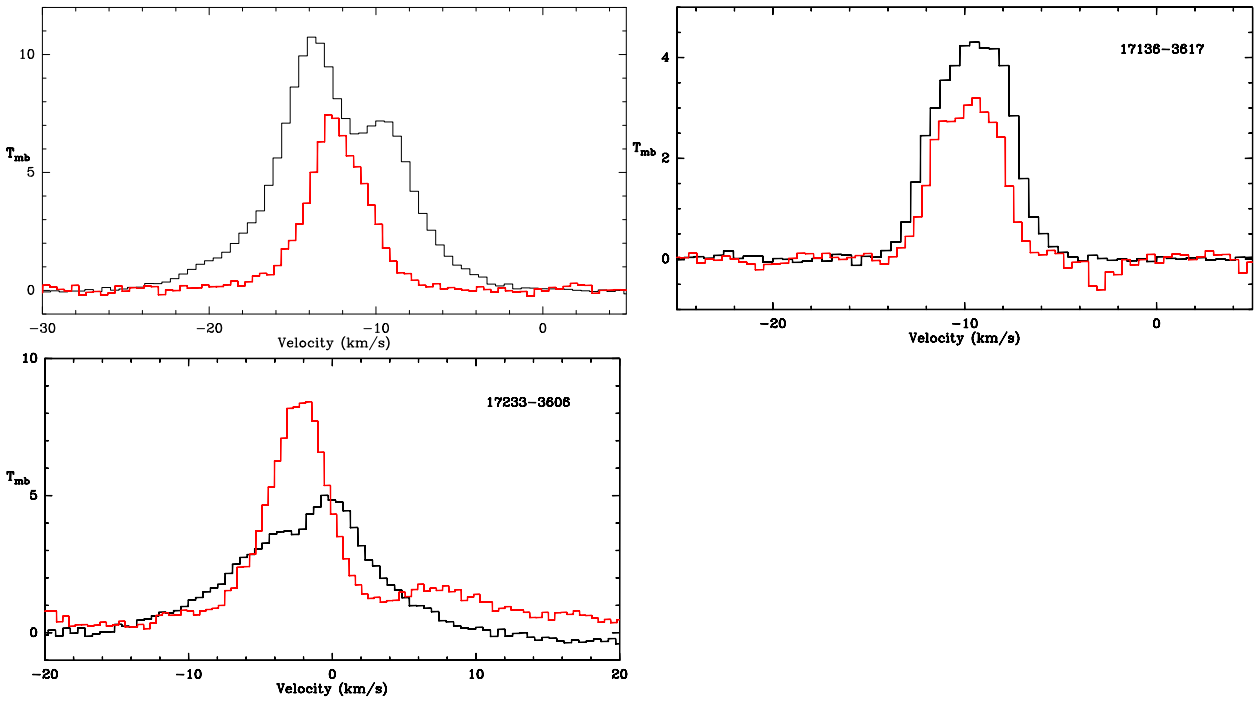

Figure 5.1: Representative spectra showing the HCO^+(4–3) (black) and $C^{17}O$(3–2) (red) lines as optically thick and thin tracers, respectively. Top left panel: 16526−3959 shows a strong blue-excess, indicating infall. Top right panel: 17136−3617 shows neither evidence for red- nor blue asymmetry. Bottom left panel: 17233−3606 shows a strong red-excess, indicating expansion.

was determined as five times the average rms error of δV. As can be seen from Tab. A.38 in the appendix, 5 sources exhibit a red-skewed profile and 12 a blue-skewed profile. The δVs obtained from the statistical analysis are consistent with the description of the HCO^+ line profile found in column five of Tab. A.36 in the appendix for the cases where one can see an asymmetry in HCO^+ line shape. Comparing the skewness δV for HCO^+(4–3) and HCO^+(1–0) separately, the sources were the gas is traced by HCO^+(4–3) have a blue-excess with E=0.3 and the sources where HCO^+(1–0) was available have a blue-excess as well with E=0.3.

5.3 Line surveys

The lines found in the 338 GHz setup are listed in table A.9 - A.4. It has to be noted that most of the lines could be found in the nine sources 12326−6245, 15278−5620, 16060−5146, 16065−5158, 16351−4722, 17016−4142, 17470−2853, 18335−0713 and 17233−3606, which following Hatchell et al. (1998) were classified line rich sources, while the 18 Sources showing only CO, CCH and weak CS emission, as well as CH_3OH emission from the lower excitation states were termed line poor. Following the method outlined in chapter 3, molecular column densities, line widths and velocity offsets were determined. In the cases where more than two optically thin lines were present, the temperature, T, could be determined

	$< T >$ (K)	$< \Delta v >$ $\mathrm{km\,s^{-1}}$	$< \theta >$ (pc)
envelope	30	5	-
hot component	160	5	0.03

Table 5.1: Mean temperatures, line widths and linear source sizes for the envelope component and the hot compact component. The linear source size was derived assuming an average distance of 5 kpc.

and in the case of optically thin and thick lines of the same species, also the source size. Sources modeled this way exhibit a two-component structure with a cold extended envelope and a compact hot core. All sources from the line-poor sample show only emission from the extended envelope in their spectra. In the cases where it was not possible to determine the temperature, T was fixed at 50 K for all species apart from HNCO, which was assumed to come from a hot component and therefore assumed to be at 150 K (Bisschop et al., 2007; Schilke et al., 2006). If the source size could not be determined, beam-averaged values for the column density are presented. The abundances were derived as N(mol)/N(H_2), with N(H_2) the total molecular gas column density obtained from the LABOCA 870 μm data. In this chapter, the word beam-averaged abundance is used to indicate that the abundances were derived with the beam-averaged column density.
The results of the LTE modeling can be found in the appendix in Tables A.39 to A.69 and in Figs. A.24 to A.51.
The average temperatures, line widths and linear source sizes for the envelope and the hot compact component can be found in Table 5.1. We could not determine an average source size for the envelope component, since the N, θ degeneracy could not be resolved for the envelope species.

Comparison among the sources in the sample has only been done for the cold envelope components CH_3OH(7–6), $C^{17}O$(3–2), $C^{34}S$(7–6), CCH(4–3) and H_2CS(10–9), which can be found in a significant number of sources.

In Fig. 5.2, the abundance ratios are plotted versus the column density and versus the ratio of 870 μm peak flux over the 8 μm flux determined over the area of one LABOCA beam.
The sources show very little spread in abundance over a large range of column density. In Fig. 5.2, the spread of the sample is shown as the marks along the y-axis. The semi-quartile range was chosen as a measure of the spread instead of the standard deviation, since the distributions of the abundance ratios are skewed. In addition, the semi-quartile range is not so strongly affected by outliers. Even when considering the range (maximum$-$minimum value) of the distributions, the abundance ratios vary less than an order of magnitude. In Fig. 5.3, the line widths of CO, CS, CH_3OH and CCH are plotted against H_2 column density derived from the 870 μm dust emission. The data has been binned in bins of 1×10^{23}cm^{-2} for values smaller 4×10^{23}cm^{-2}, and one bin for values above 4×10^{23}cm^{-2}. One can see a trend between large line-widths and large column densities.

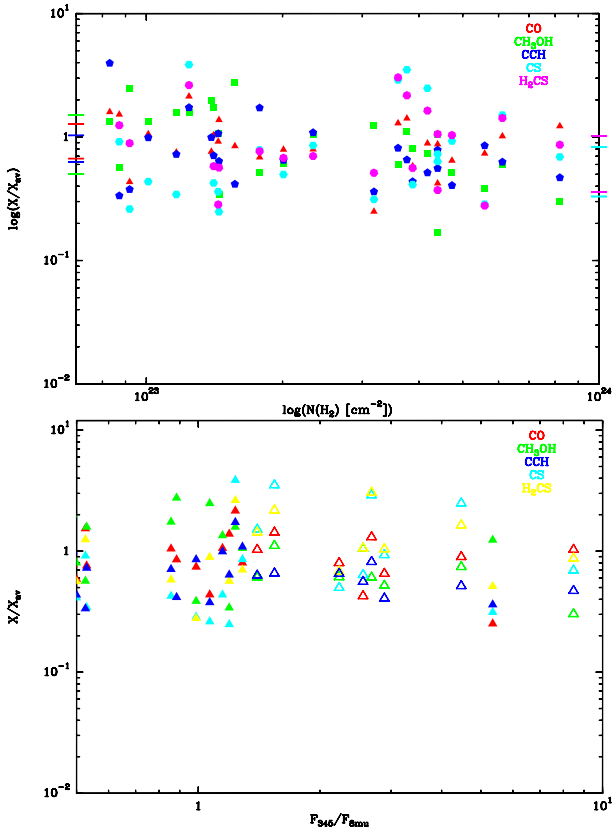

Figure 5.2: The ratios of molecular abundance over a sample averaged abundance are plotted versus H_2 column density (top panel) and versus the ratio of 870 μm/8 μm (bottom panel). The sample displays very little spread in the molecular abundance ratios, which is indicated by the horizontal markers at the y-axis, giving the semi-quartile range. The eight hot cores of the sample discussed in this chapter are shown with open triangles in the right panel.

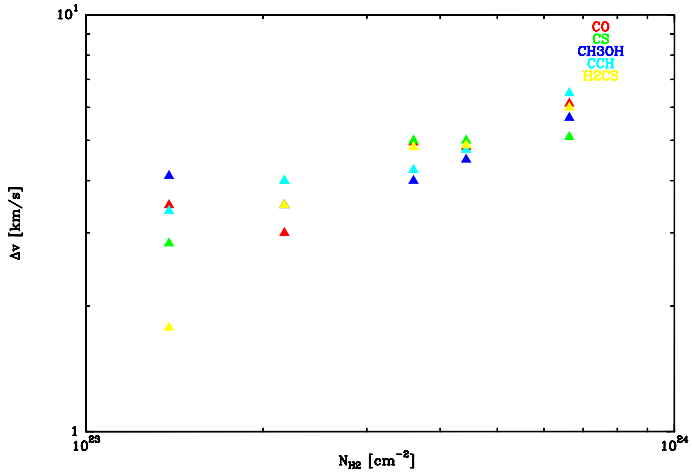

Figure 5.3: Line-widths versus H_2 column density for CO, CS, CCH and CH_3OH. The data has been binned in bins of 1×10^{23}cm^{-2} for values smaller 4×10^{23}cm^{-2}, and one bin for values above 4×10^{23}cm^{-2}.

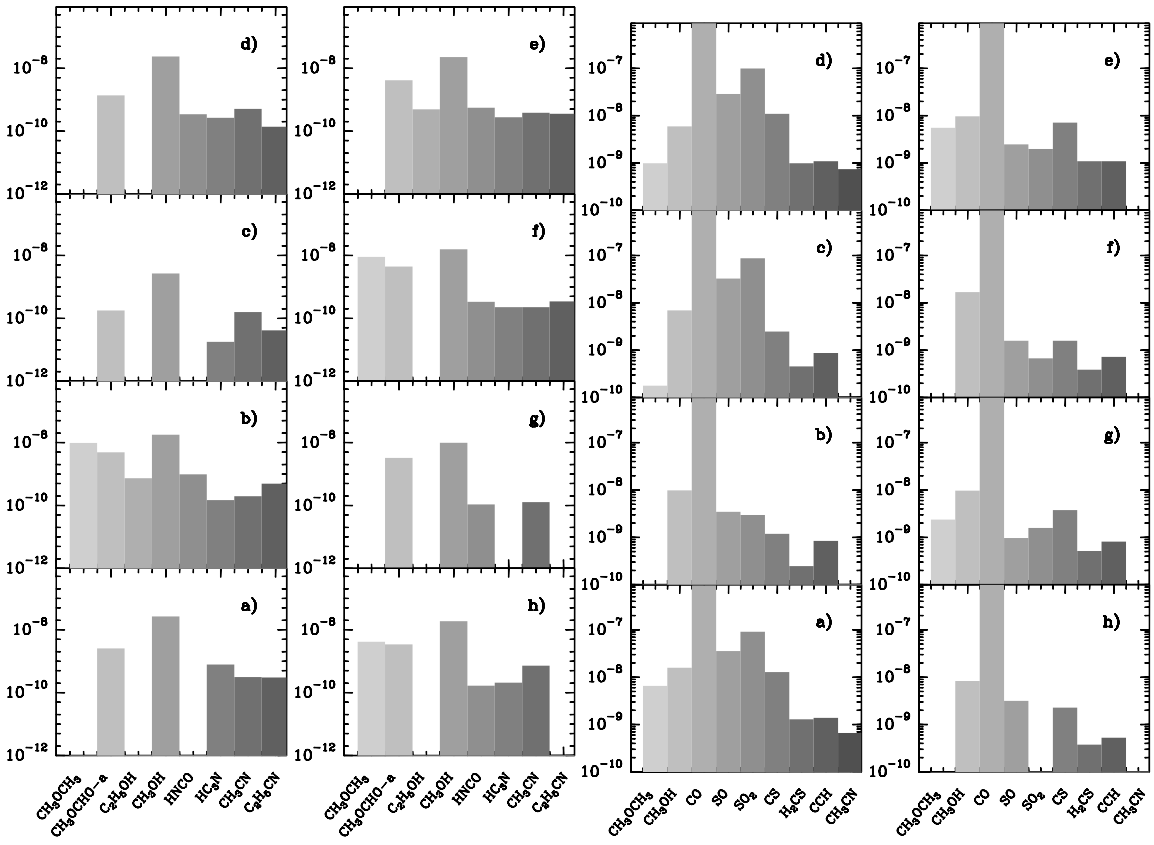

Figure 5.4: Comparison of the abundances (beam-averaged N) of the eight hot cores for the molecules originating from the hot component (left two panels) and cold component (right two panels). a) 12326−6245, b) 15278−5620, c) 16060−5146, d) 16065−5158, e) 16351−4722 , f) 17016−4142, g) 17470−2853, h) 18335−0713.

5.3.1 Hot cores

Among the sources which were classified as line-rich, nine sources exhibit a typical hot core like spectrum with high excitation lines such as the CH_3OH(7–6),vt=1 band at 337.65 GHz and complex organic molecules like CH_3OCH_3. The line rich hot core 17233−3606 was not included in the analysis in this chapter, since it was not part of this dissertation work and has been published elsewhere (Leurini et al., 2008). Here we present the data of the eight hot cores that were subject of this work. while the data of Leurini et al. (2008) are included for comparison when discussing the hot core properties in section 5.4. Including the three sources 12326−6245, 16060−5146, 16065−5158 already described in chapter 3, the beam-averaged abundances in the eight hot cores found in the sample are plotted in Fig. 5.4 for hot and cold molecules respectively.

Within the larger sample of eight sources, the effect of an enhancement in O-bearing versus N-bearing species seen for the three sources of the pilot study can be confirmed. This can be seen from Fig. 5.5, where the abundances ratios $X(mol)/X(CH_3OH)$ are compared. For a given species, the abundance ratios are constant within an order of magnitude, similar to what Requena-Torres et al. (2006) observe in the Galactic Center region. The abundances

of the N-bearing species are about an order of magnitude lower than those of the O-bearing species. As was already discussed in Chap. 3, a similar effect has been seen in high resolution studies of Orion-KL and W3(OH).

When comparing the sources with each other, 16351−4722 and 15278−5620 are most abundant in the complex organic species CH_3OCH_3, CH_3OCHO, C_2H_5CN and C_2H_5OH. The three sources of the pilot study, 12326−6245, 16060−5146 and 16065−5158 seem to be richer in S-bearing species. It has to be taken into account, however, that they were observed in more frequency setups, therefore allowing a better determination of the abundances for SO and SO_2.
Comparing their physical properties, the hot cores display similar ranges of masses, column densities and luminosities. 16060−5146, 16065−5158 and 17470−2653 show signs of infall activity in their line profiles, while 18335−0713 shows a red-skewed profile. Since all hot core sources display outflow signatures in their line wings, careful mapping of the sources with potential infall profile should be done in several molecular tracers and at higher angular resolution to clarify if the infall signature is real. The three sources potentially having infall show less N-bearing species in the hot component and have lower abundances of complex species than the other hot cores. 15278−5620 and 18335−0713 are not associated with radio continuum.
The hot cores (open triangles) display the highest ratio of 870 μm over 8 μm flux in Fig. 5.2.

5.3.2 Virial masses

We used the line widths Δv of the $C^{17}O$(3–2) lines to obtain virial masses $M_{\rm vir}$ in $M_\odot$ for the sample, according to Miettinen et al. (2006)

$$M_{\rm vir} = (0.5\Delta v^2 + 0.01T) d \Theta_{10} \kappa \ \ [M_\odot]. \tag{5.2}$$

For T in K, we assumed the dust temperature and as the angular source sizes Θ_{10} in $''$, the beam-deconvolved source sizes at the 10% flux contour as derived in the previous chapter were taken, d is the distance in kpc. As mentioned at the beginning of this chapter, maps of all sources were taken in HCO^+(4–3) to determine the peak positions. These maps were however either too small, incomplete or to noisy to derive the source size from them. In the few cases where it was possible to derive the source size as a two-dimensional Gaussian fit of the maps, the size of the HCO^+(4–3) emission agrees well with Θ_{10}. $\kappa \sim 1.3$ is a correction factor to correct for the average density dependence, $\rho \sim r^{-1.6}$ (MacLaren et al., 1988). Table A.78 lists the values of the virial masses.

5.3.3 Outer Galaxy line survey

We observed a sample of 18 sources in the outer Galaxy in CH_3OH(6–5), ^{13}CO(3–2), H_2CO(4–3), CS(7–6) and $C^{18}O$(3–2) to study the chemical composition of high mass star forming regions over a range of Galactocentric radii $R_{\rm G}$. The frequency setup was chosen to include CH_3OH and H_2CO to determine the temperatures of the regions and identify possible hot core sources through the observation of highly excited methanol lines, while

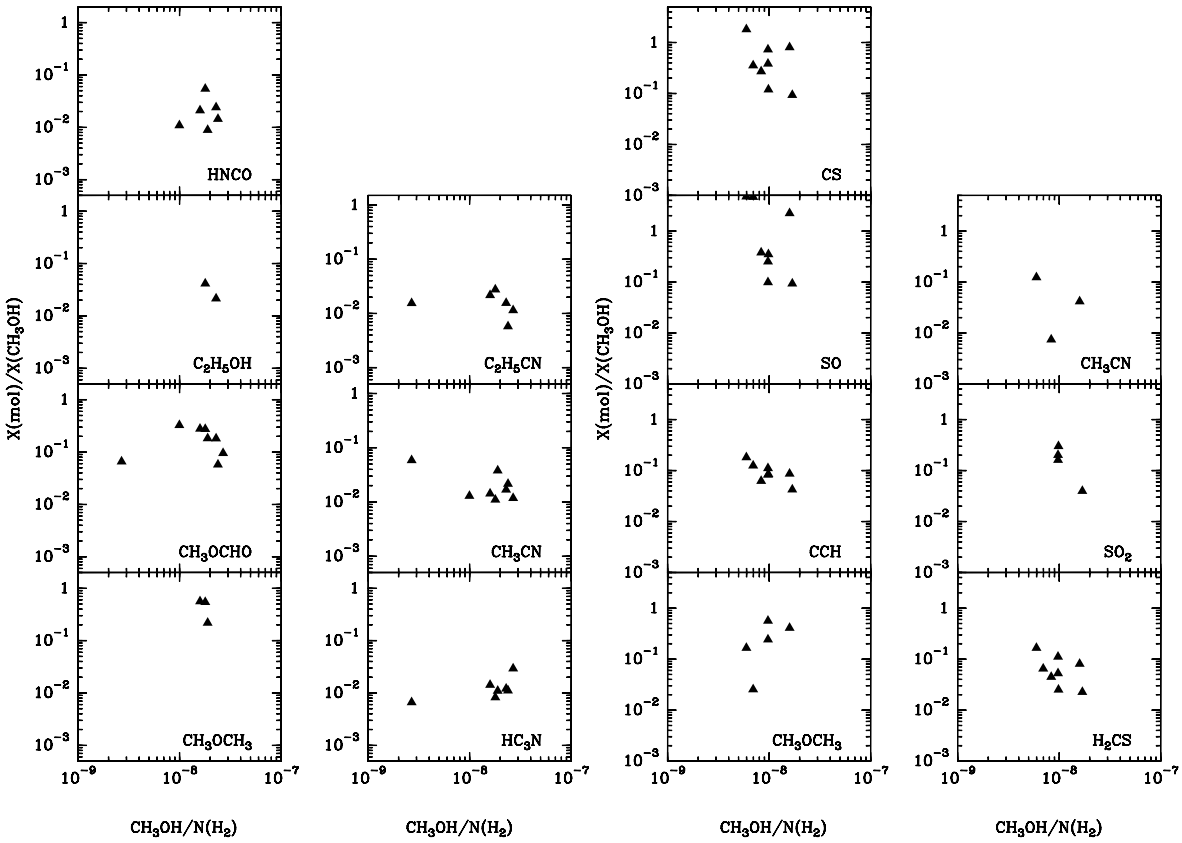

Figure 5.5: Ratio of X(mol)/X(CH_3OH) for the hot (left panel) and cold (right panel) component in the eight hot cores.

the CO lines give a measure of the column density. This sample was composed of those of the sources included in Klein et al. (2005) that are observable from the southern hemisphere with APEX. The analysis was done with XCLASS as described above for the line survey conducted for the sources in the inner Galaxy. We could only analyze the spectra of the sources 06055+2039, 06056+2131, 06058+2138, 06061+2151, 06063+2040, 06099+1800, 06117+1350 and 06155+2319 due to noisy spectra and strong baseline ripples in the remaining sources. Tables A.71 – A.77 in the appendix list the beam-averaged column densities, temperatures, line widths and abundances. The abundance histograms are shown in Figure 5.6. Table 5.2 lists the average abundances for the sources in the outer Galaxy.

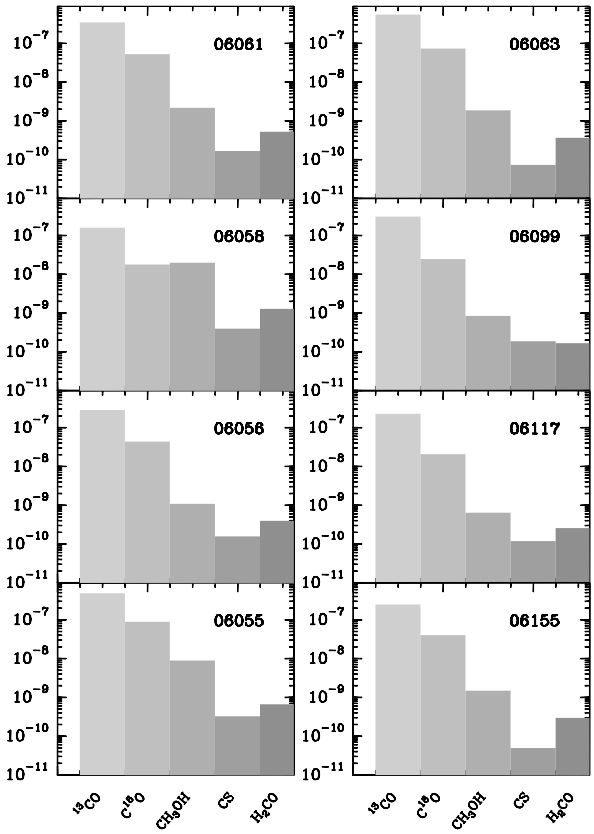

Figure 5.6: Abundances for the eight sources 06055+2039, 06056+2131, 06058+2138, 06061+2151, 06063+2040, 06099+1800, 06117+1350 and 06155+2319.

Molecule	$< N/N(H_2) >$	$< \Delta v >$ ($\mathrm{km\,s^{-1}}$)
CH_3OH	4.6e-09	3.1
H_2CO	4.7e-10	3
^{13}CO	3.2e-7	2.8
$C^{18}O$	4.4e-08	2.5
CS	1.8e-10	2.7

Table 5.2: Mean abundance values and mean line widths for the outer Galaxy sources.

5.4 Discussion

5.4.1 Line profiles

In this chapter, the molecular content of the sources in the sample is analyzed.
Studying the line profiles of the HCO^+ data, we looked for signs of in-flowing motion in the sample, which could imply ongoing gravitational collapse (Wu & Evans, 2003). Due to the formation mode of high mass stars in a complex and turbulent cluster environment, one has to be careful when assigning infall signatures to individual sources, since the line profiles can also be influenced by rotation and outflows. It is possible, on the other hand, to investigate the statistical distribution of inflow and expansion tracers in a sample of high mass star forming regions to classify whether or not a sample is likely containing a significant number of sources undergoing collapse. Among the 31 sources for which an analysis of the line profiles was possible, a large number of sources exhibit non-Gaussian line profiles. Over the sample, we find 12 sources having a blue-excess, i.e. showing self-absorption in the center and a weaker red wing - a sign of infalling motions, while 5 sources show a red-excess emission. While it still remains questionable to assign infall motions to individual sources without further analysis, we can say with confidence that the sample is dominated by infall motion, similar to the samples studied by Wyrowski et al. (2006a) and Wu et al. (2007).
Despite the fact that our tracers HCO^+(4–3) and HCO^+(1–0) trace different parts of the gas, the excess parameter is 0.3 in both cases, showing that the infall motion can be found in the extended gas traced by HCO^+(1–0) and also in the denser warmer gas traced by HCO^+(4–3). The excess parameter based on the CO(3–2) data is $E = 0$, indicating no sign for infall motions. Looking at individual sources, there is no good agreement between the asymmetry parameters derived from CO(3–2) and $C^{17}O$(3–2) compared to those derived from HCO^+. 7 of 16 sources show the same asymmetry, in 6 sources an asymmetry detected in the CO data was not detected in the HCO^+ data and in the remaining 3 sources a red-excess in the CO data was detected as blue-excess in the HCO^+ data. Caution is needed, however, when using the CO lines, particularly the lower transitions like CO(3–2) to trace motions, since the CO line shapes can be contaminated from emission in the off-positions and pick up emission from CO clouds along the line of sight. The off-position used in our observations was observed at a fixed offset relative to the pointing centers, so it cannot be excluded that contamination in CO occurs.
The sources in the radio-loud subsample show an excess parameter $E_{\rm RL} = 0.4$, while the radio-quiet sources have $E_{\rm RQ} = 0.1$. This excess of blue-skewed sources, and hence infall motions towards sources which have already developed an UCHII region was also observed by Wyrowski et al. (2006a) and Wu et al. (2007). It was proposed by Wu et al. (2007) that infall occurs preferentially at the later evolutionary stages traced by the UCHIIregions, which is consistent with our observations.
Comparing the line poor and line rich subsamples, we find that the line poor sample is dominated by infall motions with $E_{\rm poor} = 0.45$, while the line rich sample has $E_{\rm rich} = 0.08$. Since the sample of line poor sources is predominantly associated with radio continuum, it is likely that the effect seen here is linked to the above mentioned proposal that sources which have already developed UCHII regions are more likely to show signs of infall. To investigate in more detail how the occurance of infall is linked to the molecular line content of the sample,

it would be necessary to study the whole sample in line emission and infall tracers to improve the statistics and be able to distinguish between radio-loud and radio-quiet line poor sources. Four of the sources showing infall motions in their profile are offset from MIPSGAL 24 μm emission. Two of them, 14453−5912 and 15437−5343 are radio-quiet sources, while the other two, 16065−5158 and 18232−1154 are associated with radio-continuum. These four sources might be good candidates for massive collapsing cores at an early evolutionary stage. To get more confidence in understanding whether or not the observed profiles might be related to infall motions, it would be necessary to map the sources in an a higher-J transition of HCO^+ or CO in higher spatial and velocity resolution to understand how the profile changes with distance from the core.

5.4.2 Line survey

Analyzing the line survey at 338 GHz revealed two main points.

First, the overall chemical composition of the outer envelope for the sources of the sample shows very little spread between the sources. Second, the line survey revealed a total of nine hot cores among a sample of 27 sources. These nine hot cores all show a similar trend toward more O- than N-bearing species, as had already been observed in the pilot study.

The similar chemical composition of the envelopes of the sources, as seen in Figure 5.2, is interesting given that the sample encompasses sources with and without radio continuum, with and without IR associations and with a wide range of luminosities with $700 < L < 1 \times 10^6$ $L_\odot$ and masses with $30 < L < 7 \times 10^3$ $M_\odot$. If assigning the sources with unresolved near/far distance ambiguities to their far distances, one obtains a larger range of masses and luminosities. It has to be considered though that luminosities beyond 1×10^6 $L_\odot$ would be produced by objects with ZAMS spectral types < O4 (Panagia, 1973), which is unrealistic for a single object.

The fact that all sources were chosen on the basis of IRAS color selection criteria (Wood & Churchwell, 1989) might entail that the sources have a very similar chemical composition, since the IRAS colors likely select similar temperature structures of the envelopes. Samples should be composed based on different selection criteria when trying to find implications for evolutionary stages. This effect is similar to the one seen by Kurtz et al. (2000), who described a very similar abundance pattern among northern hot cores.

In Figure 5.7, it can be seen that the hot cores of our sample, as well as a number of other hot cores taken from the literature lie in a specific range of L/M and column density N. When studying the sources which are in the same parameter space without being hot cores, no correlation with radio continuum association, IR association or molecular line content appears.

With the APEX2a beam of 18″, emission from a source with a temperature of 100 K can still be detected above an average signal-to-noise ratio of 0.3 K if it has a radius of at least 0.5″. Using relation (5.3) (from Wilner et al., 1995), we estimated that assuming the sources have the observed luminosities and a minimum temperature of 100 K, which should trigger hot

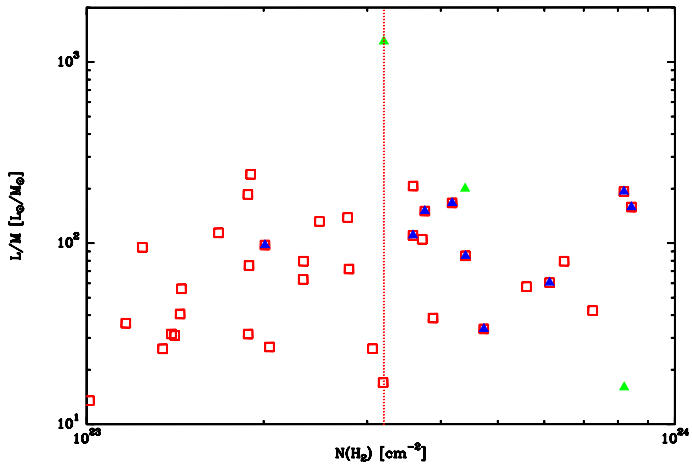

Figure 5.7: L/M ratio versus column density for the high mass star forming regions. Red squares mark the sources, blue triangles the hot cores in our sample and green triangles the hot cores G327.3-0.6, NGC6334 and 18089-1732.

core chemistry, they have radii of at least 0.7″.

$$T_{\rm d}(R) = 37 \left(\frac{L}{\rm L_\odot}\right)^{0.25} \left(\frac{R}{100\rm AU}\right)^{-0.4} \quad [\rm K] \tag{5.3}$$

Therefore, it is unlikely that we are not detecting line radiation from the hot core due to beam dilution, indicating that the sources are intrinsically line poor.
The rich chemistry in a hot core is triggered when the raising temperatures close to the newborn star evaporate molecules off the icy dust mantles. This implies that the observed sources are most likely not hot enough to form a hot core. They could be at an earlier evolutionary stage and still develop a hot core given time, but the fact that six out of seven sources have associated UCHII regions likely places them at a late evolutionary stage.
Comparison of the hot core luminosities and those of the seven sources without a hot core shows that both samples have similar median luminosities of 1.9×10^5 $\rm L_\odot$ for the sources without and 1.2×10^5 $\rm L_\odot$ for the sources with a hot core. If the luminosity came from a single massive object, this would result in similar temperatures around the young star. A possible scenario for the missing line emission is that the luminosity in the line poor sources comes from multiplicity where the individual sources do not have enough luminosity to evaporate the molecules off the ices in a radius sufficiently large to produce detectable sub-mm emission. To check this hypothesis, it is necessary to observe the sources with higher angular resolution to see whether they fragment into multiple objects.
Another possibility is that the hot core species in these sources have already been destroyed by the surrounding UV radiation field.

To investigate further whether the similar chemical compositions of our sample are a selection effect or an intrinsic property of the interstellar medium, we compared the envelope abundances derived from our sample with those derived from single dish studies of intermediate and low mass star forming regions and Giant Molecular Clouds (GMCs). We obtained beam averaged abundances from Schreyer et al. (1997) for the intermediate mass regions NGC2264 IRS1, from Helmich & van Dishoeck (1997) for the high mass regions W3 IRS4

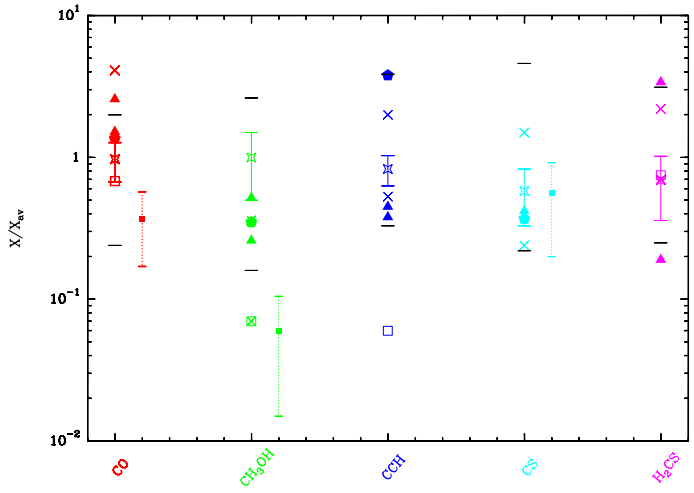

Figure 5.8: Comparison of abundance ratios per molecule. $X/X_{\rm av}$ is the ratio of observed abundance over the mean abundance of our sample. The median of our sample is shown as an open star, with error bars indicating the range expressed as semi-quartile to take into account the skewness of the distribution. Horizontal black lines indicate the range (max-min value) of our sample. Filled triangles show the envelopes of intermediate mass star forming regions, crosses those of high mass star forming regions and open squares the envelope of G34.3+0.15. The pentagon represents the Orion ridge and the small filled squares the envelopes of low mass star forming cores with the associated semi-quartile spread as dashed error bars.

and W3 IRS5 and from van Dishoeck et al. (1995) for 16293−2422. Abundances for a sample of 18 low mass star forming regions and the envelopes of pre-stellar cores were taken from Jørgensen et al. (2004, 2005). Figure 5.8 shows the ratios X/X_{av} in comparison to the abundance ratios of our sample. X_{av} is the average abundance in our sample. As one can see, the abundances for the intermediate mass star forming regions, the Orion extended ridge and the halo of G34.3+0.15 agree well with the spread found in our sample. The only values that are significantly lower than our average are the abundances of $\rm CH_3OH$ and CCH in G34.3+0.15 and $\rm CH_3OH$ in W3 IRS5.
The abundance ratios of CO and CS over the average abundance in our sample, X_{av}, in the envelopes of the low mass sources are similar to the values observed in our sample, while those of the $\rm CH_3OH$ abundace over X_{av} are significantly lower. The distributions for all three low mass source abundance ratios show a larger spread than the one found for our massive star forming sources.

Table 5.3 lists the mean abundance values for the species in the line poor subsample, the line rich subsample and the whole sample. All three have very similar mean values, within a factor of 2. Analyzing the spread in each subsample shows again that there is very little spread in the abundances for the different sources.
To compare the spread in envelope abundances of our sample with those observed by Bergin et al. (1997), we derive the abundances for our sample with the CO column density as $X/N(\rm CO)$. As can be seen in Figure 5.9, the chemical composition in the GMC cloud cores is considerably different from that of our high mass star forming sample, in that it has

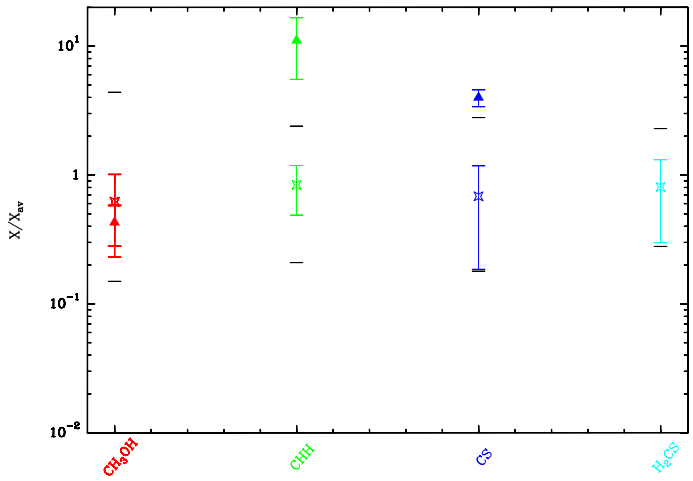

Figure 5.9: Spread in abundance ratios of our sample (open stars) compared to those in Giant Molecular cloud core (filled triangles) observed by Bergin et al. (1997). The spreads given are semi-quartile and the symbols mark the median. The horizontal black lines indicate the range (max-min value) of our sample.

higher than average abundances of CCH and CS. It has to be noted that these abundances were derived from emission mapped over arc minute scale regions, while our abundances were derived within a beam of 18″.

We compare our average abundance estimates also with typical starless core abundances (Tafalla et al., 2006), dark cloud abundances (Smith et al., 2004; Morata & Herbst, 2008) and, since many of our sources can be found in regions close to newly formed luminous stars and are likely exposed to copious amounts of UV flux, with the time-dependant model of dense photodissociation regions (PDRs) of Morata & Herbst (2008). In addition, we also compare our abundances of CO, CH_3OH and H_2CO (for the three pilot study sources and the outer Galaxy sources) with the new gas-grain interaction model of Garrod et al. (2008). The latter authors include new grain-surface reactions in their chemical network and incorporate a collapse and warm-up phase. Comparing the obtained abundances to observations of high and low mass star forming cores, they propose that the initial chemical composition of ices in low and high mass star forming regions might be different.
For CH_3OH, we observe higher abundances in our sample than in most comparison regions. While they are only a factor of a few higher than the envelopes of G34.3+0.15 and the intermediate mass star forming regions and the Orion ridge, they are about 1–2 orders of magnitude higher than in the envelopes of the low mass cores, starless cores and the GMCs. This enhancement of CH_3OH abundance in hot regions was already discussed as an indication for grain-surface formation by Menten (1987) and later by van der Tak et al. (2000a). In their model of grain-surface chemistry, Garrod et al. (2008) calculate both an early and late peak in the abundances of methanol. While our observed values do not agree with either value both in temperature and abundances, one could generalize it by saying that in the envelopes of the high and intermediate mass star forming regions we are observing the late peak of CH_3OH, while in the low mass star forming regions as well as in the regions corre-

Tracer	Line Poor Sources	Line Rich Sources	All Sources
CO	7(-5)	6(-5)	7(-5)
CH_3OH	2(-8)	1(-8)	2(-8)
CCH	2(-9)	8(-10)	1(-9)
CS	2(-9)	3(-9)	3(-9)
H_2CS	2(-10)	4(-10)	4(-10)

Table 5.3: Mean abundance values for the envelope component in the line poor sources, the line rich sources and the whole sample.

sponding to the more initial stages (the dark clouds, starless cores, GMCs), we observe the early peak of CH_3OH.
The CO abundances vary little between the different samples. Differences in the CO abundances most likely reflect freeze-out on the grains.
We observe CCH in all of our sources. As was discussed already by Beuther et al. (2008a), ethynyl can be found in all evolutionary stages of (massive) star formation. The abundances we derive are comparable to those of the regions of intermediate mass star formation and the envelope of G34.3+0.15. In the dark clouds, the early time PDRs and GMCs, the abundances of CCH are higher than in our sample, suggesting that these correspond to the early type, initial abundances, while CCH seems to be depleted in the envelopes of the intermediate and high mass star forming regions. CCH is also less abundant by a factor of about 2 in the line rich subsample of our sources compared to the line poor sample of our sources, which supports the idea that it might be removed from the gas phase at a later, hotter stage.
CS abundances are comparable to those in low and intermediate mass star forming envelopes, starless cores and early time PDRs. They are about an order of magnitude higher than in G34.3+0.15 and smaller than in Orion and GMCs. Comparing the CS/CH_3OH ratio, one could come to the conclusion that high abundances of CS are more common in unprocessed, quiescent gas, since the ratios in dark clouds, starless cores, the Orion extended ridge and GMCs are larger than one, while they are below 0.3 in the intermediate and high mass star forming regions. This is not conclusive however, since the low mass star forming regions and W3IRS5 show high ratios of CS/CH_3OH.

Now we move on to discuss the line widths of the molecules common to most sources (CH_3OH, CO, CCH, CS), which show a trend of larger line-widths toward larger dust column densities (Figure 5.3). By making the assumption that, to first order, the velocity dispersion is dominating the line-width and that thermal motions are negligible (Larson, 1981), one can take the line-widths as a measure for the velocity dispersion in the sources. McKee & Tan (2003) interpret the surface density, $\Sigma \equiv M/\pi R^2$, as a measure of pressure, since the pressure is related to the gas mass through the isothermal sound speed c by $P \equiv \rho c^2$. The gas mass is related to the virial mass through the virial parameter $\alpha_{\rm vir}$. Including a factor $\phi_{\rm p}$ to account for the geometry and magnetic fields of the clump, we obtain

$$P \equiv \phi_{\rm p} G\Sigma^2 \sim 0.88 G\Sigma^2.$$

For a detailed derivation and a description of $\phi_{\rm p}$, see the Appendix of McKee & Tan (2003)

and section 5.4.5. One can say that the sources with higher pressure give rise to larger velocity dispersion, i.e. stronger turbulence. Given that the isothermal sound speed in gas of T~ 30 K is approximately 0.3 $\mathrm{km\,s^{-1}}$, all the sources show signs of supersonical turbulence, which grows with higher column densities. Since supersonic turbulence is thought to impose density variations on the medium (McKee & Ostriker, 2007), the sources with high column density are most likely very clumpy.
On the other hand, Vázquez-Semadeni et al. (2008) argue, by comparing typical clump properties found in their simulations with observed values, that the velocity dispersions observed in high mass star forming regions are due to global infall motions rather than random turbulence. The clumps Vázquez-Semadeni et al. (2008) report as typical for their simulations of molecular cloud development agree well with the average clump values we report in Chap. 4. The fact that our sample is dominated by infall motions supports the notion that the conditions in the observed high mass star forming regions in our sample arise from global collapse rather than random turbulence. Before being able to rule out one or the other scenario however, it would be necessary to study in more detail the gas at different scales and conditions, since the molecular tracers probe infall only in a narrow range of physical conditions.

5.4.3 Hot cores

The discussion in Chap. 3 already addressed the issue of the large abundance of complex O-bearing species in the sample. It is remarkable that the same effect can be observed in all eight hot cores. According to the discussion in Chap. 3, it is possible that the complex N-bearing species have been started to be destroyed close to the heating source. In a sample of twelve well-known HMCs, Fontani et al. (2007) derive the $\mathrm{C_2H_5CN/CH_3OCH_3}$ ratios of beam-averaged column density, which are all above unity. In our sample however, these values are well below unity. Fontani et al. (2007) use the rotational diagram technique assuming optically thin lines to determine the column densities. Bisschop et al. (2007) also use rotational diagrams, they do, however, find significantly larger column densities for $\mathrm{CH_3OCH_3}$. Using the XCLASS software to model the column densities in our sample, we can take optical depth effects as well as line blending into account. To be able to reliably compare the abundances found in the three studies, it would be necessary to re-analyze the data with XCLASS to include optical depth effects for all sources.
Since $\sim$80$\%$ of the hot cores have associated radio continuum, we want to see how their properties compare to the averages from the radio loud and radio quiet subsamples. We list the median masses, L/M ratios, densities, inner radial slope, surface density and diameter (see Table 5.4). The values for the radio loud and radio quiet subsample are listed in Table 4.5.
Compared to both subsamples, they are more massive, denser, smaller and have a higher surface density, while their L/M ratio is the same. Their inner radial intensity index m_{i} is steeper.

The properties of the hot molecular cores place them in an evolutionary sequence very close to the more evolved radio loud phase, which has already developed UCHII regions. Their physical properties mark them as very extreme sources.
We checked their association with radio continuum in the RMS survey (Urquhart et al.,

	Hot Molecular Cores
$M_{0.6\ \mathrm{pc}}$ [$M_\odot$]	780
$L/M_{0.6\ \mathrm{pc}}$	147
$n_{0.6\ \mathrm{pc}}$ [cm^{-3}]	1.1×10^5
M_{10} [$M_\odot$]	1620
L/M_{10}	110
n_{10} [cm^{-3}]	3.6×10^4
m_i	-2.4
Σ [g cm^{-3}]	0.35
θ [$''$]	29

Table 5.4: Median values for the dust properties of the nine hot cores found in the survey.

2007a) and found cm continuum data for five of them. The LABOCA dust continuum overlayed with the radio interferometer data can be seen in Fig. A.23 in the appendix. Considering the evolutionary sequence Beuther et al. (2002a) proposed based on the steepness of their flux distribution (m_i), they are possible candidates of evolved hot cores in a transition phase to UCHII regions (Kurtz et al., 2000).

According to Fig. A.23, 16060−5146, 16351−4722 and 12326−6245 are the three sources where the cm continuum seems to coincide best with the peak of the dust emission. They are also the most centrally peaked sources. Together with the central location of their UCHII region this make them the more evolved among the hot core sample.
In the abundances of the hot species, 16060−5146 is the weakest among the hot cores, which again hints at the interpretation that it might be at a more evolved stage, while 16351−4722 shows strong lines in the hot component. These three sources are however also strong emitters in the cold species (T $<$ 100 K), even though one would assume that the sources at the later stages start to clear up the envelopes.

5.4.4 Virial masses

To examine the dynamical state of the clumps, the virial masses are compared to $M_{10\%}$, the continuum masses contained within the 10% flux contour. Figure 5.10 shows the ratio of the virial to continuum masses. The average ratio $M_\mathrm{vir}/M_\mathrm{cont} \sim 0.7$ (5.2) for the distance resolved sources and the sources projected to their near distance, and ~ 0.4 when the sources are projected to their far distance.
The distribution in Fig. 5.10 shows that for most sources $M_\mathrm{vir} < M_\mathrm{cont}$, reflecting the fact that we expect ongoing star formation in most sources.

We compared the luminosity to mass relation for the hot cores with the evolutionary model developed by Molinari et al. (2008), as we already did with the continuum sources in chapter 4. Fig. 5.11, which shows a cut-out of Fig. 4.13, shows the evolutionary tracks of the high mass sources modeled by Molinari et al. (2008). While they distinguish between two types of sources in their sample, the infrared primary sources (IR-P), which are indicated by the solid black line and the mm primary sources (MM-P), which are indicated by

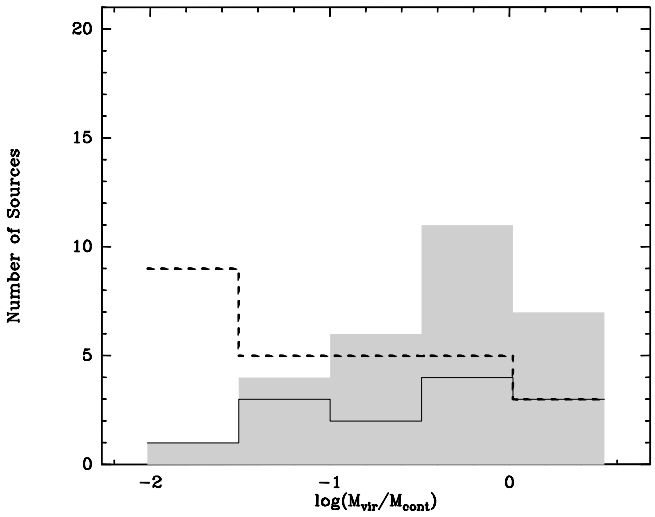

Figure 5.10: Histogram of the ratio of virial mass to continuum mass. The distance resolved sources are described by the solid line, the sources where the non-resolved distances have been projected to the near distance are shown in grey-scale and the sources projected to the far distance are shown with the dashed line.

the dashed line, our sources belong only to the infrared primary sources, as was discussed in chapter 4. The thick red and blue lines in the figure represent the modeled accretion and envelop-clearing stages respectively. Added to it are the continuum masses and bolometric luminosities of the eight hot core sources analyzed in this chapter (filled triangles), which represent the whole region including the envelope material, as well as the masses and luminosities of the hot cores themselves (filled stars). To obtain these values, we made use of the fact that the molecular lines can act as a "magnifying glass" for the innermost embedded regions. The analysis of the highly excited CH_3OH(7–6) and CH_3CN(19–18) lines allowed us to determine temperatures, source sizes and line widths of the hot components, with which we were able to calculate the virial masses and luminosities for the hot cores. Those hot cores are shown as filled stars in Fig. 5.11 and connected by a dashed line with their matching dust continuum sources. The error bars reflect the uncertainties in the line modeling done with XCLASS, when determining temperature, source size and line width. The errors on the continuum data are of the order of 20% and introduced through uncertainties in the data reduction and distance determination. It has to be noted that the values for the dust temperature T and the luminosity L were obtained from the literature. Since their errors are not know, the true uncertainties are likely to be larger. As can be seen, the hot core luminosity is consistent within the errors with the evolutionary tracks modeled by Molinari et al. (2008) for envelope masses of 700 and 2000 $M_\odot$. In all cases, the placement of the dust continuum sources with respect to the models shows that when using single dish instruments, we are observing the envelope material which is accreting onto the star, while the use of the higher excited transition lines allows us to zoom into the cloud to see the newly formed star. Comparing the masses of the hot cores with those of the evolutionary tracks of the final stars, we find that between 30–50% of the hot core mass will end up forming the star. This is naturally much higher than the few percent Molinari et al. (2008) find, since

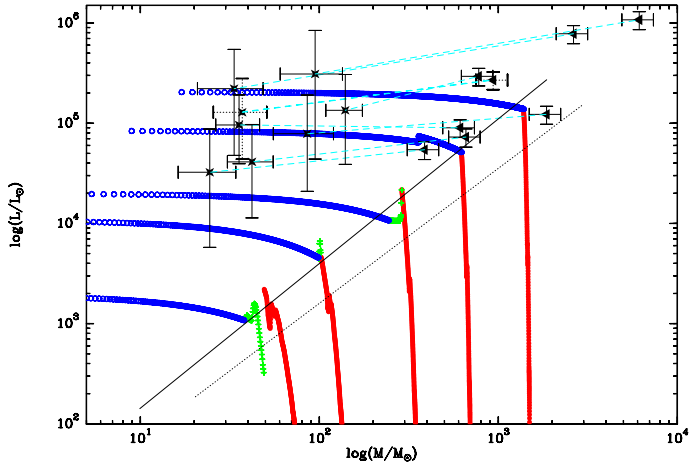

Figure 5.11: Luminosity versus mass plot adapted from Molinari (2008). The filled triangles represent the continuum masses and bolometric luminosities of the envelopes containing the hot cores, while the filled stars show the virial masses of the hot core components and the luminosities derived from modeling their core temperatures and sizes. The dashed lines connect the hot cores with their matching dust continuum envelopes. The large solid and dashed lines indicates the location of the infrared-primary (IR-P) and mm-only (MM-P) sources from Molinari (2008).

they compare the whole clump in which the hot cores are embedded. Looking at the dust continuum sources in Fig. 5.11, we find a comparable fraction of a few percent of envelope mass that will go into the formation of the star.

5.4.5 Turbulent core model

One of the models to describe high mass star formation assumes that the stars form in monolithic collapse trough disk accretion from a turbulent core (McKee & Tan, 2003). In their model, McKee & Tan (2003) describe the mean pressure in a star forming clump as

$$\frac{\bar{P}_{\rm cl}}{k} = 4.25 \times 10^8 \Sigma_{\rm cl}^2 \ {\rm K \ cm^{-3}} \tag{5.4}$$

for spherical clouds including magnetic field effects, $\frac{2}{3}$ of the cloud mass in gas and $\frac{1}{3}$ in stars, a virial parameter of order unity and with $\Sigma_{\rm cl}^2$ the observable surface density in g cm^{-2}. With the pressure of the cloud and the final mass of the star, they can express several properties of the core embedded in the cloud – the pressure at the surface of the core, $P_{\rm S,core}$, the velocity dispersion at the surface of the core, $\sigma_{\rm S}$, the radius of the core, R$_{\rm core}$, the density of H atoms at the surface of the core, $n_{\rm H,S}$, the mass accretion rate, $\dot{m}_*$ and the star forming time,$t_{*\rm f}$. Using the following equations from McKee & Tan (2003), we try to estimate the aforementioned quantities for the eight hot cores. Since the final mass, $m_{*\rm f}$, is needed for the calculations, we assume that the hot core virial mass we derive corresponds to the final mass of the core, which we translate to the final mass of the star $m_{*\rm f}$ using a star forming efficiency of 0.5, which agrees with the results seen in Fig. 5.11

$$\frac{P_{\rm S,core}}{k} = 1.06 \times 10^9 \Sigma_{\rm cl}^2 \ {\rm K\ cm^{-3}} \tag{5.5}$$

$$\sigma_S = 1.22 \left(\frac{m_{*\rm f}}{30 {\rm M}_\odot} \right)^{1/4} \Sigma_{\rm cl}^{1/4} \ {\rm km\,s^{-1}} \tag{5.6}$$

$$R_{core} = 0.051 \left(\frac{m_{*\rm f}}{30 {\rm M}_\odot} \right)^{1/2} \Sigma_{\rm cl}^{-1/2} \ {\rm pc} \tag{5.7}$$

$$n_{H,S} = 1.47 \times 10^6 \left(\frac{m_{*\rm f}}{30 {\rm M}_\odot} \right)^{-1/2} \Sigma_{\rm cl}^{3/2} \ {\rm cm^{-3}} \tag{5.8}$$

$$\dot{m}_* = 8.21 \times 10^{4-} \left(\frac{m_{*\rm f}}{30 {\rm M}_\odot} \right)^{3/4} \left(\frac{P_{\rm S,core}/k}{10^9 \ {\rm K\ cm^{-3}}} \right)^{3/8} {\rm M}_\odot \ {\rm yr^{-1}} \tag{5.9}$$

$$t_{*\rm f} = 6.4 \times 10^4 \left(\frac{m_{*\rm f}}{30 {\rm M}_\odot} \right)^{1/4} \left(\frac{10^9 \ {\rm K\ cm^{-3}}}{P_{\rm S,core}/k} \right)^{3/8} {\rm yr} \tag{5.10}$$

The resulting values can be found in Table A.79 in the Appendix. For a detailed derivation of equations 5.4 – 5.10 see McKee & Tan (2003). We used $\phi_{\bar{\rm P}} = 0.88$, which is a numerical factor describing effects of non-spherical geometry, magnetic fields and the virial parameter. We use $k_{\rm p} = 1.2$ and A=0.84 for the density structure and gas fraction, based on obtaining $n \sim r^{-1.6}$ from our radial fits in Chap. 4. Since the surface densities we obtain are on average lower than those referred to by McKee & Tan (2003), this subsequently reflects in the values we derive. The velocity dispersion is in most cases only slightly larger than the isothermal sound speed, $c_{\rm th}$, which was derived using as temperature $T_{\rm rot}$ as found in the hot core model for the core. In this case, the cores would not be as supersonically turbulent and clumpy, as proposed by McKee & Tan (2003). When comparing this with the observed values of the line-widths, as was done in section 5.4.2, we see that the observed values are much higher than those derived from Σ. It has to be noted however that the typical surface density of Σ $\sim$1 g cm^{-3} that they refer to has been derived by Plume et al. (1997) using the virial masses and sizes of the CS line emission region. We obtain accretion rates of the order of $3{\times}10^{-4}$M$_\odot$/yr and star formation times of the order of $1{\times}10^5$ yrs. These values agree well with the accretion rates Molinari et al. (2008) calculate for their high mass star formation accretion model. The core radii correspond well to the hot core sizes observed in the hot components for the hot cores. To properly predict the properties of a collapsing turbulent core with this model, it would be necessary to obtain high resolution imaging of the sources to get a better idea of the fragmentation and the actual sizes of the star forming cores. The model does, however, give a good first estimate of the core properties.

5.4.6 Outer Galaxy sample

We observed molecular lines in eight sources in the outer Galaxy. These sources have been observed by Klein et al. (2005) in the sub-mm continuum. We detected CH_3OH(6–5), $C^{17}O$(3–2), H_2CO(4–3), CS(7–6) and $C^{18}O$(3–2). The abundances we derive are on average

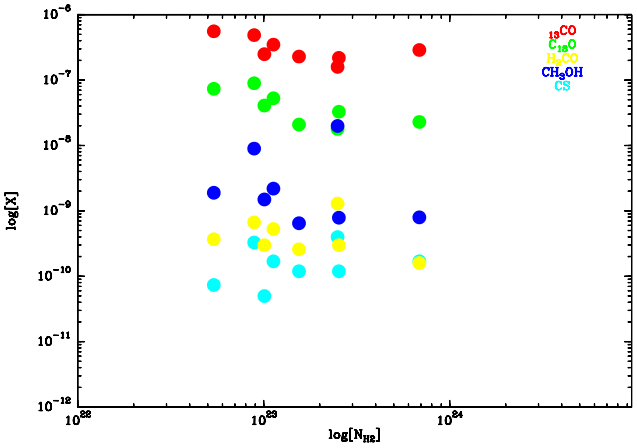

Figure 5.12: Abundances in the outer Galaxy sources vs H_2 column density.

one order of magnitude smaller than in the inner Galaxy sample. In Figure 5.12, the abundances are plotted against H_2 column density. For the two CO isotopologues and CH_3OH, there seems to be a weak trend of lower abundances with larger $N(H_2)$, which could be an effect of optical depth, while for CS and H_2CO the abundances seem constant. The abundances were, as was done for the inner Galaxy sources, compared to the average abundance values over the sample. As can be seen in Figure 5.13, the spread in abundances is not very large. It has to be noted that despite their location in the outer Galaxy, these sources are only about 2 kpc away from us. Therefore, their low chemical abundances are not an effect of resolution. The sources in the outer Galaxy are on average less massive, smaller, and less luminous regions than those in the inner Galaxy. Klein et al. (2005) apply similar FIR flux criteria ($S_{100\mu m} > 500$ Jy) as we do in our survey. They did however not include the criterion that the sources be observed in the CS survey of Bronfman et al. (1996), which traced sources with characteristics of UCHII regions. The different chemical abundances between the two samples are most likely due to source selection and represent the more evolved stage of our sample.

In all sources, we see only transitions from molecules which come from the envelope. CH_3OH(6–5) modeling resulted in an average $T_{\rm rot}$ of 20 K. In two sources, 06061-2151 and 06117-1350, several transitions of H_2CO(4–3) could be observed and resulted in temperatures of 40 and 60 K respectively.

We compare the abundances ratios for the sources in the inner and outer Galaxy as a function of Galactocentric radii (see Fig. 5.14) for CH_3OH and CS. The abundance ratios are done wit respect to the mean abundaces of the inner Galaxy sample. It can be seen that, as discussed above, the sources in the outer Galaxy are less abundant both in CH_3OH and CS than the average source in the inner Galaxy. For, both, the inner Galaxy sample and the outer Galaxy sample, no trend with Galactocentric radius can be seen. For the outer Galaxy sample it is necessary to observe more sources, since it was only possible for six sources from our sample to obtain line observations and determine the Galactocentric radius, which is not a very good statistic.

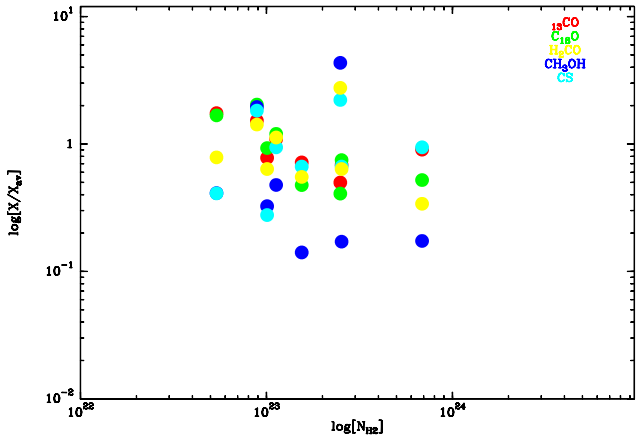

Figure 5.13: Ratios of abundance to mean abundance in the outer Galaxy sources vs H_2 column density.

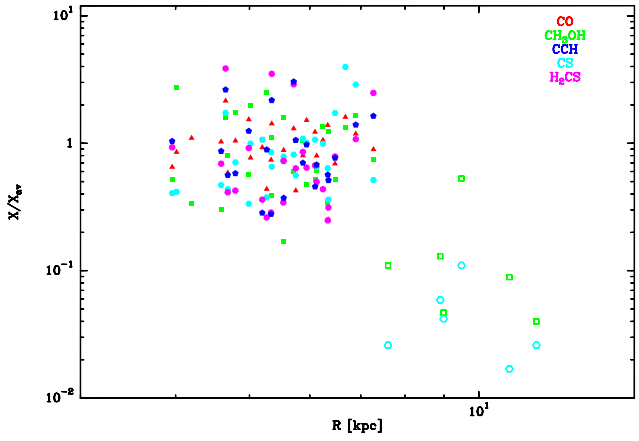

Figure 5.14: Ratios of abundance to mean abundance for all sources vs Galactocentric radius. The mean abundaces are those of the inner Galaxy sample A. The sources in the outer Galaxy are shown with open symbols.

5.4.7 Conclusions

In this chapter, the partial line survey in the 0.85 mm window was analyzed. A statistical study of the line profiles revealed that the sample is dominated by infall motions.
The line survey resulted in the discovery of nine line rich hot cores. These hot cores can be placed at a transition stage between line rich sources and UCHII regions. The enhancement of O- versus N-bearing species already seen in the pilot study could be confirmed for the hot cores found in the sample. I identified a number of sources with similar luminosities and column densities than the hot cores. These sources are not rich in molecular lines, which might either be an evolutionary effect or a result of clustered star formation in the regions, which cannot be resolved with the current resolution.
The molecular abundances of the cold extended envelopes are remarkably similar over a wide range of column densities and compare well with a number of intermediate mass objects and quiescent regions in the interstellar medium. This leads to the question how much the chemistry is influenced by the external conditions in the gas and how much by the initial composition of the ices.
Using the virial mass of the hot cores and the source size derived from the line modeling, I calculated the parameters of the star forming hot cores in the framework of the turbulent core model McKee & Tan (2003).
I compared the envelopes and the inner cores of the hot cores with the evolutionary model of Molinari et al. (2008). The inner cores were approximated through the viral mass and the luminosity derived from the modeled temperature and source size for the hot component. About 30–50% of the mass of the hot core go into the final star, which is consistent with the efficiencies predicted by McKee & Tan (2003) for the turbulent core model. while this efficiency is only of the order of a few percent when comparing the clump (envelope) with the final mass.
While the comparison of the molecular line data with the physical conditions derived from dust gave us evidence both for a global collapse scenario (infall) and for the turbulent core scenario, no conclusion can be reached to exclude one or the other.

Chapter 6

Summary & Outlook

6.1 Summary

The next few years will open up exciting new possibilities for sub-millimeter and infrared astronomers to study massive star formation in unprecedented details. The Atacama Large Millimeter Array (ALMA) in Chile will allow high resolution studies in the (sub-)mm regime from 0.3 – 9.6 mm. It will be possible to image disks at AU scales, witness the formation of planets and study the fragmentation of massive star forming cluster both in dust and molecular line emission. The Herschel satellite on the other hand will open up the wavelength range between 60 to 670 μm from space.
Both instruments will offer the star formation community unprecedented possibilities to study the formation of massive stars in great detail.
Before we can finally make use of the highly sought-after observing time with ALMA and Herschel, we should use the currently available instruments to prepare ourselves for the upcoming wealth of data, information and possibilities, since high mass star formation is still a highly obscured process, despite the vast progress being made over the last decade.
While for low mass star formation, an established formation scenario exists (André et al., 2000), several fundamentally different high mass star formation scenarios, most notably the theory of turbulent core formation (McKee & Tan, 2003) and the competitive accretion scenario (Bonnell & Bate, 2006), are being discussed. Many studies find evidence that high mass star formation proceeds similar to a modified version of low mass star formation, as is suggested by the turbulent core model. Simulations of fragmentation and molecular cloud development in a global gravitational collapse (Bonnell et al., 2001; Vázquez-Semadeni et al., 2008) on the other hand can reproduce the observed two-power law interstellar mass function and physical properties of observed massive star forming regions. We need more observational evidence to distinguish between the one or the other scenario and to classify evolutionary stages of massive star forming cores. Due to the observational challenges related to massive star formation, this is best done in large surveys and has been very successfully started in the northern hemisphere with the works of Sridharan et al. (2002) and Molinari et al. (2002) and their respective follow-up studies. The southern hemisphere however has not been studied in such a great detail yet, despite the fact that the upcoming Atacama Large Millimeter Array (ALMA) is located in the south.
In my thesis, I characterized a sample of potential high mass star forming regions by ob-

serving it with the new Atacama Pathfinder EXperiment (APEX) 12m telescope on Llano de Chajnantor in Chile, and in parts with the Australia Telescope Compact Array (ATCA). These observations were done between 86 and 810 GHz in the mm and sub-mm regime, where most of the high mass star forming activity can be observed.
A detailed summary of the results can be found at the end of each chapter, here I will summarize the main outcome of the study.

6.1.1 Three luminous southern hemisphere hot cores

A pilot study on three luminous, line rich hot cores, IRAS 12326−6245, 16060−5146 and 16065−5158, detected in the early stages of the survey was conducted to test the proposed observations with the APEX telescope. In addition to the continuum and line data obtained with APEX, the three sources were observed with ATCA. All three are luminous, massive objects. Comparison of the virial masses with the 870 μm continuum masses reveals them to likely be bound objects. The line profiles show signs of outflow activity, which is supported by the 4.5 μm emission from shocked gas that can be found in the Spitzer GLIMPSE images. 16065−5158 shows a particularly striking elongated object in the 4.5 μm images which seems to originate from the peak of the 870 μm continuum emission. Since 16065−5158 is neither associated with far infrared nor radio continuum emission and has a flatter density profile than the other two sources, it is a suitable candidate for a hot core at an early evolutionary stage. 12326−6245 and 16060−5146 are both associated with far infrared and radio continuum emission and are more centrally peaked in their density distribution than 16065−5158, which places them at a more evolved stage.
Their molecular spectra are rich in sulfur-bearing species and display a high abundance of oxygen-bearing species compared to the nitrogen-bearing species. This might be related to the dichotomy which is commonly seen in high resolution studies of hot cores. Seeing this disparity in a single dish beam might stem either from initial conditions that favored oxygen or more likely from the nitrogen-bearing species close to the central core having been already destroyed. 16060−5146 seems to have a highly complex velocity structure which becomes obvious in the double-peaked profiles observed in some of the lines.

6.1.2 Dust continuum survey

We carried out a 870 μm dust continuum survey of our sample with the new Large APEX BOlometer CAmera at APEX (LABOCA).
Physical parameters were derived from the dust emission in several ways to understand and minimize the influence of distance estimates on the results. It is important to keep in mind that when comparing sources in a non-distance limited sample, masses and densities should be analyzed within a fixed linear scale to avoid comparing physical properties on scales of clumps and clusters. Most of the sources seem to be located at their near distance and do not have a companion within 2 pc of the core, indicating that, at least considering the current single dish resolution, they are forming one massive core. On average, the objects in our sample seem to be more massive, dense and embedded than objects covered in comparable surveys, which was expected since they were chosen to be more luminous than sources in other

surveys. The masses and densities of our sources agree well with those predicted by simulations of non-turbulent, gravitationally collapsing molecular clouds (Vázquez-Semadeni et al., 2008). The sources observed in the outer Galaxy at large Galactocentric radii are less massive and dense, but do agree with the lower range of masses found in massive star forming surveys. At these large distances, we are observing on scales of cluster formation. We divided the sample into two subsamples, one radio-quiet without associated cm continuum emission and one radio-loud with cm emission. The radio-loud sources which already have associated UCHII regions are more massive, have higher luminosity-to-mass ratios and seem to concentrate more mass in a given radius. Comparing the luminosity-to-mass ratio of the two subsamples with evolutionary models does not support the hypothesis that the radio-loud and radio-quiet subsamples are at different evolutionary stages. Radial fits to the inner region of the intensity distribution point to a density profile $n \sim r^{-1.6\pm0.5}$, which is consistent with a singular isothermal sphere (Shu, 1977) described in low mass star formation. Most of the sources are located in regions of active on-going star formation within 0.1 pc of an 8.0 μm source.

6.1.3 Molecular line surveys

The molecular line observations obtained for the sample reveal that the cold extended envelopes are remarkably similar in chemical composition over a wide range of column densities and compare well with a number of intermediate mass objects and quiescent regions in the interstellar medium.

A statistical study of the line profiles revealed that the sample is dominated by infall motions. The sources are bound, with an average virial parameter $\alpha_{\rm vir}$ $\sim$1.4, which agrees well with the values predicted by the turbulent core model, while it is much higher than the value required to form massive stars in a competitive accretion scenario.

In our sample, we detected nine hot molecular cores, eight of which were analyzed in this work. The eight hot cores all show the same overabundance in oxygen-bearing species compared to nitrogen-bearing species. The hot cores in our sample are more massive, denser and more luminous than the averages from both the radio-loud and radio-quiet subsample. Combining this with the steep density profile, the hot cores observed in our sample can be tentatively placed in a transition stage between hot molecular core and UCHII region. Within the sample of eight hot cores, we believe that 16060$-$5146 and 12326$-$6245 are the most evolved. The parameters of the star forming hot cores were calculated in the framework of the turbulent core model. The accretion masses and star forming times agree well with those found in evolutionary models for massive star forming regions. Comparing the hot molecular cores with the evolutionary tracks showed that 30–50$\%$ of the core mass will end up in the final star, which is again consistent with the predictions made in the turbulent core model.

The comparison of the molecular line data with the physical conditions derived from dust continuum emission can, depending on the tracer used, show evidence both for a global collapse scenario and for the turbulent core scenario. No conclusion can however be reached to exclude one or the other.

6.2 Outlook

I was able to define the physical and chemical properties of a large sample of massive star forming regions and thus create a database of sources well suited to be studied with the high resolution capabilities of the ALMA interferometer. This work provides observational evidence which supports the idea that massive stars form through monolithic collapse of a bound core supported by turbulence. My work, however, produced also a number of findings that point towards the formation of massive stars as a result of global gravitational collapse instead of bound, turbulence-supported cores. In reality, massive star formation will most likely happen as a mixture of large scale flowing motions and turbulence supported collapse and it is our task, through high resolution studies and large scale surveys, to disentangle the different contributions.
In the following paragraphs, I will give a short overview over how some of the issues raised in this work should be observationally followed-up in the next few years.

6.2.1 Turbulent support or gravitational collapse?

One of the important issues that has to be addressed by observations is the question whether the formation of massive stars happens in an environment dominated by turbulence or in a competitive accretion scenario.
It is necessary to map the regions of massive star formation in a number of suitable infall tracers like HCO^+ and CS to study the spatial distribution of the infalling gas and disentangle contributions such as outflowing gas in the line profiles. This kind of study can be done either with large mapping arrays such as CHAMP$^+$ at APEX or HARP-B at the James Clark Maxwell Telescope (JCMT) or at even higher resolution with the Submillimeter Array (SMA).
Observing the sources at high resolution with the SMA (for those accessible from the northern hemisphere) or later with ALMA will reveal the grade of fragmentation in the clumps. Obtaining the fragmentation for a large sample of sources will be a straightforward way to answer the question whether the clumps form one or two massive cores as proposed by the turbulent core model or if they will form a number of lower mass cores.
Based on these observations, one can then derive the masses and spectral energy distributions (SEDs) of all the fragments. Once the association of all fragments to the main core has been established through line observations, this can provide us with an idea if the initial mass function (Kroupa, 2002) in these regions has been imposed on the clump during its formation (e.g. Krumholz, 2008) or if it will develop during the competitive accretion process (e.g. Bate & Bonnell, 2005; Dobbs et al., 2005). The modeling of the spectral energy distributions of a large number of sources, as is proposed here, will benefit from the use of tools like the new online SED model fitter (Robitaille et al., 2007; Molinari et al., 2008) that allows to fit a large grid of precomputed models of massive star forming evolution to the provided data.

6.2.2 Distance estimates

When studying statistical properties of a large sample of sources, it is still important to know the true distance of the sources. The distances we derive are kinematic distances

and for many of the sources, the near/far distance ambiguity could not be resolved. For those sources, it is important to resolve this ambiguity using the HI self-absorption method (Busfield et al., 2006). In this method, molecular line data of the sources are compared to HI spectra and the presence or absence of self-absorption with respect to the line velocity can indicate if the clump is located at its near or far distance. Our studies have shown that particularly the sources located at their far distance strongly influence the average properties of the sample as a whole, because they are more massive.

6.2.3 Chemical properties

The new sub-mm interferometers like the SMA, and ALMA in the future, give us the possibility to image the sources at high resolution and with a large bandwidth to probe many molecular lines simultaneously. It will be possible to disentangle the molecular contributions from components like the disks and outflows of the sources. There is evidence that the spatial distribution of the chemical species is linked to the evolutionary stages of the sources (Beuther et al., 2008b). Comparing the observational evidence with current chemical models (Garrod et al., 2008) will allow us to use the spatial occurance of certain molecules as chemical clocks and investigate grain surface reactions as a likely origin of complex organic species. Doing this kind of observations on a large number of sources will also provide a valuable database for the theorists who do the chemical modeling.

6.2.4 Stellar environment

Massive stars are thought to form exclusively in clusters and as this work has shown, the sources of our sample are located close to sites of active ongoing star formation as revealed through far-infrared Spitzer GLIMPSE data. It is an important complement to the studies of massive star formation in the sub-mm to observe their surroundings in the near-infrared, where the young massive stars are visible and jets as well as emission from the outflow cavity (Nürnberger et al., 2007) can be observed in the H_2 line. This can be done best using new instruments such as SINFONI (Spectrograph for INtegral Field Observations in the Near-Infrared) at the ESO Very Large Telescope (VLT). The near-infrared wavelengths are not only sensitive to the hot young stars but also give valuable insight into energetic phenomena through their H_2 line emission. Combining observations at these wavelengths with our sub-mm data, it is not only possible to study the cluster properties of the surrounding stars, but also can help us understand how the massive star forming site and the surrounding young cluster or OB association influence each other through feedback processes, as can be traced by On the cluster scale, the combination of high resolution sub-mm observations with the near-infrared data might help to identify where in a cluster the massive stars are formed, i.e. if they form preferentially at the centers or if the location of massive stars at or near the centers of clusters is due to dynamical mass segregation (Bonnell & Davies, 1998).

The field of massive star formation with its observational and theoretical complexity poses a challenge for observers and theorists alike. Yet we are in the fortunate situation to have a access to an unprecedented wealth of information both from superb current instruments, as well as from powerful numerical simulations. In the near future, this situation will

even be improved by the up-coming instruments opening up new wavelength ranges for us. This work has offered some constraints on the physical and chemical conditions in regions of massive star formation by observing a large number of sources. Evidence for massive star formation scenarios were proposed by putting the results in context with current theoretical models. In the future, databases of sources such as the one presented in this work will offer invaluable tools a) to analyze the detailed information provided by the new instruments in the context of the large scale evolutionary properties of the regions and b) to help theorists to improve and refine their simulations by comparison with a statistically significant number of observations.

Acknowledgments

I had the opportunity to write this thesis at the Max-Planck-Institut für Radioastronomie in the group of Prof. Karl Menten, who supported me and believed in me throughout the course of this work. Thank you!
I would like to thank my supervisors Friedrich Wyrowski and Peter Schilke for their ideas that led to this project, their continuous support and discussions and their endurance to provide countless corrections and comments on various aspects of my work.
A thank you goes to Prof. Kroupa who agreed to be the second referee of this work and to Prof. Hübel from nuclear physics and Prof. Langer from palaeontology for taking up the task to be the non-astronomy members on my committee.
Prof. Schmid-Burgk was kind enough to read through my dissertation and offer valuable comments and criticism. I would like to thank him and all the people who read parts of the manuscript for their time and effort.

During my work, I was supported by the Studienstiftung des Deutschen Volkes. I am grateful for a dissertation stipend, the mentoring and the many excellent events they offered. I acknowledge financial support for funding and travel support from Prof. Menten and the International Max-Planck Research School (IMPRS) for Astronomy and Astrophysics. Being member of the IMPRS gave me, among other things, the opportunity to take part in a number of very useful soft skill seminars and retreats. I would like to thank Eduardo and Gabi for their help in many organizational matters.

My work on the molecular line surveys would not have been possible without the people at CDMS and JPL creating and maintaining their spectroscopic databases and I would also like to thank Arnaud Belloche, who is taking care of implementing their results in the XCLASS database. This work has made much use of the ADS [1], SIMBAD [2] and the NASA/IPAC Infrared Science Archives [3].
I appreciate that Guido Kölsch in the computer department never tired of updating or fixing my laptop and hard disk.

Most of my observations were done at the APEX telescope. A big thank you goes to all the people who helped out with the hours and hours of observations, mostly Silvia Leurini, Arnaud Belloche, Sven Thorwirth, Frederic Schuller and Axel Weiss. I would like to express

[1] http://cdsads.u-strasbg.fr/
[2] http://simbad.u-strasbg.fr/simbad/
[3] http://irsa.ipac.caltech.edu/

my gratitude to everyone at the telescope for the job they are doing, particularly given the high altitude working conditions. The people at ATCA and the Australia Telescope National Facility deserve my thanks for letting me use some of their green time, helping me out with remote observations and for being so helpful and friendly during my visit to Australia. A special thank you goes to Steve, Nadia and Shari for being great companions during my marathon observing session in Narrabri in 2007.

In March 2007, I visited Helsinki University and was received warmly by Jorma Harju and Mika Juvela. Kiitos! I would also like to thank Malcolm Walmsley who provided many interesting suggestions regarding the line survey analysis in Chap. 5 and Sergio Molinari, who provided the data of the evolutionary models (Figs. 4.13 and 5.11).

During my stay at the Max-Planck Institut and as a member of IMPRS, I met too many nice people to mention all of them here, instead I would like to thank all of you for the great working atmosphere, particularly Maria, Edith Fingas, Anna and Kristina for all the help they provided. Many thanks go to Kosmas, Miguel, Maca, Laurentiu, Bérengère, Silvia, Thushara, Ed, Jens, Endrik Krügel, Dirk, Arnaud, Heiko, Fred, Sharmila, Claudia, Axel, Attila, Paola, Kazi, Lies and Peng. I had the pleasure to share my office with Hyunjoo, Yanett, Laura, Jan, Dorothea and Arturo – many thanks for all the fun times, the many discussions and plenty of chocolates!

My most heartfelt thank you goes to my family – my mother, brother and grandmother, who supported me with love and patience throughout the many years of my studies, and to my husband Leonidas, who always encouraged and supported me, particularly in the last few months.

Appendix A

A.1 Tables

Table A.1: Frequency setups for the sources from the inner Galaxy sample.

Source	RA (J2000)	Dec J(2000)	HCO^+ (4-3)	CH_3CN (16-15)	CH_3OH (6-5)	H_2CO (4-3)/(6-5)	CO (3-2)	CO (4-3)	CO (7-6)	$C^{17}O$ (3-2)
pilot study										
12326−6245	12:35:35.66	-63:02:28.0	x	x	x	x/x	x	x	x	x
16060−5146	16:09:52.37	-51:54:59.4	x	x	x	x/x	x	x	x	x
16065−5158	16:10:20.23	-52:06:08.3	x	x	x	x/x	x	x	x	x
14453−5912	14:49:07.37	-59:24:43.9	x	-	-	-	x	-	-	x
14498−5856	14:53:42.10	-59:08:53.5	x	-	-	-	x	-	-	x
15278−5620	15:31:45.41	-56:30:50.0	-	-	-	-	-	-	-	x
15394−5358	15:43:17.09	-54:07:18.1	x	-	-	-	x	-	-	x
15437−5343	15:47:32.09	-53:52:41.5	x	-	-	-	x	-	-	x
15557−5215	15:59:40.32	-52:23:32.3	x	-	-	-	x	-	-	x
16071−5142	16:10:59.16	-51:50:28.0	x	-	-	-	x	-	-	x
16076−5134	16:11:26.57	-51:41:56.8	-	-	-	-	-	-	-	x
16172−5028a	16:21:00.41	-50:35:21.1	-	-	-	-	-	-	-	x
16172−5028	16:21:02.66	-50:35:55.0	-	-	-	-	-	-	-	x
16175−5002	16:21:20.18	-50:09:48.6	-	-	-	-	-	-	-	x
16272−4837	16:30:58.42	-48:43:54.1	x	-	-	-	x	-	-	x
16351−4722	16:38:50.09	-47:28:01.6	x	-	-	-	x	-	-	x
16458−4512	16:49:30.12	-45:17:49.9	x	-	-	-	x	-	-	x
16484−4603	16:52:04.18	-46:08:26.5	x	-	-	-	x	-	-	x
16524−4300	16:56:02.54	-43:04:43.7	x	-	-	-	x	-	-	x
16562−3959	16:59:42.10	-40:03:44.6	x	-	-	-	x	-	-	x
17016−4124	17:05:10.90	-41:29:06.4	-	-	-	-	-	-	-	x
17136−3617	17:17:02.06	-36:20:57.1	x	-	-	-	x	-	-	x
17204−3636	17:23:50.88	-36:39:03.2	x	-	-	-	x	-	-	x

Continued on next page

Table A.1 – continued from previous page

Source	RA (J2000)	Dec J(2000)	HCO^+ (4-3)	CH_3CN (16-15)	CH_3OH (6-5)	H_2CO (4-3)/(6-5)	CO (3-2)	CO (4-3)	CO (7-6)	$C^{17}O$ (3-2)
17233−3606	17:26:42.98	-36:09:15.5	x	-	-	-	x	-	-	x
17258−3637	17:29:18.05	-36:40:21.0	x	-	-	-	x	-	-	x
17271−3439	17:30:26.18	-34:41:44.9	x	-	-	-	x	-	-	x
17269−3312	17:30:14.81	-33:14:48.8	x	-	-	-	x	-	-	x
17470−2853	17:50:14.52	-28:54:30.6	-	-	-	-	-	-	-	x
17589−2312	18:01:58.01	-23:12:36.7	x	-	-	-	x	-	-	x
18236−1205	18:26:25.80	-12:03:52.9	-	-	-	-	-	-	-	x
18319−0834	18:34:39.19	-08:31:25.7	-	-	-	-	-	-	-	x
18335−0711	18:36:12.58	-07:12:11.2	-	-	-	-	-	-	-	x

Source	RA (J2000)	Dec J(2000)	$V_{\rm lsr}$ $\rm km\,s^{-1}$	CH_3OH (6-5)	^{13}CO (3-2)	$C^{18}O$ (3-2)	CO (4-3)/(7-6)
06006+3015	06:03:54.3	+30:14:50.9	-9.0	x	x	-	-
06053−0622	06:07:47.9	-06:22:56.8	10.3	x	- x	-	x
06055+2039	06:08:35.4	+20:39:09.0	8.7	x	- x	x	x
06056+2131	06:08:40.3	+21:31:03.6	2.4	x	x	-	x
06058+2138	06:08:53.0	+21:38:08.7	3.3	x	x	-	x
06061+2151	06:09:06.5	+21:50:36.7	-1.1	x	x	x	x
06063+2040	06:09:21.3	+20:38:45.6	8.9	x	x	x	-
06068+2030	06:09:52.0	+20:29:53.3	8.4	x	-	-	-
06073+1249	06:10:12.3	+12:48:49.5	25.0	x	-	-	-
06099+1800	06:12:54.1	+17:59:22.0	7.6	x	x	x	x
06105+1756	06:13:26.4	+17:55:50.7	8.3	x	-	-	-
06114+1745	06:11:28.5	+17:45:46.2	7.9	x	x	-	-
06117+1350	06:14:36.1	+13:49:36.3	18.4	x	x	x	x
06155+2319	06:18:36.9	+23:18:39.3	-6.4	x	x	x	x
06581−0846	06:58:05.8	-08:47:03.2	40.0	x	-	-	-
06581−0848	06:58:01.8	-08:45:39.9	40.0	x	-	-	-
07029−1215	07:02:51.1	-12:14:20.5	12.0	x	x	-	-
09015−4843	09:03:14.8	-48:55:11.3	56.0	x	-	-	-

Table A.2: The sources from the outer Galaxy sample and their frequency setups.

ν (MHz)	Transition J
$C^{17}O$	
337060.513	3 – 2
337060.709	3 – 2
337060.831	3 – 2
337060.936	3 – 2
337060.988	3 – 2
337060.988	3 – 2
337061.050	3 – 2
337061.123	3 – 2
337061.214	3 – 2
337061.226	3 – 2
337061.471	3 – 2
337061.553	3 – 2
337061.951	3 – 2
337062.093	3 – 2

Table A.3: Identified features of CO

ν (MHz)	Transition J
$C^{34}S$	
337396.459	7 – 6
$C^{33}S$	
291485.935	6 – 5
HC_3N	
291068.427	32 – 31
337344.692	37 – 36
337825.275	37 – 36
436468.946	48 – 47

Table A.4: Identified features of CS and HC_3N

ν (MHz)	Transition J_{K_-,K_+}
$H^{13}CN$	
431659.775	$5_{0,0} - 4_{0,0}$
$HC^{15}N$	
430235.319	$5_{0,0} - 4_{0,0}$
DCN	
289644.917	$4_{0,0} - 3_{0,0}$

Table A.5: Identified features of HCN and DCN

ν (MHz)	Transition J_{K_-,K_+}
290623.405	$4_{0,4} - 3_{0,3}$
291237.767	$4_{2,3} - 3_{2,2}$
291384.264	$4_{3,1} - 3_{3,0}$
436586.486	$6_{2,5} - 5_{2,4}$
436751.038	$6_{5,2} - 5_{5,1}$
436751.040	$6_{5,1} - 5_{5,0}$
436957.489	$6_{4,2} - 5_{4,1}$
436957.311	$6_{4,3} - 5_{4,2}$
437235.976	$6_{3,3} - 5_{3,2}$

Table A.6: Identified features of H_2CO

ν (MHz)	Transition J_{K_-,K_+}
356734.2230	$4_{0,0} - 3_{0,0}$

Table A.7: Identified features of HCO^+

ν (MHz)	Transition J_{K_-,K_+}
348914.975	$28_{9,0} - 27_{9,9}$
349065.654	$28_{9,9} - 27_{9,8}$
336918.095	$26_{6,0} - 25_{6,9}$
338355.771	$27_{8,9} - 26_{8,8}$
337503.451	$27_{8,0} - 26_{8,9}$
350457.580	$28_{8,1} - 27_{8,0}$
338414.100	$27_{7,1} - 26_{7,0}$
350366.072	$26_{7,9} - 26_{5,2}$
338396.389	$27_{7,1} - 26_{7,0}$
337489.656	$27_{8,0} - 26_{8,9}$
349048.540	$28_{9,9} - 27_{9,8}$
348909.480	$28_{9,0} - 27_{9,9}$
338338.014	$27_{8,9} - 26_{8,8}$
350442.250	$28_{8,0} - 27_{8,0}$
336889.213	$26_{0,6} - 25_{0,5}$

Table A.8: Identified features of CH_3OCHO.

Table A.9: Identified features of CH_3OH

ν (MHz)	Transition J_{K_-,K_+}
CH_3OH(vt=0)	
289445.999	$21\ _{6,15}E - 22\ _{5,17}E$
289939.477	$6\ _{0,6}E - 5\ _{0,5}E$
290069.824	$6\ _{1,6}E - 5\ _{1,5}E$
290110.666	$6\ _{0,6}A^+ - 5\ _{0,5}A^+$
290117.815	$6\ _{5,1}E - 5\ _{5,0}E$
290138.890	$6\ _{5,2}E - 5\ _{5,1}E$
290145.090	$6\ _{5,1}A^- - 5\ _{5,0}A^-$
290145.090	$6\ _{5,2}A^+ - 5\ _{5,1}A^+$
290161.344	$6\ _{4,3}A^- - 5\ _{4,2}A^-$
290161.348	$6\ _{4,2}A^+ - 5\ _{4,1}A^+$
290162.430	$6\ _{4,3}E - 5\ _{4,2}E$
290183.210	$6\ _{4,2}E - 5\ _{4,1}E$
290184.690	$6\ _{2,5}A^- - 5\ _{2,4}A^-$
290189.510	$6\ _{3,4}A^+ - 5\ _{3,3}A^+$
290190.540	$6\ _{3,3}A^- - 5\ _{3,2}A^-$
290209.700	$6\ _{3,4}E - 5\ _{3,3}E$
290213.238	$6\ _{3,3}E - 5\ _{3,2}E$
290248.762	$6\ _{1,5}E - 5\ _{1,4}E$
290264.150	$6\ _{2,4}A^+ - 5\ _{2,3}A^+$
290307.376	$6\ _{2,5}E - 5\ _{2,4}E$
290307.643	$6\ _{2,4}E - 5\ _{2,3}E$
302369.900	$3\ _{0,3}E - 2\ _{1,2}E$
302913.146	$12\ _{0,12}A^+ - 11\ _{1,11}A^+$
303366.890	$1\ _{1,0}A^- - 1\ _{0,1}A^-$
336865.110	$12\ _{1,11}A^- - 12\ _{0,12}A^-$
337135.873	$3\ _{3,0}E - 4\ _{2,2}E$
337838.089	$20\ _{6,14}E - 21\ _{5,16}E$
338124.502	$7\ _{0,7}E - 6\ _{0,6}E$
338344.628	$7\ _{1,7}E - 6\ _{1,6}E$
338404.580	$7\ _{6,2}E - 6\ _{6,1}E$
338408.681	$7\ _{0,7}A^+ - 6\ _{0,6}A^+$
338430.933	$7\ _{6,1}E - 6\ _{6,0}E$
338442.344	$7\ _{6,1}A^+ - 6\ _{6,0}A^+$
338442.344	$7\ _{6,2}A^- - 6\ _{6,1}A^-$
338456.499	$7\ _{5,2}E - 6\ _{5,1}E$
338475.290	$7\ _{5,3}E - 6\ _{5,2}E$
338486.337	$7\ _{5,2}A^- - 6\ _{5,1}A^-$
338486.337	$7\ _{5,3}A^+ - 6\ _{5,2}A^+$
338504.099	$7\ _{4,4}E - 6\ _{4,3}E$

Continued on next page

Table A.9 – continued from previous page

ν (MHz)	Transition J_{K_-,K_+}
338512.627	$7\ _{4,4}A^- - 6\ _{4,3}A^-$
338512.639	$7\ _{4,3}A^+ - 6\ _{4,2}A^+$
338512.856	$7\ _{2,6}A^- - 6\ _{2,5}A^-$
338530.249	$7\ _{4,3}E - 6\ _{4,2}E$
338540.795	$7\ _{3,5}A^+ - 6\ _{3,4}A^+$
338543.204	$7\ _{3,4}A^- - 6\ _{3,3}A^-$
338559.928	$7\ _{3,5}E - 6\ _{3,4}E$
338583.195	$7\ _{3,4}E - 6\ _{3,3}E$
338614.999	$7\ _{1,6}E - 6\ _{1,5}E$
338639.939	$7\ _{2,5}A^+ - 6\ _{2,4}A^+$
338721.630	$7\ _{2,5}E - 6\ _{2,4}E$
338722.940	$7\ _{2,6}E - 6\ _{2,5}E$
349107.020	$14\ _{1,13}A^- - 14\ _{0,14}A^-$
350103.118	$1\ _{1,1}A^+ - 0\ _{0,0}A^+$
350285.485	$8\ _{2,6}A - 8\ _{1,8}A$
350421.585	$8\ _{1,7}A - 7\ _{2,5}A$
350687.730	$4\ _{0,4}E - 3\ _{1,3}E$
430207.126	$12\ _{2,11}E - 12\ _{1,12}E$
431356.366	$9\ _{1,9}A^+ - 8\ _{1,8}A^+$
CH_3OH(vt=1)	
289355.020	$6\ _{3,4}E - 5\ _{3,3}E$
289402.490	$6\ _{2,4}E - 5\ _{2,3}E$
289414.030	$6\ _{2,4}A^+ - 5\ _{2,3}A^+$
289415.043	$6\ _{5,2}E - 5\ _{5,1}E$
289416.391	$6\ _{4,2}E - 5\ _{4,1}E$
289420.240	$6\ _{2,5}A^- - 5\ _{2,4}A^-$
289423.499	$6\ _{5,1}E - 5\ _{5,0}E$
289427.600	$6\ _{1,6}E - 5\ _{1,5}E$
289428.212	$6\ _{4,2}A^+ - 5\ _{4,1}A^+$
289428.212	$6\ _{4,3}A^- - 5\ _{4,2}A^-$
289429.140	$6\ _{3,3}A^- - 5\ _{3,2}A^-$
289429.140	$6\ _{3,4}A^+ - 5\ _{3,3}A^+$
289429.756	$6\ _{0,6}E - 5\ _{0,5}E$
289443.541	$6\ _{2,5}E - 5\ _{2,4}E$
289475.610	$6\ _{1,5}E - 5\ _{1,4}E$
289511.110	$6\ _{0,6}A^+ - 5\ _{0,5}A^+$
289710.460	$6\ _{1,5}A^- - 5\ _{1,4}A^-$
337297.439	$7\ _{1,7}A^+ - 6\ _{1,6}A^+$
337463.671	$7\ _{6,1}A^+ - 6\ _{6,0}A^+$
337463.671	$7\ _{6,2}A^- - 6\ _{6,1}A^-$
337490.523	$7\ _{6,2}E - 6\ _{6,1}E$

Continued on next page

Table A.9 – continued from previous page

ν (MHz)	Transition J_{K_-,K_+}
337519.067	$7\ _{3,5}E - 6\ _{3,4}E$
337546.048	$7\ _{5,2}A^- - 6\ _{5,1}A^-$
337546.048	$7\ _{5,3}A^+ - 6\ _{5,2}A^+$
337581.663	$7\ _{4,4}E - 6\ _{4,3}E$
337605.255	$7\ _{2,5}E - 6\ _{2,4}E$
337610.580	$7\ _{6,1}E - 6\ _{6,0}E$
337610.624	$7\ _{3,4}E - 6\ _{3,3}E$
337625.679	$7\ _{2,5}A^+ - 6\ _{2,4}A^+$
337635.655	$7\ _{2,6}A^- - 6\ _{2,5}A^-$
337642.365	$7\ _{1,7}E - 6\ _{1,6}E$
337643.864	$7\ _{0,7}E - 6\ _{0,6}E$
337648.167	$7\ _{5,3}E - 6\ _{5,2}E$
337655.204	$7\ _{3,4}A^- - 6\ _{3,3}A^-$
337655.204	$7\ _{3,5}A^+ - 6\ _{3,4}A^+$
337671.194	$7\ _{2,6}E - 6\ _{2,5}E$
337685.490	$7\ _{4,3}A^+ - 6\ _{4,2}A^+$
337685.490	$7\ _{4,4}A^- - 6\ _{4,3}A^-$
337685.490	$7\ _{5,2}E - 6\ _{5,1}E$
337707.547	$7\ _{1,6}E - 6\ _{1,5}E$
337748.783	$7\ _{0,7}A^+ - 6\ _{0,6}A^+$
337969.414	$7\ _{1,6}A^- - 6\ _{1,5}A^-$
350287.710	$15\ _{3,13}E - 16\ _{4,13}E$

ν (MHz)	Transition J_{K_-,K_+}
SO_2	
301896.629	$19_{2,8} - 19_{1,9}$
338611.810	$20_{1,9} - 19_{2,8}$
338305.993	$18_{4,4} - 18_{3,5}$
430228.649	$24_{0,4} - 23_{1,3}$
430232.313	$21_{2,0} - 20_{1,9}$
430347.559	$26_{5,1} - 26_{4,2}$
$^{34}SO_2$	
338320.356	$13_{2,2} - 12_{1,1}$

Table A.10: Identified features of SO_2

ν (MHz)	Transition N_J;J,F
SO	
337197.845	$8_7 - 7_6$
337198.022	$8_7 - 7_6$
337198.620	$8_7 - 7_6$
337199.371	$8_7 - 7_6$
430339.544	$10_{10} - 9_9$
^{34}SO	
290562.238	$7_6 - 6_5$
337580.147	$8_8 - 7_7$

Table A.11: Identified features of SO

ν (MHz)	Transition J_{K_-,K_+}
338138.120	$35_{5,0} - 36_{3,3}$
348991.444	$37_{1,6} - 36_{1,5}$
338447.690	$37_{0,7} - 36_{0,6}$
338139.368	$45_{3,3} - 45_{1,4}$
338213.505	$37_{1,7} - 36_{1,6}$
337050.895	$35_{3,2} - 34_{3,1}$

Table A.12: Identified features of CH_2CHCN

ν (MHz)	Transition J_{K_-,K_+}
337420.925	$21_{2,9} - 20_{3,8}$
337421.340	$21_{2,9} - 20_{3,8}$
337421.754	$21_{2,9} - 20_{3,8}$
337421.755	$21_{2,9} - 20_{3,8}$
337708.629	$31_{2,0} - 31_{1,1}$
337708.630	$31_{2,0} - 31_{1,1}$
337720.213	$31_{2,0} - 31_{1,1}$
337722.337	$7_{4,4} - 6_{3,3}$
337723.014	$7_{4,4} - 6_{3,3}$
337730.717	$7_{4,4} - 6_{3,3}$
337731.903	$7_{4,3} - 6_{3,3}$
337732.197	$7_{4,3} - 6_{3,3}$
337770.599	$7_{4,4} - 6_{3,4}$
337778.008	$7_{4,4} - 6_{3,4}$
337779.488	$7_{4,3} - 6_{3,4}$
337787.190	$7_{4,3} - 6_{3,4}$
337787.867	$7_{4,3} - 6_{3,4}$
337790.105	$7_{4,3} - 6_{3,4}$
349794.210	$16_{2,4} - 17_{1,7}$
349794.210	$16_{2,5} - 17_{1,6}$
349796.590	$16_{2,4} - 17_{1,6}$
349797.680	$16_{2,5} - 17_{1,7}$
349798.971	$16_{2,4} - 17_{1,6}$
349801.150	$16_{2,5} - 17_{1,7}$
349802.998	$11_{2,9} - 10_{1,0}$
349803.000	$11_{2,9} - 10_{1,0}$
349806.089	$11_{2,9} - 10_{1,0}$
349809.179	$11_{2,9} - 10_{1,0}$

Table A.13: Identified features of CH_3OCH_3

Table A.14: Identified features of CH_3CN

ν (MHz)	Transition $J_{K-,K+}$
CH_3CN(vt=0)	
349024.210	$19_8 - 18_8$
349024.918	$19_8 - 18_8$
349024.983	$19_8 - 18_8$
349025.006	$19_8 - 18_8$
349025.009	$19_8 - 18_8$
349025.691	$19_8 - 18_8$
349124.335	$19_7 - 18_7$
349125.249	$19_7 - 18_7$
349125.298	$19_7 - 18_7$
349125.315	$19_7 - 18_7$
349125.319	$19_7 - 18_7$
349126.212	$19_7 - 18_7$
349211.193	$19_6 - 18_6$
349212.285	$19_6 - 18_6$
349212.321	$19_6 - 18_6$
349212.332	$19_6 - 18_6$
349212.338	$19_6 - 18_6$
349213.413	$19_6 - 18_6$
349284.748	$19_5 - 18_5$
349285.991	$19_5 - 18_5$
349286.016	$19_5 - 18_5$
349286.022	$19_5 - 18_5$
349286.029	$19_5 - 18_5$
349287.259	$19_5 - 18_5$
349344.971	$19_4 - 18_4$
349346.337	$19_4 - 18_4$
349346.353	$19_4 - 18_4$
349346.356	$19_4 - 18_4$
349346.363	$19_4 - 18_4$
349347.719	$19_4 - 18_4$
349391.836	$19_3 - 18_3$
349393.299	$19_3 - 18_3$
349393.307	$19_3 - 18_3$
349393.307	$19_3 - 18_3$
349393.315	$19_3 - 18_3$
349394.770	$19_3 - 18_3$
349425.326	$19_2 - 18_2$
349426.857	$19_2 - 18_2$
349426.858	$19_2 - 18_2$

Continued on next page

Table A.14 – continued from previous page

ν (MHz)	Transition J_{K_-,K_+}
349426.860	$19_2 - 18_2$
349426.866	$19_2 - 18_2$
349428.391	$19_2 - 18_2$
349445.425	$19_1 - 18_1$
349446.994	$19_1 - 18_1$
349446.997	$19_1 - 18_1$
349446.997	$19_1 - 18_1$
349447.003	$19_1 - 18_1$
349448.569	$19_1 - 18_1$
349452.126	$19_0 - 18_0$
350166.558	$19_1 - 18_1$
350168.128	$19_1 - 18_1$
350168.129	$19_1 - 18_1$
350168.133	$19_1 - 18_1$
350168.216	$19_1 - 18_1$
350169.787	$19_1 - 18_1$
350443.301	$19_0 - 18_0$
350444.883	$19_0 - 18_0$
350444.885	$19_0 - 18_0$
350444.887	$19_0 - 18_0$
350444.971	$19_0 - 18_0$
350446.555	$19_0 - 18_0$
350550.902	$19_2 - 18_2$
350552.431	$19_2 - 18_2$
350552.435	$19_2 - 18_2$
350552.439	$19_2 - 18_2$
350552.520	$19_2 - 18_2$
350554.050	$19_2 - 18_2$

ν (MHz)	Transition J_{K_-,K_+}
HNCO	
350333.346	$16_{1,16} - 15_{1,15}$
350333.293	$16_{1,16} - 15_{1,15}$
350332.481	$16_{1,16} - 15_{1,15}$
350333.344	$16_{1,16} - 15_{1,15}$
350333.347	$16_{1,16} - 15_{1,15}$
350334.158	$16_{1,16} - 15_{1,15}$

Table A.15: transitions of HNCO

ν (MHz)	Transition J
290452.224	17–16
290479.904	17–16
290496.516	17–16
290502.054	17–16

Table A.16: Identified features of CH_3CCH

ν (MHz)	Transition N,J,F
349337.741	$4,\frac{9}{2},\frac{9}{2} - 3,\frac{7}{2},\frac{7}{2}$
349339.067	$4,\frac{9}{2},\frac{7}{2} - 3,\frac{7}{2},\frac{5}{2}$
349399.342	$4,\frac{7}{2},\frac{7}{2} - 3,\frac{5}{2},\frac{5}{2}$
349400.692	$4,\frac{7}{2},\frac{5}{2} - 3,\frac{5}{2},\frac{3}{2}$
436660.999	$5,\frac{11}{2},\frac{11}{2} - 4,\frac{9}{2},\frac{9}{2}$
436661.893	$5,\frac{11}{2},\frac{9}{2} - 4,\frac{9}{2},\frac{7}{2}$
436723.078	$5,\frac{9}{2},\frac{9}{2} - 4,\frac{7}{2},\frac{7}{2}$
436723.915	$5,\frac{9}{2},\frac{7}{2} - 4,\frac{7}{2},\frac{5}{2}$

Table A.17: Identified features of CCH

ν (MHz)	Transition J_{K_-,K_+}
337727.095	$19_{7,2} - 19_{6,3}$
337747.000	$19_{7,3} - 19_{6,4}$

Table A.18: Identified features of C_2H_5OH

ν (MHz)	Transition J_{K_-,K_+}
C_2H_5CN(v=0)	
290251.693	$32_{4,8} - 31_{4,7}$
337347.584	$38_{3,6} - 37_{3,5}$
337441.720	$13_{6,7} - 14_{4,0}$
337445.861	$37_{4,3} - 36_{4,2}$
337515.901	$52_{8,5} - 52_{7,6}$
338142.851	$37_{3,4} - 36_{3,3}$
338278.145	$35_{2,3} - 34_{2,2}$
349379.897	$39_{2,7} - 38_{2,6}$
349379.897	$39_{2,8} - 38_{2,7}$
349392.335	$39_{1,8} - 38_{1,7}$
349392.335	$39_{1,9} - 38_{1,8}$
349396.195	$39_{3,6} - 38_{3,5}$
349396.195	$39_{3,7} - 38_{3,6}$
349442.939	$39_{0,0} - 38_{0,9}$
349442.939	$39_{0,9} - 38_{0,8}$
349547.007	$39_{9,1} - 38_{9,0}$
349547.024	$39_{9,0} - 38_{9,9}$
349730.780	$39_{8,2} - 38_{8,1}$
349731.298	$39_{8,1} - 38_{8,0}$
349796.027	$39_{4,6} - 38_{4,5}$
350139.636	$41_{1,1} - 40_{1,0}$
350145.088	$41_{0,1} - 40_{0,0}$
350684.959	$45_{7,8} - 46_{4,3}$
350687.840	$39_{6,3} - 38_{6,2}$
C_2H_5CN(v=1)	
349790.242	$30_{3,8} - 29_{2,7}$
349791.092	$30_{2,8} - 29_{3,7}$
350685.177	$31_{8,3} - 31_{8,3}$

Table A.19: Identified features of C_2H_5CN

Frequency (MHz)	Transition	Velocity v km/s	δ (v) km/s	$\int T_{mB}\Delta v$ K km/s	$\delta\int T_{mB}\Delta v$ K km/s	Δv km/s	δ (Δv)
289939.477	$6_{0,6}$E-$5_{0,5}$E	-90.7	0.1	17.1	0.3	10.8	0.2
290069.824	$6_{1,6}$E-$5_{1,5}$E	-91.0	0.0	21.0	0.2	9.5	0.1
290110.666	$6_{0,6}A^+$-$5_{0,5}A^+$	-91.1	0.1	22.1	0.6	9.0	0.2
290117.815	$6_{5,1}$E-$5_{5,0}$E	-86.9	0.9	7.2	1.3	16.2	1.2
290248.762	$6_{1,5}$E-$5_{1,4}$E	-91.2	0.1	16.7	0.3	11.6	0.3
290264.150	$6_{2,4}A^+$-$5_{2,3}A^+$	-89.6	0.2	11.2	0.3	14.9	0.5
338124.502	$7_{0,7}$E-$6_{0,6}$E	-91.0	0.1	10.0	0.1	9.9	0.6
338344.628	$7_{1,7}$E-$6_{1,6}$E	-91.3	0.0	10.0	0.0	10.8	0.8
338614.999	$7_{1,6}$E-$6_{1,5}$E	-92.0	0.1	20.4	1.2	9.8	0.3
338639.939	$7_{2,5}$A-$6_{2,4}$A	-92.0	0.1	29.8	0.4	10.5	0.2

Table A.20: Line Parameters for CH_3OH in 16060-5146

Frequency (MHz)	Transition	Velocity v km/s	δ (v) km/s	$\int T_{\rm mB}\Delta v$ K km/s	$\delta\int T_{\rm mB}\Delta v$ K km/s	Δv km/s	δ (Δv) km/s
290264.150	$6_{2,4}A^+$-$5_{2,3}A^+$	-39.1	0.1	7.4	7.4	6.2	0.3
290248.762	$6_{1,5}$E-$5_{1,4}$E	-39.3	0.0	7.6	7.6	6.6	0.4
290209.700	$6_{3,4}$E-$5_{3,3}$E	-39.6	0.0	7.6	7.6	5.8	0.3
290213.238	$6_{3,3}$E-$5_{3,2}$E	-39.2	1.5	12.0	12.0	6.3	0.3
290145.090	$6_{5,1}A^-$-$5_{5,0}A^-$	-39.2	1.5	12.0	12.0	6.3	0.3
290138.890	$6_{5,2}$E-$5_{5,1}$E	-39.6	0.0	7.6	7.6	5.8	0.3
290117.815	$6_{5,1}$E-$5_{5,0}$E	-39.2	1.5	12.0	12.0	6.3	0.3
290110.666	$6_{0,6}$A-$5_{0,5}$A	-39.2	1.5	12.0	12.0	6.3	0.3
290069.824	$6_{1,6}$E-$5_{1,5}$E	-40.2	0.1	1.6	1.6	4.2	0.3
289939.477	$6_{0,6}$E-$5_{0,5}$E	-39.2	0.0	18.0	18.0	5.8	0.0
337838.089	$20_{6,14}$E-$21_{5,16}$E	-37.1	0.4	3.0	3.0	11.8	1.6
338124.502	$7_{0,7}$E-$6_{0,6}$E	-39.3	0.0	16.8	16.8	6.2	0.1
338344.628	$7_{1,7}$E-$6_{1,6}$E	-39.4	0.0	21.5	21.4	6.2	0.1
338408.681	$7_{0,7}$A-$6_{0,6}$A	-39.4	0.0	22.1	22.1	6.2	0.1
338430.933	$7_{6,1}$E-$6_{6,0}$E	-39.7	0.1	1.5	1.5	4.2	0.3
338442.344	$7_{6,1}A^+$-$6_{6,0}A^+$	-39.8	0.4	2.1	2.1	4.8	1.0
338456.499	$7_{5,2}$E-$6_{5,1}$E	-40.00	0.2	2.5	2.5	4.6	0.4
338475.290	$7_{5,3}$E-$6_{5,2}$E	-39.6	0.1	3.5	3.5	5.8	0.3
338504.099	$7_{4,4}$E-$6_{4,3}$E	-40.9	0.8	7.7	7.7	8.2	1.7
338530.249	$7_{4,3}$E-$6_{4,2}$E	-39.8	0.2	5.3	5.3	6.1	0.4
338559.928	$7_{3,5}$E-$6_{3,4}$E	-39.8	0.1	7.5	7.5	5.8	0.2
338583.195	$7_{3,4}$E-$6_{3,3}$E	-39.5	0.1	8.7	8.7	6.1	0.1
338614.999	$7_{1,6}$E-$6_{1,5}$E	-38.3	0.0	27.6	27.6	7.6	0.1
338639.939	$7_{2,5}A^+$-$6_{2,4}A^+$	-39.3	0.1	10.7	10.7	6.4	0.2
$CH_3OH(v_t=1)$							
337969.414	$7_{1,6}A^-$-$6_{1,5}A^-$,vt=1	-39.6	0.1	1.3	1.3	4.4	0.3
337625.679	$7_{2,5}A^+$-$6_{2,4}A^+$	-39.2	0.0	17.0	17.1	6.0	0.0
337655.204	$7_{3,5}A^+$-$6_{3,4}A^+$	-39.1	0.0	12.0	12.0	5.9	0.1
337671.194	$7_{2,6}$E-$6_{2,5}$E	-39.7	0.1	1.2	1.2	3.7	0.2
337685.490	$7_{5,2}$E-$6_{5,1}$E	-39.9	0.3	1.0	1.0	4.1	0.7
337685.490	$7_{4,4}A^-$-$6_{4,3}A^-$	-39.9	0.1	0.6	0.6	4.0	0.3
337685.490	$7_{4,3}A^+$-$6_{4,2}A^+$	-39.9	0.2	0.7	0.7	3.5	0.3
337707.547	$7_{1,6}$E-$6_{1,5}$E	-39.8	0.3	0.7	0.7	4.2	0.5
337748.783	$7_{0,7}$A-$6_{0,6}$A	-39.7	0.3	0.7	0.7	3.9	0.5

Table A.21: Line Parameters for CH_3OH in 12326−6245

Frequency (MHz)	Transition	Velocity v km/s	δ (v) km/s	$\int T_{mB}\Delta v$ K km/s	$\delta\int T_{mB}\Delta v$ K km/s	Δv km/s	δ (Δv)
290248.762	$6_{1,5}$E-$5_{1,4}$E,vt=0	−61.9	0.2	9.8	9.8	7.9	0.4
290264.150	$6_{2,4}A^+$-$5_{2,3}A^+$	−60.8	0.1	5.4	5.4	7.7	0.1
290117.815	$6_{5,1}$E-$5_{5,0}$E	−61.8	0.1	5.9	5.8	9.5	0.7
290110.666	$6_{0,6}A^+$-$5_{0,5}A^+$	−62.1	0.0	5.9	5.8	6.4	0.3
290069.824	$6_{1,6}$E-$5_{1,5}$E	−62.1	0.0	2.6	2.6	8.8	0.3
289939.477	$6_{0,6}$E-$5_{0,5}$E	−62.1	0.0	15.1	15.1	6.7	0.1
338124.502	$7_{0,7}$E-$6_{0,6}$E	−62.0	0.0	14.1	14.1	6.9	0.1
338344.628	$7_{1,7}$E-$6_{1,6}$E	−61.7	0.1	11.4	11.0	7.6	0.1
338408.681	$7_{0,7}A^+$-$6_{0,6}A^+$	−62.0	0.1	12.5	12.5	7.1	0.2
338430.933	$7_{6,1}$E-$6_{6,0}$E	−62.2	0.0	18.0	18.0	6.9	0.1
338442.344	$7_{6,1}$A-$6_{6,0}$A	−61.9	0.2	23.1	23.1	7.7	0.4
338456.499	$7_{5,2}$E-$6_{5,1}$E	−58.9	0.1	1.0	1.0	2.8	0.3
338475.290	$7_{5,3}$E-$6_{5,2}$E	−61.6	0.5	2.3	2.3	6.7	1.2
338486.377	$7_{5,2}A^-$-$6_{5,1}A^-$	−60.6	0.4	3.1	3.1	6.5	1.1
338486.377	$7_{5,3}A^+$-$6_{5,2}A^+$	−60.5	0.3	2.7	2.7	4.7	0.5
338504.099	$7_{4,4}$E-$6_{4,3}$E	−63.2	0.4	9.5	9.5	13.7	1.0
338530.249	$7_{4,3}$E-$6_{4,2}$E	−59.7	0.8	4.5	4.5	6.4	2.9
338559.928	$7_{3,5}$E-$6_{3,4}$E	−60.2	0.1	6.4	6.4	6.7	0.3
338583.195	$7_{3,4}$E-$6_{3,3}$E	−61.8	0.3	5.3	5.3	6.0	0.5
338614.999	$7_{1,6}$E-$6_{1,5}$E	−61.9	0.0	10.2	10.2	9.1	0.1
338639.939	$7_{2,5}A^+$-$6_{2,4}A^+$	−60.4	0.1	22.3	22.3	9.4	0.1
338722.940	$7_{2,6}$E-$6_{2,5}$E	−61.6	0.1	8.6	8.7	7.8	0.2

Table A.22: Line Parameters for CH_3OH in 16065-5158

Frequency (MHz)	Transition	Velocity v km/s	δ (v) km/s	$\int T_{mB}\Delta v$ K km/s	$\delta\int T_{mB}\Delta v$ K km/s	Δv km/s	δ (Δv)
294098.900	16_6-15_6	-62.4	0.3	7.9	0.3	13.304	0.730
294098.900	16_6-15_6	-59.6	0.2	9.0	0.4	12.835	0.796
294098.900	16_6-15_6	-60.9	0.1	14.2	0.4	8.873	0.321
294161.025	16_5-15_5	-61.2	0.1	11.9	0.3	8.533	0.252
294161.025	16_5-15_5	-61.3	0.4	9.5	0.9	8.280	0.994
294161.025	16_5-15_5	-58.5	0.1	20.1	0.2	12.159	0.131
294211.856	16_4-15_4	-62.0	0.4	14.8	0.8	18.8	1.3
294211.856	16_4-15_4	-61.2	0.3	3.5	0.3	8.8	0.8
294251.472	16_3-15_3	-62.5	0.4	4.2	0.3	13.0	1.3

Table A.23: Line Parameters for CH_3CN in 16065-5158

Frequency (MHz)	Transition	Velocity v km/s	δ (v) km/s	$\int T_{mB}\Delta v$ K km/s	$\delta\int T_{mB}\Delta v$ K km/s	Δv km/s	δ (Δv)
294098.818	16_6-15_6	-40.1	0.4	1.4	0.2	7.9	1.2
294098.900	16_6-15_6	-40.2	0.9	1.1	0.4	5.5	1.4
294098.902	16_6-15_6	-39.8	0.1	2.3	0.1	5.8	0.3
294161.025	16_5-15_5	-40.0	0.1	4.3	0.1	5.6	0.1
294161.025	16_5-15_5	-39.9	0.3	3.6	0.4	5.5	0.8
294161.025	16_5-15_5	-41.1	0.1	10.4	0.2	7.0	0.2
294211.890	16_4-15_4	-40.4	0.4	3.6	0.7	5.4	0.7
294211.890	16_4-15_4	-40.2	0.3	3.4	0.4	5.4	0.5
294251.456	16_3-15_3	-40.0	0.1	2.9	0.1	5.5	0.2
294251.456	16_3-15_3	-40.3	0.1	3.8	0.1	6.1	0.3
294251.456	16_3-15_3	-40.5	0.2	1.7	0.1	4.7	0.4
294279.757	16_2-15_2	-40.4	0.4	1.1	0.2	5.7	1.2

Table A.24: Line Parameters for CH_3CN in 12326-6245

Frequency (MHz)	Transition	Velocity v km/s	δ (v) km/s	$\int T_{mB}\Delta v$ K km/s	$\delta\int T_{mB}\Delta v$ K km/s	Δv km/s	δ (Δv)
294098.900	16_6-15_6	-92.8	0.6	3.8	0.3	16.7	1.3
294098.900	16_6-15_6	-87.9	0.5	1.8	0.2	9.1	1.5
294098.900	16_6-15_6	-85.6	0.5	1.8	0.2	9.1	1.4
294159.883	16_5-15_5	-92.2	0.6	2.6	0.2	12.4	1.2
294162.124	16_5-15_5	-92.8	0.5	5.9	0.4	15.2	1.1
294211.856	16_4-15_4	-63.9	0.5	5.9	0.4	15.1	1.1
294211.856	16_4-15_4	-40.9	0.4	5.9	0.3	15.2	1.0
294251.472	16_3-15_3	-90.0	0.3	8.9	0.5	13.6	0.9
294251.472	16_3-15_3	-94.1	0.5	7.1	0.4	19.2	1.5

Table A.25: Line Parameters for CH_3CN in 16060-5146

Frequency (MHz)	Transition	Velocity v km/s	δ (v) km/s	$\int T_{mB}\Delta v$ K km/s	Δv km/s	δ (Δv)
290623.405	$4_{0,4}$-$3_{0,3}$	-63.4	0.1	40.4	10.1	0.1
291237.767	$4_{2,3}$-$3_{2,2}$	-62.4	0.1	10.5	7.1	0.3
436586.486	$6_{2,5}$-$5_{2,4}$	-61.1	0.2	23.3	9.2	0.4
436957.311	$6_{4,3}$-$5_{4,2}$	-61.7	0.4	11.4	8.3	1.1
436957.311	$6_{4,3}$-$5_{4,2}$	-62.3	0.6	23.6	13.4	1.8
437199.5	$6_{3,4}$-$5_{3,3}$	-61.9	0.4	34.2	12.2	1.6
437235.976	$6_{3,3}$-$5_{3,2}$	-61.5	0.4	37.6	11.6	1.3

Table A.26: Line Parameters for H_2CO in 16065-5158

Frequency (MHz)	Transition	Velocity v km/s	δ (v) km/s	$\int T_{mB}\Delta v$ K km/s	$\delta\int T_{mB}\Delta v$ K km/s	Δv km/s	δ (Δv)
290623.405	$4_{0,4}$-$3_{0,3}$	-39.6	0.0	23.0	0.2	6.1	0.0
291380.5	$4_{3,2}$-$3_{3,1}$	-39.6	0.1	8.7	0.1	7.1	0.2
291384.264	$4_{3,1}$-$3_{3,0}$	-43.4	0.0	8.7	0.0	7.1	0.2
291237.767	$4_{2,3}$-$3_{2,2}$	-39.8	0.0	12.6	0.1	6.3	0.1
436957.311	$6_{4,3}$-$5_{4,2}$	-41.3	0.6	30.2	1.9	23.5	2.0
437199.5	$6_{3,4}$-$5_{3,3}$	-39.8	0.1	22.5	0.9	6.8	0.3
437235.976	$6_{3,3}$-$5_{3,2}$	-39.4	0.1	25.8	0.9	6.9	0.3

Table A.27: Line Parameters for H_2CO in 12326-6245

Frequency (MHz)	Transition	Velocity v km/s	δ (v) km/s	$\int T_{mB}\Delta v$ K km/s	$\delta\int T_{mB}\Delta v$ K km/s	Δv km/s	δ (Δv)
290623.405	$4_{0,4}$-$3_{0,4}$	-92.1	0.0	26.7	26.7	9.4	0.1
291380.5	$4_{3,2}$-$3_{3,1}$	-92.1	0.1	11.0	11.0	13.0	0.5
291384.264	$4_{3,1}$-$3_{3,0}$	-96.0	0.0	11.0	11.0	9.7	0.2
291237.767	$4_{2,3}$-$3_{2,2}$	-92.0	0.1	15.8	15.9	10.8	0.1
436586.486	$6_{2,5}$-$5_{2,4}$	-91.6	0.3	15.6	15.6	11.9	0.6
436957.311	$6_{4,3}$-$5_{4,2}$	-93.8	0.3	12.1	12.1	13.0	0.8
437199.5	$6_{3,4}$-$5_{3,3}$	-93.4	0.5	15.7	15.7	11.7	1.5
437235.976	$6_{3,3}$-$5_{3,2}$	-93.7	0.3	14.1	14.1	11.0	0.8

Table A.28: Line Parameters for H_2CO in 16060-5146

Table A.29: Sources observed with LABOCA at 870 μm in the inner Galaxy sample. a) f: field, d:diffuse emission, e: extended,non-diffuse emission,bs: bowshock, c: cavity, b: bubble.

Source	R.A. (J2000)	Dec. (J2000)	l	b	$d_{\rm near}$ kpc	$d_{\rm far}$ kpc	$R_{\rm G}$ kpc	Mult. (2pc)	Mult. (field)	8μm Morph[a]. (8μm)	multicolumn1crms (mJy/beam)
08448−4343	8:46:33.4	-43:54:32.2	263.77	-0.43	1.0		8.7	1	1	-	150
12326−6245	12:35:35.1	-63:02:29.0	301.14	-0.22	4.4		7.3	1	1	f,d	100
12383−6128	12:41:19.2	-61:44:38.8	301.73	1.10	4.5		7.2	3	4	f,d	130
13079−6218	13:11:13.3	-62:34:40.6	305.21	0.21	4.9		6.9	1	4	c,bs	140
13134−6242	13:16:43.3	-62:58:31.0	305.80	-0.24	2.9	7.0	7.2	2	3	f	150
14164−6028	14:20: 7.9	-60:42: 2.5	313.58	0.33	3.5	8.2	6.6	1	1	f	150
14206−6151	14:24:22.8	-62:05:23.3	313.58	-1.15	3.9	7.8	6.5	1	2	f	140
14453−5912	14:49: 7.3	-59:24:45.9	317.41	0.11	2.9	9.7	6.7	1	2	ridge	160
14498−5856	14:53:42.5	-59:08:56.3	318.05	0.09	3.5	9.1	6.3	1	1	f	130
15278−5620	15:31:45.4	-56:30:54.9	323.74	-0.26	3.4		6.1	2	2	b	160
15394−5358	15:43:16.5	-54:07:20.8	326.47	0.70	11.4	11.3	6.4	1	1	f	170
15437−5343	15:47:32.7	-53:52:40.4	327.12	0.51	5.2	9.0	5.0	1	4	f	70
15557−5215	15:59:40.3	-52:23:29.9	329.47	0.50	4.3	10.4	5.3	2	4	b	50
16060−5146	16:09:52.6	-51:54:56.2	330.95	-0.18	5.4	9.4	4.6	1	4	f,d	50
16065−5158	16:10:19.8	-52:06:10.0	330.88	-0.37	4.0	10.8	5.4	2	6	c	50
16071−5142	16:10:59.5	-51:50:23.9	331.13	-0.24	5.2		4.7	1	5	f	50
16076−5134	16:11:26.9	-51:41:53.0	331.28	-0.19	5.2		4.7	1	4	f,d	50
16172−5028	16:21: 2.6	-50:35:13.2	333.13	-0.43	3.6		5.5	3	10	f,d	80
16175−5002	16:21:20.1	-50:09:49.1	333.47	-0.16	3.1	12.1	5.9	1	7	f,d	70
16272−4837	16:30:58.5	-48:43:52.5	335.58	-0.29	3.4	12.0	5.6	1	1	?	190
16318−4724	16:35:33.7	-47:31:10.8	336.99	-0.03	9.3		3.7	1	4	bs	130
16351−4722	16:38:50.4	-47:28: 0.5	337.40	-0.40	3.2	12.5	5.7	1	1	f	140

Continued on next page

Table A.29 – continued from previous page

Source	R.A. (J2000)	Dec. (J2000)	l	b	$d_{\rm near}$ kpc	$d_{\rm far}$ kpc	$R_{\rm G}$ kpc	Mult. (2pc)	Mult. (field)	8μm Morph[a]. (8μm)	rms (mJy/beam)
16385−4619	16:42:13.7	-46:25:29.2	338.57	-0.14	6.1	9.7	3.6	1	1	f,d	200
16445−4459	16:48: 4.8	-45:05: 6.5	340.25	-0.04	9.8		3.4	1	2	b?	260
16458−4512	16:49:30.1	-45:17:55.1	340.25	-0.37	12.1		5.0	2	3	bs	180
16484−4603	16:52: 3.8	-46:08:25.6	339.88	-1.26	2.8		5.9	1	1	-	190
16489−4431	16:52:33.4	-44:36:20.7	341.13	-0.35	3.4	12.6	5.4	1	1	f	330
16524−4300	16:56: 2.9	-43:04:46.8	342.71	0.13	3.6	12.7	5.2	1	1	f	220
16562−3959	16:59:41.6	-40:03:41.2	345.49	1.47	1.7		6.9	1	3	d	280
17016−4142	17:05:10.8	-41:29: 5.5	345.00	-0.22	2.9	13.5	5.8	1	1	f	220
17136−3617	17:17: 1.3	-36:21: 1.4	350.50	0.96	2.1		6.5	2	3	e	100
17158−3901	17:19:20.2	-39:03:53.1	348.55	-0.98	14.4	14.3	6.2	1	5	e,c	120
17204−3636	17:23:50.4	-36:39: 1.3	351.04	-0.34	3.0	13.8	5.5	1	1	f,d	90
17220−3609	17:25:25.1	-36:12:44.2	351.58	-0.35	10.4	10.4	2.3	1	1	c	100
17233−3606	17:26:42.6	-36:09:18.2	351.77	-0.54	0.7	16.1	7.8	5	5	f	100
17244−3536	17:27:48.9	-35:39:14.8	352.32	-0.44	2.2	14.6	6.3	1	1	f	100
17258−3637	17:29:17.3	-36:40:16.8	351.63	-1.25	2.4		6.1	1	5	-	100
17269−3312	17:30:17.2	-33:13:54.9	354.61	0.47	4.3	12.6	4.2	2	4	b	90
17271−3439	17:30:26.6	-34:41:44.5	353.41	-0.36	3.2	13.6	5.3	1	4	e	70
17278−3541	17:31:15.1	-35:44:49.0	352.62	-1.08	0.4		8.1	4	4	f	90
17470−2853	17:50:14.3	-28:54:32.4	0.55	-0.85	9.6		1.1	1	4	e	120
17545−2357	17:57:34.5	-23:58: 4.1	5.64	0.24	2.4	14.5	6.1	1	1	f	100
17589−2312	18:01:57.8	-23:12:33.3	6.80	-0.26	3.8	13.1	4.8	1	1	f	100
18232−1154	18:25:54.6	-11:52:36.5	19.47	0.17	1.6	14.4	7.0	5	5	f,d	100
18236−1205	18:26:25.7	-12:04: 0.3	19.36	-0.03	2.4	13.6	6.2	1	1	f,d	100
18319−0834	18:34:39.0	-8:31:36.6	23.44	-0.18	10.0	10.0	4.0	1	11	f,d	80
18335−0713	18:36:12.4	-7:12:11.1	24.79	0.08	6.0	9.4	4.0	1	6	f,d	80

Table A.30: Sources observed with LABOCA at 870 μm in the inner Galaxy sample. [a)] dust temperatures from Faundez et al. (2004); [b)] the bolometric luminosities are based on IRAS fluxes taken from Faundez et al. (2004), Walsh et al. (1997) and Purcell et al. (2006) and have been scaled to match our distance estimates. c) Molecular tracer used to determine velocity. $C^{17}O$(3-2), CS(2-1) (Bronfman et. al, 1996),HCO^+(4-3), H_2CO(5-4).

Source	$S_{\rm peak}$ (Jy/beam)	$S_{\rm int}$ (Jy)	FWHM ($''$)	$T^{a)}_{\rm dust}$ (K)	$N(\rm H_2)$ $\times 10^{23}$ cm^{-2}	$L^{b)}_{\rm near}$ $\times 10^5$ L$_\odot$	multicolumn1c$L^{b)}_{\rm far}$ $\times 10^5$ L$_\odot$	$v_{\rm LSR}$ km s^{-1}	mol[c].
08448−4343	3.5	20.4	36.7	25	1.3	2.0		3.7	CS
12326−6245	19.9	42.6	24.7	40	4.2	270.0		−39.3	$C^{17}O$
12383−6128	1.7	23.5	64.0	27	0.6	48.2		−39.3	HCO^+
13079−6218	11.6	35.8	26.9	36	2.8	280.0		−41.6	HCO^+
13134−6242	11.3	20.1	16.9	35	2.8	29.1	170.0	−32.4	HCO^+
14164−6028	1.9	3.7	19.9	29	0.6	9.5	50.7	−46.5	CS
14206−6151	1.2	5.0	35.3	27	0.4	12.7	52.2	−49.6	HCO^+
14453−5912	2.8	13.5	33.9	30	0.8	29.1	333.0	−40.6	$C^{17}O$
14498−5856	4.8	14.2	23.1	30	1.4	35.3	238.0	−50.2	$C^{17}O$
15278−5620	6.7	16.2	19.4	30	2.0	54.6		−50.3	$C^{17}O$
15394−5358	8.3	28.0	27.5	25	3.2	249.0	246.0	−41.1	$C^{17}O$
15437−5343	3.4	10.4	23.3	34	0.9	61.8	184.0	−83.9	$C^{17}O$
15557−5215	2.6	9.8	31.0	27	0.9	24.1	141.0	−68.3	$C^{17}O$
16060−5146	46.2	81.0	19.8	46	8.2	784.0	2380.0	−91.0	$C^{17}O$
16065−5158	17.9	41.8	25.9	40	3.8	295.0	2120.0	−62.2	$C^{17}O$
16071−5142	12.3	26.0	20.4	29	3.9	82.5		−87.2	$C^{17}O$
16076−5134	4.7	27.9	34.3	33	1.2	215.0		−88.2	$C^{17}O$
16172−5028	24.3	0.0	34.5	33	6.5	460.0		−52.7	$C^{17}O$

Continued on next page

Table A.30 – continued from previous page

Source	$S_{\rm peak}$ (Jy/beam)	$S_{\rm int}$ (Jy)	FWHM ($''$)	$T^{a)}_{\rm dust}$ (K)	$N(\rm H_2)$ $\times 10^{23}$ cm^{-2}	$L^{b)}_{\rm near}$ $\times 10^3$ L$_\odot$	$L^{b)}_{\rm far}$ $\times 10^3$ L$_\odot$	$v_{\rm LSR}$ km s^{-1}	mol^{c}.
16175−5002	7.8	26.9	25.6	30	2.3	0.0		−43.7	$C^{17}O$
16272−4837	8.8	29.2	24.7	27	3.1	30.7	376.0	−48.0	H2CO
16318−4724	9.3	15.3	15.7	33	2.5	501.0		−120.9	CS
16351−4722	15.0	35.5	21.6	36	3.6	90.3	1430.0	−41.0	$C^{17}O$
16385−4619	3.1	7.7	21.2	33	0.8	119.0	299.0	−117.0	CS
16445−4459	3.0	8.7	23.7	31	0.9	248.0		−121.9	CS
16458−4512	4.4	23.3	42.8	29	1.4	518.0		−51.6	$C^{17}O$
16484−4603	6.8	20.8	28.5	35	1.7	59.4		−32.2	$C^{17}O$
16489−4431	2.2	6.1	24.0	28	0.7	15.3	207.0	−41.5	HCO^+
16524−4300	5.0	21.9	32.4	31	1.4	41.3	519.0	−41.5	$C^{17}O$
16562−3959	16.6	91.2	37.1	38	3.7	59.4		−12.8	$C^{17}O$
17016−4142	15.9	37.9	22.1	32	4.4	73.0	1600.0	−23.0	$C^{17}O$
17136−3617	6.6	36.4	37.5	31	1.9	129.0		−11.3	$C^{17}O$
17158−3901	6.8	34.6	24.0	32	1.9	1140.0	1120.0	−16.0	HCO^+
17204−3636	3.9	14.4	28.2	30	1.2	15.2	316.0	−18.2	$C^{17}O$
17220−3609	24.0	55.0	21.3	30	7.2	736.0	734.0	−98.5	CS
17233−3606	46.3	98.6	32.6	45	8.4	12.4	6910.0	3.4	$C^{17}O$
17244−3536	3.2	13.7	28.9	31	0.9	16.1	705.0	−10.2	HCO^+
17258−3637	18.1	0.0	28.6	42	3.6	196.0		−12.5	$C^{17}O$
17269−3312	8.1	15.8	25.7	31	2.3	52.3	440.0	−15.9	$C^{17}O$
17271−3439	22.6	0.0	33.6	35	5.6	184.0	3310.0	−21.8	$C^{17}O$
17278−3541	5.9	14.8	27.6	30	2.0	0.6		−0.4	CS
17470−2853	20.3	47.4	20.0	30	6.1	1080.0		19.0	$C^{17}O$
17545−2357	3.1	16.7	34.5	30	0.9	12.8	473.0	8.3	HCO^+
17589−2312	4.7	14.9	26.5	30	1.4	20.5	251.0	20.3	$C^{17}O$
18232−1154	6.3	15.0	20.1	30	1.9	9.5	747.0	26.3	H2CO

Continued on next page

Table A.30 – continued from previous page

Source	$S_{\rm peak}$ (Jy/beam)	$S_{\rm int}$ (Jy)	FWHM ($''$)	$T_{\rm dust}^{a)}$ (K)	$N(\rm H_2)$ $\times10^{23}$ cm^{-2}	$L_{\rm near}^{b)}$ $\times10^{3}$ L$_\odot$	$L_{\rm far}^{b)}$ $\times10^{3}$ L$_\odot$	$v_{\rm LSR}$ km s^{-1}	mol^{c}.
18236−1205	2.8	13.0	29.2	26	1.0	4.8	148.0	15.9	C^{17}O
18319−0834	6.2	16.9	22.8	30	1.9	931.0		101.4	C^{17}O
18335−0713	15.7	34.5	28.0	30	4.7	123.0	307.0	110.0	C^{17}O

Source	RA (J2000)	Dec (J2000)	$S_{\rm peak}$ Jy	$S_{\rm int}$ Jy	D kpc	R kpc	FWHM (")
07255−2012a	7:27:41.5	-20:20:05.34	2.3e(01)	9.9e(01)	9.8	15.7	33.1
07255−2012b	7:27:42.6	-20:18:53.5	2.5e(01)	1.5e	9.8	15.7	40.4
07257−2033	7:27:56.3	-20:40:10.9	2.0e(01)	7.3e(01)	9.2	15.6	30.2
07538−3359	7:55:44.1	-34:07:06.3	6.7e(02)	2.6e(01)	11.5	15.0	30.0
07519−3404	7:53:52.4	-34:12:29.3	1.5e(01)	4.4e(01)	11.34	16.3	25.7
08282−4545	8:29:53.3	-45:55:09.4	1.7e(01)	3.4e(01)	14.0	18.6	17.1

Table A.31: Properties of the LABOCA 870 μm emission for the outer Galaxy sources.

Table A.32: Dust properties derived from the LABOCA 870 μm emission. Sources marked * have distances larger 5.9 kpc. For those sources, the angular diameter at 0.6 pc is smaller than the beam, therefore the peak fluxes have been used for derivation of the masses $M_{0.6\ \mathrm{pc}}$.

Source	M^n_{10}	$M^n_{0.6\ \mathrm{pc}}$	M^f_{10}	$M^f_{0.6\ \mathrm{pc}}$	L/M_{10}	$L/M_{0.6\ \mathrm{pc}}$
	$M_\odot$	$M_\odot$	$M_\odot$	$M_\odot$	$L_\odot/M_\odot$	$L_\odot/M_\odot$
08448−4343	77	86	77	86	26	23
12326−6245	1620	937	1620	937	166	287
12383−6128	1933	165	1933	165	24	290
13079−6218	2021	701	2021	701	138	399
13134−6242	404	375	2369	1516	71	77
14164−6028	142	108	761	435	66	87
14206−6151	288	110	1184	273	44	114
14453−5912	418	185	4783	851	69	157
14498−5856	631	315	4257	1324	55	111
15278−5620	559	388	559	388	97	140
15394−5358*	14680	4550	14680	4550	16	54
15437−5343	656	262	1954	782	94	235
15557−5215	1648	247	9608	1085	14	97
16060−5146	4070	2638	12360	8013	192	297
16065−5158	1962	779	14110	4821	150	378
16071−5142	2139	985	2139	985	38	83
16076−5134	2268	404	2268	372	94	531
16172−5028	5791	1357	5791	1357	79	338
16175−5002	852	495	12820	3748	79	338
16272−4837	1175	674	14410	4869	26	45
16318−4724*	3804	2383	3804	2383	131	210
16351−4722	817	614	12920	6185	110	147
16385−4619*	777	334	1959	842	153	355
16445−4459*	2911	894	2911	894	85	277
16458−4512*	16450	2242	16450	2242	31	231
16484−4603	521	311	521	311	114	190
16489−4431	299	153	4051	1272	51	99
16524−4300	1016	366	12770	2536	40	112
16562−3959	565	494	565	494	105	120
17016−4142	858	661	18750	8842	85	110
17136−3617	537	342	537	342	239	376
17158−3901*	36230	4273	36230	4273	31	266
17204−3636	420	247	8777	2426	36	61
17220−3609*	17360	8614	17360	8614	42	85
17233−3606	78	129	43830	24070	158	95

Continued on next page

Table A.32 – continued from previous page

Source	M^n_{10} $M_\odot$	$M^n_{0.6\ \mathrm{pc}}$ $M_\odot$	M^f_{10} $M_\odot$	$M^f_{0.6\ \mathrm{pc}}$ $M_\odot$	L/M_{10} $L_\odot/M_\odot$	$L/M_{0.6\ \mathrm{pc}}$ $L_\odot/M_\odot$
17244−3536	201	154	8811	2187	79	104
17258−3637	948	580	948	580	206	337
17269−3312	829	525	6970	4054	63	99
17271−3439	3202	1185	57710	11290	57	155
17278−3541	23	28	23	28	26	22
17470−2853*	17850	6142	17850	6142	60	175
17545−2357	332	183	12320	2136	38	69
17589−2312	663	339	8113	2669	30	60
18232−1154	126	135	9931	4295	75	70
18236−1205	353	188	10940	2049	13	25
18319−0834*	5015	2061	5014	2061	185	451
18335−0713*	3662	1864	9101	4632	33	65

Table A.33: Dust properties derived from the LABOCA 870 μm emission.

Source	$n(\mathrm{H_2})^n_{10}$ (10^4 cm^{-3})	$n(\mathrm{H_2})^n_{0.6\ pc}$ (10^4 cm^{-3})	$n(\mathrm{H_2})^f_{10}$ (10^4 cm^{-3})	$n(\mathrm{H_2})^f_{0.6\ pc}$ (10^4 cm^{-3})	Θ^n (pc)	Θ^f (pc)
08448−4343	2.8	1.2	2.8	1.2	0.4	0.4
12326−6245	3.6	13.4	3.6	13.4	1.1	1.1
12383−6128	0.2	2.4	0.2	2.4	3.2	3.2
13079−6218	1.6	10.0	1.6	10.0	1.6	1.6
13134−6242	4.1	5.4	1.7	21.7	0.7	1.6
14164−6028	0.7	1.6	0.3	6.2	0.8	2.0
14206−6151	0.3	1.6	0.1	3.9	1.5	3.0
14453−5912	0.5	2.6	0.1	12.2	1.4	4.7
14498−5856	1.0	4.5	0.4	18.9	1.3	3.3
15278−5620	2.0	5.6	2.0	5.6	1.0	1.0
15394−5358	0.8	65.1	0.8	65.1	3.9	3.9
15437−5343	0.5	3.8	0.3	11.2	1.6	2.7
15557−5215	0.3	3.5	0.1	15.5	2.7	6.5
16060−5146	6.5	37.8	3.7	114.6	1.2	2.2
16065−5158	1.7	11.2	0.6	69.0	1.5	4.1
16071−5142	2.6	14.1	2.6	14.1	1.4	1.4
16076−5134	0.4	5.8	0.4	5.3	2.5	2.5
16172−5028	2.6	19.4	2.6	19.4	1.9	1.9
16175−5002	1.9	7.1	0.5	53.6	1.1	4.3
16272−4837	2.9	9.6	0.8	69.7	1.1	3.8
16318−4724	1.4	34.1	1.4	34.1	2.1	2.1

Continued on next page

Table A.33 – continued from previous page

Source	$n(\mathrm{H_2})^n_{10}$ (10^4 cm^{-3})	$n(\mathrm{H_2})^n_{0.6\ pc}$ (10^4 cm^{-3})	$n(\mathrm{H_2})^f_{10}$ (10^4 cm^{-3})	$n(\mathrm{H_2})^f_{0.6\ pc}$ (10^4 cm^{-3})	Θ^n (pc)	Θ^f (pc)
16351−4722	3.8	8.8	1.0	88.5	0.9	3.5
16385−4619	0.4	4.8	0.3	12.1	1.8	2.8
16445−4459	0.2	12.8	0.2	12.8	3.5	3.5
16458−4512	0.2	32.1	0.2	32.1	6.3	6.3
16484−4603	1.4	4.5	1.4	4.5	1.1	1.1
16489−4431	0.6	2.2	0.2	18.2	1.2	4.3
16524−4300	0.7	5.2	0.2	36.3	1.7	5.9
16562−3959	4.7	7.1	4.7	7.1	0.7	0.7
17016−4142	4.7	9.5	1.0	126.5	0.8	3.9
17136−3617	1.5	4.9	1.5	4.9	1.0	1.0
17158−3901	0.2	61.1	0.2	61.1	8.7	8.7
17204−3636	1.0	3.5	0.2	34.7	1.1	5.0
17220−3609	2.4	123.2	2.4	123.2	2.8	2.8
17233−3606	46.5	1.8	2.0	344.4	0.2	4.1
17244−3536	1.0	2.2	0.2	31.3	0.8	5.6
17258−3637	2.6	8.3	2.6	8.3	1.0	1.0
17269−3312	2.3	7.5	0.8	58.0	1.0	3.0
17271−3439	2.8	16.9	0.7	161.5	1.5	6.5
17278−3541	6.0	0.4	6.0	0.4	0.2	0.2
17470−2853	1.3	87.9	1.3	87.9	3.5	3.5
17545−2357	0.7	2.6	0.1	30.6	1.2	7.1
17589−2312	1.0	4.9	0.3	38.2	1.3	4.4
18232−1154	3.4	1.9	0.4	61.5	0.5	4.3
18236−1205	0.7	2.7	0.1	29.3	1.1	6.3
18319−0834	0.6	29.5	0.6	29.5	3.0	3.0
18335−0713	2.7	26.7	1.7	66.3	1.6	2.6

Source	M	$n(\mathrm{H_2})$	Θ	L^a)	L/M	$N(\mathrm{H_2})$
	$\mathrm{M_\odot}$	$\mathrm{cm^{-3}}$	pc	$\mathrm{L_\odot}$	$\mathrm{L_\odot/M_\odot}$	
07255−2012a	2.76e+02	2.68e+03	1.47e+00	-	-	3.39e-02
07255−2012b	4.26e+02	2.27e+03	1.80e+00	-	-	3.51e-02
07257−2033	2.02e+02	2.58e+03	1.34e+00	8.70e+03	4.31e+01	2.98e-02
07538−3359	1.13e+02	7.48e+02	1.67e+00	3.40e+03	3.02e+01	1.07e-02
07519−3404	1.87e+02	2.05e+03	1.41e+00	7.00e+03	3.74e+01	2.50e-02
08282−4545	2.21e+02	4.38e+03	1.16e+00	2.20e+04	9.96e+01	4.37e-02

Table A.34: Properties of the outer Galaxy sources derived from LABOCA 870 μm emission. M, $n(\mathrm{H_2})$ and $N(\mathrm{H_2})$ are the masses, mean densities and column densities for the sources. Θ is the linear diameter of the sources derived from the FWHM. a) IRAS luminosities taken from Wouterloot $\&$ Brand 1989. The entry "-" indicates that no luminosity was available.

Source	m_i	p	Source	m_i	p
08448−4343	-1.7	-1.3			
12326−6245	-2.7	-2.3	16458−4512	-1.3	-0.9
12383−6128	-0.9	-0.6	16484−4603	-2.0	-1.6
13079−6218	-2.2	-1.8	16489−4431	-2.0	-1.6
13134−6242	-2.8	-2.4	16524−4300	-1.8	-1.4
14164−6028	-2.4	-2.0	16562−3959	-1.8	-1.4
14206−6151	-1.6	-1.3	17016−4142	-2.2	-1.9
14453−5912	-1.7	-1.3	17136−3617	-1.8	-1.4
14498−5856	-2.0	-1.6	17158−3901	-1.6	-1.2
15278−5620	-2.4	-2.0	17204−3636	-2.0	-1.6
15394−5358	-2.2	-1.8	17220−3609	-2.5	-2.1
15437−5343	-2.2	-1.8	17233−3606	-2.5	-2.1
15557−5215	-1.3	-0.9	17244−3536	-2.0	-1.7
16060−5146	-2.9	-2.5	17258−3637	-1.8	-1.4
16065−5158	-1.8	-1.4	17269−3312	-2.2	-1.8
16071−5142	-2.5	-2.1	17271−3439	-1.7	-1.3
16076−5134	-1.9	-1.5	17278−3541	-1.2	-0.9
16172−5028	-1.4	-1.0	17470−2853	-1.8	-1.4
16175−5002	-2.1	-1.7	17545−2357	-1.7	-1.3
16272−4837	-2.3	-1.9	17589−2312	-2.1	-1.8
16318−4724	-2.6	-2.2	18236−1205	-1.7	-1.3
16351−4722	-2.6	-2.2	18232−1154	-2.3	-1.9
16385−4619	-2.2	-1.8	18319−0834	-2.0	-1.6
16445−4459	-1.9	-1.5	18335−0713	-2.2	-1.8

Table A.35: Results of the radial fit on the dust continuum data

Source	Area	v_{lsr}	Δv	
	K.km s^{-1}	km s^{-1}	km s^{-1}	
12326−6245	27.1	−39.4	6.1	a
12383−6128	3.1	−39.3	3.2	b
13079−6218	16.8	−41.5	7.7	b
13134−6242	5.9	−32.5	5.1	a,b
14164−6028	1.5	−46.2	5.1	-
14206−6151	1.6	−52.6	6.8	-
14453−5912	3.0	−40.6	2.9	a
14498−5856	6.7	−49.9	3.2	a
15394−5358	24.6	−40.6	5.4	a,d
15437−5343	2.9	−83.8	4.2	-
15557−5215	7.5	−67.7	4.1	-
16060−5146	58.8	−92.0	9.9	a
16065−5158	48.2	−62.6	8.3	a
16071−5142	10.6	−87.2	6.2	a,d
16272−4837	10.1	−47.0	5.2	b
16351−4722	16.2	−40.3	5.6	c
16458−4512	7.7	−51.2	5.0	a,b?
16484−4603	9.0	−31.9	5.0	-
16489−4431	2.8	−41.3	2.9	-
16524−4300	6.6	−41.8	5.1	b?
16562−3959	84.4	−12.6	8.6	b?
17136−3617	22.4	−9.6	4.6	-
17158−3901	6.9	−15.9	6.1	c
17233−3606	50.7	−1.6	10.8	a,c
17244−3536	4.8	−10.2	4.3	a,c
17258−3637	26.6	−11.1	7.3	c
17271−3439	15.7	−16.4	8.1	d
17545−2357	4.3	8.3	2.7	-

Table A.36: Line parameters for HCO^+(4-3). a: outflow; b: Inflow ; c: Expansion; d: self-absorption. Sources with an entry '-' could be modeled with a Gaussian line profile.

Source	Area K.km s^{-1}	v$_{lsr}$ km s^{-1}	Δv km s^{-1}
12326−6245	31.3	0.1	−39.4
15278−5620	11.9	0.1	−49.8
16060−5146	56.5	0.2	−91.5
16065−5158	34.2	0.3	−62.4
14453−5912	10.8	0.2	−40.1
14498−5856	13.4	0.2	−49.8
15394−5358	7.2	0.2	−40.6
15437−5343	9.2	0.2	−83.4
15557−5215	3.2	0.2	−67.9
16071−5142	17.4	0.2	−86.8
16076−5134	15.7	0.8	−87.8
16172−5028	24.8	0.4	−52.2
16172−5028a	16.2	0.1	−49.6
16175−5002	16.3	0.1	−43.3
16351−4722	36.8	0.3	−40.5
16458−4512	7.6	0.3	−51.2
16484−4603	18.8	0.2	−31.9
16524−4300	11.0	0.2	−41.0
16562−3959	31.2	0.3	−12.4
17016−4124	14.7	0.2	−26.6
17136−3617	13.8	0.3	−9.8
17136−3617	13.8	0.3	−9.8
17204−3636	7.4	0.2	−17.8
17258−3637	34.6	0.3	−12.1
17269−3312	4.6	0.2	−21.4
17271−3439	31.2	0.2	−15.5
17589−2312	10.5	0.2	20.7
17470−2853	43.7	0.3	17.9
18319−0834	10.3	0.3	101.8
18236−1205	7.3	0.2	26.8
18335−0713	21.7	0.3	110.4

Table A.37: Line parameters of the Gaussian fits for $C^{17}O$(3–2).

Source	δV
12326−6245	-0.03±0.02
14453−5912	-0.21±0.06
14498−5856	-0.04±0.02
15278−5620[a)]	0.06±0.05
15394−5358	0.37±0.08
15437−5343	-0.12±0.05
15557−5215	-0.11±0.18
16060−5146	-0.16±0.01
16065−5158	-0.12±0.01
16071−5142	0.0±0.07
16076−5134[a)]	-0.38±0.05
16351−4722	0.04±0.01
16458−4512	-0.25±0.05
16484−4603	0.0±0.02
16524−4300	-0.49±0.07
16562−3959	-0.3±0.01
17136−3617	0.06±0.03
17233−3606	0.57±0.08
17258−3637	0.2±0.03
17470−2853[a)]	-0.16±0.14
18232−1154[a)]	-0.18±0.11
18236−1205[a)]	0.39±0.08
18319−0834[a)]	-0.23±0.07
18335−0713[a)]	0.13±0.04

Table A.38: Asymmetry parameter δV. Sources with $\delta V > 0.1$ show a significant red shift, while sources with $\delta V < 0.1$ show a significant blue shift. For sources marked $^{a)}$, δV was determined using HCO^+(1-0) and $H^{13}CO^+$(1-0) from Purcell et al. (2006).

Species	Size (")	$T_{\rm ex}$ (K)	$N_{\rm b}$(mol) ($\rm cm^{-2}$)	$N_{\rm s}$(mol) ($\rm cm^{-2}$)	Δv ($\rm km\,s^{-1}$)	Offset ($\rm km\,s^{-1}$)	$N_{\rm b}/N_{\rm H_2}$	
CCH	-[a]	15	4.3(14)	-	2.5	-0.8	5.2(-09)	[c]
CH_3OH	-[a]	18	4.3(14)	-	4.0	0.0	2.2(-08)	[d]
CO	-[a]	50[a]	1.8(15)	1.0(19)	2.0	-0.5	1.0(-04)	[c], [f]

[a] Fixed Parameter;[b] based on weak or partially blended lines only; [c] based on one or a few lines only; [d] includes vibrationally excited lines; [e] non-LTE, see text; [f] based on isotopologues, see text. The column labeled Offset shows the offset in velocity relative to the systemic velocity of the source. $N_{\rm s}$ are the source averaged column densities, $N_{\rm b}$ are the beam averaged column densities and $N_{\rm b}/N_{\rm H_2}$ gives beam averaged abundances.

Table A.39: Results of the line modeling for 14453−5912

Species	Size (")	$T_{\rm ex}$ (K)	$N_{\rm b}$(mol) ($\rm cm^{-2}$)	$N_{\rm s}$(mol) ($\rm cm^{-2}$)	Δv ($\rm km\,s^{-1}$)	Offset ($\rm km\,s^{-1}$)	$N_{\rm b}/N_{\rm H_2}$	
CCH	-[a]	45	1.2(14)	-	2.5	-0.8	8.3(-10)	[c]
CH_3OH	-[a]	30	1.2(14)	-	4.0	0.0	5.5(-09)	[d]
CO	-[a]	50[a]	8.0(14)	1.5(19)	4.0	-0.5	8.3(-05)	[c], [f]
CS	-[a]	50[a]	8.0(14)	-	1.5	0.0	6.2(-10)	[c], [f]
H_2CS	-[a]	50[a]	1.5(19)	-	3.0	0.0	2.1(-10)	[c]

[a] Fixed Parameter;[b] based on weak or partially blended lines only; [c] based on one or a few lines only; [d] includes vibrationally excited lines; [e] non-LTE, see text; [f] based on isotopologues, see text. The column labeled Offset shows the offset in velocity relative to the systemic velocity of the source. $N_{\rm s}$ are the source averaged column densities, $N_{\rm b}$ are the beam averaged column densities and $N_{\rm b}/N_{\rm H_2}$ gives beam averaged abundances.

Table A.40: Results of the line modelling for 14498−5856

Species	Size (")	$T_{\rm ex}$ (K)	$N_{\rm b}$(mol) ($\rm cm^{-2}$)	$N_{\rm s}$(mol) ($\rm cm^{-2}$)	Δv ($\rm km\,s^{-1}$)	Offset ($\rm km\,s^{-1}$)	$N_{\rm b}/N_{\rm H_2}$	
CCH	-[a]	50[a]	1.5(14)	-	2.5	-0.6	4.7(-10)	[c]
CH_3CN	-[a]	110	1.5(14)	-	4.5	0.0	7.8(-11)	
CH_3OCH_3	-[a]	100	2.5(13)	-	4.5	0.0	4.7(-09)	[b]
CH_3OH	1.0	140	2.5(13)	8.0(17)	3.0	0.0	7.8(-09)	[d]
	-[a]	20	1.5(15)	-	3.0	0.0	2.0(-08)	
CO	-[a]	50[a]	1.5(15)	6.0(18)	4.0	0.0	1.6(-05)	[c], *f*
CS	-[a]	50[a]	8.0(17)	-	5.0	0.0	7.8(-10)	[c], *f*
H_2CS	-[a]	50[a]	2.5(15)	-	3.0	0.0	1.9(-10)	[c]

[a] Fixed Parameter;[b] based on weak or partially blended lines only; [c] based on one or a few lines only; [d] includes vibrationally excited lines; [e] non-LTE, see text; [f] based on isotopologues, see text. The column labeled Offset shows the offset in velocity relative to the systemic velocity of the source. $N_{\rm s}$ are the source averaged column densities, $N_{\rm b}$ are the beam averaged column densities and $N_{\rm b}/N_{\rm H_2}$ gives beam averaged abundances.

Table A.41: Results of the line modelling for 15394−5358

Species	Size (")	$T_{\rm ex}$ (K)	$N_{\rm b}$(mol) ($\rm cm^{-2}$)	$N_{\rm s}$(mol) ($\rm cm^{-2}$)	Δv ($\rm km\,s^{-1}$)	Offset ($\rm km\,s^{-1}$)	$N_{\rm b}/N_{\rm H_2}$	
CCH	-[a]	50[a]	3.8(13)	-	2.5	-1.3	4.4(-10)	[c]
CH_3OH	1.0[a]	150[a]	3.8(13)	5.0(17)	2.5	0.0	1.7(-08)	[d]
	-[a]	13	5.0(17)	-	2.5	0.0	9.2(-09)	
CO	-[a]	50[a]	1.5(15)	1.0(19)	3.5	0.0	9.5(-05)	[c], *f*
CS	-[a]	50[a]	8.0(14)	-	4.0	0.0	2.3(-09)	[c], *f*
H_2CS	-[a]	50[a]	8.0(14)	-	4.0	-1.0	4.6(-10)	[c]

[a] Fixed Parameter;[b] based on weak or partially blended lines only; [c] based on one or a few lines only; [d] includes vibrationally excited lines; [e] non-LTE, see text; [f] based on isotopologues, see text. The column labeled Offset shows the offset in velocity relative to the systemic velocity of the source. $N_{\rm s}$ are the source averaged column densities, $N_{\rm b}$ are the beam averaged column densities and $N_{\rm b}/N_{\rm H_2}$ gives beam averaged abundances.

Table A.42: Results of the line modelling for 15437−5343

Species	Size (")	$T_{\rm ex}$ (K)	$N_{\rm b}$(mol) ($\rm cm^{-2}$)	$N_{\rm s}$(mol) ($\rm cm^{-2}$)	Δv ($\rm km\,s^{-1}$)	Offset ($\rm km\,s^{-1}$)	$N_{\rm b}/N_{\rm H_2}$	
CCH	-[a]	60	4.5(13)	-	2.5	-1.3	4.9(-10)	[c]
CH_3CN	-[a]	30	4.5(13)	-	3.0	-4.0	1.1(-09)	
CH_3OH	-[a]	17	1.0(14)	-	6.0	0.0	4.0(-08)	[d]
CO	-[a]	50[a]	1.0(14)	3.0(18)	4.0	0.0	2.7(-05)	[c], [f]
CS	-[a]	50[a]	3.7(15)	-	3.0	0.0	6.5(-10)	[c], [f]
H_2CS	-[a]	150[a]	3.7(15)	-	4.0	-1.0	3.3(-10)	[c]
HNCO	-[a]	150[a]	3.0(18)	-	5.0	-2.4	6.5(-10)	[c]
SO_2	-[a]	50[a]	2.5(18)	-	6.0	8.0	6.5(-09)	[e]

[a] Fixed Parameter;[b] based on weak or partially blended lines only; [c] based on one or a few lines only; [d] includes vibrationally excited lines; [e] non-LTE, see text; [f] based on isotopologues, see text. The column labeled Offset shows the offset in velocity relative to the systemic velocity of the source. $N_{\rm s}$ are the source averaged column densities, $N_{\rm b}$ are the beam averaged column densities and $N_{\rm b}/N_{\rm H_2}$ gives beam averaged abundances.

Table A.43: Results of the line modelling for 15557−5215

Species	Size (")	$T_{\rm ex}$ (K)	$N_{\rm b}$(mol) ($\rm cm^{-2}$)	$N_{\rm s}$(mol) ($\rm cm^{-2}$)	Δv ($\rm km\,s^{-1}$)	Offset ($\rm km\,s^{-1}$)	$N_{\rm b}/N_{\rm H_2}$	
CCH	-[a]	50[a]	2.2(14)	-	4.5	-2.0	5.7(-10)	[c]
CH_3CN	-[a]	20	2.2(14)	-	4.5	-1.0	5.2(-09)	
CH_3OH	1.0[a]	180	2.0(15)	6.0(17)	4.0	2.0	4.6(-09)	[d]
	-[a]	17	2.0(15)	-	4.0	0.0	1.3(-08)	
CO	-[a]	50[a]	6.0(17)	1.7(19)	6.0	0.0	3.6(-05)	[c], [f]
CS	-[a]	50[a]	1.8(15)	-	5.0	0.0	1.0(-09)	[c], [f]
H_2CS	-[a]	50[a]	5.0(15)	-	5.5	0.5	2.1(-10)	[c]
HNCO	-[a]	150[a]	5.0(15)	-	5.0	-2.4	1.8(-10)	[c]

[a] Fixed Parameter;[b] based on weak or partially blended lines only; [c] based on one or a few lines only; [d] includes vibrationally excited lines; [e] non-LTE, see text; [f] based on isotopologues, see text. The column labeled Offset shows the offset in velocity relative to the systemic velocity of the source. $N_{\rm s}$ are the source averaged column densities, $N_{\rm b}$ are the beam averaged column densities and $N_{\rm b}/N_{\rm H_2}$ gives beam averaged abundances.

Table A.44: Results of the line modelling for 16071−5142

Species	Size (")	T_{ex} (K)	N_b(mol) (cm^{-2})	N_s(mol) (cm^{-2})	Δv ($km\,s^{-1}$)	Offset ($km\,s^{-1}$)	N_b/N_{H_2}	
C_2H_5CN	-[a]	150[a]	1.3(14)	-	4.0	1.0	3.6(-10)	[b]
C_2H_5OH	-[a]	150[a]	1.3(14)	-	2.0	1.0	5.0(-10)	[b]
CCH	-[a]	60	1.8(14)	-	4.0	1.0	1.1(-09)	[c]
CH_3CN	1.8	170	1.8(14)	1.4(16)	4.0	2.0	3.9(-10)	
CH_3OCH_3	-[a]	50[a]	3.8(14)	-	4.5	1.0	5.6(-09)	[b]
CH_3OCHO-a	-[a]	150[a]	3.8(14)	-	3.0	1.0	4.2(-09)	[b]
CH_3OH	1.8	170	1.4(16)	8.5(17)	3.0	2.0	2.3(-08)	[d]
	-[a]	35	1.4(14)	-	3.0	0.0	9.8(-09)	
CO	-[a]	50[a]	2.0(15)	3.5(19)	4.3	1.40	8.1(-05)	[c], [f]
CS	-[a]	50[a]	2.0(15)	-	5.0	1.0	7.2(-09)	[c], [f]
H_2CS	-[a]	50[a]	1.5(15)	-	4.8	1.0	1.1(-09)	[c]
HC_3N	-[a]	130	1.5(15)	-	5.0	1.0	2.8(-10)	[c]
HNCO	-[a]	150[a]	8.5(17)	-	8.5	3.0	5.6(-10)	[c]
SO	-[a]	50[a]	8.4(15)	-	4.0	1.0	2.5(-09)	[e], [f]
SO_2	-[a]	50[a]	3.5(15)	-	4.0	1.0	2.0(-09)	[e]

[a] Fixed Parameter;[b] based on weak or partially blended lines only; [c] based on one or a few lines only; [d] includes vibrationally excited lines; [e] non-LTE, see text; [f] based on isotopologues, see text. The column labeled Offset shows the offset in velocity relative to the systemic velocity of the source. N_s are the source averaged column densities, N_b are the beam averaged column densities and N_b/N_{H_2} gives beam averaged abundances.

Table A.45: Results of the line modelling for 16351−4722

Species	Size (")	T_{ex} (K)	N_b(mol) (cm^{-2})	N_s(mol) (cm^{-2})	Δv ($km\,s^{-1}$)	Offset ($km\,s^{-1}$)	N_b/N_{H_2}	
CCH	-[a]	50[a]	1.8(14)	-	4.5	-1.3	1.3(-09)	[c]
CH_3OH	-[a]	15	1.8(14)	-	4.0	-1.00	3.2(-08)	[d]
CO	-[a]	50[a]	4.5(15)	8.0(18)	4.0	-1.0	4.8(-05)	[c], [f]

[a] Fixed Parameter;[b] based on weak or partially blended lines only; [c] based on one or a few lines only; [d] includes vibrationally excited lines; [e] non-LTE, see text; [f] based on isotopologues, see text. The column labeled Offset shows the offset in velocity relative to the systemic velocity of the source. N_s are the source averaged column densities, N_b are the beam averaged column densities and N_b/N_{H_2} gives beam averaged abundances.

Table A.46: Results of the line modelling for 16458−4512

Species	Size (")	$T_{\rm ex}$ (K)	$N_{\rm b}$(mol) ($\rm cm^{-2}$)	$N_{\rm s}$(mol) ($\rm cm^{-2}$)	Δv ($\rm km\,s^{-1}$)	Offset ($\rm km\,s^{-1}$)	$N_{\rm b}/N_{\rm H_2}$	
CCH	-[a]	50[a]	2.2(14)	-	3.5	-1.0	1.3(-09)	[c]
CH_3CN	-[a]	60	2.2(14)	-	4.5	0.0	1.5(-10)	
CH_3OH	-[a]	35	2.5(13)	-	6.0	0.0	7.8(-09)	[d]
CO	-[a]	50[a]	2.5(13)	1.9(19)	3.6	0.0	9.5(-05)	[c], [f]
CS	-[a]	50[a]	1.3(15)	-	3.5	-0.5	1.6(-09)	[c], [f]
H_2CS	-[a]	50[a]	1.3(15)	-	6.0	-2.0	3.6(-10)	[c]

[a] Fixed Parameter;[b] based on weak or partially blended lines only; [c] based on one or a few lines only; [d] includes vibrationally excited lines; [e] non-LTE, see text; [f] based on isotopologues, see text. The column labeled Offset shows the offset in velocity relative to the systemic velocity of the source. $N_{\rm s}$ are the source averaged column densities, $N_{\rm b}$ are the beam averaged column densities and $N_{\rm b}/N_{\rm H_2}$ gives beam averaged abundances.

Table A.47: Results of the line modelling for 16484−4603

Species	Size (")	$T_{\rm ex}$ (K)	$N_{\rm b}$(mol) ($\rm cm^{-2}$)	$N_{\rm s}$(mol) ($\rm cm^{-2}$)	Δv ($\rm km\,s^{-1}$)	Offset ($\rm km\,s^{-1}$)	$N_{\rm b}/N_{\rm H_2}$	
CCH	-[a]	50[a]	2.0(14)	-	2.5	0.3	1.4(-09)	[c]
CH_3OH	-[a]	18	2.0(14)	-	3.0	0.0	1.7(-08)	[d]
CO	-[a]	50[a]	2.5(15)	1.0(19)	3.0	0.5	5.8(-05)	[c], [f]
CS	-[a]	50[a]	2.5(15)	-	2.5	0.5	9.0(-10)	[c], [f]
H_2CS	-[a]	50[a]	1.0(19)	-	2.0	1.0	1.0(-10)	[c]

[a] Fixed Parameter;[b] based on weak or partially blended lines only; [c] based on one or a few lines only; [d] includes vibrationally excited lines; [e] non-LTE, see text; [f] based on isotopologues, see text. The column labeled Offset shows the offset in velocity relative to the systemic velocity of the source. $N_{\rm s}$ are the source averaged column densities, $N_{\rm b}$ are the beam averaged column densities and $N_{\rm b}/N_{\rm H_2}$ gives beam averaged abundances.

Table A.48: Results of the line modelling for 16524−4300

Species	Size (")	$T_{\rm ex}$ (K)	$N_{\rm b}$(mol) ($\rm cm^{-2}$)	$N_{\rm s}$(mol) ($\rm cm^{-2}$)	Δv ($\rm km\,s^{-1}$)	Offset ($\rm km\,s^{-1}$)	$N_{\rm b}/N_{\rm H_2}$	
CCH	-[a]	50[a]	1.4(15)	-	4.0	0.0	3.8(-09)	[c]
CH_3CN	-[a]	30	1.4(15)	-	4.5	-2.0	6.7(-10)	
CH_3OH	-[a]	20	2.5(14)	-	6.0	0.0	2.7(-08)	[d]
CO	-[a]	50[a]	2.5(14)	3.3(19)	4.0	-1.0	7.3(-05)	[c], *f*
CS	-[a]	50[a]	1.0(16)	-	4.0	-1.0	2.7(-09)	[c], *f*
H_2CS	-[a]	50[a]	1.0(16)	-	4.0	-1.0	5.1(-10)	[c]
SO	-[a]	50[a]	3.3(19)	-	4.0	0.0	2.7(-09)	[e], *f*
SO_2	-[a]	50[a]	2.7(19)	-	4.0	0.0	1.6(-09)	[e]

[a] Fixed Parameter;[b] based on weak or partially blended lines only; [c] based on one or a few lines only; [d] includes vibrationally excited lines; [e] non-LTE, see text; [f] based on isotopologues, see text. The column labeled Offset shows the offset in velocity relative to the systemic velocity of the source. $N_{\rm s}$ are the source averaged column densities, $N_{\rm b}$ are the beam averaged column densities and $N_{\rm b}/N_{\rm H_2}$ gives beam averaged abundances.

Table A.49: Results of the line modelling for 16562−3959

Species	Size (")	$T_{\rm ex}$ (K)	$N_{\rm b}$(mol) ($\rm cm^{-2}$)	$N_{\rm s}$(mol) ($\rm cm^{-2}$)	Δv ($\rm km\,s^{-1}$)	Offset ($\rm km\,s^{-1}$)	$N_{\rm b}/N_{\rm H_2}$	
CCH	-[a]	30	4.0(14)	-	4.0	0.0	2.2(-09)	[c]
CH_3OH	-[a]	20	4.0(14)	-	3.0	0.0	8.4(-09)	[d]
CO	-[a]	50[a]	1.5(15)	9.2(18)	3.0	-0.50	4.3(-05)	[c], *f*
CS	-[a]	50[a]	1.5(15)	-	3.5	-0.5	2.0(-09)	[c], *f*
H_2CS	-[a]	50[a]	9.2(18)	-	4.0	-1.0	2.8(-10)	[c]
HNCO	-[a]	150[a]	7.7(18)	-	5.0	-2.4	3.9(-10)	[c]

[a] Fixed Parameter;[b] based on weak or partially blended lines only; [c] based on one or a few lines only; [d] includes vibrationally excited lines; [e] non-LTE, see text; [f] based on isotopologues, see text. The column labeled Offset shows the offset in velocity relative to the systemic velocity of the source. $N_{\rm s}$ are the source averaged column densities, $N_{\rm b}$ are the beam averaged column densities and $N_{\rm b}/N_{\rm H_2}$ gives beam averaged abundances.

Table A.50: Results of the line modelling for 17136−3617

Species	Size (")	$T_{\rm ex}$ (K)	$N_{\rm b}$(mol) ($\rm cm^{-2}$)	$N_{\rm s}$(mol) ($\rm cm^{-2}$)	Δv ($\rm km\,s^{-1}$)	Offset ($\rm km\,s^{-1}$)	$N_{\rm b}/N_{\rm H_2}$	
CCH	-[a]	50[a]	3.8(14)	-	4.0	0.5	2.1(-09)	[c]
CH_3OH	-[a]	20	3.8(14)	-	4.0	0.0	4.8(-09)	[d]
CO	-[a]	50[a]	8.5(14)	1.4(19)	4.0	0.5	6.7(-05)	[c], *f*
CS	-[a]	50[a]	8.5(14)	-	3.0	1.0	1.7(-09)	[c], *f*
H_2CS	-[a]	50[a]	1.4(19)	-	4.0	0.0	1.7(-10)	[c]

[a] Fixed Parameter;[b] based on weak or partially blended lines only; [c] based on one or a few lines only; [d] includes vibrationally excited lines; [e] non-LTE, see text; [f] based on isotopologues, see text. The column labeled offset shows the offset in velocity relative to the systemic velocity of the source. $N_{\rm s}$ are the source averaged column densities, $N_{\rm b}$ are the beam averaged column densities and $N_{\rm b}/N_{\rm H_2}$ gives beam averaged abundances.

Table A.51: Results of the line modelling for 17136−3617, Offset position

Species	Size (")	$T_{\rm ex}$ (K)	$N_{\rm b}$(mol) ($\rm cm^{-2}$)	$N_{\rm s}$(mol) ($\rm cm^{-2}$)	Δv ($\rm km\,s^{-1}$)	Offset ($\rm km\,s^{-1}$)	$N_{\rm b}/N_{\rm H_2}$	
CCH	-[a]	50[a]	1.1(14)	-	3.0	0.0	9.4(-10)	[c]
CH_3OH	-[a]	15	1.1(14)	-	4.0	0.0	2.6(-08)	[d]
CO	-[a]	50[a]	3.0(15)	6.6(18)	2.8	0.0	4.7(-05)	[c], *f*
CS	-[a]	50[a]	3.0(15)	-	4.0	0.0	8.6(-10)	[c], *f*

[a] Fixed Parameter;[b] based on weak or partially blended lines only; [c] based on one or a few lines only; [d] includes vibrationally excited lines; [e] non-LTE, see text; [f] based on isotopologues, see text. The column labeled Offset shows the offset in velocity relative to the systemic velocity of the source. $N_{\rm s}$ are the source averaged column densities, $N_{\rm b}$ are the beam averaged column densities and $N_{\rm b}/N_{\rm H_2}$ gives beam averaged abundances.

Table A.52: Results of the line modelling for 17204−3636

Species	Size (")	$T_{\rm ex}$ (K)	$N_{\rm b}$(mol) ($\rm cm^{-2}$)	$N_{\rm s}$(mol) ($\rm cm^{-2}$)	Δv ($\rm km\,s^{-1}$)	Offset ($\rm km\,s^{-1}$)	$N_{\rm b}/N_{\rm H_2}$	
CCH	-[a]	50[a]	5.0(14)	-	5.0	0.0	1.4(-09)	[c]
CH_3OH	-[a]	18	5.0(14)	-	4.0	-1.0	8.4(-09)	[d]
CO	-[a]	50[a]	3.0(15)	3.3(19)	5.0	-0.5	7.5(-05)	[c], *f*
CS	-[a]	50[a]	3.0(15)	-	5.0	-0.5	1.7(-09)	[c], *f*
H_2CS	-[a]	50[a]	3.3(19)	-	5.0	0.5	1.7(-10)	[c]
HNCO	-[a]	150[a]	2.7(19)	-	5.0	12.0	2.0(-10)	[c]

[a] Fixed Parameter;[b] based on weak or partially blended lines only; [c] based on one or a few lines only; [d] includes vibrationally excited lines; [e] non-LTE, see text; [f] based on isotopologues, see text. The column labeled Offset shows the offset in velocity relative to the systemic velocity of the source. $N_{\rm s}$ are the source averaged column densities, $N_{\rm b}$ are the beam averaged column densities and $N_{\rm b}/N_{\rm H_2}$ gives beam averaged abundances.

Table A.53: Results of the line modelling for 17258−3637

Species	Size (")	$T_{\rm ex}$ (K)	$N_{\rm b}$(mol) ($\rm cm^{-2}$)	$N_{\rm s}$(mol) ($\rm cm^{-2}$)	Δv ($\rm km\,s^{-1}$)	Offset ($\rm km\,s^{-1}$)	$N_{\rm b}/N_{\rm H_2}$	
CH_3OH	-[a]	30	3.0(14)	-	4.0	0.0	5.5(-09)	[d]
CO	-[a]	50[a]	3.0(14)	4.5(18)	3.0	-0.5	6.7(-05)	[c], *f*

[a] Fixed Parameter;[b] based on weak or partially blended lines only; [c] based on one or a few lines only; [d] includes vibrationally excited lines; [e] non-LTE, see text; [f] based on isotopologues, see text. The column labeled Offset shows the offset in velocity relative to the systemic velocity of the source. $N_{\rm s}$ are the source averaged column densities, $N_{\rm b}$ are the beam averaged column densities and $N_{\rm b}/N_{\rm H_2}$ gives beam averaged abundances.

Table A.54: Results of the line modelling for 17269−3312

Species	Size (")	T_{ex} (K)	N_b(mol) (cm^{-2})	N_s(mol) (cm^{-2})	Δv ($km\,s^{-1}$)	Offset ($km\,s^{-1}$)	N_b/N_{H_2}	
CCH	-[a]	50[a]	1.3(14)	-	3.0	0.0	9.2(-10)	[c]
CH_3OH	-[a]	15	1.3(14)	-	3.0	0.0	2.8(-08)	[d]
CO	-[a]	50[a]	4.0(15)	1.1(19)	2.8	0.0	6.4(-05)	[c], *f*
CS	-[a]	50[a]	4.0(15)	-	3.0	-1.0	1.1(-09)	[c], *f*
H_2CS	-[a]	50[a]	1.1(19)	-	3.0	-2.0	2.1(-10)	[c]

[a] Fixed Parameter;[b] based on weak or partially blended lines only; [c] based on one or a few lines only; [d] includes vibrationally excited lines; [e] non-LTE, see text; [f] based on isotopologues, see text. The column labeled Offset shows the offset in velocity relative to the systemic velocity of the source. N_s are the source averaged column densities, N_b are the beam averaged column densities and N_b/N_{H_2} gives beam averaged abundances.

Table A.55: Results of the line modelling for 17589−2312

Species	Size (")	T_{ex} (K)	N_b(mol) (cm^{-2})	N_s(mol) (cm^{-2})	Δv ($km\,s^{-1}$)	Offset ($km\,s^{-1}$)	N_b/N_{H_2}	
CCH	-[a]	35	5.0(14)	-	5.0	0.0	8.2(-10)	[c]
CH_3CN	-[a]	180	5.0(14)	-	5.0	-1.0	1.3(-10)	
CH_3OCH_3	-[a]	100	8.0(13)	-	4.5	-2.0	4.1(-09)	[b]
CH_3OCHO-a	-[a]	150[a]	8.0(13)	-	6.0	-3.0	3.3(-09)	[b]
CH_3OH	1.0[a]	190	2.5(15)	2.0(18)	4.0	-2.0	1.0(-08)	[d]
	-[a]	25	2.5(15)	-	4.0	-2.0	9.8(-09)	
CO	-[a]	50[a]	2.0(15)	4.7(19)	5.5	-1.0	6.4(-05)	[c], *f*
CS	-[a]	50[a]	2.0(15)	-	5.0	-1.5	3.8(-09)	[c], *f*
H_2CS	-[a]	50[a]	2.0(18)	-	5.0	-1.5	5.2(-10)	[c]
HC_3N	0.8	240	6.2(15)	4.0(12)	7.0	1.0	1.3(-14)	[c]
	10.0	40	6.0(15)	2.0(12)	7.0	1.0	7.7(-13)	
HNCO	-[a]	150[a]	6.0(15)	-	5.0	-2.0	1.1(-10)	[c]
SO	-[a]	50[a]	4.7(19)	-	4.0	-2.2	9.8(-10)	[e], *f*
SO_2	-[a]	50[a]	3.9(19)	-	6.0	-2.0	1.6(-09)	[e]

[a] Fixed Parameter;[b] based on weak or partially blended lines only; [c] based on one or a few lines only; [d] includes vibrationally excited lines; [e] non-LTE, see text; [f] based on isotopologues, see text. The column labeled Offset shows the offset in velocity relative to the systemic velocity of the source. N_s are the source averaged column densities, N_b are the beam averaged column densities and N_b/N_{H_2} gives beam averaged abundances.

Table A.56: Results of the line modelling for 17470−2853

Species	Size (")	$T_{\rm ex}$ (K)	$N_{\rm b}$(mol) ($\rm cm^{-2}$)	$N_{\rm s}$(mol) ($\rm cm^{-2}$)	Δv ($\rm km\,s^{-1}$)	Offset ($\rm km\,s^{-1}$)	$N_{\rm b}/N_{\rm H_2}$	
CCH	-[a]	25	1.3(14)	-	4.0	2.0	1.3(-09)	[c]
CH_3OH	-[a]	20	1.3(14)	-	6.0	0.0	2.2(-08)	[d]
CO	-[a]	50[a]	2.2(15)	8.0(18)	2.9	0.0	6.6(-05)	[c], *f*
CS	-[a]	50[a]	2.2(15)	-	5.0	0.0	1.1(-09)	[c], *f*

[a] Fixed Parameter;[b] based on weak or partially blended lines only; [c] based on one or a few lines only; [d] includes vibrationally excited lines; [e] non-LTE, see text; [f] based on isotopologues, see text. The column labeled Offset shows the offset in velocity relative to the systemic velocity of the source. $N_{\rm s}$ are the source averaged column densities, $N_{\rm b}$ are the beam averaged column densities and $N_{\rm b}/N_{\rm H_2}$ gives beam averaged abundances.

Table A.57: Results of the line modelling for 18236−1205

Species	Size (")	$T_{\rm ex}$ (K)	$N_{\rm b}$(mol) ($\rm cm^{-2}$)	$N_{\rm s}$(mol) ($\rm cm^{-2}$)	Δv ($\rm km\,s^{-1}$)	Offset ($\rm km\,s^{-1}$)	$N_{\rm b}/N_{\rm H_2}$	
CCH	-[a]	20	8.5(13)	-	3.0	-6.0	5.4(-10)	[c]
CH_3OH	-[a]	15	8.5(13)	-	6.0	0.0	4.5(-08)	[d]
CO	-[a]	50[a]	7.0(15)	1.0(19)	4.0	0.0	5.3(-05)	[c], *f*

[a] Fixed Parameter;[b] based on weak or partially blended lines only; [c] based on one or a few lines only; [d] includes vibrationally excited lines; [e] non-LTE, see text; [f] based on isotopologues, see text. The column labeled Offset shows the offset in velocity relative to the systemic velocity of the source. $N_{\rm s}$ are the source averaged column densities, $N_{\rm b}$ are the beam averaged column densities and $N_{\rm b}/N_{\rm H_2}$ gives beam averaged abundances.

Table A.58: Results of the line modelling for 18319−0834

Species	Size (")	$T_{\rm ex}$ (K)	$N_{\rm b}$(mol) ($\rm cm^{-2}$)	$N_{\rm s}$(mol) ($\rm cm^{-2}$)	Δv ($\rm km\,s^{-1}$)	Offset ($\rm km\,s^{-1}$)	$N_{\rm b}/N_{\rm H_2}$	
CCH	-[a]	70	2.5(14)	-	4.0	2.00	5.3(-10)	[c]
CH_3CN	1.5	110	2.5(14)	5.0(16)	3.0	2.0	7.2(-10)	
	-[a]	50[a]	5.0(16)	-	3.0	2.0	6.3(-11)	
CH_3OCH_3	-[a]	150[a]	3.4(14)	-	2.5	0.0	4.2(-09)	[b]
CH_3OCHO-a	-[a]	150[a]	3.0(13)	2.0(15)	6.0	0.0	3.6(-09)	[b]
CH_3OH	1.0[a]	180	3.0(13)	3.0(18)	5.0	-2.0	1.9(-08)	[d]
	-[a]	30	2.0(15)	-	6.0	-2.0	8.4(-09)	
CO	-[a]	50[a]	2.0(15)	2.3(19)	4.8	-3.0	4.0(-05)	[c], *f*
CS	-[a]	50[a]	2.0(15)	-	5.0	-2.0	2.3(-09)	[c], *f*
H_2CS	-[a]	50[a]	1.7(15)	-	5.0	-2.0	3.8(-10)	[c]
HC_3N	-[a]	150[a]	3.0(18)	-	7.0	0.0	2.1(-10)	[c]
HNCO	-[a]	150[a]	9.2(15)	-	5.0	1.0	1.7(-10)	[c]
SO	-[a]	50[a]	4.0(15)	-	6.0	-1.0	3.2(-09)	[e], *f*

[a] Fixed Parameter;[b] based on weak or partially blended lines only; [c] based on one or a few lines only; [d] includes vibrationally excited lines; [e] non-LTE, see text; [f] based on isotopologues, see text. The column labeled Offset shows the offset in velocity relative to the systemic velocity of the source. $N_{\rm s}$ are the source averaged column densities, $N_{\rm b}$ are the beam averaged column densities and $N_{\rm b}/N_{\rm H_2}$ gives beam averaged abundances.

Table A.59: Results of the line modelling for 18335−0713

Species	Size (")	$T_{\rm ex}$ (K)	$N_{\rm b}$(mol) ($\rm cm^{-2}$)	$N_{\rm s}$(mol) ($\rm cm^{-2}$)	Δv ($\rm km\,s^{-1}$)	Offset ($\rm km\,s^{-1}$)	$N_{\rm b}/N_{\rm H_2}$	
C_2H_5CN	-[a]	150[a]	1.0(14)	-	6.0	0.0	5.0(-10)	[b]
C_2H_5OH	-[a]	150[a]	1.0(14)	-	2.0	0.0	7.5(-10)	[b]
CCH	-[a]	50[a]	1.5(14)	-	4.0	0.0	8.5(-10)	[c]
CH_3CN	0.8	170	1.5(14)	2.0(16)	4.0	-1.0	1.9(-10)	
CH_3OCH_3	-[a]	150[a]	1.7(14)	-	4.5	0.0	9.9(-09)	[b]
CH_3OCHO-a	-[a]	150[a]	1.7(14)	-	5.0	0.0	5.0(-09)	[b]
CH_3OH	1.2	150[a]	2.0(16)	8.0(17)	3.0	0.0	1.7(-08)	[d]
	-[a]	20	3.9(13)	-	3.0	0.0	9.9(-09)	
CO	-[a]	50[a]	2.0(15)	1.2(19)	3.0	1.0	5.0(-05)	[c], *f*
CS	-[a]	50[a]	2.0(15)	-	4.0	0.0	1.2(-09)	[c], *f*
H_2CS	-[a]	50[a]	1.0(15)	-	3.0	0.0	2.5(-10)	[c]
HC_3N	-[a]	150[a]	1.0(15)	-	5.0	1.0	1.5(-10)	[c]
HNCO	-[a]	150[a]	8.00(17)	-	8.5	-1.8	9.9(-10)	[c]
SO	-[a]	50[a]	3.5(15)	-	4.0	-2.0	3.5(-09)	[e], *f*
SO_2	-[a]	50[a]	2.00(15)	-	4.0	-4.0	3.0(-09)	[e]

[a] Fixed Parameter;[b] based on weak or partially blended lines only; [c] based on one or a few lines only; [d] includes vibrationally excited lines; [e] non-LTE, see text; [f] based on isotopologues, see text. The column labeled Offset shows the offset in velocity relative to the systemic velocity of the source. $N_{\rm s}$ are the source averaged column densities, $N_{\rm b}$ are the beam averaged column densities and $N_{\rm b}/N_{\rm H_2}$ gives beam averaged abundances.

Table A.60: Results of the line modelling for 15278−5620

Species	Size (")	$T_{\rm ex}$ (K)	$N_{\rm b}$(mol) ($\rm cm^{-2}$)	$N_{\rm s}$(mol) ($\rm cm^{-2}$)	Δv ($\rm km\,s^{-1}$)	Offset ($\rm km\,s^{-1}$)	$N_{\rm b}/N_{\rm H_2}$	
CCH	-[a]	50[a]	2.8(14)	-	4.0	-11.5	2.3(-09)	[c]
CH_3OH	-[a]	25	2.8(14)	-	4.0	-9.8	2.6(-08)	[d]
CO	-[a]	50[a]	3.2(15)	2.0(19)	5.0	-9.8	1.4(-04)	[c], *f*
CS	-[a]	50[a]	3.2(15)	-	6.0	-9.8	9.7(-09)	[c], *f*
H_2CS	-[a]	50[a]	2.0(19)	-	4.0	-9.8	9.7(-10)	[c]
SO	-[a]	50[a]	1.7(19)	-	3.0	-9.8	4.8(-09)	[e], *f*
SO_2	-[a]	50[a]	1.2(15)	-	4.0	-11.0	7.2(-09)	[e]

[a] Fixed Parameter;[b] based on weak or partially blended lines only; [c] based on one or a few lines only; [d] includes vibrationally excited lines; [e] non-LTE, see text; [f] based on isotopologues, see text. The column labeled Offset shows the offset in velocity relative to the systemic velocity of the source. $N_{\rm s}$ are the source averaged column densities, $N_{\rm b}$ are the beam averaged column densities and $N_{\rm b}/N_{\rm H_2}$ gives beam averaged abundances.

Table A.61: Results of the line modelling for 16076−5134

Species	Size (")	$T_{\rm ex}$ (K)	$N_{\rm b}$(mol) ($\rm cm^{-2}$)	$N_{\rm s}$(mol) ($\rm cm^{-2}$)	Δv ($\rm km\,s^{-1}$)	Offset ($\rm km\,s^{-1}$)	$N_{\rm b}/N_{\rm H_2}$	
CCH	-[a]	50[a]	4.5(14)	-	6.0	-7.3	1.0(-09)	[c]
CH_3OH	-[a]	25	4.5(14)	-	4.0	-6.9	2.7(-09)	[d]
CO	-[a]	50[a]	1.2(15)	2.9(19)	5.0	-7.2	5.5(-05)	[c], *f*
CS	-[a]	50[a]	1.2(15)	-	4.0	-7.3	1.8(-09)	[c], *f*
H_2CS	-[a]	50[a]	2.9(19)	-	4.0	-7.3	1.4(-10)	[c]

[a] Fixed Parameter;[b] based on weak or partially blended lines only; [c] based on one or a few lines only; [d] includes vibrationally excited lines; [e] non-LTE, see text; [f] based on isotopologues, see text. The column labeled Offset shows the offset in velocity relative to the systemic velocity of the source. $N_{\rm s}$ are the source averaged column densities, $N_{\rm b}$ are the beam averaged column densities and $N_{\rm b}/N_{\rm H_2}$ gives beam averaged abundances.

Table A.62: Results of the line modelling for 16172−5028

Species	Size (")	$T_{\rm ex}$ (K)	$N_{\rm b}$(mol) ($\rm cm^{-2}$)	$N_{\rm s}$(mol) ($\rm cm^{-2}$)	Δv ($\rm km\,s^{-1}$)	Offset ($\rm km\,s^{-1}$)	$N_{\rm b}/N_{\rm H_2}$	
CCH	-[a]	50[a]	4.5(14)	-	6.0	-7.3	1.8(-09)	[c]
CH_3OH	-[a]	17	4.5(14)	-	4.0	-5.6	1.8(-08)	[d]
CO	-[a]	50[a]	4.5(15)	1.5(19)	3.0	-5.5	4.9(-05)	[c], *f*
CS	-[a]	50[a]	4.5(15)	-	4.0	-5.6	1.2(-09)	[c], *f*
H_2CS	-[a]	50[a]	1.5(19)	-	4.0	-5.6	1.2(-10)	[c]

[a] Fixed Parameter;[b] based on weak or partially blended lines only; [c] based on one or a few lines only; [d] includes vibrationally excited lines; [e] non-LTE, see text; [f] based on isotopologues, see text. The column labeled Offset shows the offset in velocity relative to the systemic velocity of the source. $N_{\rm s}$ are the source averaged column densities, $N_{\rm b}$ are the beam averaged column densities and $N_{\rm b}/N_{\rm H_2}$ gives beam averaged abundances.

Table A.63: Results of the line modelling for 16172−5028

Species	Size (")	$T_{\rm ex}$ (K)	$N_{\rm b}$(mol) ($\rm cm^{-2}$)	$N_{\rm s}$(mol) ($\rm cm^{-2}$)	Δv ($\rm km\,s^{-1}$)	Offset ($\rm km\,s^{-1}$)	$N_{\rm b}/N_{\rm H_2}$	
CCH	-[a]	50[a]	3.3(14)	-	4.0	-1.0	1.4(-09)	[c]
CH_3OH	-[a]	20	3.3(14)	-	4.0	0.0	1.7(-08)	[d]
CO	-[a]	50[a]	4.0(15)	1.4(19)	3.0	0.0	5.1(-05)	[c], [f]
CS	-[a]	50[a]	4.0(15)	-	4.0	0.0	2.1(-09)	[c], [f]
H_2CS	-[a]	50[a]	1.4(19)	-	4.0	0.0	2.6(-10)	[c]

[a] Fixed Parameter;[b] based on weak or partially blended lines only; [c] based on one or a few lines only; [d] includes vibrationally excited lines; [e] non-LTE, see text; [f] based on isotopologues, see text. The column labeled Offset shows the offset in velocity relative to the systemic velocity of the source. $N_{\rm s}$ are the source averaged column densities, $N_{\rm b}$ are the beam averaged column densities and $N_{\rm b}/N_{\rm H_2}$ gives beam averaged abundances.

Table A.64: Results of the line modelling for 16175−5002

Species	Size (")	$T_{\rm ex}$ (K)	$N_{\rm b}$(mol) ($\rm cm^{-2}$)	$N_{\rm s}$(mol) ($\rm cm^{-2}$)	Δv ($\rm km\,s^{-1}$)	Offset ($\rm km\,s^{-1}$)	$N_{\rm b}/N_{\rm H_2}$	
C_2H_5CN	1.0	150[a]	5.0(16)	5.0(16)	4.0	-3.6	3.4(-10)	[b]
CCH	-[a]	50[a]	1.5(14)	-	5.0	-3.7	7.3(-10)	[c]
CH_3CN	1.5	160	3.2(14)	1.5(16)	5.0	-4.5	2.3(-10)	
CH_3OCH_3	-[a]	150[a]	3.2(14)	-	4.5	-3.6	9.1(-09)	[b]
CH_3OCHO-a	-[a]	150[a]	1.5(16)	-	5.0	-3.6	4.5(-09)	[b]
CH_3OH	1.5	170	1.0(14)	1.0(18)	4.0	-3.5	1.6(-08)	[d]
	-[a]	15	4.0(15)	-	4.0	-3.5	1.7(-08)	
CO	-[a]	50[a]	4.0(15)	1.4(19)	5.0	-3.6	2.7(-05)	[c], [f]
CS	-[a]	50[a]	2.0(15)	-	5.0	-3.6	1.6(-09)	[c], [f]
H_2CS	-[a]	50[a]	2.0(15)	-	5.5	-4.0	3.9(-10)	[c]
HC_3N	-[a]	150[a]	1.00(18)	-	5.0	-3.60	2.3(-10)	[c]
HNCO	-[a]	150[a]	6.9(15)	-	7.0	-5.5	3.4(-10)	[c]
SO	-[a]	50[a]	7.50(15)	-	5.0	-3.60	1.6(-09)	[e], [f]
SO_2	-[a]	50[a]	7.5(15)	-	4.0	-3.60	6.8(-10)	[e]

[a] Fixed Parameter;[b] based on weak or partially blended lines only; [c] based on one or a few lines only; [d] includes vibrationally excited lines; [e] non-LTE, see text; [f] based on isotopologues, see text. The column labeled Offset shows the offset in velocity relative to the systemic velocity of the source. $N_{\rm s}$ are the source averaged column densities, $N_{\rm b}$ are the beam averaged column densities and $N_{\rm b}/N_{\rm H_2}$ gives beam averaged abundances.

Table A.65: Results of the line modelling for 17016−4142

Species	Size (")	$T_{\rm ex}$ (K)	$N_{\rm b}$(mol) ($\rm cm^{-2}$)	$N_{\rm s}$(mol) ($\rm cm^{-2}$)	Δv ($\rm km\,s^{-1}$)	Offset ($\rm km\,s^{-1}$)	$N_{\rm b}/N_{\rm H_2}$	
CCH	-[a]	50[a]	6.2(14)	-	4.5	11.0	1.1(-09)	[c]
CH_3OH	-[a]	20	6.2(14)	-	6.0	0.0	6.3(-09)	[d]
CO	-[a]	50[a]	3.5(15)	3.1(19)	3.9	0.0	4.6(-05)	[c], [f]
CS	-[a]	50[a]	3.5(15)	-	3.3	0.0	7.2(-10)	[c], [f]
H_2CS	-[a]	50[a]	3.1(19)	-	3.0	-0.4	1.0(-10)	[c]
HNCO	-[a]	150[a]	2.6(19)	-	3.0	6.4	7.2(-11)	[c]

[a] Fixed Parameter;[b] based on weak or partially blended lines only; [c] based on one or a few lines only; [d] includes vibrationally excited lines; [e] non-LTE, see text; [f] based on isotopologues, see text. The column labeled Offset shows the offset in velocity relative to the systemic velocity of the source. $N_{\rm s}$ are the source averaged column densities, $N_{\rm b}$ are the beam averaged column densities and $N_{\rm b}/N_{\rm H_2}$ gives beam averaged abundances.

Table A.66: Results of the line modelling for 17271−3439

Species	Size (")	$T_{\rm ex}$ (K)	$N_{\rm b}$(mol) ($\rm cm^{-2}$)	$N_{\rm s}$(mol) ($\rm cm^{-2}$)	Δv ($\rm km\,s^{-1}$)	Offset ($\rm km\,s^{-1}$)	$N_{\rm b}/N_{\rm H_2}$	
C_2H_5CN	-[a]	150[a]	6.0(13)	-	3.0	0.0	3.1(-10)	[b]
CCH	-[a]	50[a]	6.0(13)	-	4.0	0.0	1.4(-09)	[c]
CH_3CCH	-[a]	50[a]	2.8(14)	-	5.5	0.0	7.7(-09)	[c]
CH_3CN	7.0	20	2.8(14)	1.0(15)	5.4	0.0	6.6(-10)	
	1.6	100	1.5(15)	8.0(15)	5.4	0.0	3.2(-10)	
CH_3OCH_3	-[a]	70	1.5(15)	-	4.5	0.0	6.6(-09)	[b]
CH_3OCHO-a	-[a]	150[a]	1.0(15)	-	3.0	0.0	2.6(-09)	[b]
CH_3OH	1.3	200	1.3(14)	1.0(18)	3.0	-1.0	2.7(-08)	[d]
	12.0	50[a]	8.0(15)	1.0(16)	4.0	0.0	1.6(-08)	
CO	-[a]	50[a]	6.3(13)	2.8(19)	4.5	-0.5	1.2(-04)	[c], [f]
CS	-[a]	50[a]	1.3(15)	-	6.0	0.0	1.3(-08)	[c], [f]
DCN	-[a]	150[a]	1.3(15)	-	6.0	0.0	1.5(-10)	
H_2CO	-[a]	20	5.0(14)	-	5.0	-1.0	1.0(-09)	[e]
	1.6	250	5.0(14)	2.0(16)	5.0	-1.0	8.2(-10)	
H_2CS	-[a]	50[a]	1.0(18)	-	5.0	0.0	1.3(-09)	[c]
HC_3N	1.6	100	5.2(15)	2.0(16)	6.0	-5.0	8.2(-10)	[c]
HNCO	1.6	75	2.8(19)	3.0(16)	6.0	0.0	1.2(-09)	[c]
SO	10.0	50[a]	2.6(15)	3.0(16)	6.0	0.0	3.6(-08)	[e], [f]
SO_2	-[a]	35	2.6(15)	-	6.0	0.0	9.2(-08)	[e]

[a] Fixed Parameter;[b] based on weak or partially blended lines only; [c] based on one or a few lines only; [d] includes vibrationally excited lines; [e] non-LTE, see text; [f] based on isotopologues, see text. The column labeled Offset shows the offset in velocity relative to the systemic velocity of the source. $N_{\rm s}$ are the source averaged column densities, $N_{\rm b}$ are the beam averaged column densities and $N_{\rm b}/N_{\rm H_2}$ gives beam averaged abundances.

Table A.67: Results of the line modelling for 12326−6128

Species	Size (")	$T_{\rm ex}$ (K)	$N_{\rm b}$(mol) ($\rm cm^{-2}$)	$N_{\rm s}$(mol) ($\rm cm^{-2}$)	Δv ($\rm km\,s^{-1}$)	Offset ($\rm km\,s^{-1}$)	$N_{\rm b}/N_{\rm H_2}$	
C_2H_5CN	10.0	150[a]	1.0(14)	1.0(14)	3.0	0.0	4.2(-11)	[b]
CCH	-[a]	50[a]	2.4(13)	-	10.0	-4.0	8.8(-10)	[c]
CH_3CCH	-[a]	100	5.0(14)	-	7.5	-1.50	4.4(-09)	[c]
CH_3CN	1.1	170	5.0(14)	1.5(16)	5.5	4.0	9.9(-11)	
	1.0[a]	180	2.5(15)	3.0(16)	5.5	-5.0	1.6(-10)	
CH_3OCH_3	-[a]	150[a]	2.5(15)	-	2.0	2.0	1.8(-10)	[b]
CH_3OCHO-a	-[a]	150[a]	1.5(16)	-	2.0	0.0	1.8(-10)	[b]
CH_3OH	1.0[a]	170	5.6(13)	5.0(17)	3.0	5.0	2.6(-09)	[d]
	1.0[a]	170	3.0(16)	5.0(17)	3.0	-5.0	2.6(-09)	
	-[a]	30	9.2(13)	-	7.0	-2.0	7.0(-09)	
CO	-[a]	50[a]	1.0(14)	6.3(19)	9.0	-0.5	9.2(-05)	[c], [f]
CS	10.0	55	1.0(14)	6.0(15)	7.0	-0.5	2.5(-09)	[c], [f]
H_2CO	-[a]	20	1.0(14)	-	9.0	-2.0	5.8(-10)	[e]
	1.0	250	1.0(14)	2.0(17)	7.0	-2.0	1.1(-09)	
H_2CS	-[a]	50[a]	5.0(17)	-	10.0	-0.5	4.6(-10)	[c]
HC_3N	-[a]	150[a]	1.5(15)	-	6.0	0.0	1.8(-11)	[c]
HNCO	1.0[a]	80	1.5(15)	5.0(16)	6.0	-2.0	2.6(-10)	[c]
SO	4.0	40	4.0(15)	4.0(17)	6.0	-0.5	3.3(-08)	[e], [f]
SO_2	-[a]	30	4.0(15)	-	10.0	0.0	8.8(-08)	[e]

[a] Fixed Parameter;[b] based on weak or partially blended lines only; [c] based on one or a few lines only; [d] includes vibrationally excited lines; [e] non-LTE, see text; [f] based on isotopologues, see text. The column labeled Offset shows the offset in velocity relative to the systemic velocity of the source. $N_{\rm s}$ are the source averaged column densities, $N_{\rm b}$ are the beam averaged column densities and $N_{\rm b}/N_{\rm H_2}$ gives beam averaged abundances.

Table A.68: Results of the line modelling for 16060−5146

Species	Size (")	$T_{\rm ex}$ (K)	$N_{\rm b}$(mol) ($\rm cm^{-2}$)	$N_{\rm s}$(mol) ($\rm cm^{-2}$)	Δv ($\rm km\,s^{-1}$)	Offset ($\rm km\,s^{-1}$)	$N_{\rm b}/N_{\rm H_2}$	
C_2H_5CN	-[a]	150[a]	5.0(13)	5.0(13)	3.0	2.0	1.5(-10)	[b]
CCH	-[a]	50[a]	4.0(10)	-	6.0	-1.0	1.1(-09)	[c]
CH_3CCH	-[a]	50[a]	4.0(10)	-	7.0	0.0	1.0(-08)	[c]
CH_3CN	5.0	30	3.2(14)	3.0(15)	4.5	-1.0	7.3(-10)	
	0.7	250	3.2(14)	1.0(17)	4.5	-1.0	5.2(-10)	
CH_3OCH_3	-[a]	200	0.3(16)	-	2.5	3.0	4.5(-09)	[b]
CH_3OCHO-a	-[a]	150[a]	3.0(15)	-	3.0	0.0	1.4(-09)	[b]
CH_3OH	1.8	140	3.0(15)	7.0(17)	6.0	1.5	2.4(-08)	[d]
	13.0	30	2.1(14)	5.0(15)	6.0	e	5.9(-09)	
CO	-[a]	50[a]	1.0(17)	4.0(19)	5.5	-0.5	1.1(-04)	[c], [f]
CS	4.0	90	1.5(14)	7.0(16)	5.0	0.0	1.1(-08)	[c], [f]
H_2CO	1.2	350	1.3(15)	2.0(17)	6.0	-0.5	3.1(-09)	[e]
	-[a]	30	1.3(15)	-	6.0	-0.5	1.0(-09)	
H_2CS	-[a]	50[a]	4.0(14)	-	6.0	0.0	1.0(-09)	[c]
HC_3N	0.8	240	4.0(14)	4.0(16)	7.0	1.0	2.7(-10)	[c]
	10.0	40	7.0(17)	2.0(15)	7.0	1.0	1.6(-09)	
HC_3HO	-[a]	150[a]	6.9(15)	-	10.0	-2.0	8.7(-10)	[c]
HCN	4.0	150[a]	5.0(15)	3.0(16)	6.0	0.0	4.9(-09)	[c], [f]
HNCO	-[a]	150[a]	4.0(19)	-	6.0	1.0	3.5(-10)	[c]
SO	8.0	30	3.3(19)	5.0(16)	7.0	1.0	2.9(-08)	[e], [f]
SO_2	-[a]	30	7.0(16)	-	8.0	0.0	1.0(-07)	[e]
	-[a]	250	3.3(15)	-	8.0	0.0	3.5(-09)	

[a] Fixed Parameter;[b] based on weak or partially blended lines only; [c] based on one or a few lines only; [d] includes vibrationally excited lines; [e] non-LTE, see text; [f] based on isotopologues, see text. The column labeled Offset shows the offset in velocity relative to the systemic velocity of the source. $N_{\rm s}$ are the source averaged column densities, $N_{\rm b}$ are the beam averaged column densities and $N_{\rm b}/N_{\rm H_2}$ gives beam averaged abundances.

Table A.69: Results of the line modelling for 16065−5158

Line	Size	T_{ex}	N(mol)	Δ v	Offset	N_b/N_{H_2}	N_{H_2}
	"	K	cm^{-2}	km/s	km/s		cm^{-2}
^{13}CO	-[a]	50[a]	4.4(16)	3.0	0.5	4.9(-07)	8.9e+22
$C^{18}O$	-[a]	50[a]	8.0(15)	2.5	0.5	9.0(-08)	8.9e+22
CH_3OH	-[a]	15	8.0(14)	3.0	0.0	9.0(-09)	8.9e+22
CS	-[a]	50[a]	2.9(13)	3.0	0.5	3.3(-10)	8.9e+22
H_2CO	-[a]	50[a]	6.0(13)	3.0	0.0	6.7(-10)	8.9e+22

[a] Fixed Parameter;[b] based on weak or partially blended lines only; [c] based on one or a few lines only; [d] includes vibrationally excited lines; [e] non-LTE, see text; [f] based on isotopologues, see text.

Table A.70: Result of the line modelling for 06055+2039

Line	Size	T_{ex}	N(mol)	Δ v	Offset	N_b/N_{H_2}	N_{H_2}
	"	K	cm^{-2}	km/s	km/s		cm^{-2}
^{13}CO	-[a]	50[a]	5.5(16)	3.7	0.1	2.2(-07)	2.54e+23
$C^{18}O$	-[a]	50[a]	8.3(15)	2.9	0.25	3.3(-08)	2.54e+23
CH_3OH	-[a]	20	2.0(14)	3.0	0.0	7.9(-10)	2.54e+23
CS	-[a]	50[a]	3.0(13)	3.3	0.0	1.2(-10)	2.54e+23
H_2CO	-[a]	50[a]	7.5(13)	3.0	0.0	3.0(-10)	2.54e+23

[a] Fixed Parameter;[b] based on weak or partially blended lines only; [c] based on one or a few lines only; [d] includes vibrationally excited lines; [e] non-LTE, see text; [f] based on isotopologues, see text.

Table A.71: Result of the line modelling for 06056+2131

Line	Size	T_{ex}	N(mol)	Δ v	Offset	N_b/N_{H_2}	N_{H_2}
	"	K	cm^{-2}	km/s	km/s		cm^{-2}
^{13}CO	-[a]	50[a]	4.0(16)	3.9	-0.10	1.6(-07)	2.5e+23
$C^{18}O$	-[a]	50[a]	4.5(15)	3.4	0.0	1.8(-08)	2.5e+23
CH_3OH	-[a]	15	5.0(15)	4.0	0.0	2.0(-08)	2.5e+23
CS	-[a]	50[a]	1.0(14)	3.9	-0.20	4.0(-10)	2.5e+23
H_2CO	-[a]	60	3.3(14)	4.0	0.0	1.3(-09)	2.5e+23

[a] Fixed Parameter;[b] based on weak or partially blended lines only; [c] based on one or a few lines only; [d] includes vibrationally excited lines; [e] non-LTE, see text; [f] based on isotopologues, see text.

Table A.72: Result of the line modelling for 06058+2138

Line	Size	T_{ex}	N(mol)	Δ v	Offset	N_b/N_{H_2}	N_{H_2}
	"	K	cm^{-2}	km/s	km/s		cm^{-2}
^{13}CO	-[a]	50[a]	4.0(16)	2.3	0.0	3.5(-07)	1.13e+23
$C^{18}O$	-[a]	50[a]	6.0(15)	2.5	0.5	5.3(-08)	1.13e+23
CH_3OH	-[a]	20	2.5(14)	3.0	1.0	2.2(-09)	1.13e+23
CS	-[a]	50[a]	1.9(13)	2.4	0.2	1.7(-10)	1.13e+23
H_2CO	-[a]	50[a]	6.0(13)	3.0	1.0	5.3(-10)	1.13e+23

[a] Fixed Parameter;[b] based on weak or partially blended lines only; [c] based on one or a few lines only; [d] includes vibrationally excited lines; [e] non-LTE, see text; [f] based on isotopologues, see text.

Table A.73: Result of the line modelling for 06061+2151

Line	Size	T_{ex}	N(mol)	Δ v	Offset	N_b/N_{H_2}	N_{H_2}
	"	K	cm^{-2}	km/s	km/s		cm^{-2}
^{13}CO	-[a]	50[a]	3.0(16)	2.40	0.0	5.6(-07)	5.4e+22
$C^{18}O$	-[a]	50[a]	4.0(15)	2.0	0.0	7.4(-08)	5.4e+22
CH_3OH	-[a]	20	1.0(14)	3.0	0.0	1.9(-09)	5.4e+22
CS	-[a]	50[a]	4.0(12)	2.0	0.0	7.4(-11)	5.4e+22
H_2CO	-[a]	40	2.0(13)	3.0	0	3.7(-10)	5.4e+22

[a] Fixed Parameter;[b] based on weak or partially blended lines only; [c] based on one or a few lines only; [d] includes vibrationally excited lines; [e] non-LTE, see text; [f] based on isotopologues, see text.

Table A.74: Result of the line modelling for 06063+2040

Line	Size	T_{ex}	N(mol)	Δ v	Offset	N_b/N_{H_2}	N_{H_2}
	"	K	cm^{-2}	km/s	km/s		cm^{-2}
^{13}CO	-[a]	60	2.0(17)	3.0	0.0	2.9(-07)	6.88e+23
$C^{18}O$	-[a]	50[a]	1.6(16)	2.5	0.0	2.3(-08)	6.88e+23
CH_3OH	-[a]	20	5.5(14)	3.0	0.0	8.0(-10)	6.88e+23
CS	-[a]	50[a]	1.2(14)	2.8	-0.20	1.7(-10)	6.88e+23
H_2CO	-[a]	50[a]	1.1(14)	3.0	0.0	1.6(-10)	6.88e+23

[a] Fixed Parameter;[b] based on weak or partially blended lines only; [c] based on one or a few lines only; [d] includes vibrationally excited lines; [e] non-LTE, see text; [f] based on isotopologues, see text.

Table A.75: Result of the line modelling for 06099+1800

Line	Size	T_{ex}	N(mol)	Δ v	Offset	N_b/N_{H_2}	N_{H_2}
	"	K	cm^{-2}	km/s	km/s		cm^{-2}
^{13}CO	-[a]	50[a]	3.5(16)	2.5	0.7	2.3(-07)	1.55e+23
$C^{18}O$	-[a]	50[a]	3.3(15)	2.5	1.0	2.1(-08)	1.55e+23
CH_3OH	-[a]	25	1.0(14)	3.0	0.0	6.5(-10)	1.55e+23
CS	-[a]	50[a]	1.9(13)	2.3	0.9	1.2(-10)	1.55e+23
H_2CO	-[a]	60	4.0(13)	3.0	0	2.6(-10)	1.55e+23

[a] Fixed Parameter;[b] based on weak or partially blended lines only; [c] based on one or a few lines only; [d] includes vibrationally excited lines; [e] non-LTE, see text; [f] based on isotopologues, see text.

Table A.76: Result of the line modelling for 06117+1350

Line	Size	T_{ex}	N(mol)	Δ v	Offset	N_b/N_{H_2}	N_{H_2}
	"	K	cm^{-2}	km/s	km/s		cm^{-2}
^{13}CO	-[a]	50[a]	2.5(16)	1.6	-0.2	2.5(-07)	1.01e+23
$C^{18}O$	-[a]	50[a]	4.1(15)	1.4	-0.2	4.1(-08)	1.01e+23
CH_3OH	-[a]	25	1.5(14)	3.0	0.0	1.5(-09)	1.01e+23
CS	-[a]	50[a]	5.0(12)	1.5	-0.2	5.0(-11)	1.01e+23
H_2CO	-[a]	50[a]	3.0(13)	2.0	0.0	3.0(-10)	1.01e+23

[a] Fixed Parameter;[b] based on weak or partially blended lines only; [c] based on one or a few lines only; [d] includes vibrationally excited lines; [e] non-LTE, see text; [f] based on isotopologues, see text.

Table A.77: Result of the line modelling for 06155+2319

Source	M_{vir} ($M_\odot$)
12326-6245	1.2e+03
14453-5912	3.3e+02
14498-5856	1.1e+03
15278-5620	4.8e+02
15394-5358	3.3e+03
15437-5343	1.1e+03
15557-5215	2.3e+03
16076-5134	3.4e+03
16060-5146	5.3e+03
16065-5158	2.4e+03
16071-5142	2.6e+03
16172-5028	2.5e+03
16175-5002	5.5e+02
16351-4722	8.6e+02
16458-4512	5.4e+03
16484-4603	7.4e+02
16524-4300	8.2e+02
16562-3959	6.2e+02
17016-4142	1.1e+03
17136-3617	5.2e+02
17204-3636	4.8e+02
17258-3637	1.4e+03
17269-3312	5.2e+02
17271-3439	1.2e+03
17470-2853	5.6e+03
17589-2312	5.5e+02
18236-1205	5.2e+02
18319-0834	2.6e+03
18335-0713	2.0e+03

Table A.78: Virial masses.

Source	$P_{\rm clump}/k$ 1.0×10^{8} (K cm^{-3})	$P_{\rm S,core}/k$ 1.0×10^{8} (K cm^{-3})	$\sigma_{\rm S}$ 1.0×10^{-1} (km s^{-1})	$c_{\rm th}$ 1.0×10^{-1} (km s^{-1})	$R_{\rm core}$ 1.0×10^{-2} (pc)	$n_{\rm H,S}$ 1.0×10^{5} (cm^{-3})	$\dot{\rm m}_{*}$ 1.0×10^{-4} (M$_\odot$yr^{-1})	t_{*f} 1.0×10^{4} (yr)
12326−3606	1.1	2.9	9.3	8.5	5.5	7.0	3.6	9.1
15278−5620	0.3	0.8	7.2	7.4	6.1	3.4	1.7	13.0
16060−5146	13.8	34.4	12.3	7.9	2.8	47.6	8.4	3.5
16065−5158	1.3	3.3	13.2	7.1	10.3	4.0	10.3	11.9
16065−5158	1.5	3.8	9.5	7.9	5.0	8.9	3.9	8.1
17016−4142	3.1	7.7	10.8	7.9	4.6	13.8	5.7	6.5
17470−2853	0.2	0.6	9.7	8.3	13.0	1.4	4.1	20.5
18335−0713	0.7	1.7	10.7	8.1	9.6	3.1	5.5	13.6

Table A.79: Parameters of the cores derived from the surface density Σ under the assumption of the turbulent core model (McKee & Tan,2003).

A.2 Figures

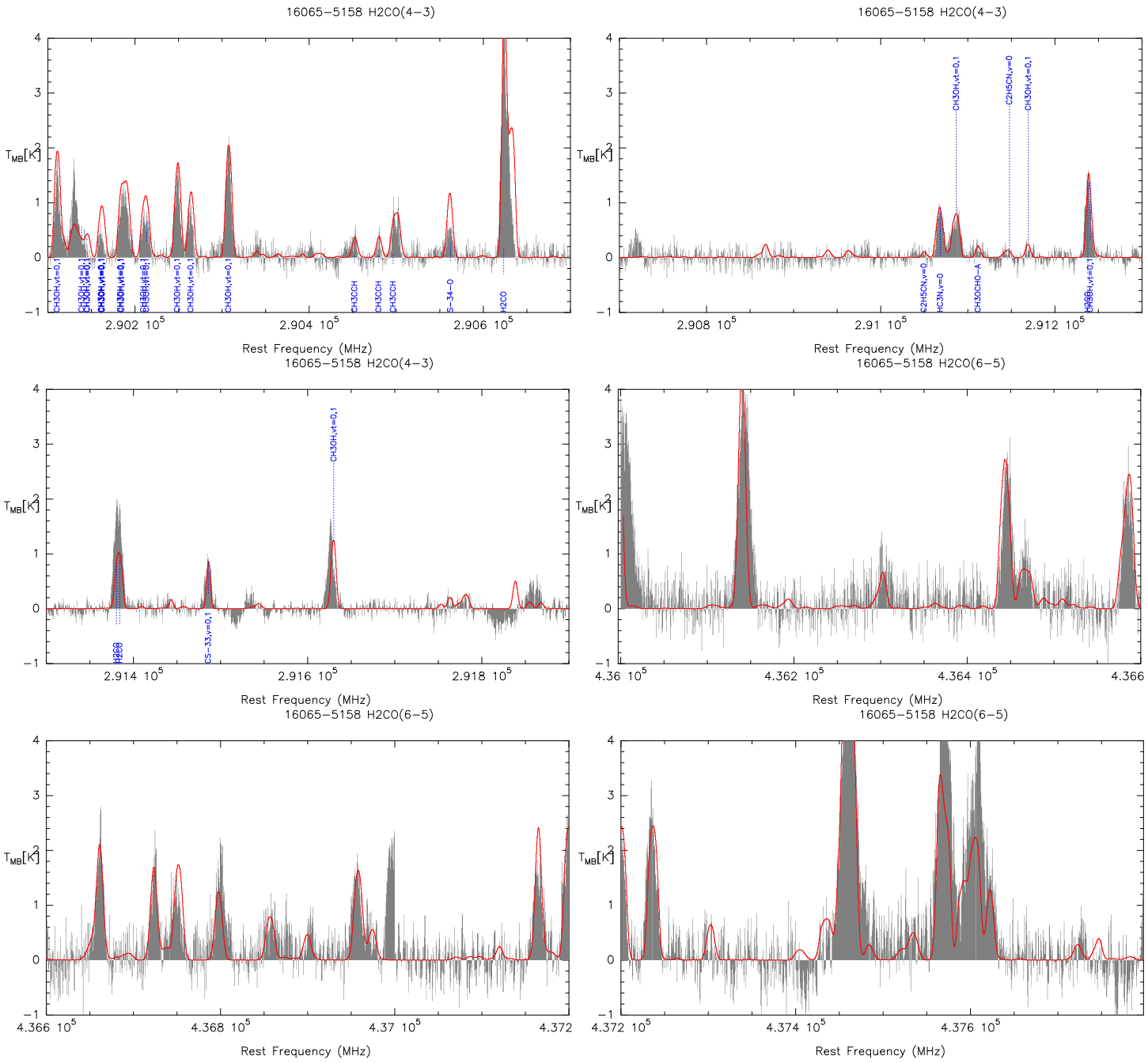

Figure A.1: Molecular emission of 16065-5158. The best fit synthetic spectrum is overplotted (solid line).

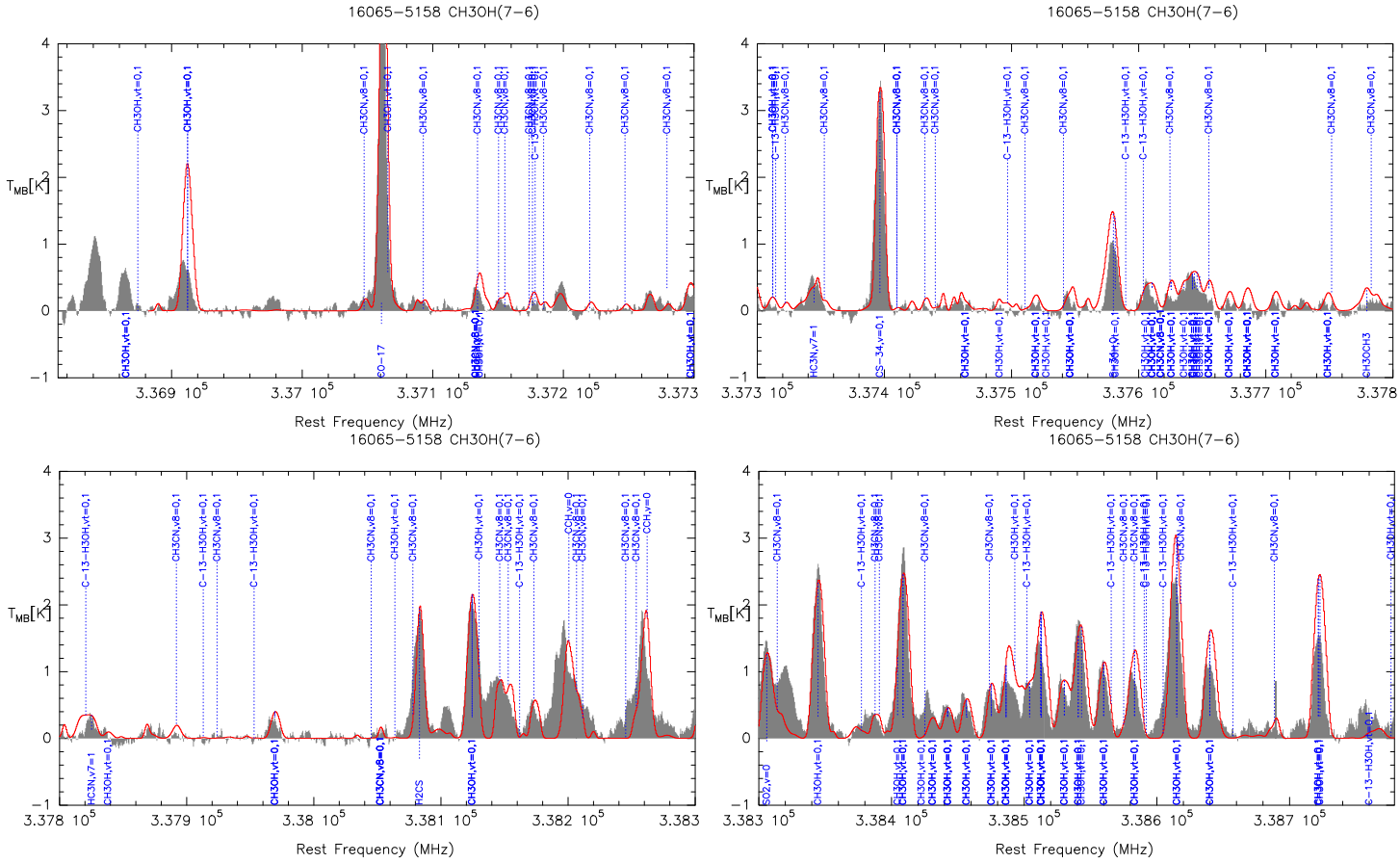

Figure A.2: Molecular emission of 16065-5158. The best fit synthetic spectrum is overplotted (solid line).

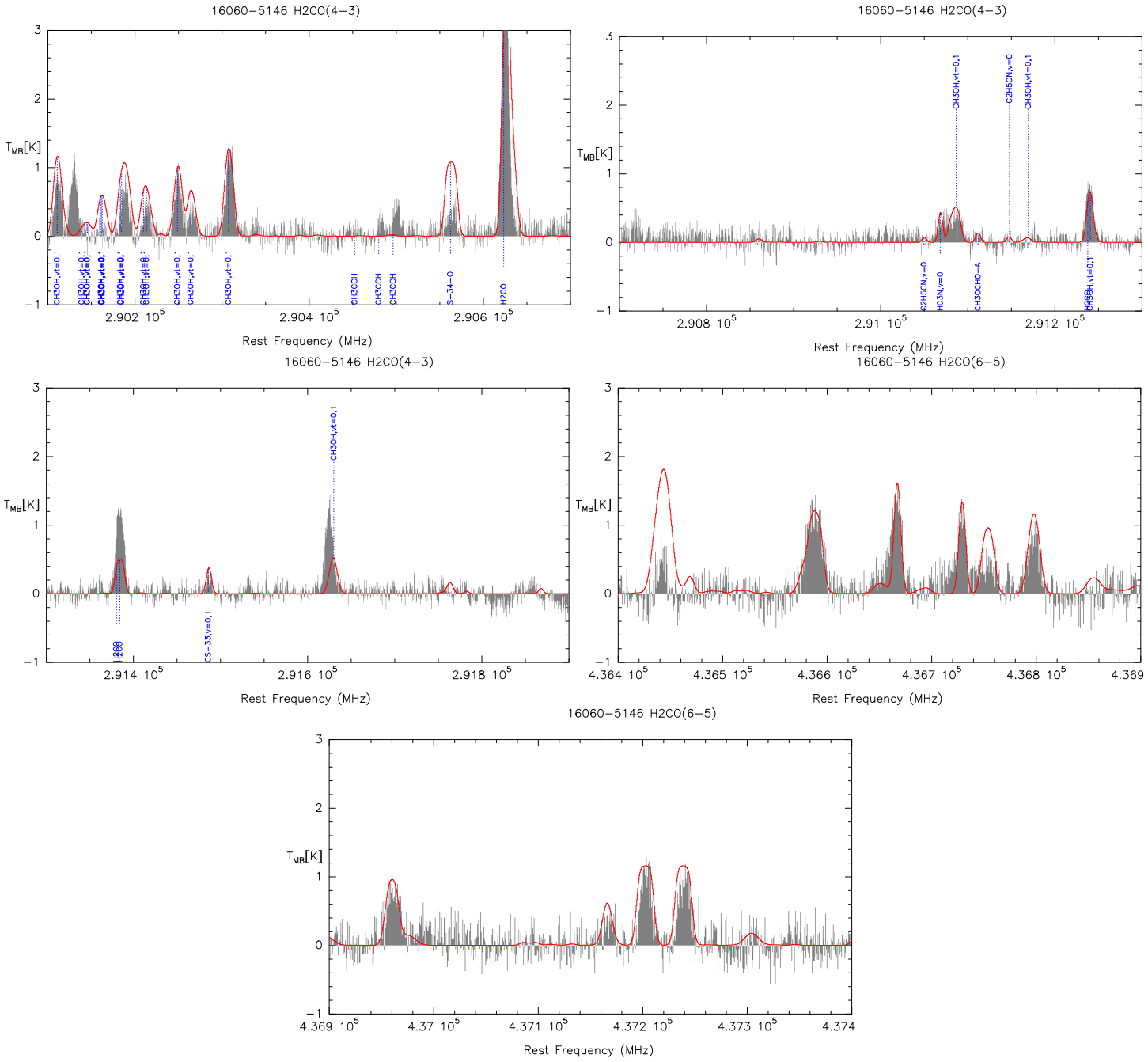

Figure A.3: Molecular emission of 16060-5146. The best fit synthetic spectrum is overplotted (solid line).

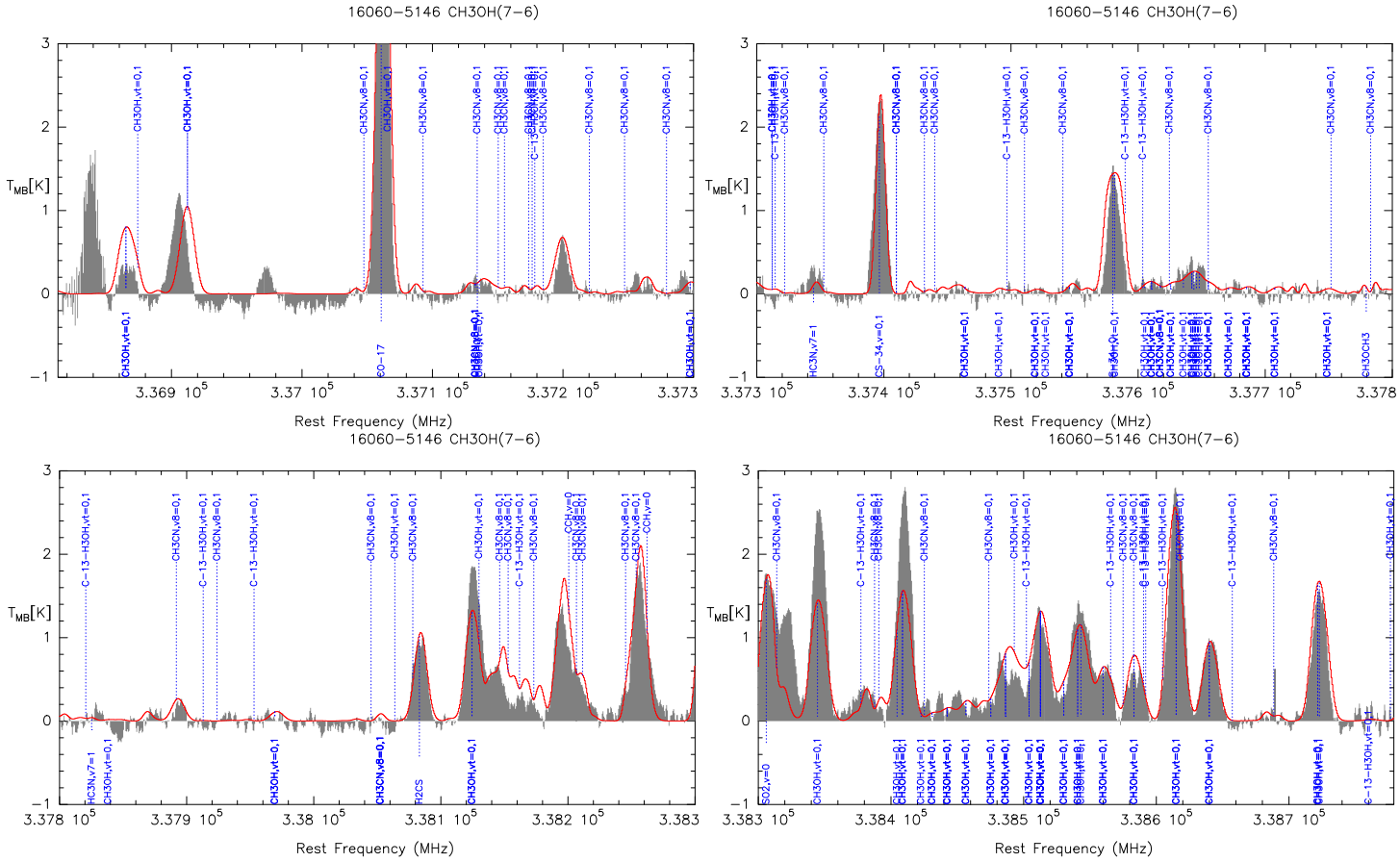

Figure A.4: Molecular emission of 16060-5146. The best fit synthetic spectrum is overplotted (solid line).

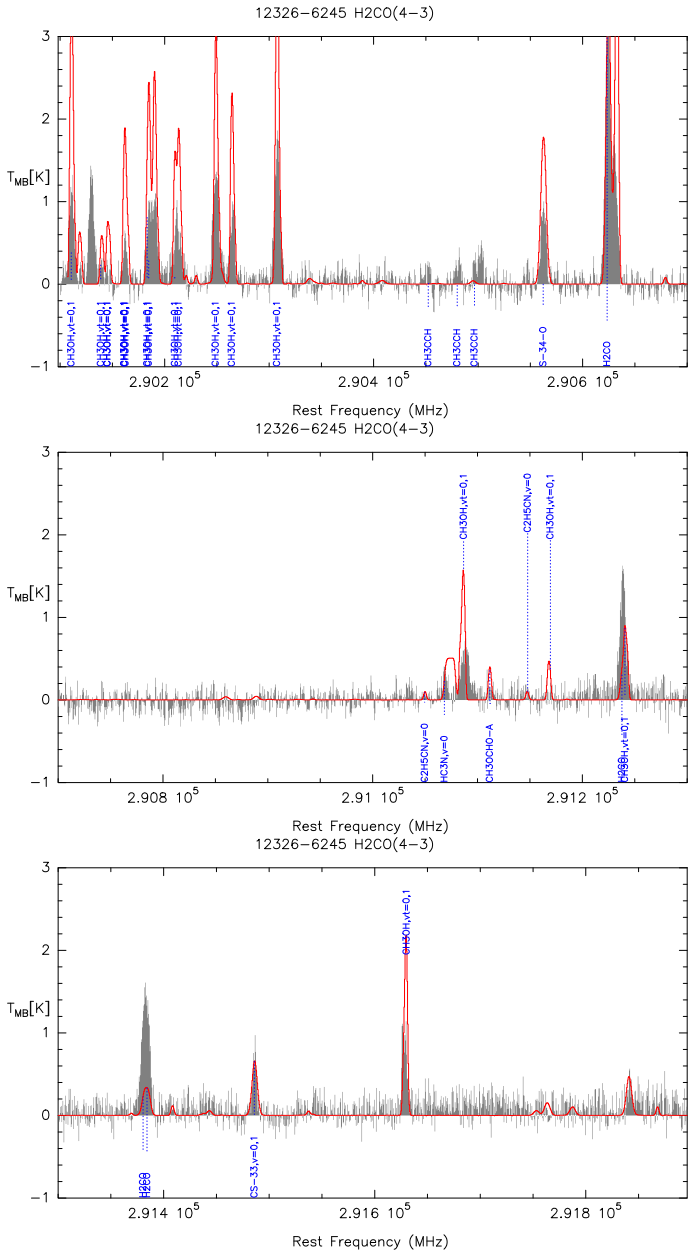

Figure A.5: Molecular emission of 12326-6245. The best fit synthetic spectrum is overplotted (solid line).

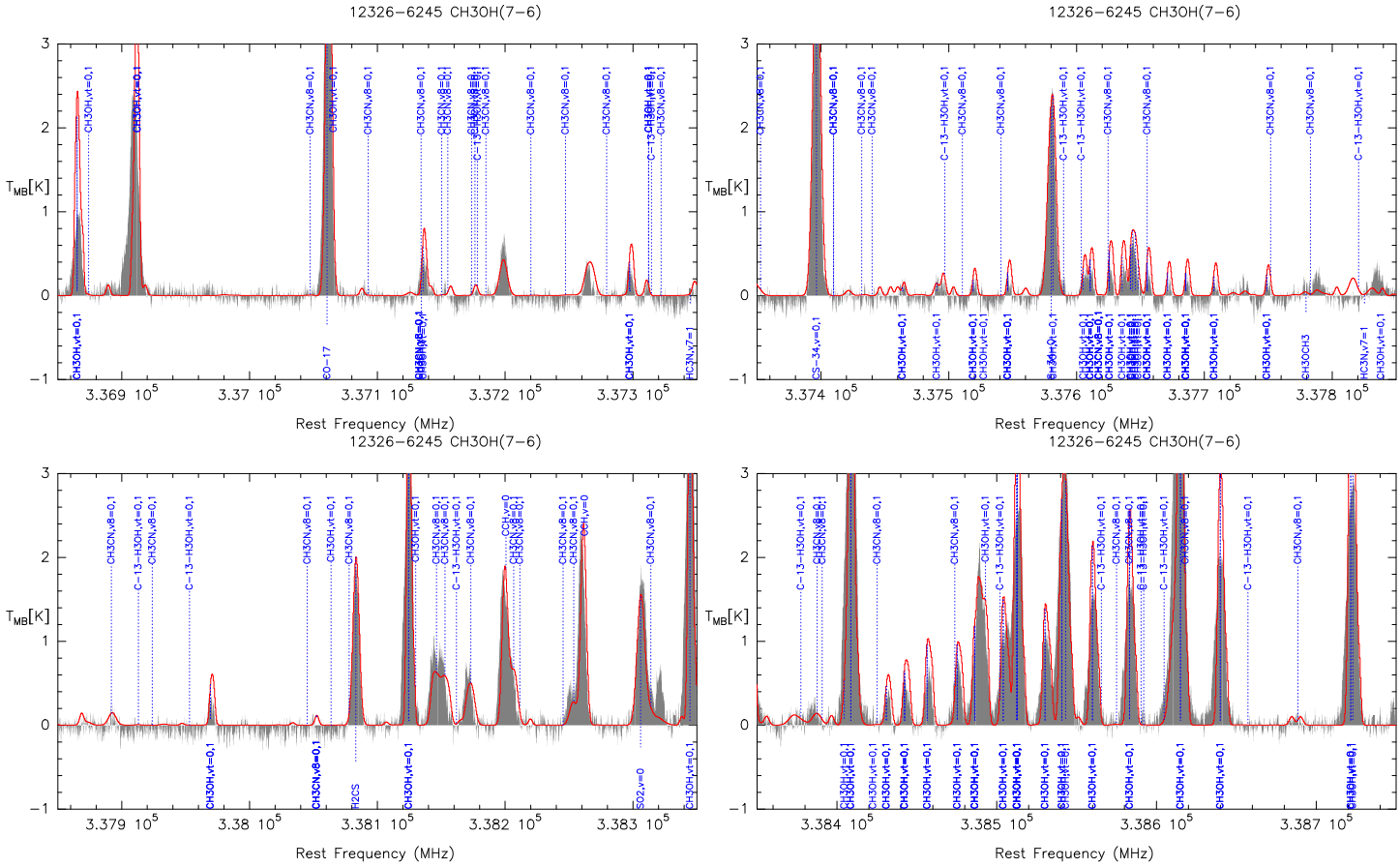

Figure A.6: Molecular emission of 12326-6245. The best fit synthetic spectrum is overplotted (solid line).

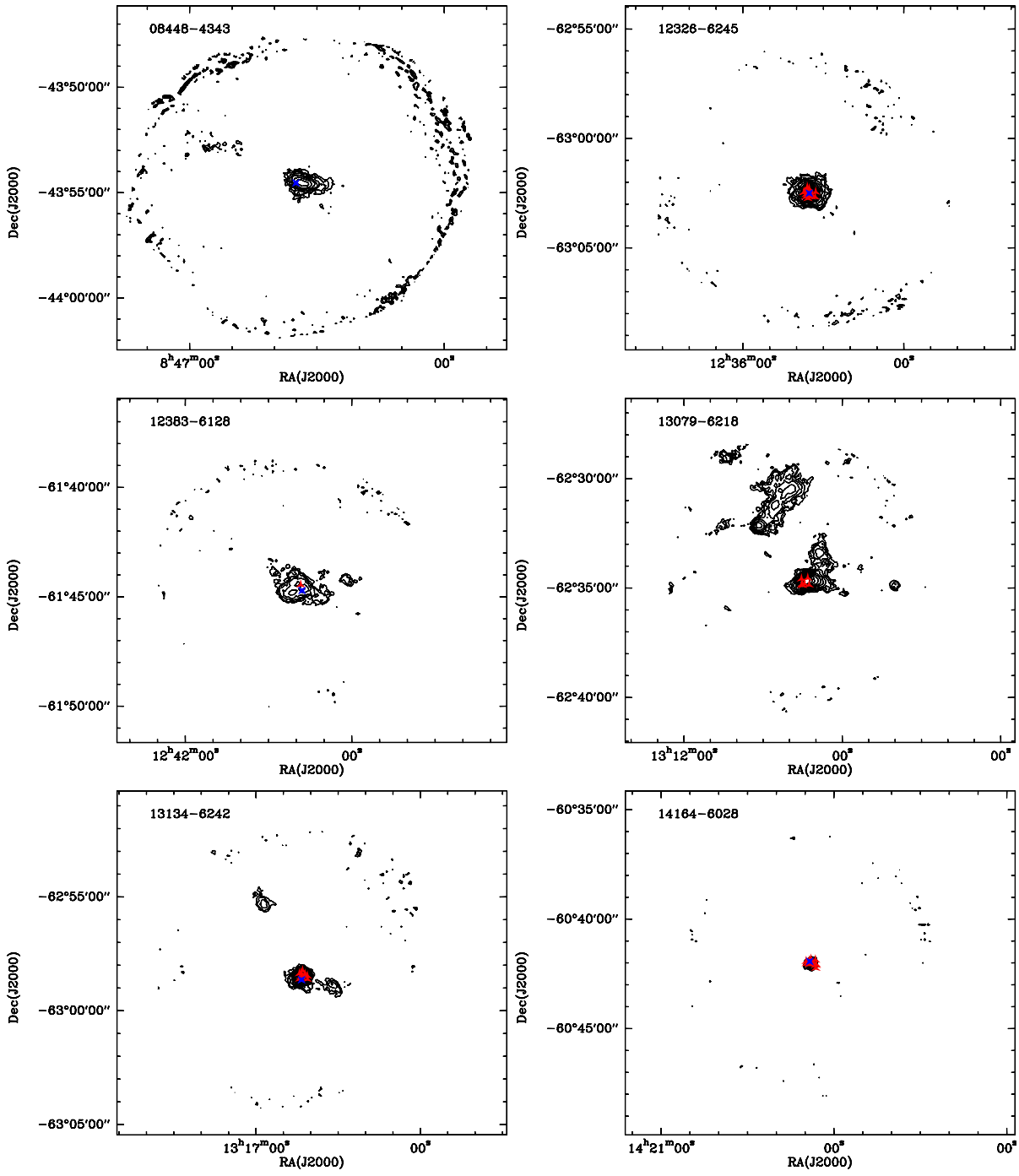

Figure A.7: LABOCA 870 μm data. Contours start at 3 σ with steps of 1.4 σ. The blue stars mark the location of the MSX associated MSX point source, while the red triangles mark the location of the GLIMPSE 8 μm point source.

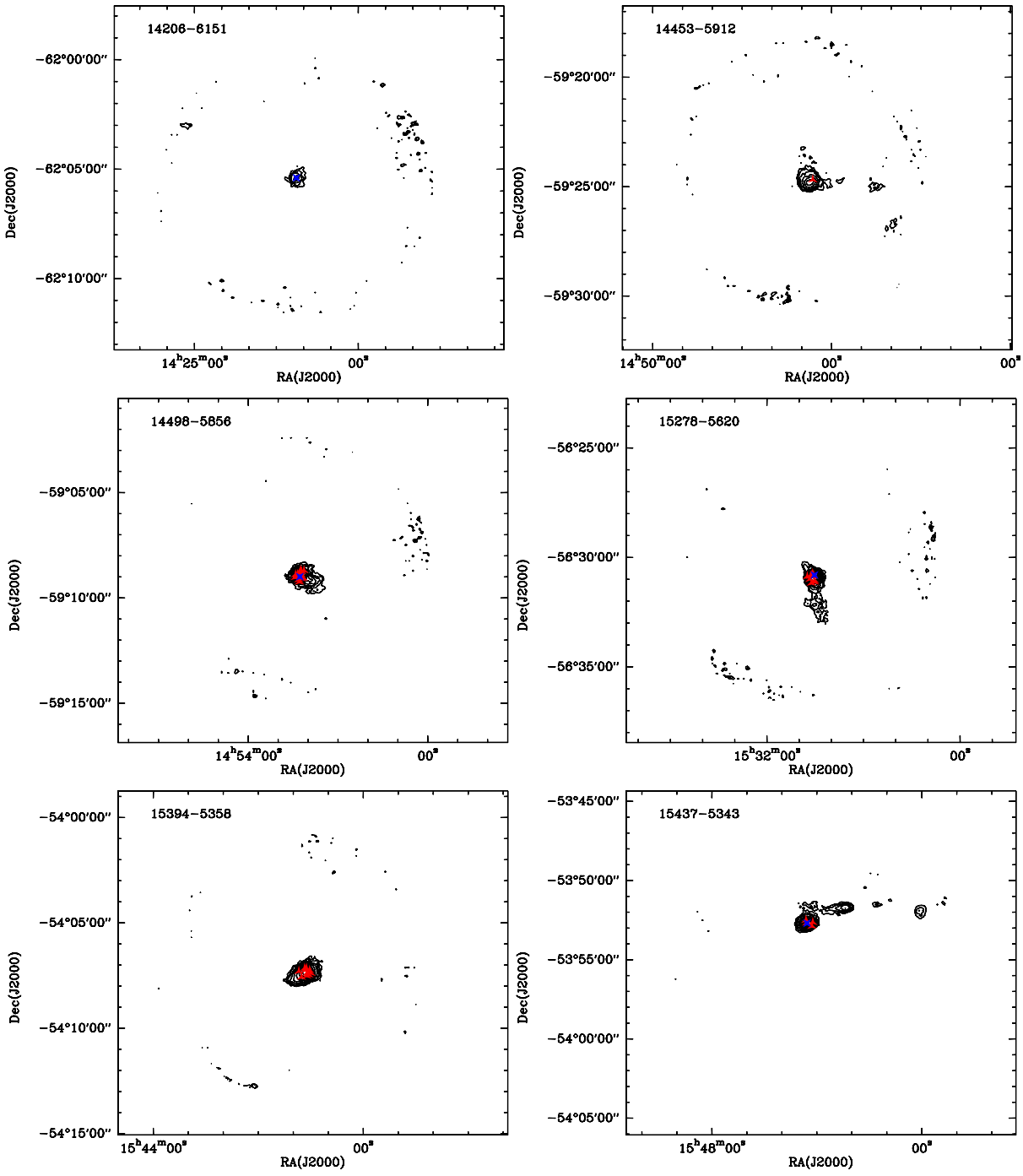

Figure A.8: LABOCA 870 μm data. Contours start at 3 σ with steps of 1.4 σ. The blue stars mark the location of the MSX associated MSX point source, while the red triangles mark the location of the GLIMPSE 8 μm point source.

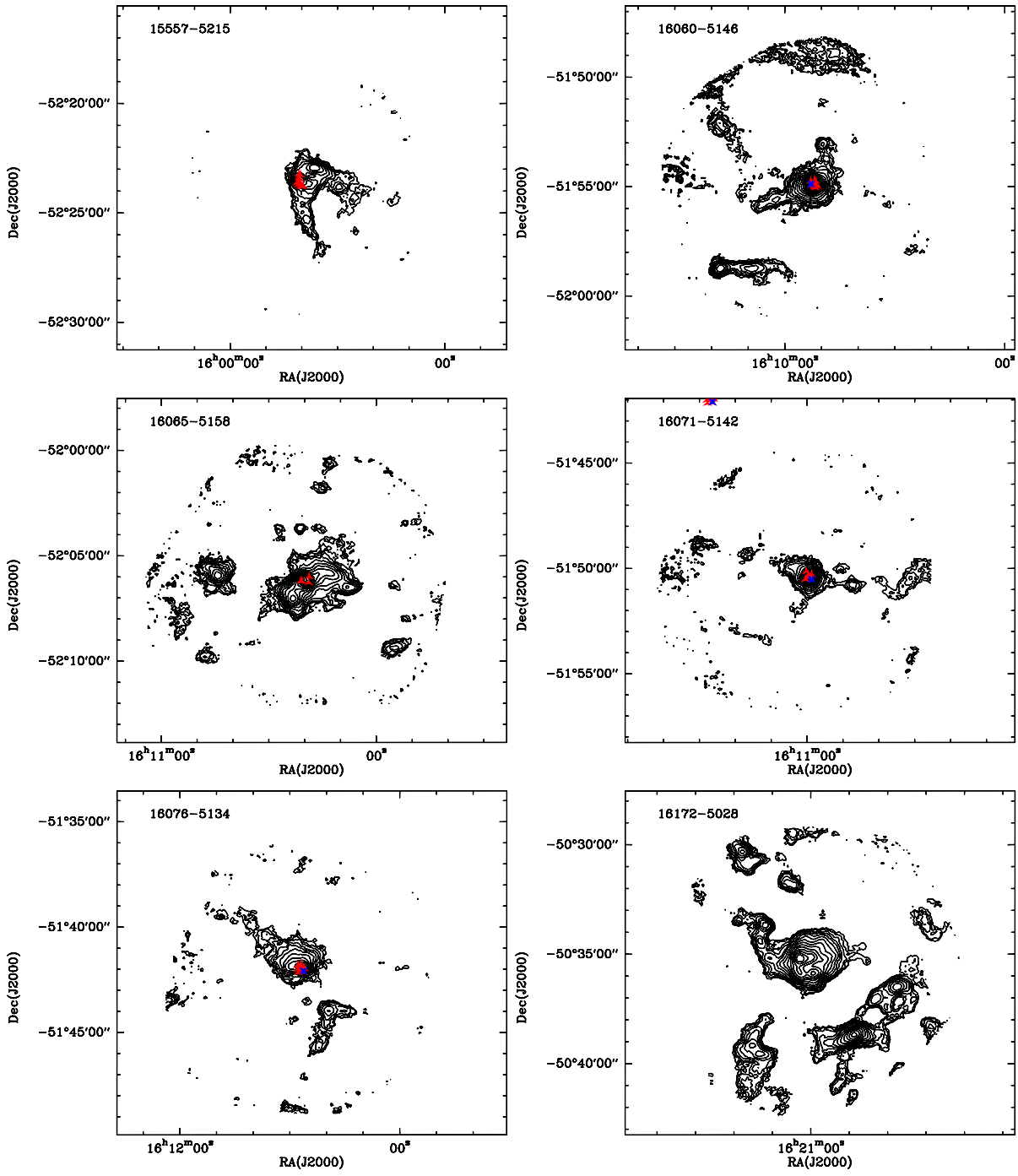

Figure A.9: LABOCA 870 μm data. Contours start at 3 σ with steps of 1.4 σ. The blue stars mark the location of the MSX associated MSX point source, while the red triangles mark the location of the GLIMPSE 8 μm point source.

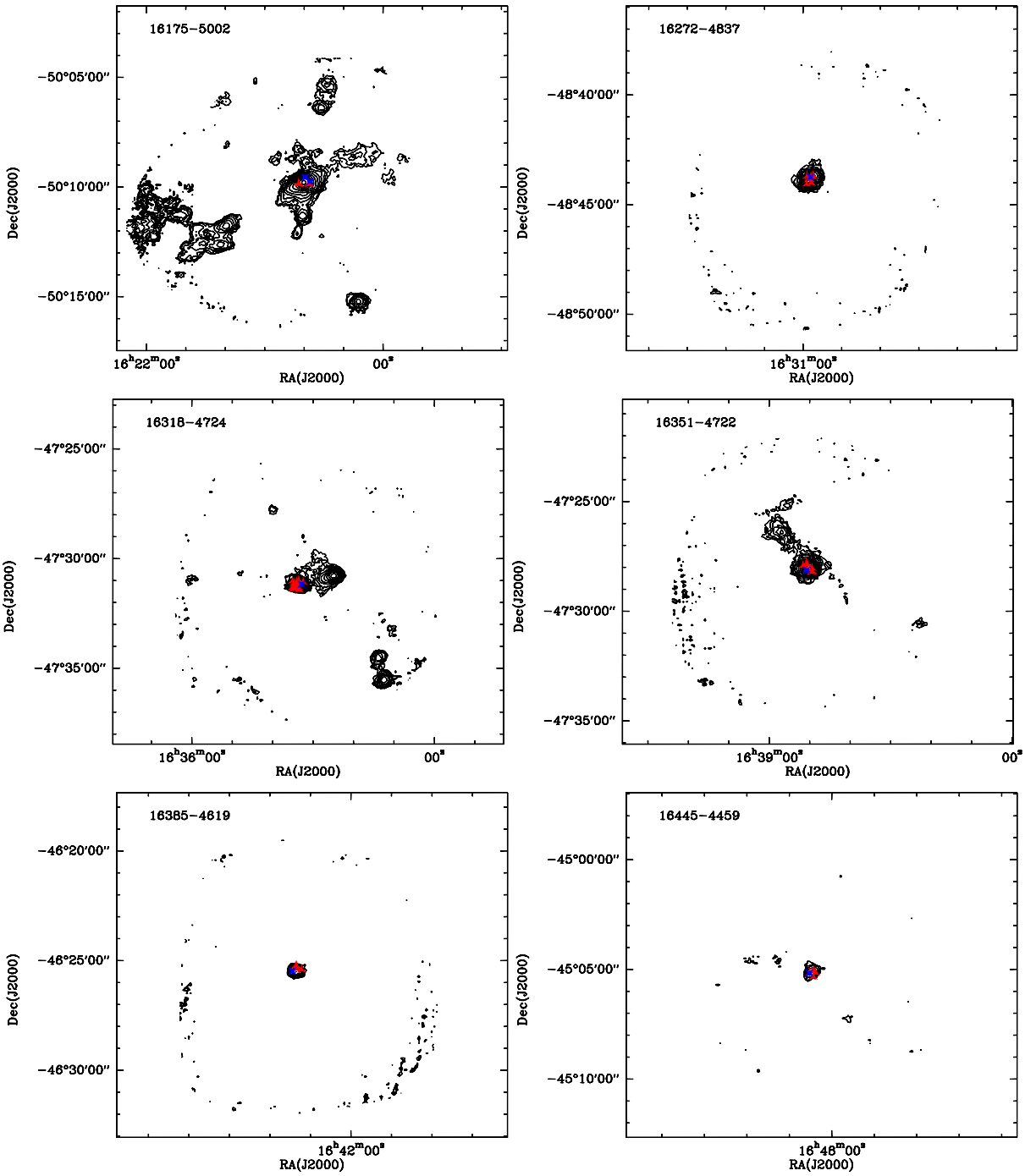

Figure A.10: LABOCA 870 μm data. Contours start at 3 σ with steps of 1.4 σ. The blue stars mark the location of the MSX associated MSX point source, while the red triangles mark the location of the GLIMPSE 8 μm point source.

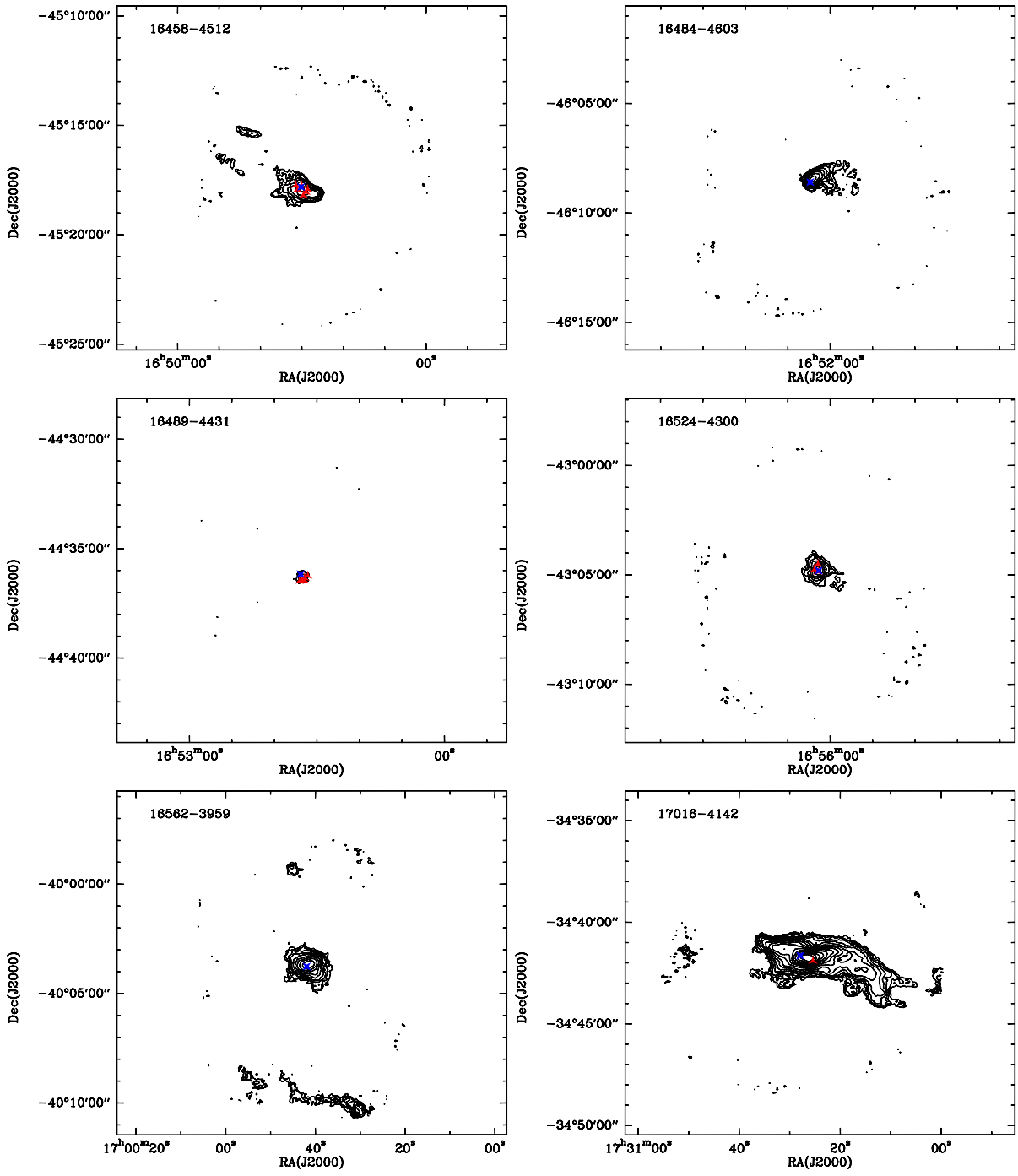

Figure A.11: LABOCA 870 μm data. Contours start at 3 σ with steps of 1.4 σ. The blue stars mark the location of the MSX associated MSX point source, while the red triangles mark the location of the GLIMPSE 8 μm point source.

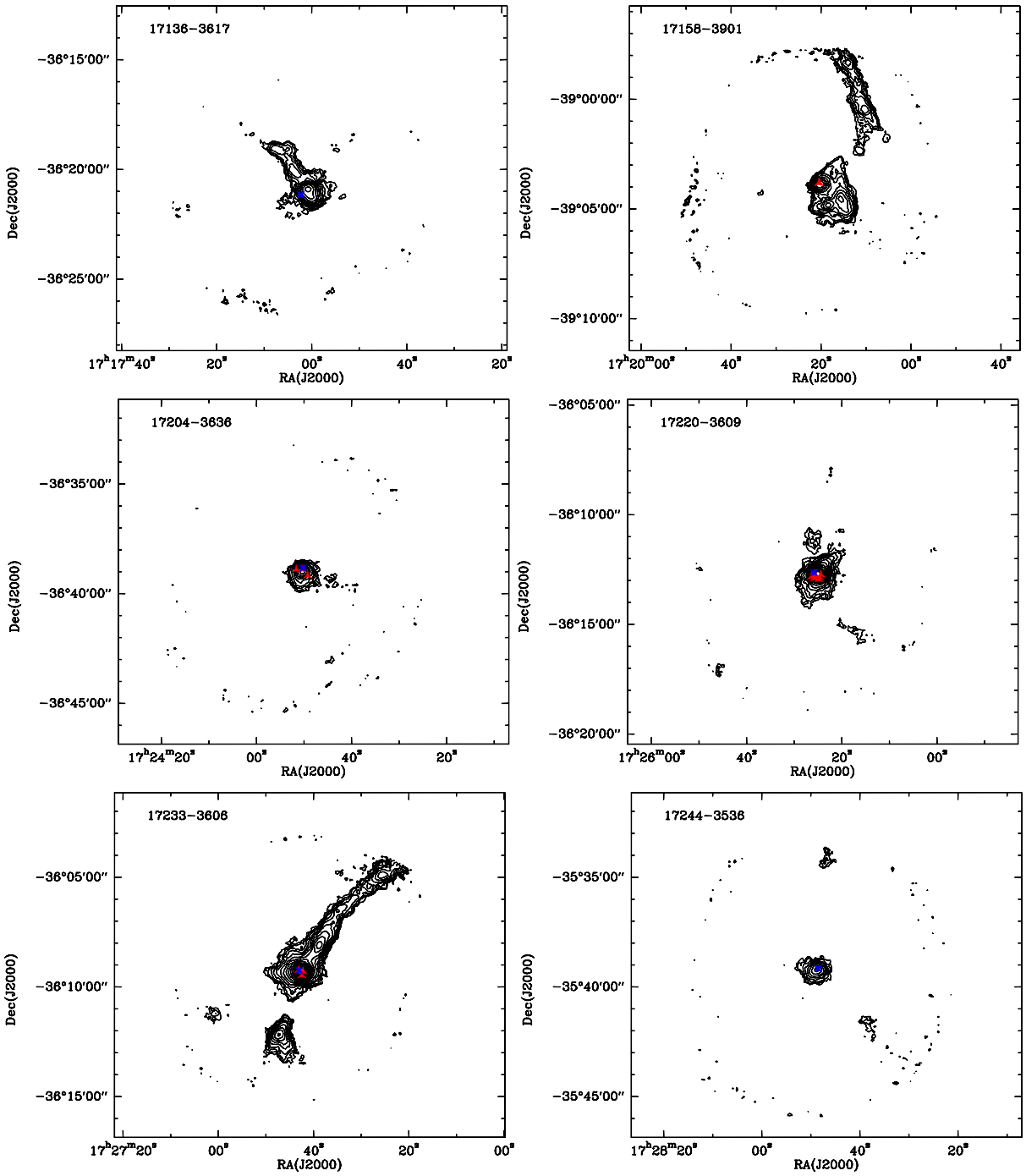

Figure A.12: LABOCA 870 μm data. Contours start at 3 σ with steps of 1.4 σ. The blue stars mark the location of the MSX associated MSX point source, while the red triangles mark the location of the GLIMPSE 8 μm point source.

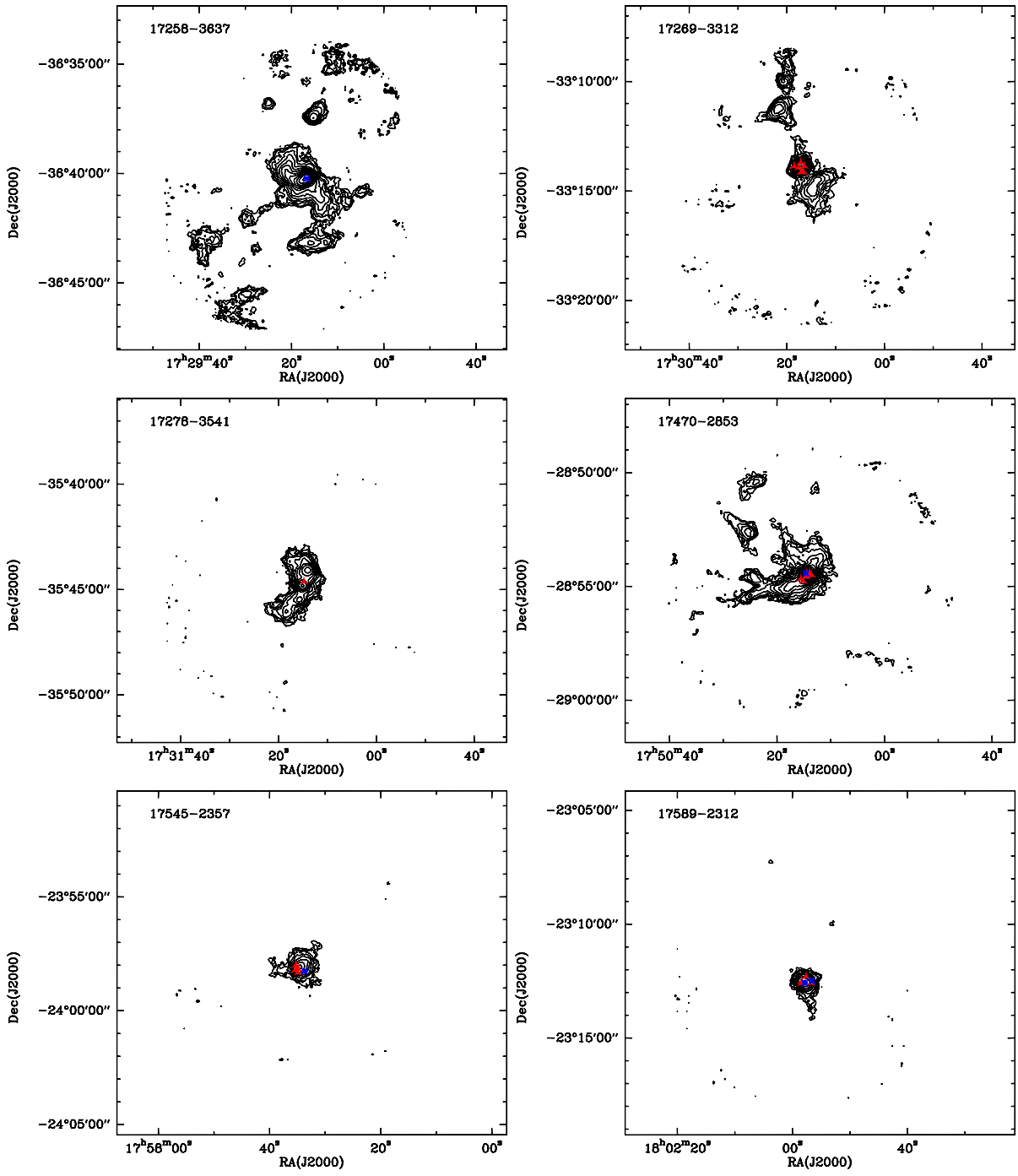

Figure A.13: LABOCA 870 μm data. Contours start at 3 σ with steps of 1.4 σ. The blue stars mark the location of the MSX associated MSX point source, while the red triangles mark the location of the GLIMPSE 8 μm point source.

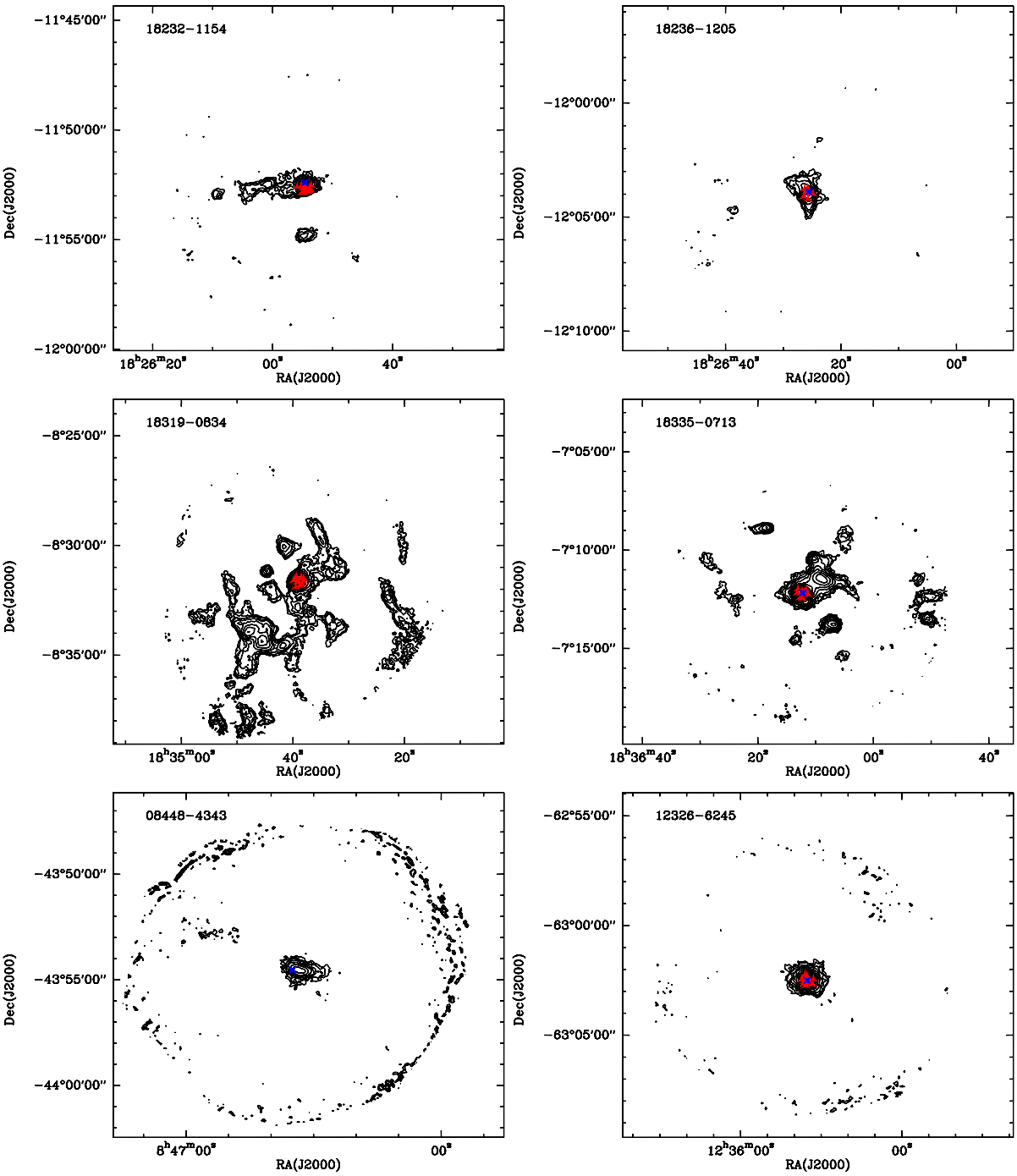

Figure A.14: LABOCA 870 μm data. Contours start at 3 σ with steps of 1.4 σ. The blue stars mark the location of the MSX associated MSX point source, while the red triangles mark the location of the GLIMPSE 8 μm point source.

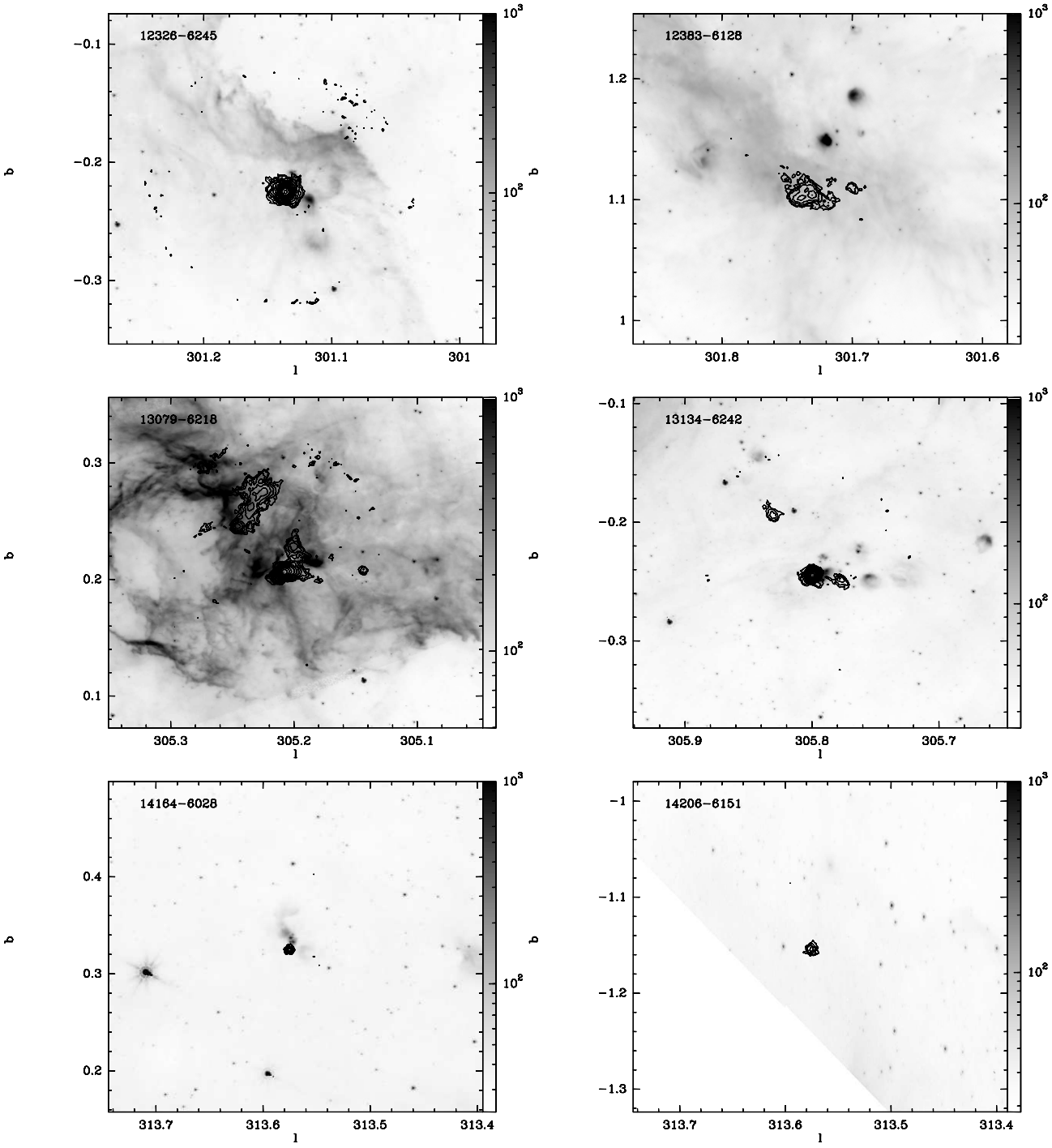

Figure A.15: LABOCA 870 μm data (as contours) overplotted on Spitzer GLIMPSE 8 μm data. Contours start at 3 σ with steps of 1.4 σ.

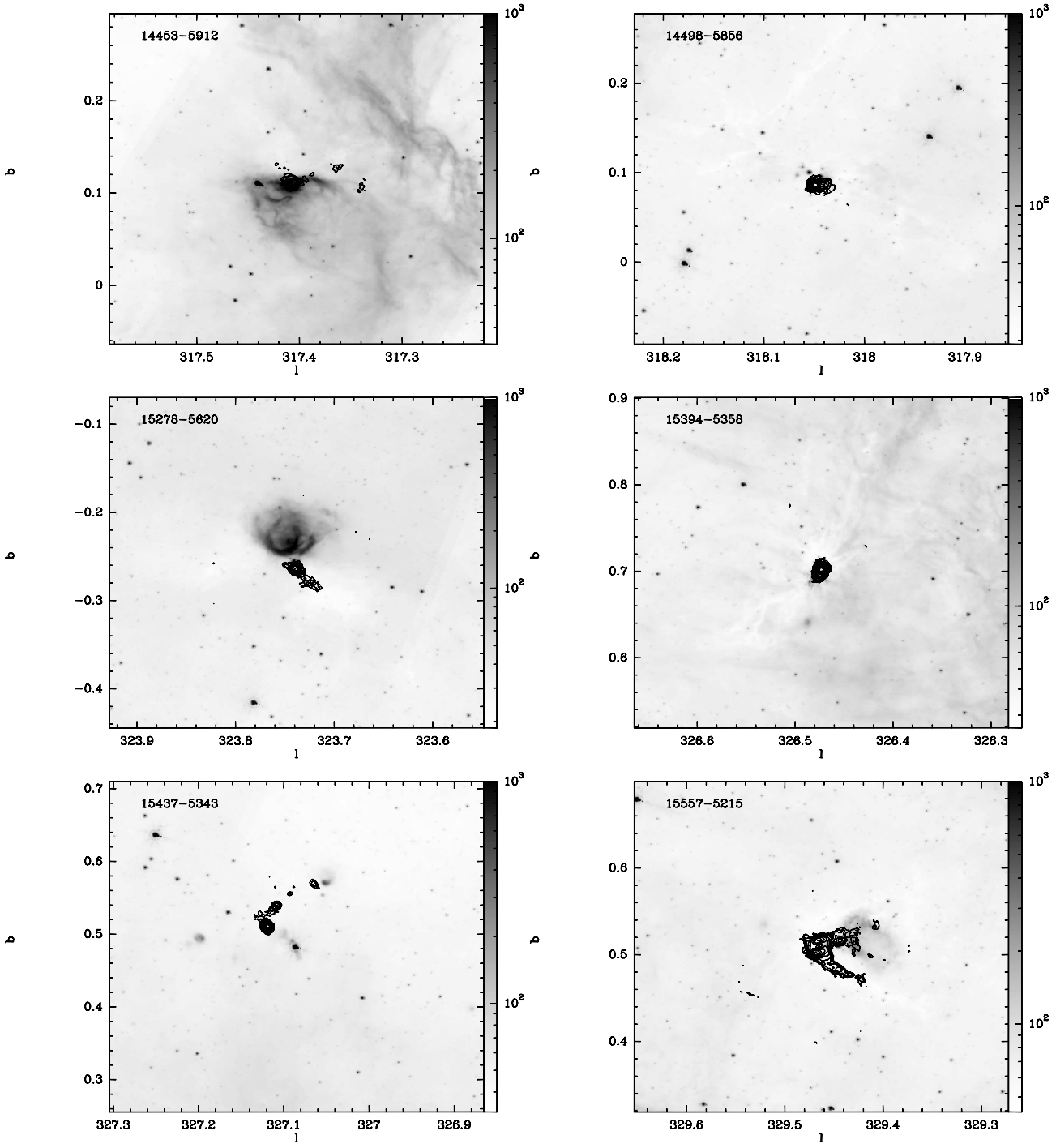

Figure A.16: LABOCA 870 μm data (as contours) overplotted on Spitzer GLIMPSE 8 μm data. Contours start at 3 σ with steps of 1.4 σ.

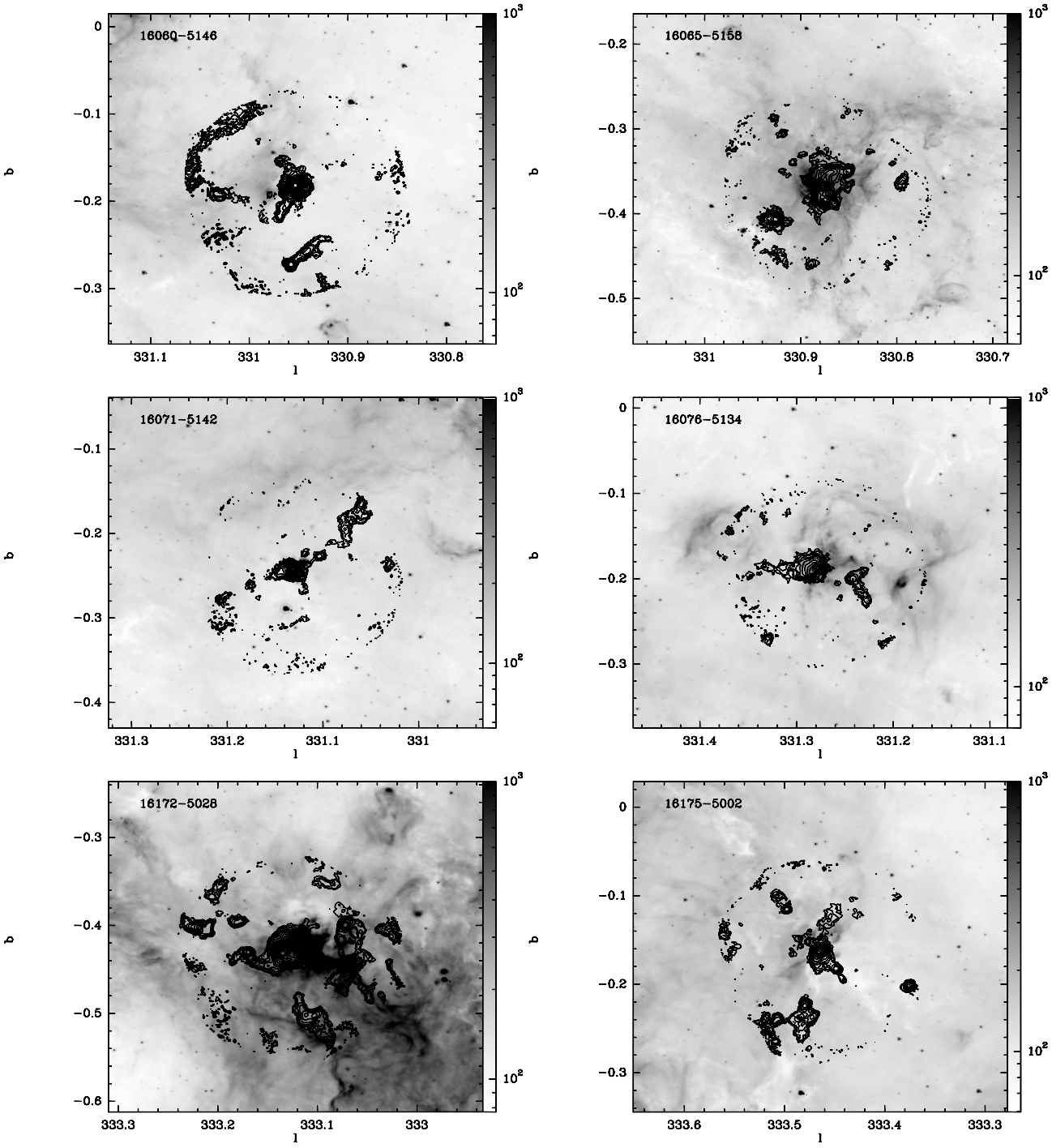

Figure A.17: LABOCA 870 μm data (as contours) overplotted on Spitzer GLIMPSE 8 μm data. Contours start at 3 σ with steps of 1.4 σ.

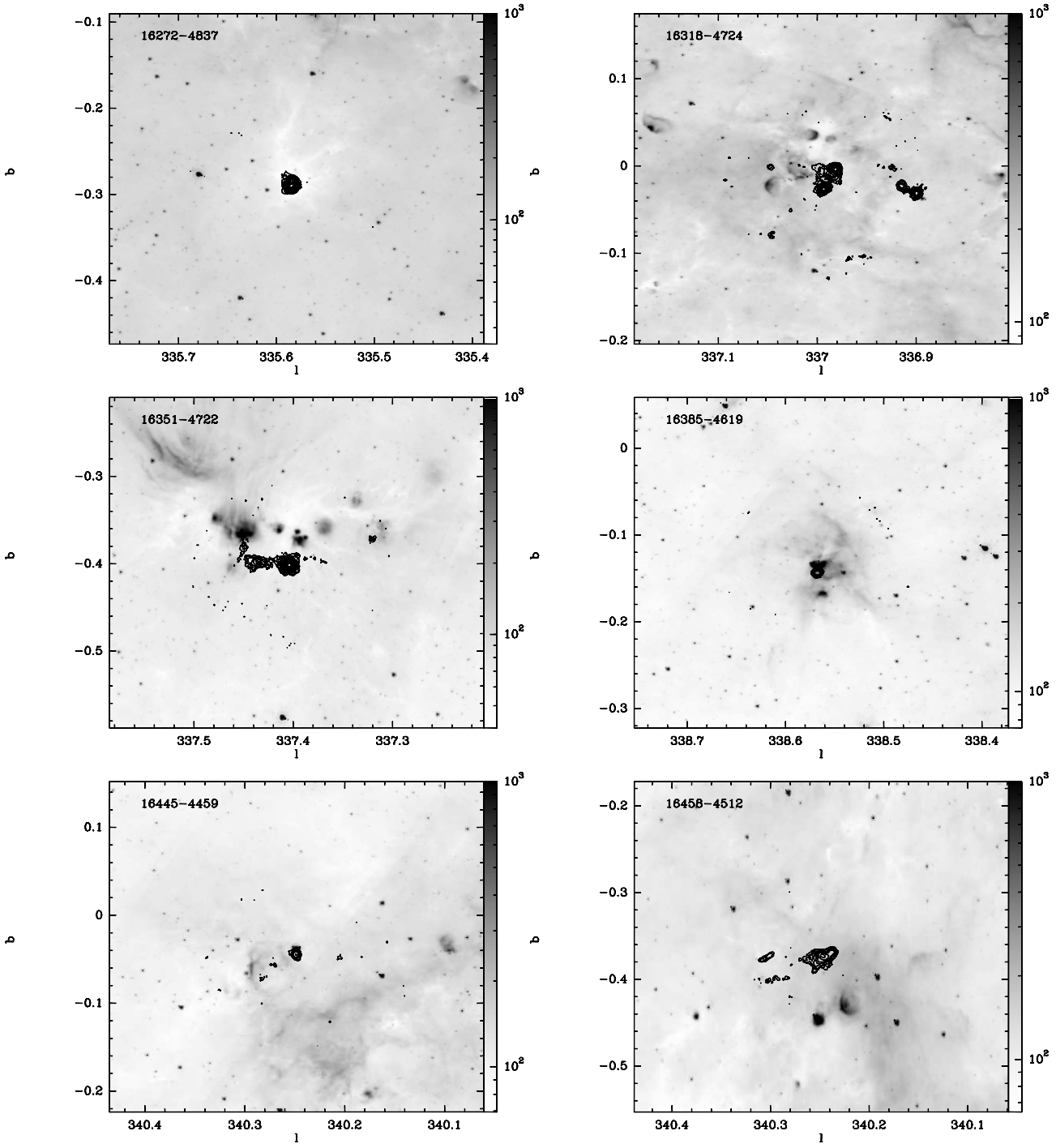

Figure A.18: LABOCA 870 μm data (as contours) overplotted on Spitzer GLIMPSE 8 μm data. Contours start at 3 σ with steps of 1.4 σ.

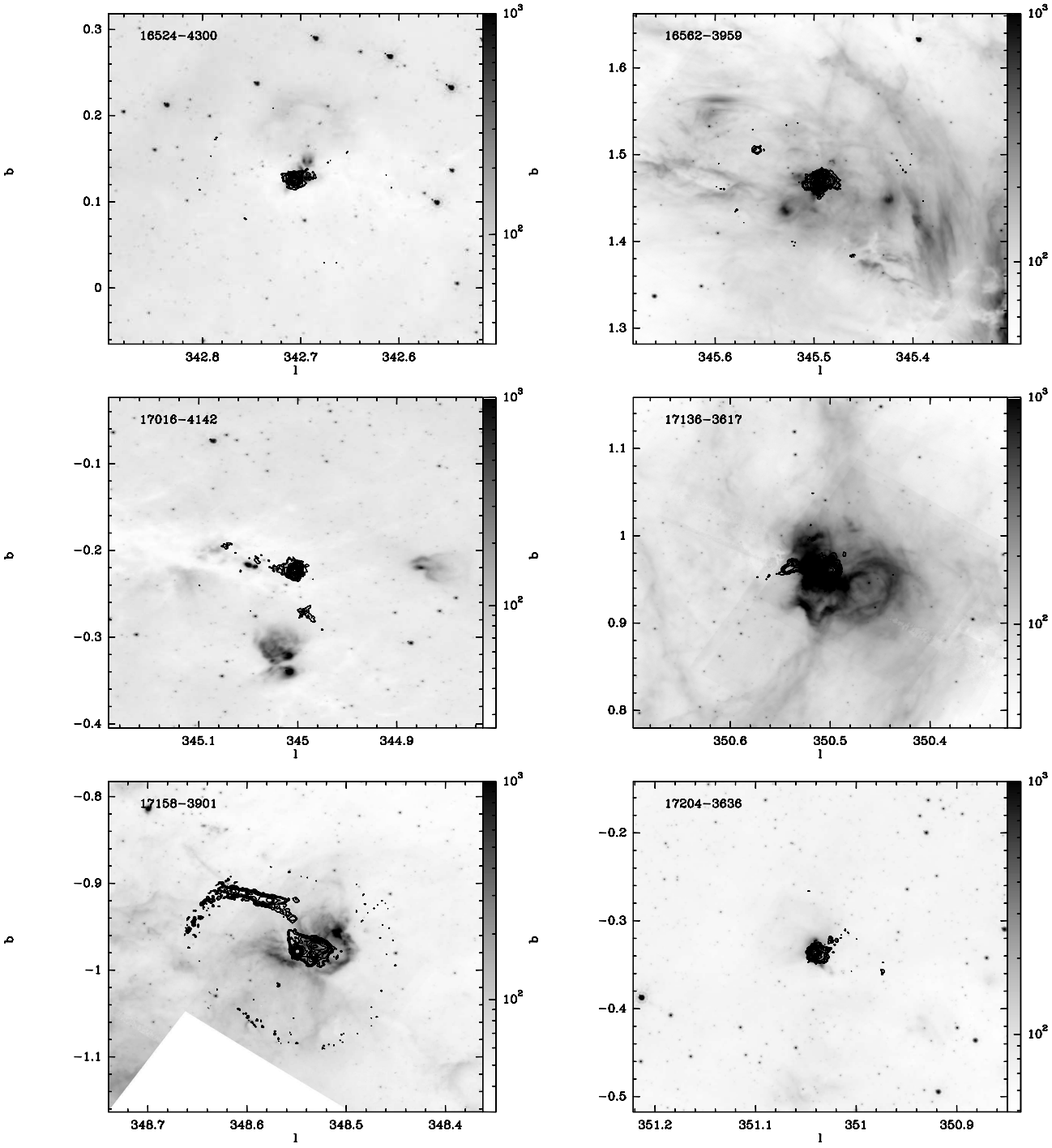

Figure A.19: LABOCA 870 μm data (as contours) overplotted on Spitzer GLIMPSE 8 μm data. Contours start at 3 σ with steps of 1.4 σ.

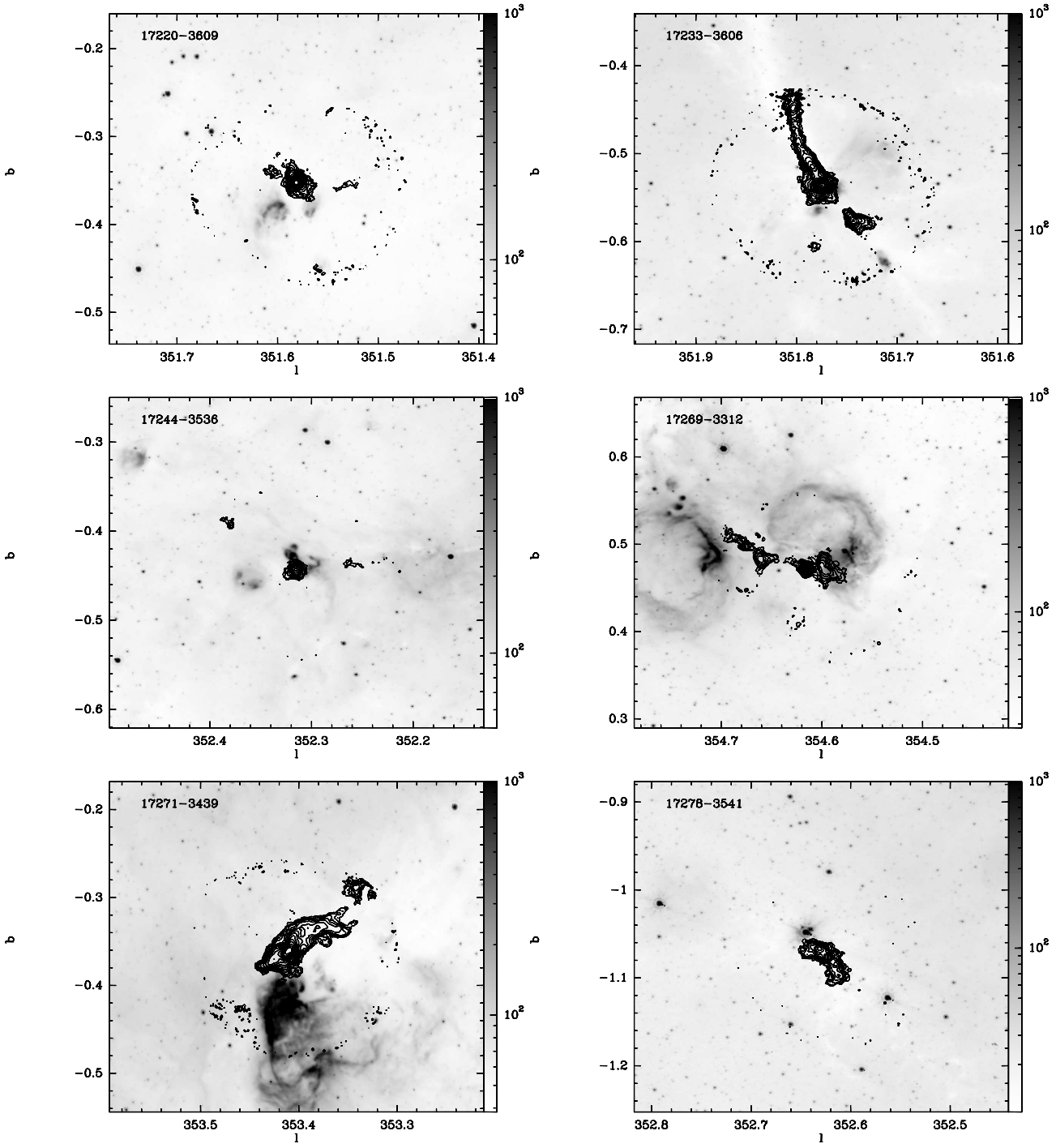

Figure A.20: LABOCA 870 μm data (as contours) overplotted on Spitzer GLIMPSE 8 μm data. Contours start at 3 σ with steps of 1.4 σ.

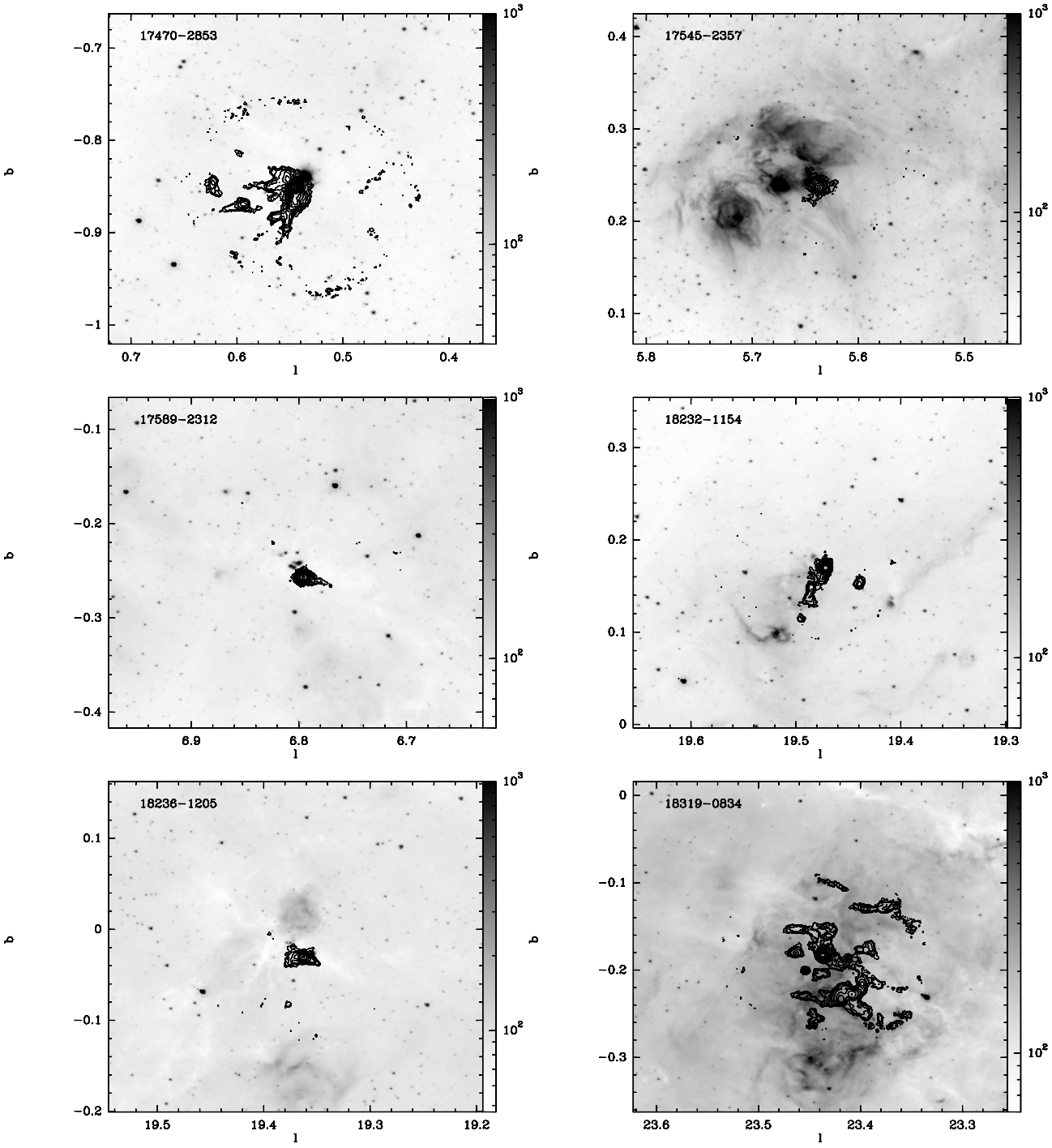

Figure A.21: LABOCA 870 μm data (as contours) overplotted on Spitzer GLIMPSE 8 μm data. Contours start at 3 σ with steps of 1.4 σ.

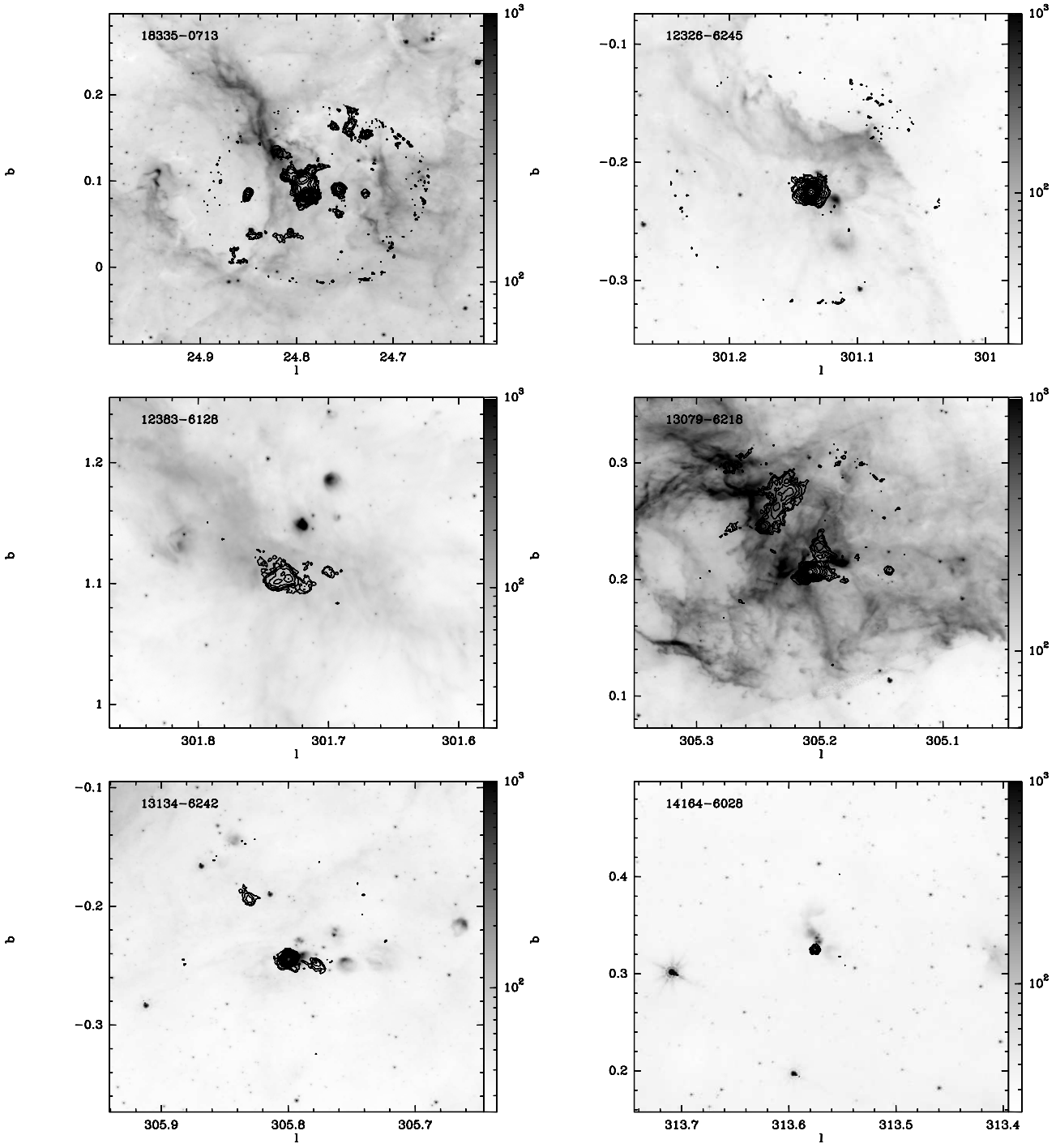

Figure A.22: LABOCA 870 μm data (as contours) overplotted on Spitzer GLIMPSE 8 μm data. Contours start at 3 σ with steps of 1.4 σ.

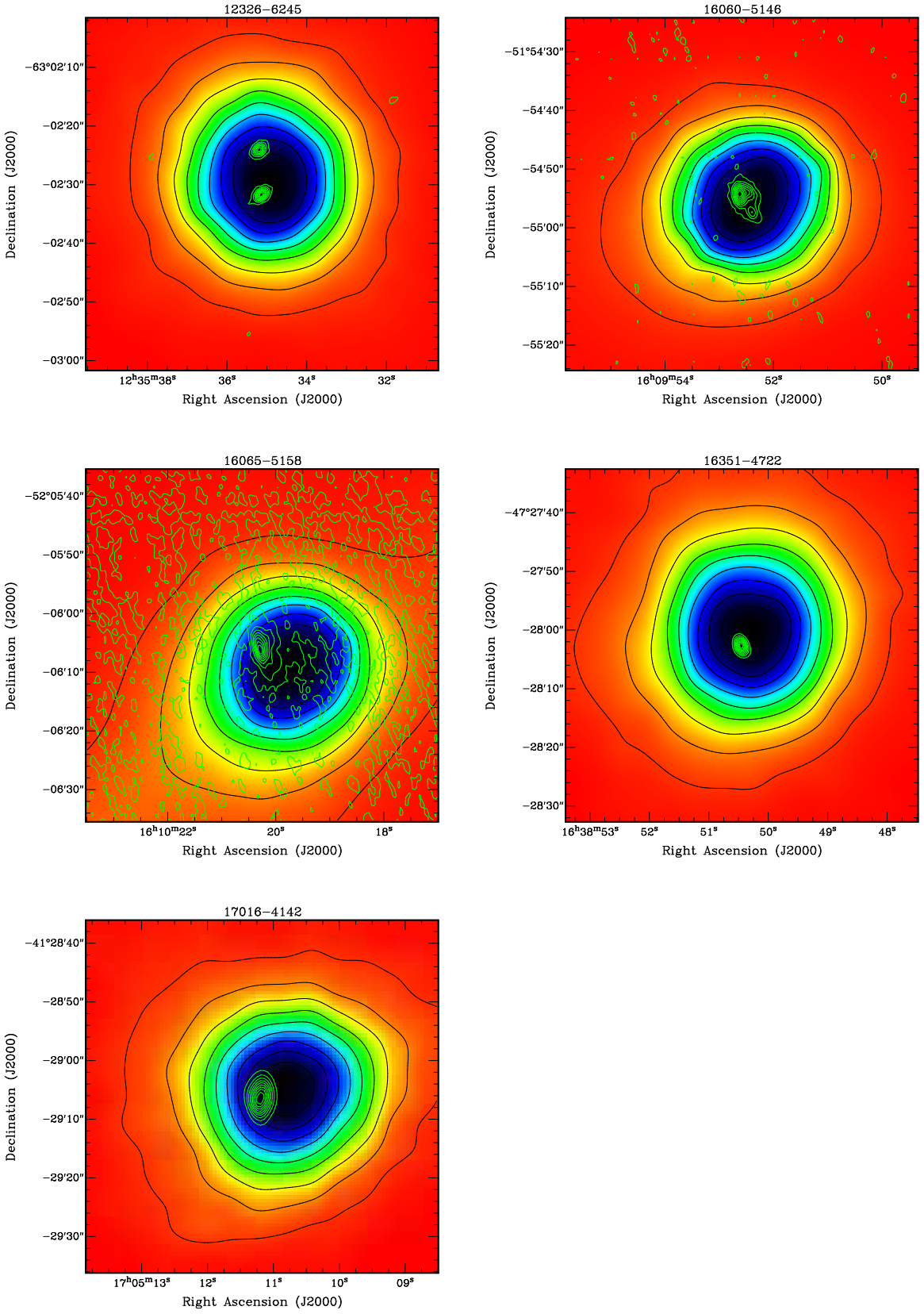

Figure A.23: The LABOCA 870μm emission (color-scale and black contours) with the RMS 3cm continuum emission (Urquhart et al. 2007) on top (green contours). For the source 17016-4124, only 6 cm emission data was available.

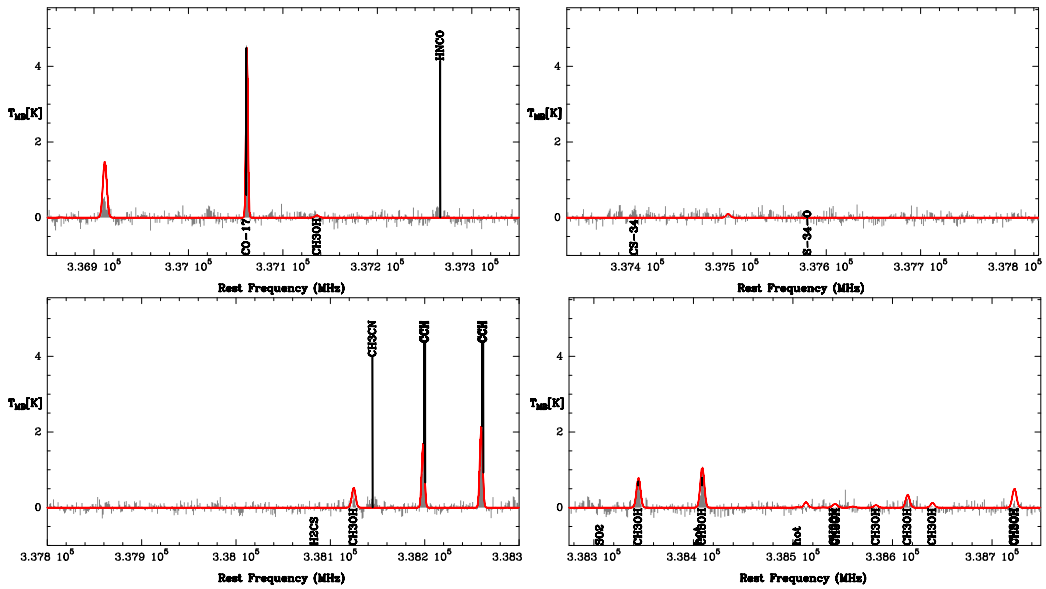

Figure A.24: 338 GHz setup for 14453-5912. The synthetic model spectrum is shown in red.

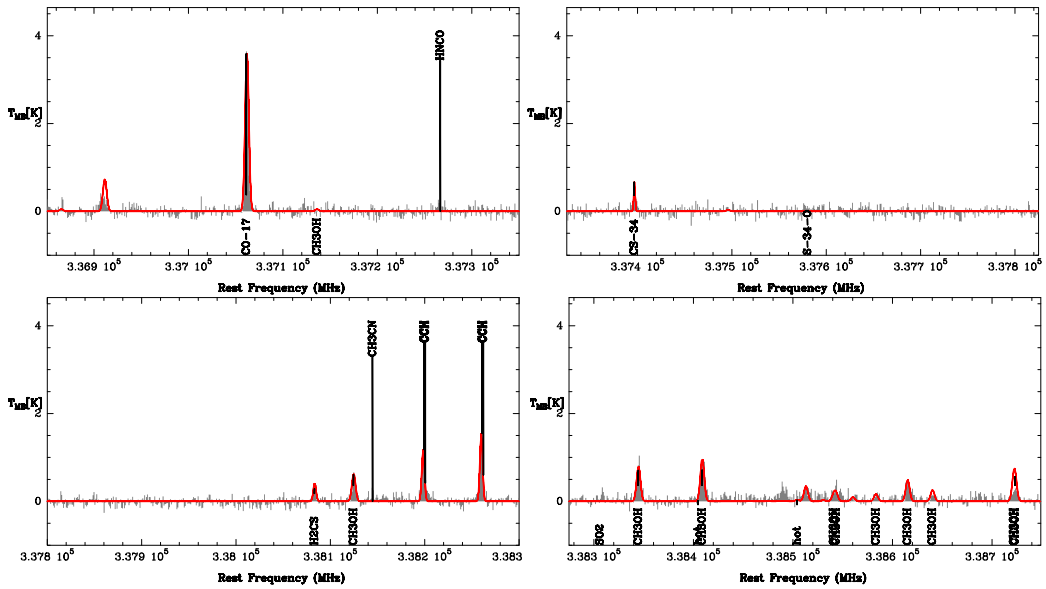

Figure A.25: 338 GHz setup for 14498-5856. The synthetic model spectrum is shown in red.

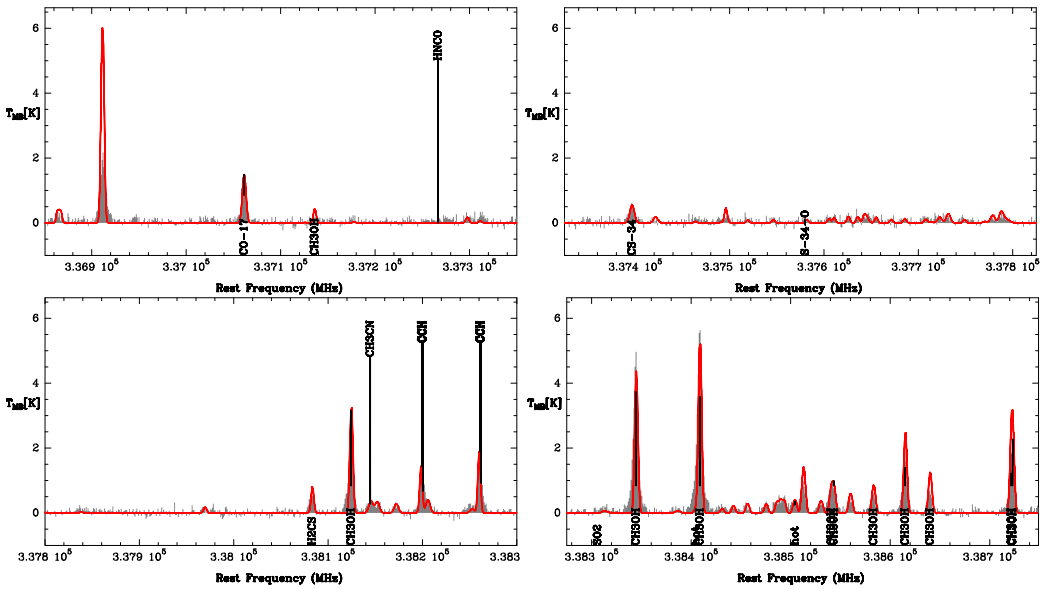

Figure A.26: 338 GHz setup for 15394-5358. The synthetic model spectrum is shown in red.

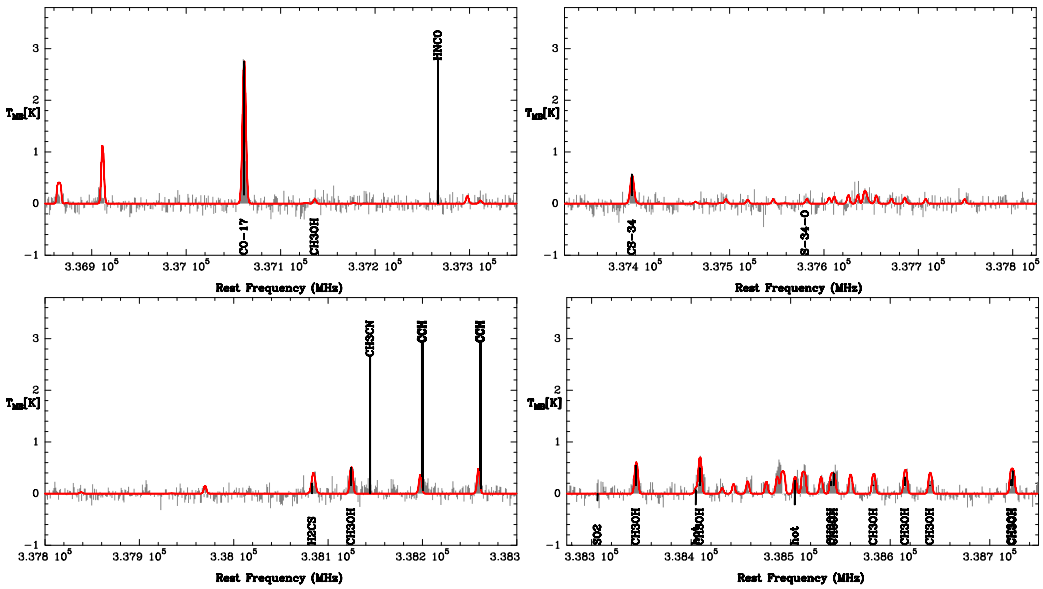

Figure A.27: 338 GHz setup for 15437-5343. The synthetic model spectrum is shown in red.

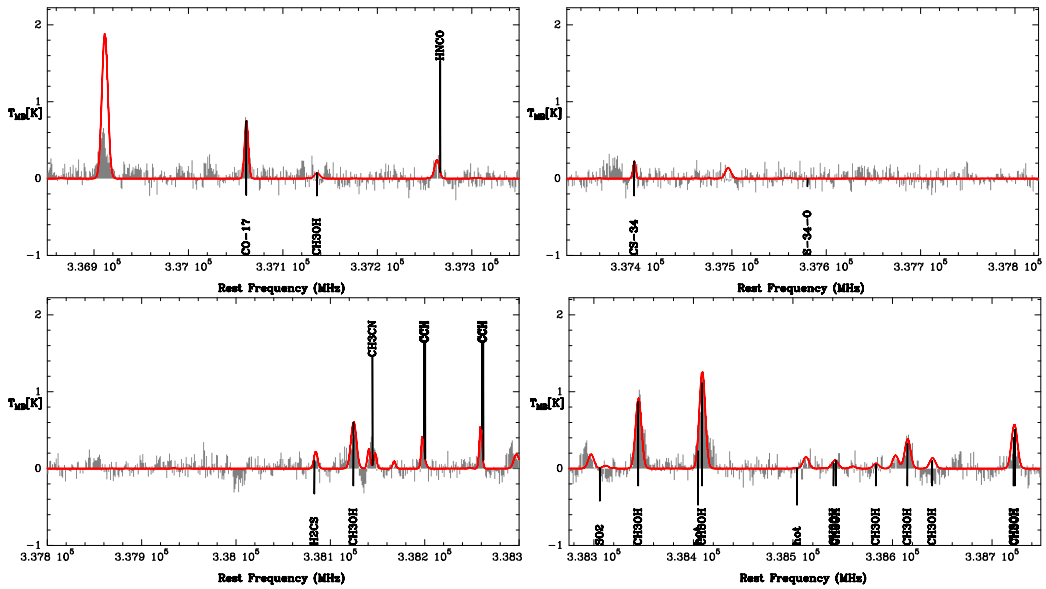

Figure A.28: 338 GHz setup for 15557-5215. The synthetic model spectrum is shown in red.

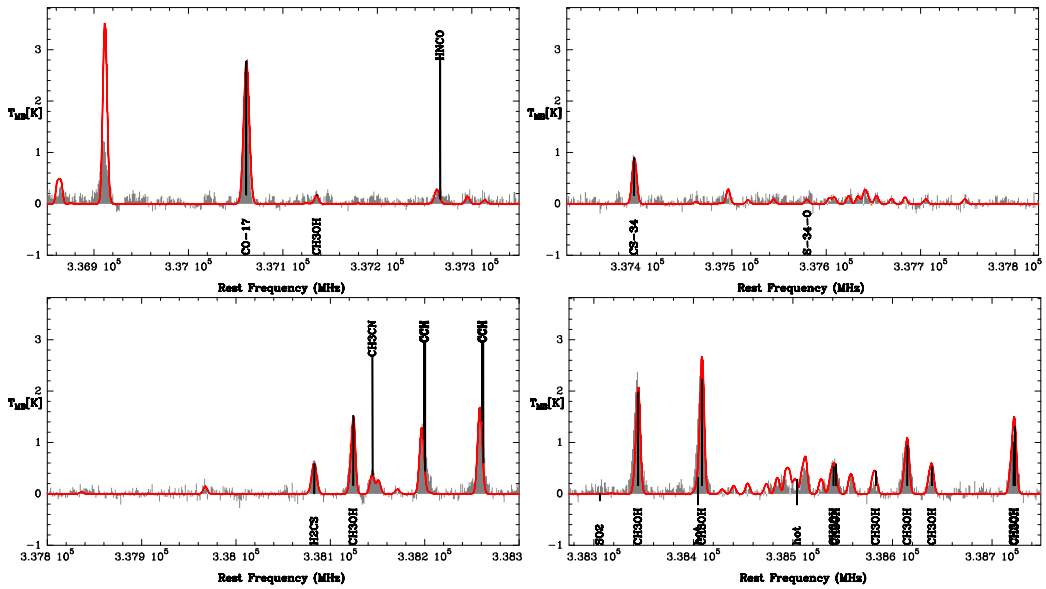

Figure A.29: 338 GHz setup for 16071-5142. The synthetic model spectrum is shown in red.

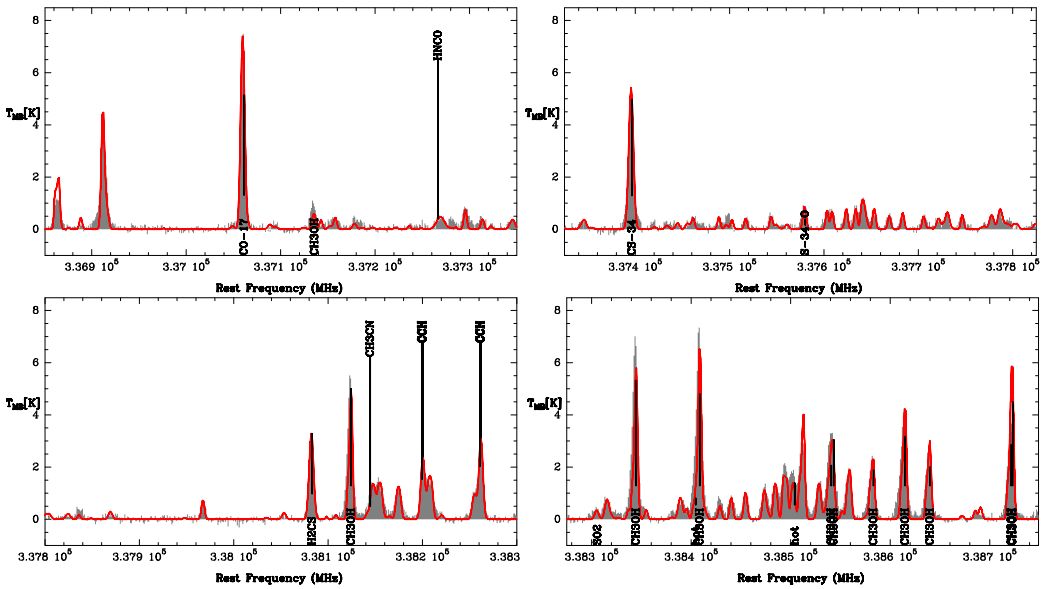

Figure A.30: 338 GHz setup for 16351-4722. The synthetic model spectrum is shown in red.

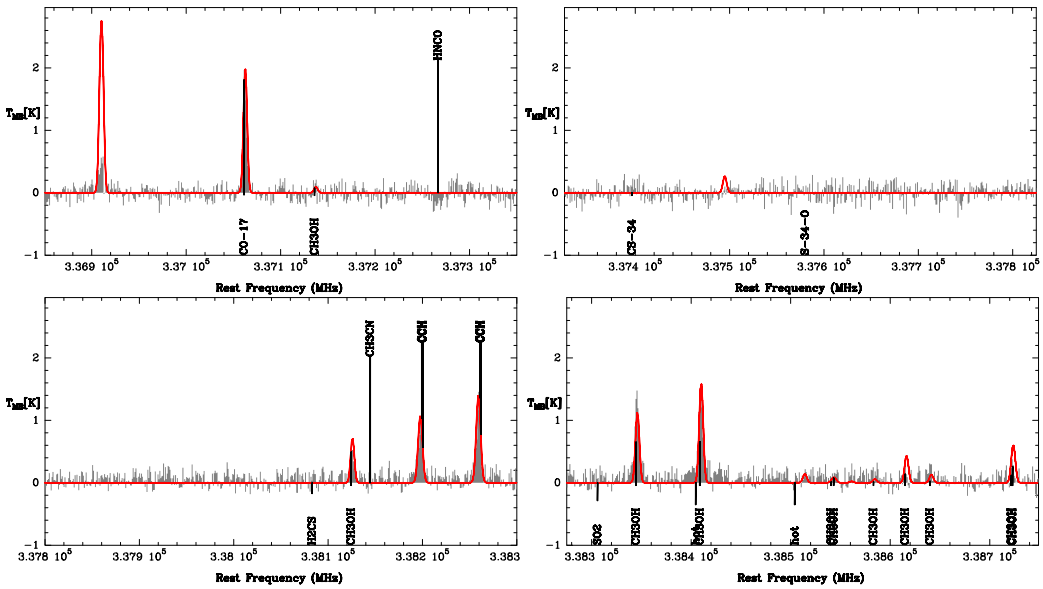

Figure A.31: 338 GHz setup for 16458-4512. The synthetic model spectrum is shown in red.

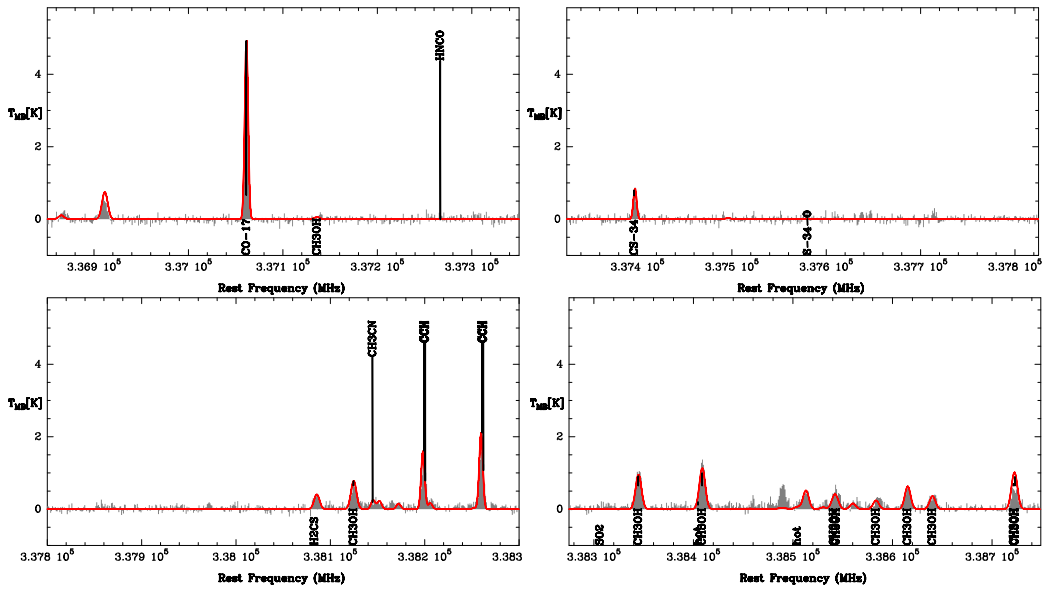

Figure A.32: 338 GHz setup for 16484-4603. The synthetic model spectrum is shown in red.

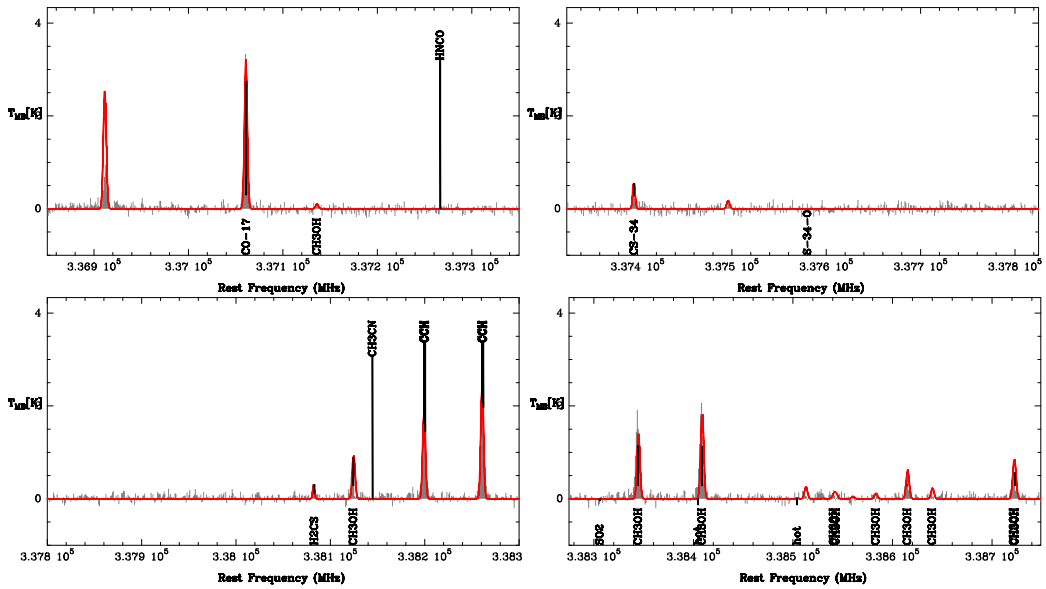

Figure A.33: 338 GHz setup for 16524-4300. The synthetic model spectrum is shown in red.

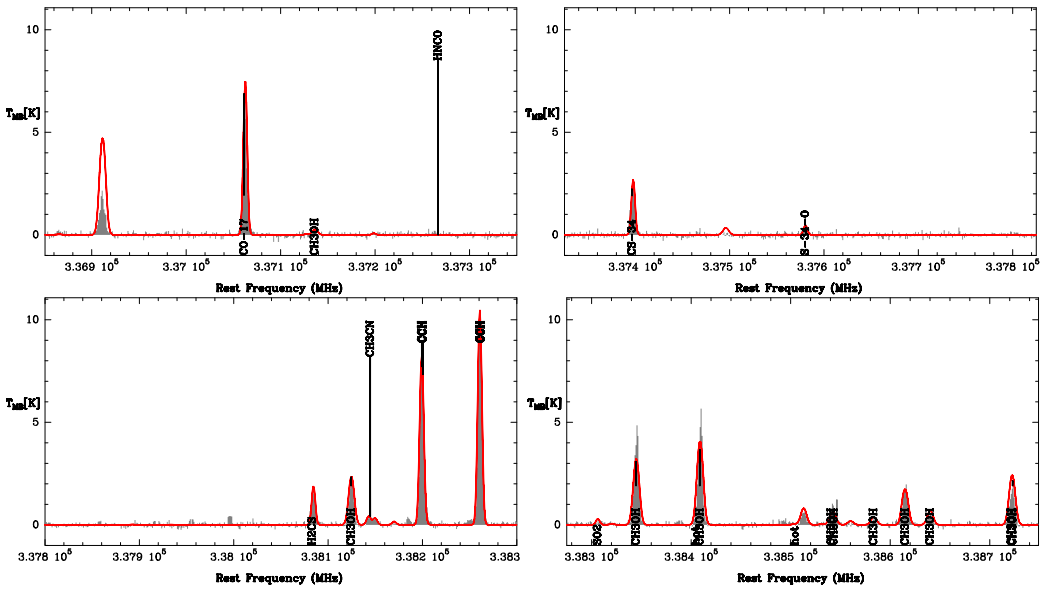

Figure A.34: 338 GHz setup for 16562-3959. The synthetic model spectrum is shown in red.

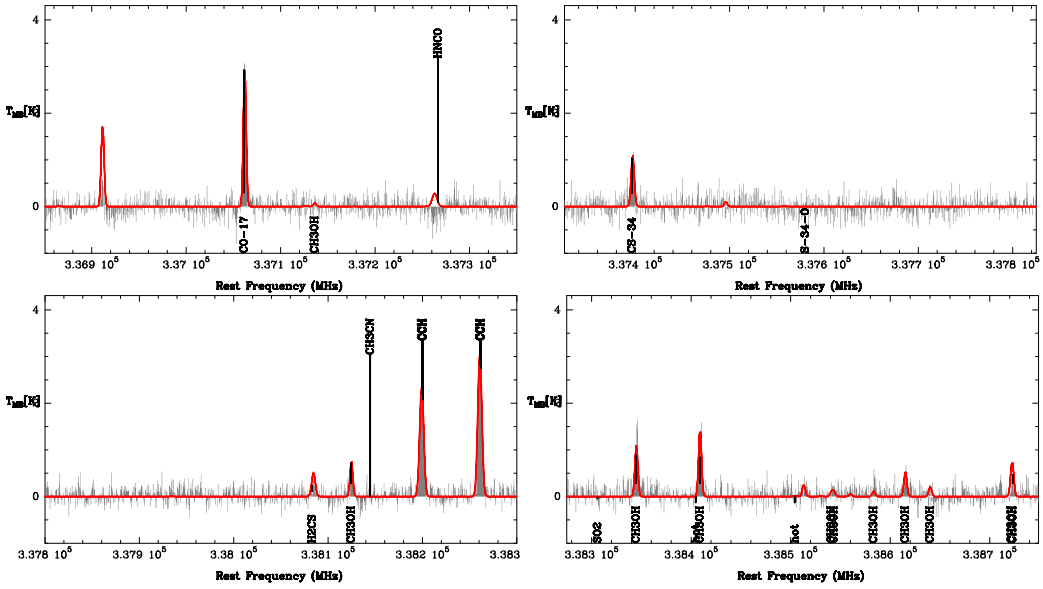

Figure A.35: 338 GHz setup for 17136-3617. The synthetic model spectrum is shown in red.

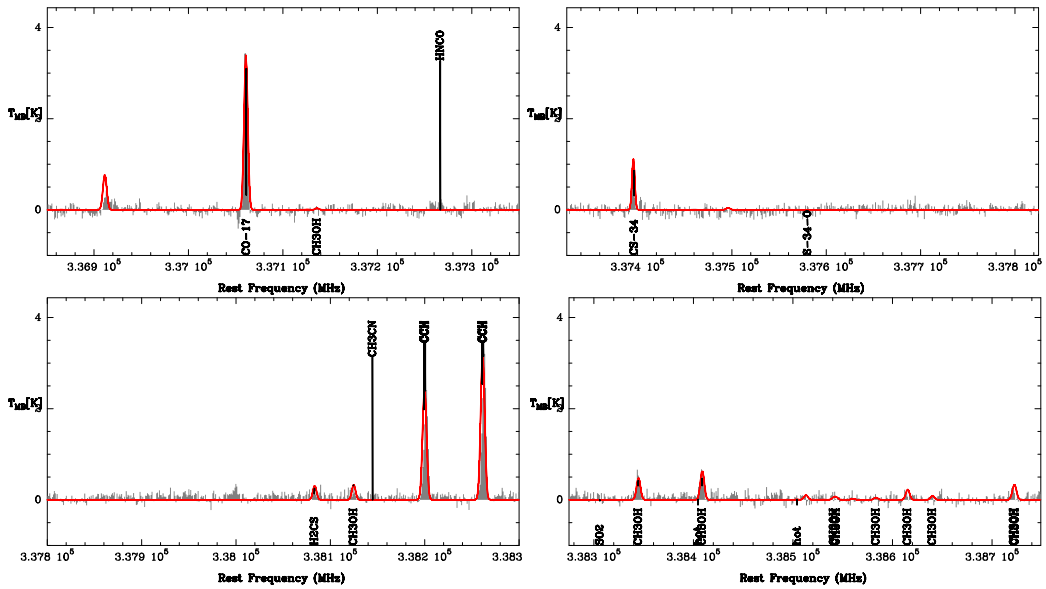

Figure A.36: 338 GHz setup for 17136-3617. The synthetic model spectrum is shown in red.

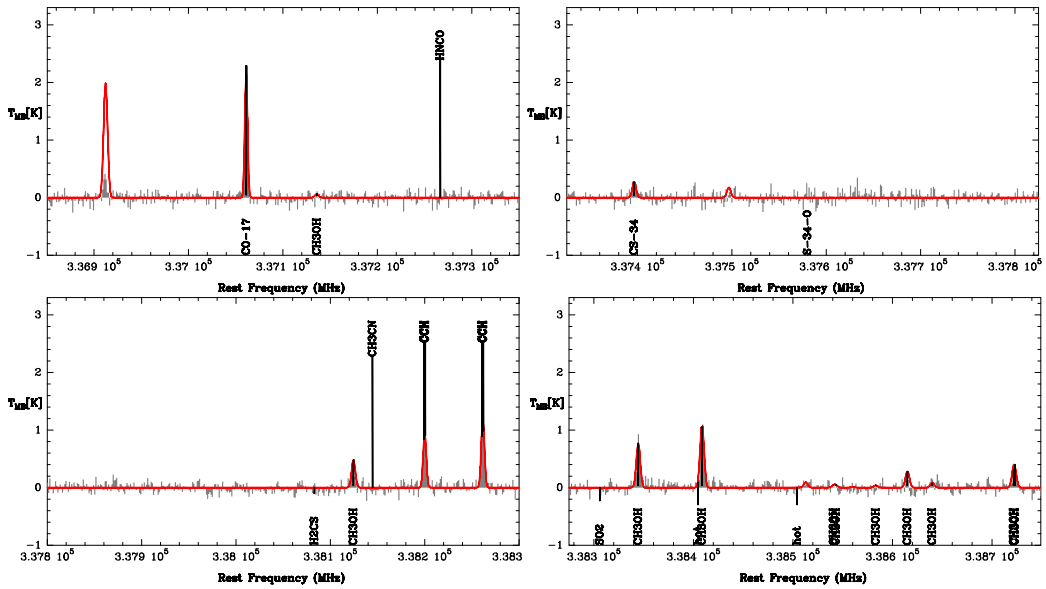

Figure A.37: 338 GHz setup for 17204-3636. The synthetic model spectrum is shown in red.

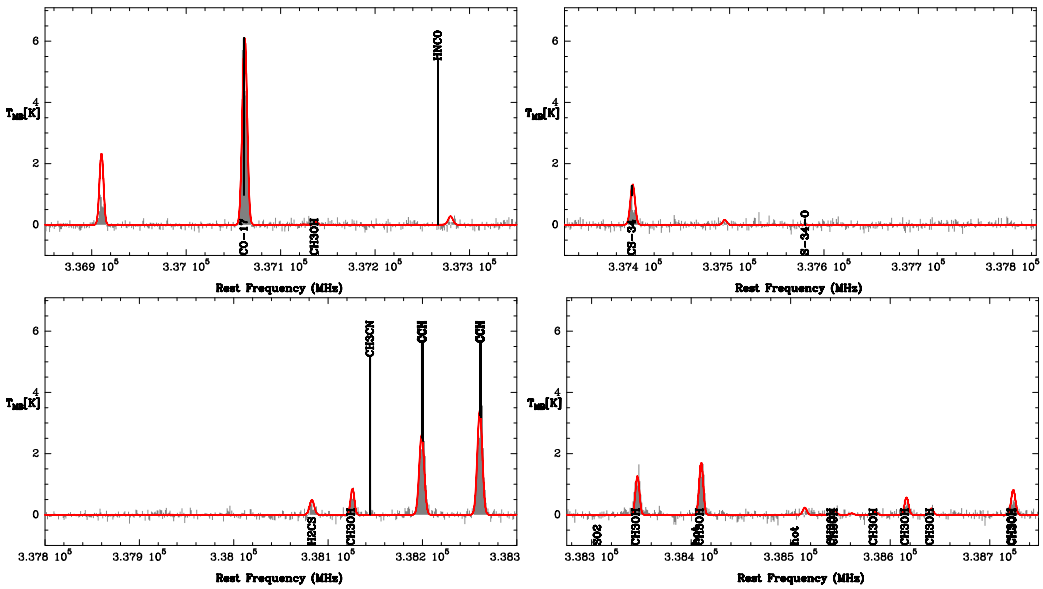

Figure A.38: 338 GHz setup for 17258-3637. The synthetic model spectrum is shown in red.

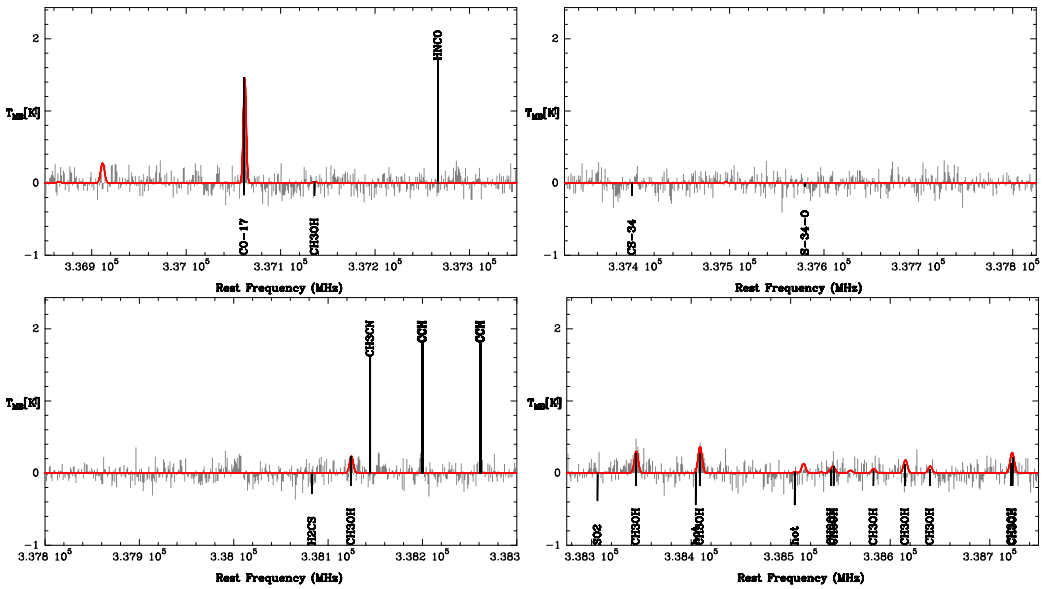

Figure A.39: 338 GHz setup for 17269-3312. The synthetic model spectrum is shown in red.

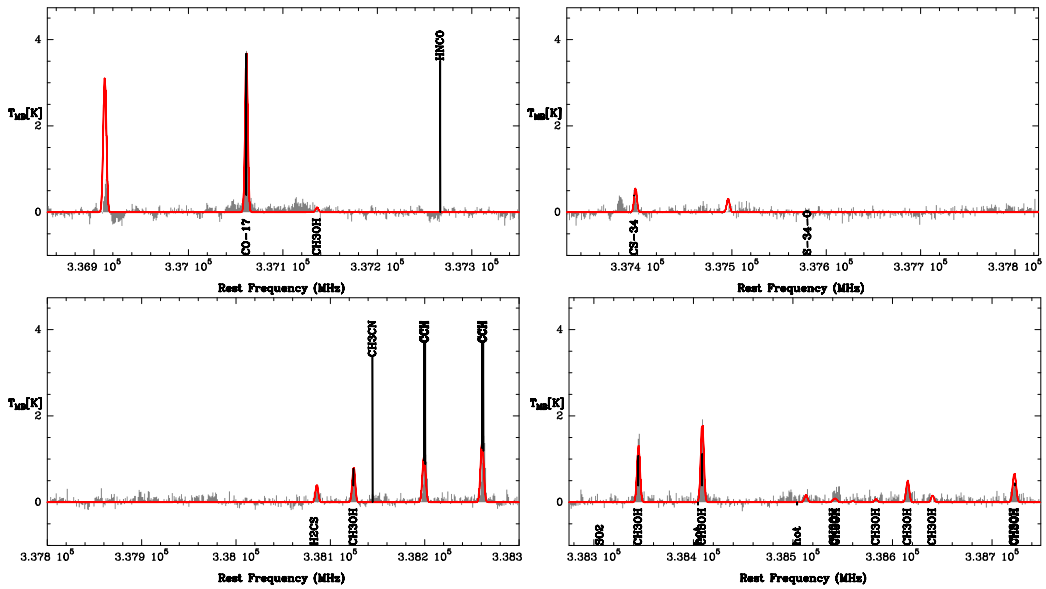

Figure A.40: 338 GHz setup for 17589-2312. The synthetic model spectrum is shown in red.

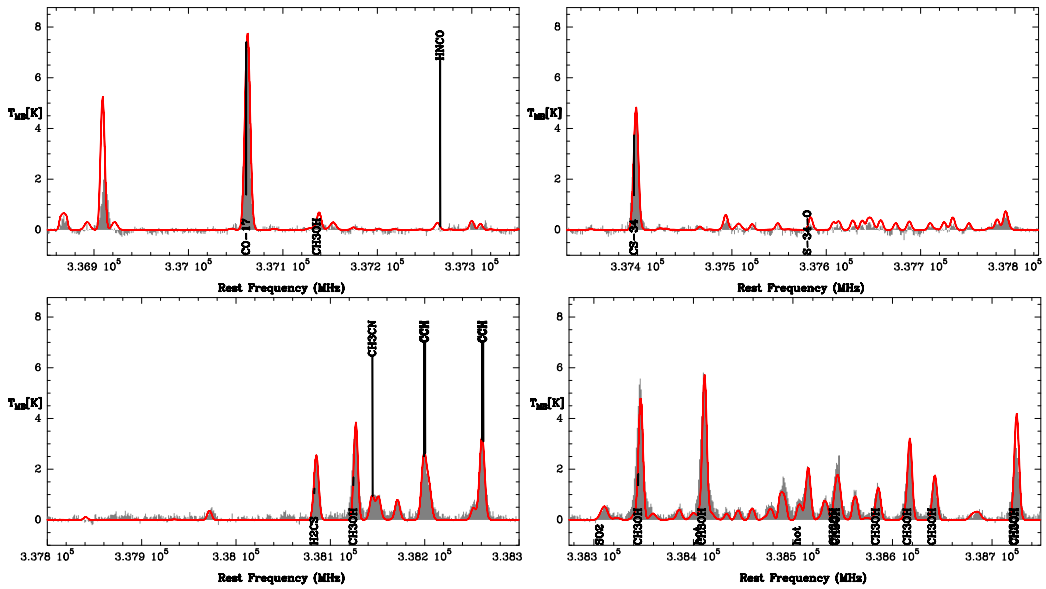

Figure A.41: 338 GHz setup for 17470-2853. The synthetic model spectrum is shown in red.

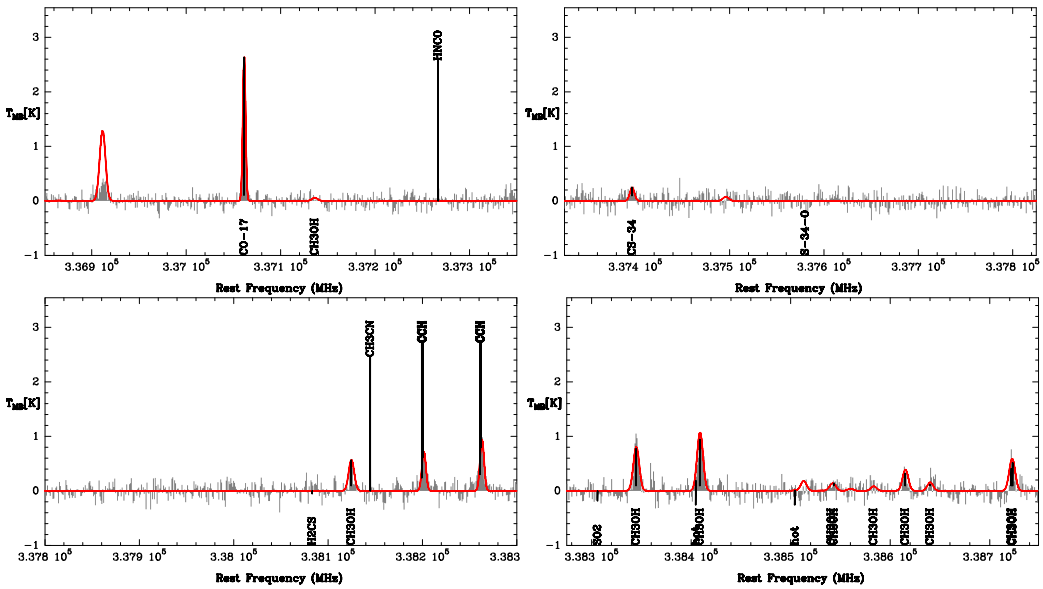

Figure A.42: 338 GHz setup for 18236-1205. The synthetic model spectrum is shown in red.

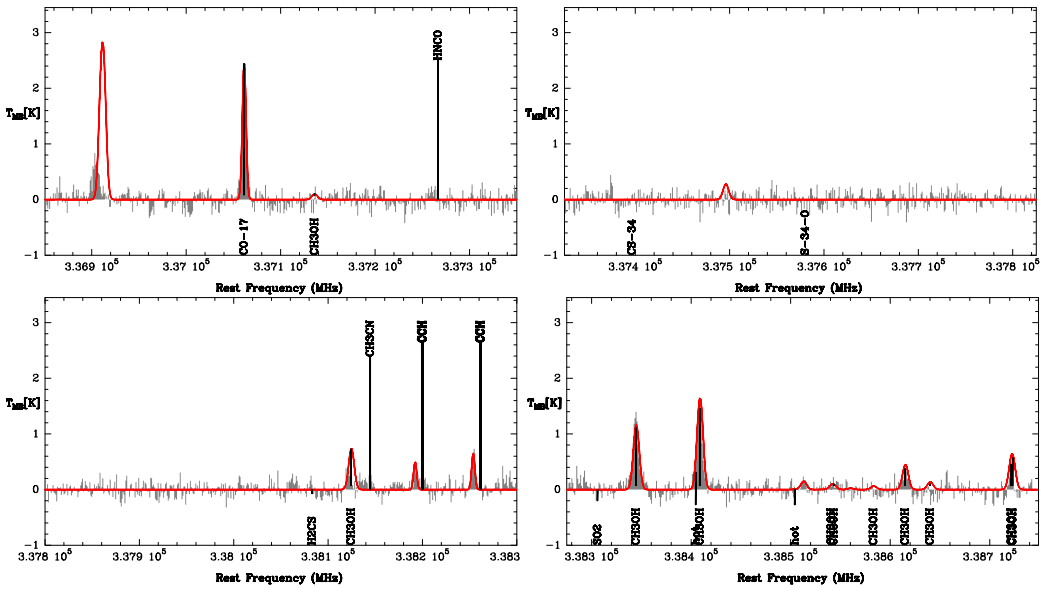

Figure A.43: 338 GHz setup for 18319-0834. The synthetic model spectrum is shown in red.

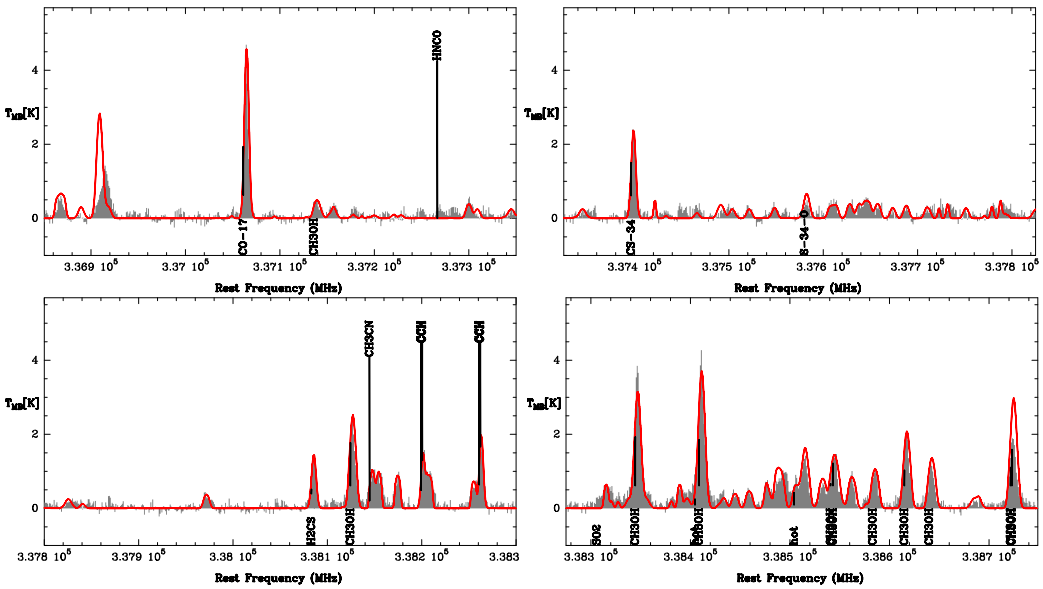

Figure A.44: 338 GHz setup for 18335-0713. The synthetic model spectrum is shown in red.

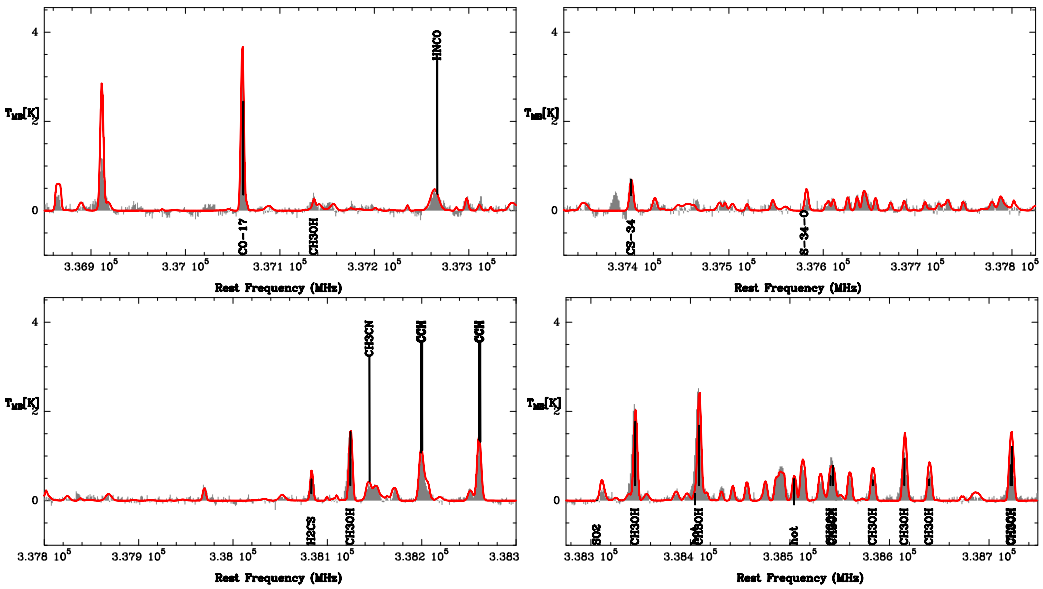

Figure A.45: 338 GHz setup for 15278-5620. The synthetic model spectrum is shown in red.

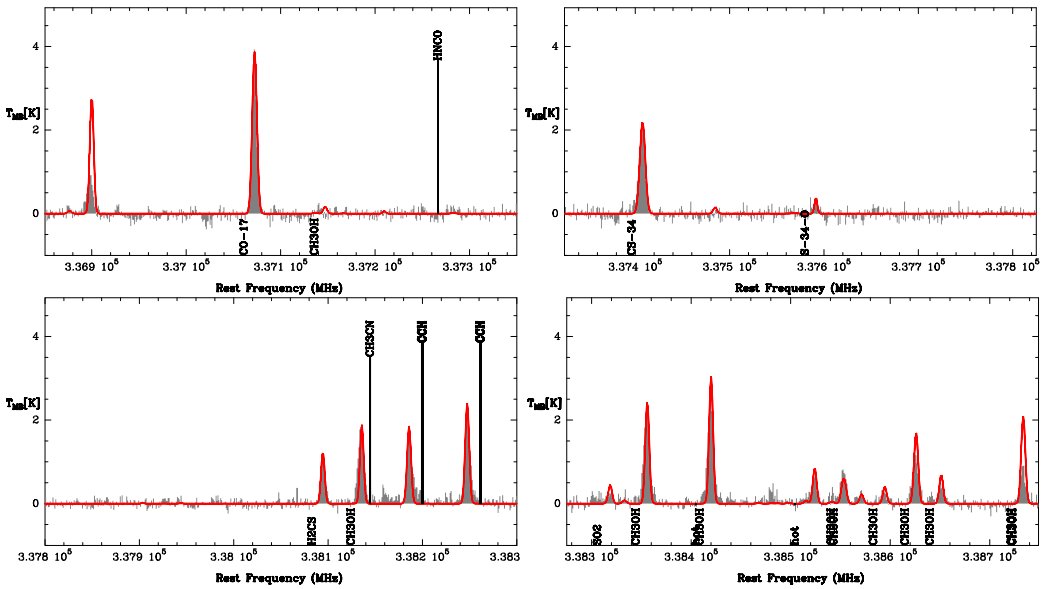

Figure A.46: 338 GHz setup for 16076-5134. The synthetic model spectrum is shown in red.

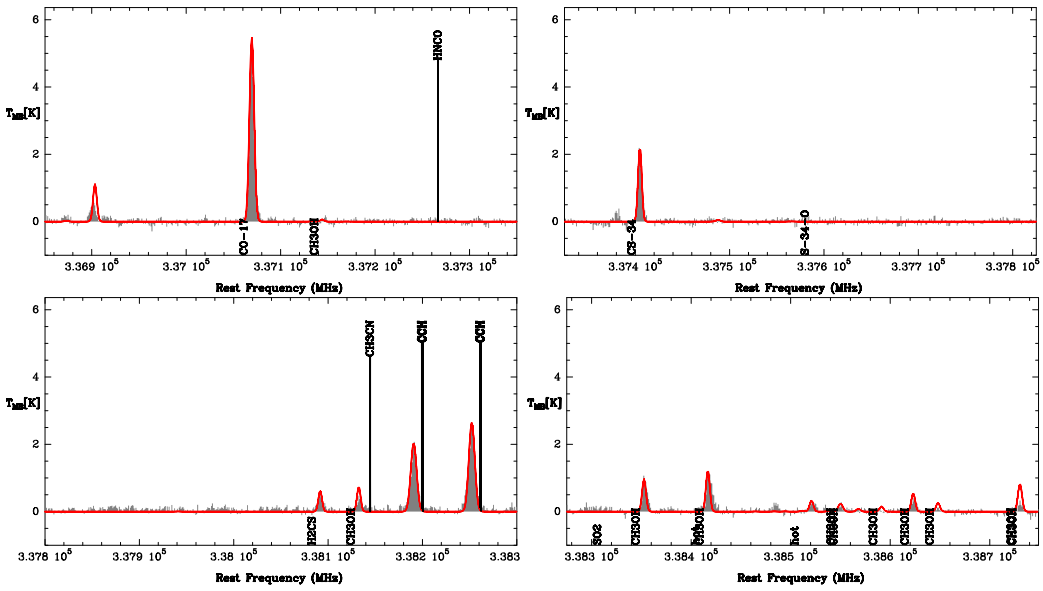

Figure A.47: 338 GHz setup for 16172-5028. The synthetic model spectrum is shown in red.

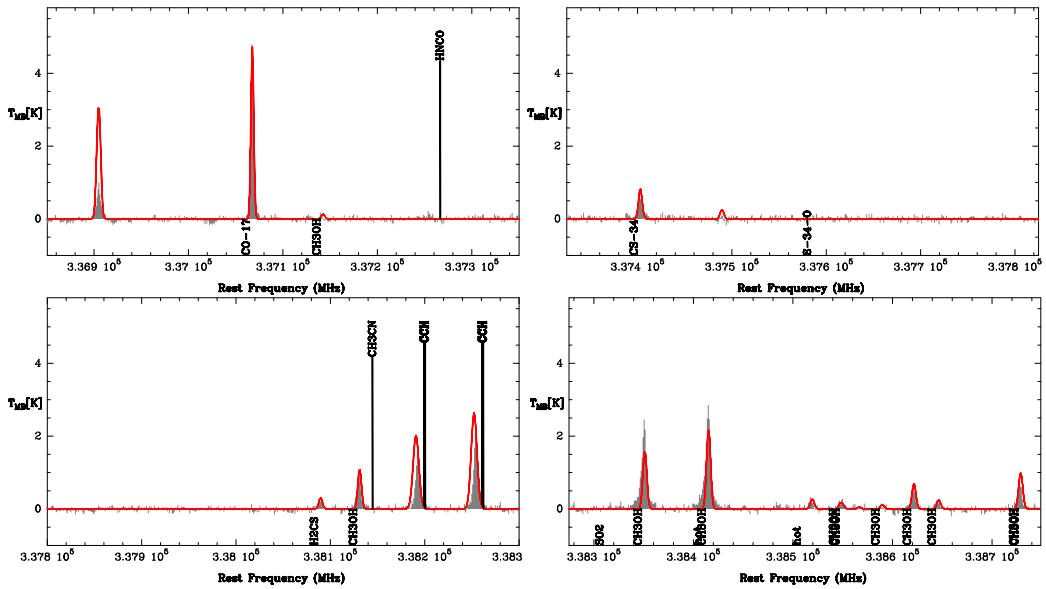

Figure A.48: 338 GHz setup for 16172-5028. The synthetic model spectrum is shown in red.

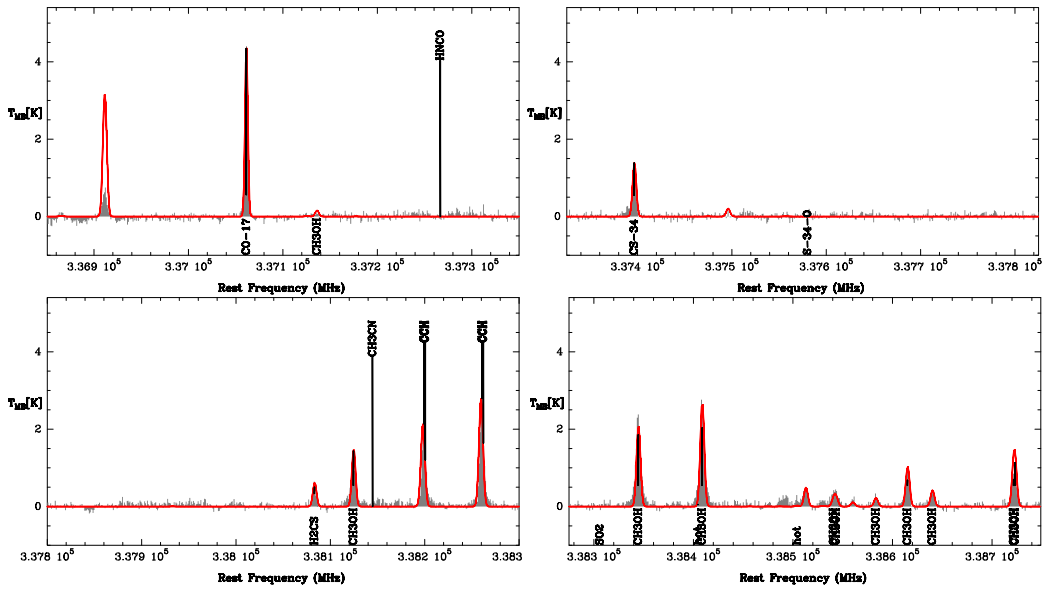

Figure A.49: 338 GHz setup for 16175-5002. The synthetic model spectrum is shown in red.

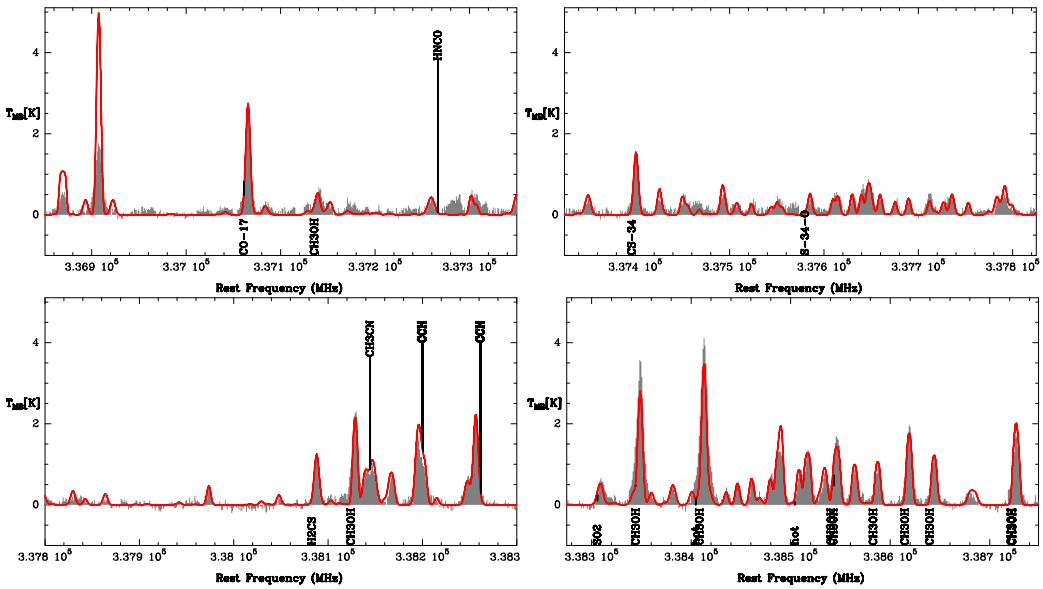

Figure A.50: 338 GHz setup for 17016-4142. The synthetic model spectrum is shown in red.

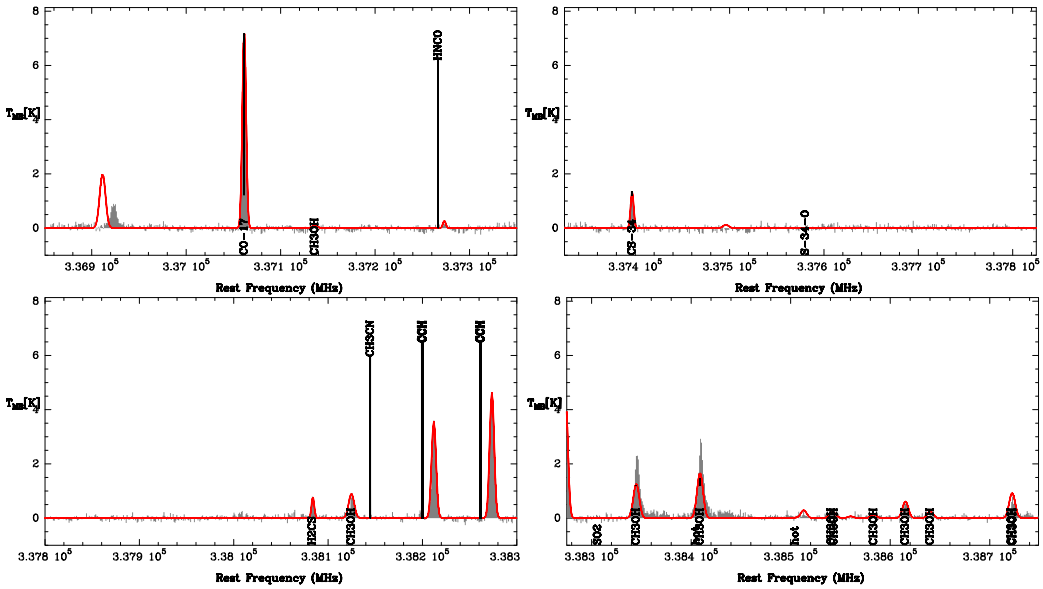

Figure A.51: 338 GHz setup for 17271-3439. The synthetic model spectrum is shown in red.

A.3 Report

A change in intensity ratios found in identical observations between summer 2006 and summer 2007

C. Hieret & P. Schilke

28.08.2007

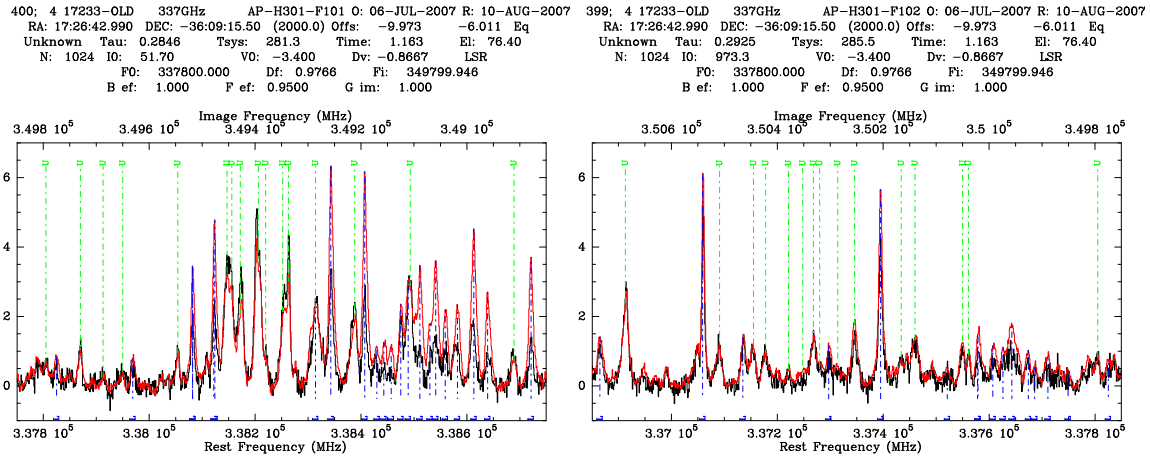

Figure A.52: Setup at 338 GHz in 17233-3606 for both ffts units. The spectrum observed in August 2006 is overplotted in red on the spectrum of July 2007 (black). The green tags mark the USB lines, the blue tags the LSB lines.

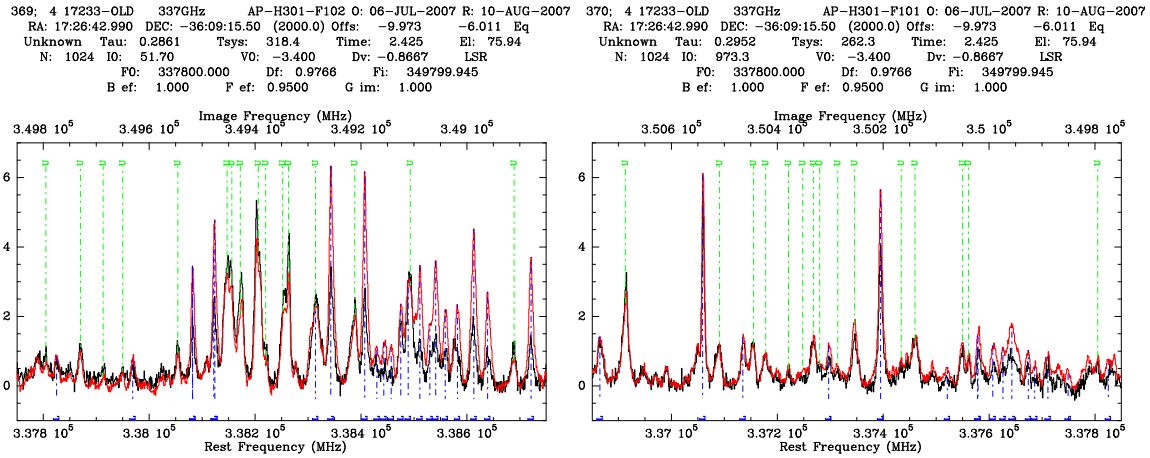

Figure A.53: Setup at 338 GHz in 17233-3606 for both ffts units. In this setup, the ffts units have been switched in the July 2007 observations. The spectrum observed in August 2006 is overplotted in red on the spectrum of July 2007 (black). The green tags mark the USB lines, the blue tags the LSB lines.

Description of the Observations

Several observations done in summer 2006 with the APEX 2a receiver were re-observed this July, using the same setups and positions. Comparing this observations to the one from summer 2006, S. Leurini and S. Thorwirth observed a change in intensity affecting several sources and frequency setups. The same has been reported by A. Belloche regarding another project, which is not included here.
The data of 2007 has been observed on the 06.07.2007.

As a first check, we made sure that pointing and focus corrections were properly applied, that the quality of the pointing was good and that the pointing source was observed at the right position in both years.

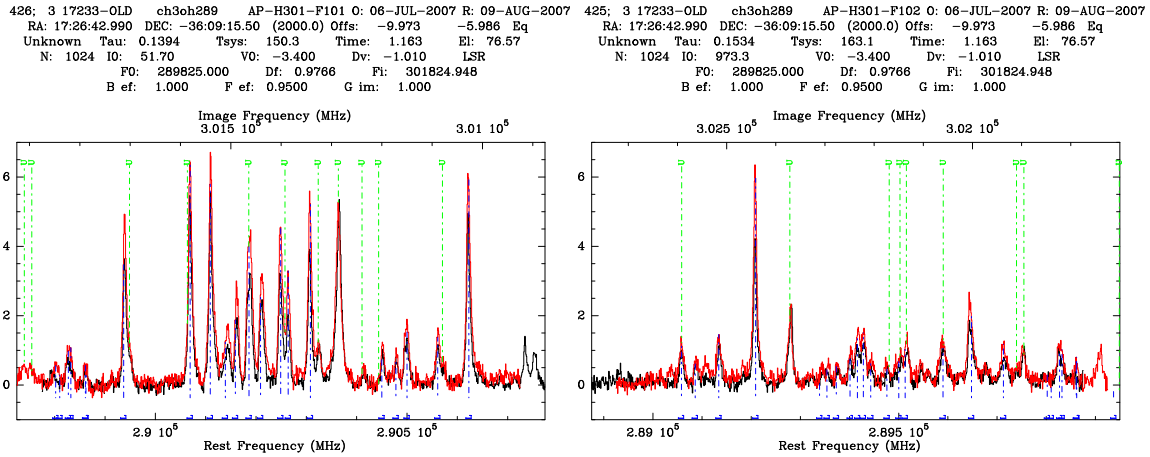

Figure A.54: Setup at 290 GHz in 17233-3606 for both ffts units. The spectrum observed in August 2006 is overplotted in red on the spectrum of July 2007 (black).The green tags mark the USB lines, the blue tags the LSB lines. Note the 50 MHz shift between the two setups.

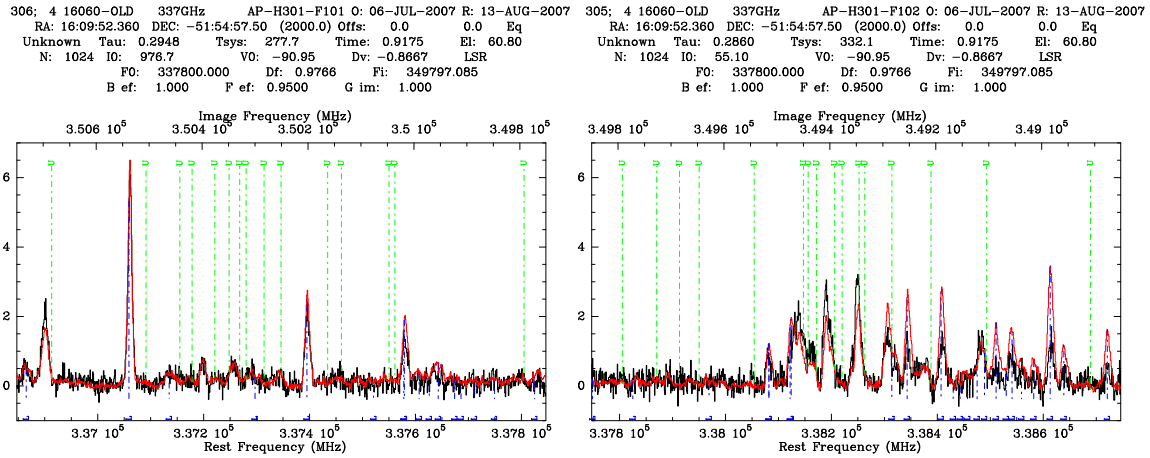

Figure A.55: Setup at 338 GHz in 16060-5146 for both ffts units. The spectrum observed in August 2006 is overplotted in red on the spectrum of July 2007 (black). left figure: July 2007 FFTS101 and August 2006 FFTS102. right figure: July 2007 FFTS102 and August 2006 FFTS101. The green tags mark the USB lines, the blue tags the LSB lines.

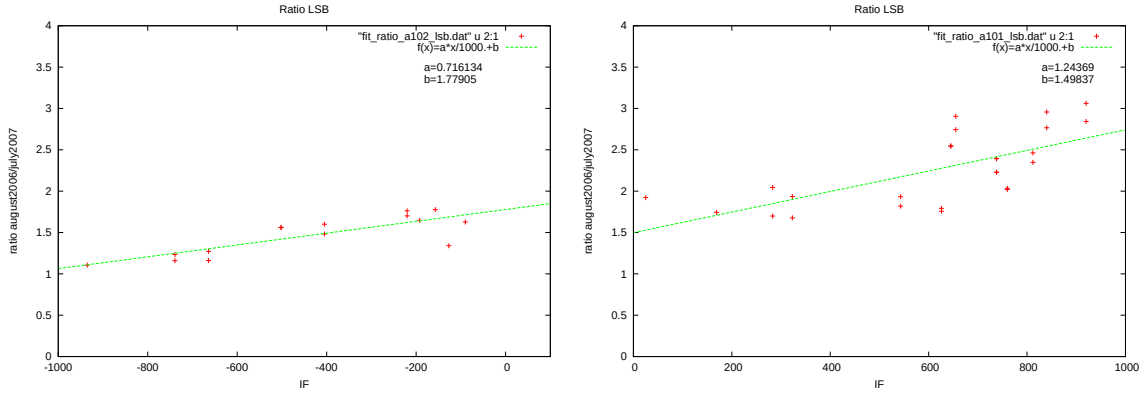

Figure A.56: The fits for the LSB line ratios for each ffts unit in 17233-3606 at 338 GHz. left figure: FFTS 102 for August 2006 and FFTS 101 and FFTs 102 for July 2007. right figure: FFTS 101 for August 2006 and FFTS 101 and FFTs 102 for July 2007. The fit parameters a and b are shown in the plot.

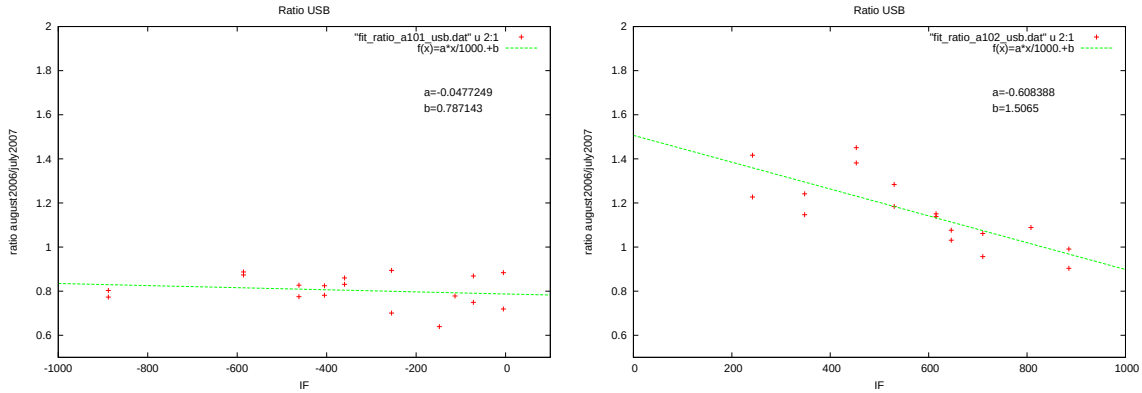

Figure A.57: The fits for the USB line ratios for each ffts unit in 17233-3606 at 338 GHz. Left figure: FFTS 101 for August 2006 and FFTS 101 and FFTs 102 for July 2007. right figure: FFTS unit 102 for August 2006 and FFTS 101 and FFTs 102 for July 2007.The fit parameters a and b are shown in the plot.

This change in intensities seems to be not uniform over the whole band. In order to analysis this problem further, we have obtained the ratios of the areas under the lines for each sideband and plotted them versus IF frequency. This was then fitted with a linear fit (f(x)=ax+b) for each ffts unit seperately.

Fits to the Line Ratios in USB and LSB

Comparison of the Fits

338 GHz

In the lower sideband, there is a clear trend visible in the data of 17233-3606, were the line ratios get bigger over the band. There is a small inconsistency at the edges of the two IFs, so that one cannot say for sure that the trend is consistent over the two units, but given

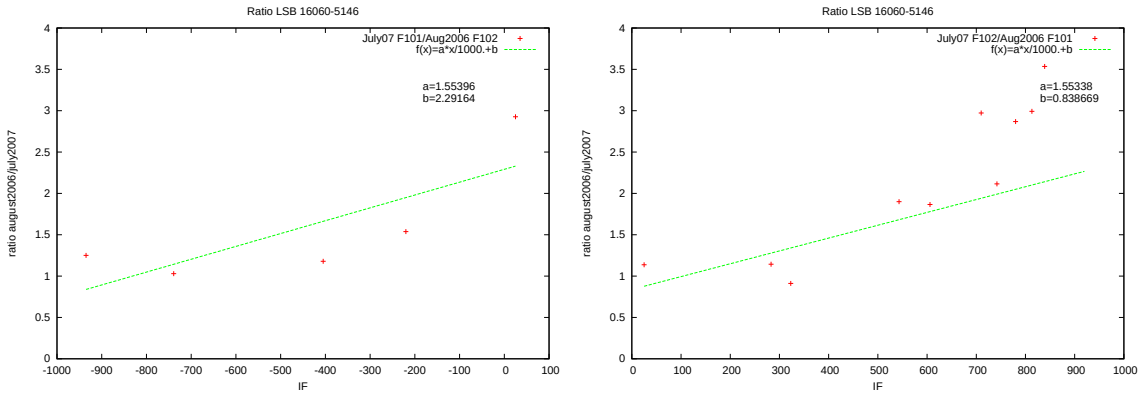

Figure A.58: The fits for the LSB line ratios for each ffts unit in 16060-5146 at 338 GHz. Left figure: FFTS 102 for August 2006 and FTTS 101 for July 2007. right figure: FFTS unit 101 for August 2006 and FTTS 102 for July 2007.The fit parameters a and b are shown in the plot.

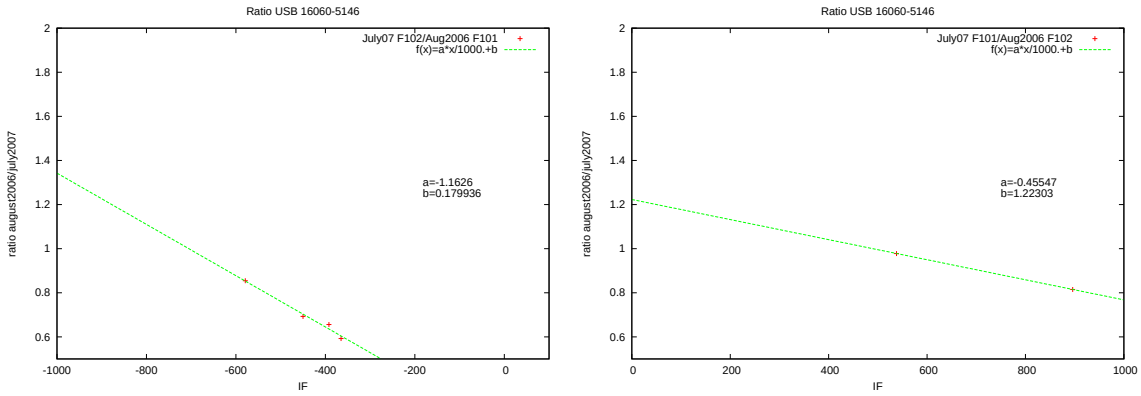

Figure A.59: The fits for the USB line ratios for each ffts unit in 16060-5146 at 338 GHz. Left figure: FFTS 101 for August 2006 and FTTS 102 for July 2007. right figure: FFTS unit 102 for August 2006 and FTTS 101 for July 2007.The fit parameters a and b are shown in the plot.

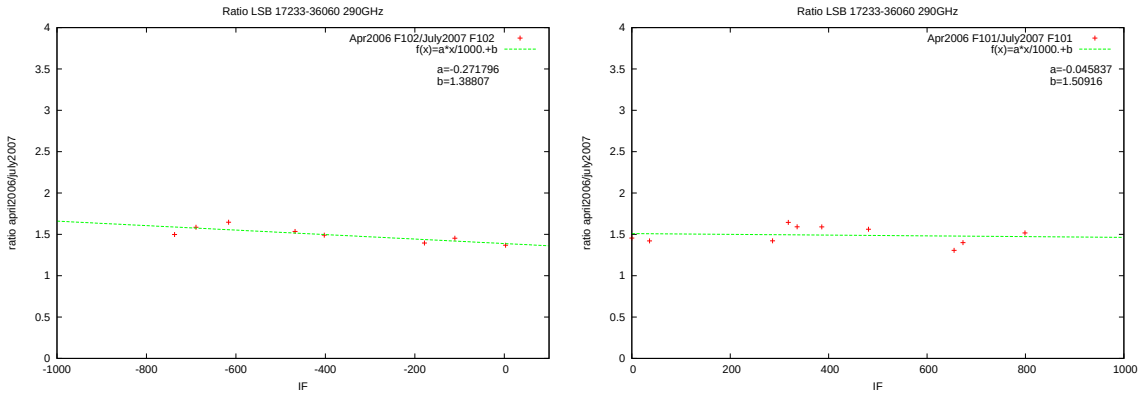

Figure A.60: The fits for the LSB line ratios for each ffts unit in 17233-3606 at 290 GHz. Left figure: FFTS 102 for August 2006 and July 2007. right figure: FFTS 101 for August 2006 and July 2007.The fit parameters a and b are shown in the plot.

the fact that the quality of the spectra is known to degrade somewhat towards the edges of the units, it looks like the trend continues in both units within the errors introduced by taking into account line ratios from the edges of the ffts units. One can also see that the trend is the same, irregardless of which unit (ffts 101 or 102) was used for the observations.
16060-5146 shows a similar trend. It has to be taken into account however that in the spectra of 16060-5146 not as many lines as in 17233-3606 are visible and the weaker ones are often very noisy. The continuos trend in 17233-3606 seems to be the more reliable one.
For the upper sideband, a trend is not so clearly visible. In 17233-3606 it looks like there is a trend to lower ratios over the band, even though for the IF -1000 to 0 MHz band, the fit shows only a very weak trend. In the same band in 16060-5146, the downwards trend is stronger.

290 GHz

For the 290 GHz spectra in 17233-3606, we only obtained a fit for the LSB, due to a lack of suitable data points in the USB.
In both FFTS units, the line ratio is roughly constant, about 1.4 for IF -1000 to 100 MHz and 1.5 for IF 0 to 1000 MHz.
When comparing the results for 290 GHz with those for 338 GHz, it has to be noted that the backends for 290 GHz were shifted by 50 MHz with respect to each other between July 2007 and April 2006 and that the receiver was tuned again when swhitching from 338 GHz to 290 GHz.

Errors in the Plots

To get a rough idea about the errors in the fits, one has to take into account that 16060-5146 is not as line rich as 17233-3606, so the lines are either weaker and therefore noisier, leading to larger errors in the fits, or not even there, in which case the fits have to be done with less data points. Therefore the fits of 17233-3606 seem more reliable.
In case of line blendings, where the contributions from each sideband can't be detangtled, the points were not included in the fit. The same applies to points where one spectrum was so noisy that no reliable ratio could be calculated.

Summary of Fit Results

To summarise, one can say that for the LSB there is a trend towards larger line ratios with growing IF frequency, which is displayed both in 17233-3606 and 16060-5146 at 338 GHz. In the USB, the trend seems to be reverse with the exception of the IF range -1000 to 0 MHz in 17233-3606 which seems constant.
After tuning the receiver to 290 GHz (to a setup with the backend units shifted by 50 MHz compared to April 2006), the trend is no longer visible in the LSB. Now the ratios seems to be constant over the IF range, even though not at the same level in both FFTS units. For the USB no fit could be obtained.

Possible Solutions

An intensity ratio as the one we are seeing in the data can in general have two main reasons. It might either be a problem in the receiver, which was replaced between the two sets of observations (Winter 2006) or a pointing problem. We have checked the pointing in both years and are fairly sure that it was ok both times, but nevertheless a map around the sources should be done to check for extended structure in the sources which could explain a possible intensity offset in case of wrong pointing. Silvia Leurini had already send setups and coordinates to Christophe Risacher to do these maps.
Another scenario that needs to be checked is how the intensity ratios behave when the FFTS units are shifted with respect to each other.

Bibliography

Adams, F. C. 1991, ApJ, 382, 544

André, P., Ward-Thompson, D., & Barsony, M. 2000, Protostars and Planets IV, 59

Araya, E., Hofner, P., Kurtz, S., Bronfman, L., & DeDeo, S. 2005, ApJS, 157, 279

Bally, J., Moeckel, N., & Throop, H. 2005, in Astronomical Society of the Pacific Conference Series, Vol. 341, Chondrites and the Protoplanetary Disk, ed. A. N. Krot, E. R. D. Scott, & B. Reipurth, 81–+

Bally, J. & Zinnecker, H. 2005, AJ, 129, 2281

Bate, M. R. & Bonnell, I. A. 2005, MNRAS, 356, 1201

Beltrán, M. T., Brand, J., Cesaroni, R., et al. 2006, A&A, 447, 221

Benjamin, R. A., Churchwell, E., Babler, B. L., et al. 2003, PASP, 115, 953

Bergin, E. A., Goldsmith, P. F., Snell, R. L., & Langer, W. D. 1997, ApJ, 482, 285

Beuther, H., Churchwell, E. B., McKee, C. F., & Tan, J. C. 2007, in Protostars and Planets V, ed. B. Reipurth, D. Jewitt, & K. Keil, 165–180

Beuther, H., Schilke, P., Menten, K. M., et al. 2002a, ApJ, 566, 945

Beuther, H., Schilke, P., Menten, K. M., et al. 2005, ApJ, 633, 535

Beuther, H., Schilke, P., Sridharan, T. K., et al. 2002b, A&A, 383, 892

Beuther, H., Semenov, D., Henning, T., & Linz, H. 2008a, ApJ, 675, L33

Beuther, H. & Shepherd, D. 2005, in Cores to Clusters: Star Formation with Next Generation Telescopes, ed. M. S. N. Kumar, M. Tafalla, & P. Caselli, 105–119

Beuther, H., Walsh, A., Schilke, P., et al. 2002c, A&A, 390, 289

Beuther, H., Zhang, Q., Bergin, E. A., & Sridharan, T. K. 2008b, ArXiv e-prints

Beuther, H., Zhang, Q., Reid, M. J., et al. 2006a, ApJ, 636, 323

Beuther, H., Zhang, Q., Sridharan, T. K., Lee, C.-F., & Zapata, L. A. 2006b, A&A, 454, 221

Bisschop, S. E., Jørgensen, J. K., van Dishoeck, E. F., & de Wachter, E. B. M. 2007, A&A, 465, 913

Blake, G. A., Mundy, L. G., Carlstrom, J. E., et al. 1996, ApJ, 472, L49+

Bonnell, I. A. & Bate, M. R. 2006, MNRAS, 370, 488

Bonnell, I. A., Clarke, C. J., Bate, M. R., & Pringle, J. E. 2001, MNRAS, 324, 573

Bonnell, I. A. & Davies, M. B. 1998, MNRAS, 295, 691

Bronfman, L., Nyman, L.-A., & May, J. 1996, A&AS, 115, 81

Busfield, A. L., Purcell, C. R., Hoare, M. G., et al. 2006, MNRAS, 366, 1096

Cabrit, S. & Bertout, C. 1990, ApJ, 348, 530

Carey, S. J., Feldman, P. A., Redman, R. O., et al. 2000, ApJ, 543, L157

Carey, S. J., Noriega-Crespo, A., Mizuno, D. R., et al. 2006, in Bulletin of the American Astronomical Society, Vol. 38, Bulletin of the American Astronomical Society, 1023–+

Caselli, P., Hasegawa, T. I., & Herbst, E. 1993, ApJ, 408, 548

Caswell, J. L. 1998, MNRAS, 297, 215

Caswell, J. L. 2001, MNRAS, 326, 805

Cesaroni, R. 2008, Ap&SS, 313, 23

Cesaroni, R., Galli, D., Lodato, G., Walmsley, C. M., & Zhang, Q. 2007, in Protostars and Planets V, ed. B. Reipurth, D. Jewitt, & K. Keil, 197–212

Cesaroni, R., Olmi, L., Walmsley, C. M., Churchwell, E., & Hofner, P. 1994, ApJ, 435, L137

Charnley, S. B., Tielens, A. G. G. M., & Millar, T. J. 1992, ApJ, 399, L71

Churchwell, E., Walmsley, C. M., & Wood, D. O. S. 1992, A&A, 253, 541

Comito, C., Schilke, P., Phillips, T. G., et al. 2005, ApJS, 156, 127

Cyganowski, C. J., Whitney, B. A., Holden, E., et al. 2008, ArXiv e-prints

Dobbs, C. L., Bonnell, I. A., & Clark, P. C. 2005, MNRAS, 360, 2

Egan, M. P., Price, S. D., & Kraemer, K. E. 2003, in Bulletin of the American Astronomical Society, Vol. 35, Bulletin of the American Astronomical Society, 1301–+

Faúndez, S., Bronfman, L., Garay, G., et al. 2004, A&A, 426, 97

Fontani, F., Pascucci, I., Caselli, P., et al. 2007, A&A, 470, 639

Friedel, D. N., Snyder, L. E., Turner, B. E., & Remijan, A. 2004, ApJ, 600, 234

Garay, G., Brooks, K. J., Mardones, D., & Norris, R. P. 2006, ApJ, 651, 914

Garrod, R. T., Weaver, S. L. W., & Herbst, E. 2008, ApJ, 682, 283

Guilloteau, S. & Dutrey, A. 2008, Ap&SS, 313, 95

Güsten, R., Nyman, L. Å., Schilke, P., et al. 2006, A&A, 454, L13

Hatchell, J., Thompson, M. A., Millar, T. J., & MacDonald, G. H. 1998, A&AS, 133, 29

Hatchell, J. & van der Tak, F. F. S. 2003, A&A, 409, 589

Helmich, F. P. & van Dishoeck, E. F. 1997, A&AS, 124, 205

Henning, T., Lapinov, A., Schreyer, K., Stecklum, B., & Zinchenko, I. 2000, A&A, 364, 613

Heyminck, S., Kasemann, C., Güsten, R., de Lange, G., & Graf, U. U. 2006, A&A, 454, L21

Hildebrand, R. H. 1983, QJRAS, 24, 267

Hill, T., Burton, M. G., Minier, V., et al. 2005, MNRAS, 363, 405

Hill, T., Thompson, M. A., Burton, M. G., et al. 2006, MNRAS, 368, 1223

Högbom, J. A. 1974, A&AS, 15, 417

Hopkins, A. M., Miller, C. J., Connolly, A. J., et al. 2002, AJ, 123, 1086

Hunter, T. R., Churchwell, E., Watson, C., et al. 2000, AJ, 119, 2711

Jørgensen, J. K., Schöier, F. L., & van Dishoeck, E. F. 2004, A&A, 416, 603

Jørgensen, J. K., Schöier, F. L., & van Dishoeck, E. F. 2005, A&A, 437, 501

Kalberla, P. M. W. 2003, ApJ, 588, 805

Kalberla, P. M. W., Dedes, L., Kerp, J., & Haud, U. 2007, A&A, 469, 511

Kennicutt, R. C. 2005, in IAU Symposium, Vol. 227, Massive Star Birth: A Crossroads of Astrophysics, ed. R. Cesaroni, M. Felli, E. Churchwell, & M. Walmsley, 3–11

Klein, B., Philipp, S. D., Krämer, I., et al. 2006, A&A, 454, L29

Klein, R., Posselt, B., Schreyer, K., Forbrich, J., & Henning, T. 2005, ApJS, 161, 361

Kroupa, P. 2002, Science, 295, 82

Krumholz, M. R. 2008, in Astronomical Society of the Pacific Conference Series, Vol. 387, Massive Star Formation: Observations Confront Theory, ed. H. Beuther, H. Linz, & T. Henning, 200–+

Krumholz, M. R., McKee, C. F., & Klein, R. I. 2005, Nature, 438, 332

Kumar, M. S. N. & Grave, J. M. C. 2007, A&A, 472, 155

Kurtz, S., Cesaroni, R., Churchwell, E., Hofner, P., & Walmsley, C. M. 2000, Protostars and Planets IV, 299

Larson, R. B. 1981, MNRAS, 194, 809

Leurini, S., Hieret, C., Thorwirth, S., et al. 2008, A&A, 485, 167

Leurini, S., Schilke, P., Menten, K. M., et al. 2004, A&A, 422, 573

Leurini, S., Schilke, P., Parise, B., et al. 2006, A&A, 454, L83

Leurini, S., Schilke, P., Wyrowski, F., & Menten, K. M. 2007, A&A, 466, 215

Liu, S.-Y. 2005, in IAU Symposium, Vol. 231, Astrochemistry: Recent Successes and Current Challenges, ed. D. C. Lis, G. A. Blake, & E. Herbst, 217–226

MacDonald, G. H., Gibb, A. G., Habing, R. J., & Millar, T. J. 1996, A&AS, 119, 333

MacLaren, I., Richardson, K. M., & Wolfendale, A. W. 1988, ApJ, 333, 821

MacLeod, G. C., Scalise, E. J., Saedt, S., Galt, J. A., & Gaylard, M. J. 1998, AJ, 116, 1897

Mangum, J. G., Wooten, A., Wadiak, E. J., & Loren, R. B. 1990, ApJ, 348, 542

Mangum, J. G. & Wootten, A. 1993, ApJS, 89, 123

Mardones, D., Myers, P. C., Tafalla, M., et al. 1997, ApJ, 489, 719

McKee, C. F. & Ostriker, E. C. 2007, ARA&A, 45, 565

McKee, C. F. & Tan, J. C. 2003, ApJ, 585, 850

McLaughlin, D. E. & Pudritz, R. E. 1996, ApJ, 469, 194

Menten, K. M. 1987, PhD thesis, , Bonn University, (1987)

Menten, K. M. 1991, ApJ, 380, L75

Miettinen, O., Harju, J., Haikala, L. K., & Pomrén, C. 2006, A&A, 460, 721

Minier, V., Burton, M. G., Hill, T., et al. 2005, A&A, 429, 945

Minier, V., Ellingsen, S. P., Norris, R. P., & Booth, R. S. 2003, A&A, 403, 1095

Molinari, S., Brand, J., Cesaroni, R., & Palla, F. 2000, A&A, 355, 617

Molinari, S., Pezzuto, S., Cesaroni, R., et al. 2008, A&A, 481, 345

Molinari, S., Testi, L., Rodríguez, L. F., & Zhang, Q. 2002, ApJ, 570, 758

Morata, O. & Herbst, E. 2008, MNRAS, 390, 1549

Mueller, K. E., Shirley, Y. L., Evans, II, N. J., & Jacobson, H. R. 2002, ApJS, 143, 469

Müller, H. S. P., Schlöder, F., Stutzki, J., et al. 2005, in IAU Symposium, Vol. 235, IAU Symposium, 62P–+

Müller, H. S. P., Thorwirth, S., Roth, D. A., & Winnewisser, G. 2001, A&A, 370, L49

Nummelin, A., Bergman, P., Hjalmarson, Å., et al. 2000, ApJS, 128, 213

Nürnberger, D. E. A., Chini, R., Eisenhauer, F., et al. 2007, A&A, 465, 931

Olmi, L., Cesaroni, R., Hofner, P., et al. 2003, A&A, 407, 225

Olmi, L., Cesaroni, R., & Walmsley, C. M. 1993, A&A, 276, 489

Ossenkopf, V. & Henning, T. 1994, A&A, 291, 943

Osterloh, M., Henning, T., & Launhardt, R. 1997, ApJS, 110, 71

Palla, F. & Stahler, S. W. 1992, ApJ, 392, 667

Palla, F. & Stahler, S. W. 1993, ApJ, 418, 414

Panagia, N. 1973, AJ, 78, 929

Pickett, H. M., Poynter, I. R. L., Cohen, E. A., et al. 1998, Journal of Quantitative Spectroscopy and Radiative Transfer, 60, 883

Pillai, T., Wyrowski, F., Carey, S. J., & Menten, K. M. 2006, A&A, 450, 569

Plume, R., Jaffe, D. T., Evans, II, N. J., Martin-Pintado, J., & Gomez-Gonzalez, J. 1997, ApJ, 476, 730

Purcell, C. R., Balasubramanyam, R., Burton, M. G., et al. 2006, MNRAS, 367, 553

Reid, M. J., Argon, A. L., Masson, C. R., Menten, K. M., & Moran, J. M. 1995, ApJ, 443, 238

Requena-Torres, M. A., Martín-Pintado, J., Rodríguez-Franco, A., et al. 2006, A&A, 455, 971

Richards, P. J., Little, L. T., Heaton, B. D., & Toriseva, M. 1987, MNRAS, 228, 43

Risacher, C., Vassilev, V., Monje, R., et al. 2006, A&A, 454, L17

Robitaille, T. P., Whitney, B. A., Indebetouw, R., & Wood, K. 2007, ApJS, 169, 328

Robitaille, T. P., Whitney, B. A., Indebetouw, R., Wood, K., & Denzmore, P. 2006, ApJS, 167, 256

Rodgers, S. D. & Charnley, S. B. 2001, ApJ, 546, 324

Schilke, P., Benford, D. J., Hunter, T. R., Lis, D. C., & Phillips, T. G. 2001, ApJS, 132, 281

Schilke, P., Comito, C., Thorwirth, S., et al. 2006, A&A, 454, L41

Schilke, P., Phillips, T. G., & Mehringer, D. M. 1999, in The Physics and Chemistry of the Interstellar Medium, Proceedings of the 3rd Cologne-Zermatt Symposium, held in Zermatt, September 22-25, 1998, Eds.: V. Ossenkopf, J. Stutzki, and G. Winnewisser, GCA-Verlag Herdecke, ISBN 3-928973-95-9, 330–+

Schöier, F. L., Jørgensen, J. K., van Dishoeck, E. F., & Blake, G. A. 2002, A&A, 390, 1001

Schreyer, K., Helmich, F. P., van Dishoeck, E. F., & Henning, T. 1997, A&A, 326, 347

Shirley, Y. L., Evans, II, N. J., Young, K. E., Knez, C., & Jaffe, D. T. 2003, ApJS, 149, 375

Shirley, Y. L., Wu, J., Shane Bussmann, R., & Wootten, A. 2008, in Astronomical Society of the Pacific Conference Series, Vol. 387, Massive Star Formation: Observations Confront Theory, ed. H. Beuther, H. Linz, & T. Henning, 401–+

Shu, F. H. 1977, ApJ, 214, 488

Shu, F. H., Adams, F. C., & Lizano, S. 1987, ARA&A, 25, 23

Siringo, G., Weiss, A., Kreysa, E., et al. 2007, The Messenger, 129, 2

Smith, I. W. M., Herbst, E., & Chang, Q. 2004, MNRAS, 350, 323

Sridharan, T. K., Beuther, H., Schilke, P., Menten, K. M., & Wyrowski, F. 2002, ApJ, 566, 931

Sutton, E. C., Jaminet, P. A., Danchi, W. C., & Blake, G. A. 1991, ApJS, 77, 255

Sutton, E. C., Peng, R., Danchi, W. C., et al. 1995, ApJS, 97, 455

Tafalla, M., Santiago-García, J., Myers, P. C., et al. 2006, A&A, 455, 577

Tan, J. C. 2006, ArXiv Astrophysics e-prints

Tan, J. C. & McKee, C. F. 2002, in Astronomical Society of the Pacific Conference Series, Vol. 267, Hot Star Workshop III: The Earliest Phases of Massive Star Birth, ed. P. Crowther, 267–+

Turner, B. E. 1991, ApJS, 76, 617

Urquhart, J. S., Busfield, A. L., Hoare, M. G., et al. 2007a, A&A, 461, 11

Urquhart, J. S., Busfield, A. L., Hoare, M. G., et al. 2007b, A&A, 474, 891

van der Tak, F. 2008, in Astronomical Society of the Pacific Conference Series, Vol. 387, Massive Star Formation: Observations Confront Theory, ed. H. Beuther, H. Linz, & T. Henning, 101–+

Van der Tak, F. F. S., Boonman, A. M. S., Braakman, R., & van Dishoeck, E. F. 2003, A&A, 412, 133

van der Tak, F. F. S., Boonman, A. M. S., Braakman, R., & van Dishoeck, E. F. 2003, A&A, 412, 133

van der Tak, F. F. S., van Dishoeck, E. F., & Caselli, P. 2000a, A&A, 361, 327

van der Tak, F. F. S., van Dishoeck, E. F., Evans, II, N. J., & Blake, G. A. 2000b, ApJ, 537, 283

van Dishoeck, E. F., Blake, G. A., Jansen, D. J., & Groesbeck, T. D. 1995, ApJ, 447, 760

Vázquez-Semadeni, E., Ballesteros-Paredes, J., Klessen, R. S., & Jappsen, A. K. 2008, in Astronomical Society of the Pacific Conference Series, Vol. 387, Massive Star Formation: Observations Confront Theory, ed. H. Beuther, H. Linz, & T. Henning, 240–+

Viti, S., Collings, M. P., Dever, J. W., McCoustra, M. R. S., & Williams, D. A. 2004, MNRAS, 354, 1141

Walmsley, C. M., Cesaroni, R., Churchwell, E., & Hofner, P. 1992, in Astronomische Gesellschaft Abstract Series, 93–93

Walsh, A. J., Burton, M. G., Hyland, A. R., & Robinson, G. 1998, MNRAS, 301, 640

Walsh, A. J., Hyland, A. R., Robinson, G., & Burton, M. G. 1997, MNRAS, 291, 261

Watt, S. & Mundy, L. G. 1999, ApJS, 125, 143

Williams, S. J., Fuller, G. A., & Sridharan, T. K. 2004, A&A, 417, 115

Wilner, D. J., De Pree, C. G., Welch, W. J., & Goss, W. M. 2001, ApJ, 550, L81

Wilner, D. J., Welch, W. J., & Forster, J. R. 1995, ApJ, 449, L73+

Wolfire, M. G. & Cassinelli, J. P. 1987, ApJ, 319, 850

Wood, D. O. S. & Churchwell, E. 1989, ApJ, 340, 265

Wouterloot, J. G. A. & Brand, J. 1989, A&AS, 80, 149

Wu, J. & Evans, II, N. J. 2003, ApJ, 592, L79

Wu, Y., Henkel, C., Xue, R., Guan, X., & Miller, M. 2007, ApJ, 669, L37

Wu, Y., Wei, Y., Zhao, M., et al. 2004, A&A, 426, 503

Wyrowski, F., Heyminck, S., Güsten, R., & Menten, K. M. 2006a, A&A, 454, L95

Wyrowski, F., Menten, K. M., Schilke, P., et al. 2006b, A&A, 454, L91

Wyrowski, F., Schilke, P., Walmsley, C. M., & Menten, K. M. 1999, ApJ, 514, L43

Yorke, H. W. & Sonnhalter, C. 2002, ApJ, 569, 846

Zinchenko, I., Henkel, C., & Mao, R. Q. 2000, A&A, 361, 1079

Zinnecker, H. & Yorke, H. W. 2007, ARA&A, 45, 481

Ich versichere, daß ich diese Arbeit selbständig verfaßt und keine anderen als die angegebenen Quellen und Hilfsmittel benutzt, sowie Zitate kenntlich gemacht habe.